THE UNIVERSITY of ADELAIDE

Metamorphic and isotopic characterisation of Proterozoic belts at the margins of the North and West Australian Cratons

JADE ANDERSON

Department of Earth Sciences
University of Adelaide

This thesis is submitted in fulfillment of the requirements for the degree of Doctor of Philosophy

November 2015

Table of contents

Abstract

The tectonic evolution of the cratonic elements of Proterozoic Australia has been debated for over 20 years. There is a growing view that plate margin processes were involved in the tectonic evolution and growth of the pre-Cryogenian elements of Australia, however the timing, nature and configuration of cratonic amalgamation remains contentious. This study investigates the metamorphic, geochronological and isotopic evolution of key or debated areas of Proterozoic Australia, focusing on the proposed southern margin of the Archean to Paleoproterozoic North Australian Craton (NAC) in the Arunta Region, and eastern margin of the Archean to Paleoproterozoic West Australian Craton (WAC) in the Rudall Province. The overall aim of this study is to provide new constraints on Proterozoic tectonism in the Arunta Region and Rudall Province in order to better understand the timing and nature of Proterozoic Australia assembly.

In the southern Aileron Province (Arunta Region), the Mount Hay area and Adla Domain occur close to the proposed Paleoproterozoic southern margin of the NAC. Pressure–temperature (*P–T*) constraints indicate the attainment of peak metamorphic conditions of ~8–10 kbar, ~850−900 °C for Mount Hay and the adjacent Capricorn Ridge, and ~7–10 kbar, ~850−900 °C for the Adla Domain fabrics. The granulite facies metamorphism postdates a period of extensive basin development in the Arunta Region between c. 1805−1780 Ma. This basin development was associated with magmatism and localised high temperature–low pressure (HTLP) metamorphism. Hf isotopic data on late Paleoproterozoic granitoids (c. 1650–1625 Ma) from the Aileron Province have isotopic compositions close to CHUR (εHf -6.2 to +1.5) and crustal model ages between 2200–2700 Ma. The granitoids are broadly contemporaneous with the c. 1640–1635 Ma Liebig Orogeny in the Warumpi Province, which involved coeval mafic magmatism, suggesting at least some component of extension. The Paleoproterozoic tectonic evolution of the Arunta Region (southern NAC) is considered to have involved a long-lived (>150 Ma) margin with an overall extensional character punctuated by comparatively localised and short lived periods of thickening.

In the central Aileron Province, the tectonothermal evolution of the Anmatjira Range Province has been debated considerably over the last 20 years. The timing and metamorphic evolution of the Anmatjira Range was investigated using monazite U–Pb geochronology and *P–T* pseudosections calculated for high temperature granulite facies metapelites in the south-eastern Anmatjira Range. Estimated peak conditions of ~870–920 °C and ~6.5–7.2 kbar were attained at c. 1580–1555 Ma, followed by a clockwise retrograde evolution. In the absence of concurrent magmatism, and lack of evidence of decompression from high-*P* conditions, the most probable driver for this metamorphism is heating largely driven by high-heat production from older granites (c. 1820–1760 Ma) in the region.

To the west, the Rudall Province (eastern WAC) is one of the few localities of Proterozoic, Barrovian-style metamorphism in Australia. In several previous studies, the Rudall Province has been considered to record the collision of the WAC and NAC during the Yapungku Orogeny at c. 1780 Ma. However, prior to this study, medium-*P* assemblages interpreted to have grown during the Yapunkgu Orogeny (inferred thermal gradients of minimum ~60–80 °C/kbar) had not been directly age-constrained. Monazite age data on metasedimentary rocks from both medium-*P* and high temperature–low pressure (HTLP) assemblages, and zircon U–Pb age data from a medium-*P,* garnet-diopside bearing mafic amphibolite yield age populations between c. 1380 and 1275 Ma, with one monazite age population of c. 1665 Ma. No evidence for older c. 1780 Ma metamorphism was found in this study. The large age population range of c. 1380–

1275 Ma yielded in this study may be a response of a stage-wise tectonic evolution, involving the accretion of ribbons. If the Yapunkgu Orogeny does reflect the collision between the WAC and NAC, it most likely did not occur until the Mesoproterozoic, contemporaneous with initial breakup stages of supercontinent Nuna.

The overall results of this work support a long-lived, retreating margin on the southern NAC during the late Paleoproterozoic, prior to the assembly of cratonic Australia in the Mesoproterozoic. The proposed Mesoproterozoic assembly negates the need for Australian cratons to be in close proximity in supercontinent Nuna reconstructions.

Declaration

I certify that this work contains no material which has been accepted for the award of any other degree or diploma in my name, in any university or other tertiary institution and, to the best of my knowledge and belief, contains no material previously published or written by another person, except where due reference has been made in the text. In addition, I certify that no part of this work will, in the future, be used in a submission in my name, for any other degree or diploma in any university or other tertiary institution without the prior approval of the University of Adelaide and where applicable, any partner institution responsible for the joint-award of this degree.

I give consent to this copy of my thesis when deposited in the University Library, being made available for loan and photocopying, subject to the provisions of the Copyright Act 1968.

The author acknowledges that copyright of published works contained within this thesis resides with the copyright holder(s) of those works.

I also give permission for the digital version of my thesis to be made available on the web, via the University's digital research repository, the Library Search and also through web search engines, unless permission has been granted by the University to restrict access for a period of time.

18/11/2015

JADE ANDERSON DATE

Publications arising from this thesis

Journal articles

Anderson, J. R., Kelsey, D. E., Hand, M. and Collins W.J. 2013. Conductively driven, high-thermal gradient metamorphism in the Anmatjira Range, central Australia. Journal of Metamorphic Geology, 31(9): 1003–1026.

Anderson, J. R., Kelsey, D. E., Hand, M and Collins W.J. Submitted. Constraints on the timing and conditions of metamorphism on the Paleoproterozoic North Australian Craton margin. Precambrian Research.

Conference abstracts

Anderson, J. R., Kelsey, D. E., Hand, M and Collins W.J. 2013. ca. 1750 Ma arc-related metamorphism in the southern Arunta Complex, central Australia? Goldschmidt, Florence, Italy.

Anderson, J. R., Kelsey, D. E., Hand, M and Collins W.J 2012. P–T conditions and timing of metamorphic belts in the central and southern Arunta Region. International Geologic Congress, Brisbane, Australia.

Statement of authorship

Where indicated at the beginning of each chapter, parts of the research presented in this thesis have been published, are under review or are in preparation to be submitted to scientific journals. The contribution of each author is described below.

ANDERSON, J. R. (Candidate)

Chapters 1 and 4: Project design; sample selection; petrography; SEM; LA−ICP−MS; EPMA data collection; all calculations and data processing; P−T modelling; data interpretation; manuscript design and composition.

Chapter 2: Project design; fieldwork; sample selection; petrography; part SEM; part LA−ICP−MS data collection; part EPMA data collection; calculations and data processing; P−T modelling; data interpretation; manuscript design and composition.

Chapter 3: Project design; sample selection; LA−MC−ICPMS data collection; data processing; data interpretation; manuscript design and composition.

I certify that the above statement is accurate and give permission for the relevant manuscripts to be included in this thesis.

SIGNED DATE

KELSEY, D. E., HAND, M., COLLINS, W. J. (Supervisors)

Chapters 1−4: Project design; fieldwork assistance; guidance with data interpretation and P−T modelling; manuscript review.

I certify that the above statement is accurate and give permission for the relevant manuscripts to be included in this thesis.

SIGNED

SIGNED

SIGNED

LAWSON-WYATT, M.

Chapter 2: fieldwork; part LA−ICP−MS; part SEM; part EPMA data collection; assistance with data interpretation.

I certify that the above statement is accurate and give permission for the relevant manuscript to be included in this thesis.

Acknowledgements

Thinking about my PhD, I've been very fortunate to have many people who have been of great support professionally and personally.

Firstly, I am extremely grateful for the extensive support and guidance of my supervisors David Kelsey, Martin Hand and Bill Collins throughout my PhD. Their extensive knowledge of central Australia, metamorphic geology, and many, many other aspects of Geology, along with their patience(!) throughout my PhD has helped me immensely- I couldn't ask for better supervisors.

A huge thanks must also go to Ben Wade, Aoife McFadden, Ken Neubauer and Angus Netting over at Adelaide Microscopy for their time and willingness to help with analytical work, as well as the many carbon coats on short notice over the years! Hugh Smithies at the Geological Survey of Western Australia is thanked for kindly allowing us access to the Rudall Province legacy samples and for his assistance with maps and the Rudall study. Thanks to David Maidment for his very helpful discussions on the Rudall Province. Thanks also to Honours students Bel Wong, Maddison-Lawson Wyatt and Courtney Fields, whose U–Pb and metamorphic work on the Arunta Region has been enormously helpful in unravelling the Arunta, and who have been great to work with.

Past and present PhDers Dee, Katherine, Kat, Morgan, Lachy, Kieran, Dan, Russell, Frank, Kathryn, Naomi and Lisa have been a great company and source of support over the past few years. More recently, a big thank you to Alec and Bonnie, who have been wonderful company in the write-up box. Katie Howard has also been amazing in providing lab support, and booking (and unbooking) numerous laser sessions. Thanks to Justin for his support over the last few years.

Thank you to my friends Lisa, Megan, Jacqui, Ferial and Adelle- you are all pretty awesome. Finally, thanks to Mum, Dad and Hayley. You are always there for me and have given me more support and encouragement than I could ask for with everything I do.

Introduction and thesis outline

The Paleo to Mesoproterozoic (*c.* 1850−1200 Ma) is an important timeline for understanding the evolution of Proterozoic Australia and the configuration of Australia in the development of supercontinent Nuna (Zhang et al., 2012; Pisarevsky et al., 2014). Recent reviews of global paleomagnetic data suggest that Nuna existed by *c*. 1750−1650 Ma and lasted at least until *c.* 1450 Ma (Zhang et al., 2012; Pisarevsky et al., 2014). Despite some differences in proposed cratonic paleogeography and the timing of the assembly of Nuna, these reconstructions suggested that the three major cratonic blocks of Australia, the West Australian Craton (WAC), North Australian Craton (NAC) and South Australian Craton (SAC), the latter including east Antarctica, formed a key component of Nuna (Fig. 1).

In comparison to many other Paleoproterozoic Terrains, Australia has comparatively less juvenile crust and evidence for considerable recycling and reworking (e.g. Etheridge et al., 1987; Wyborn et al., 1992; Betts et al., 2011). Consequently, it has been debated whether the tectonic evolution of Proterozoic Australia was dominated by intracratonic (Etheridge et al., 1987; Wyborn, 1988; Oliver et al., 1991) or plate margin processes (e.g. Myers et al., 1996; Giles et al., 2002; Bagas, 2004; Maidment et al., 2005; Betts and Giles, 2006; Wade et al., 2006; Bagas et al., 2008; Betts et al., 2008; Payne et al., 2009). There is a growing number of more recent plate tectonic models that favour the operation of plate margin processes during the Paleoproterozoic to Mesoproterozoic and advocate for the amalgamation and/or accretion of major cratonic elements of Australia during this time (e.g. Betts and Giles, 2006; Cawood and Korsch, 2008; Payne et al., 2009; Ahmad and Scrimgeour, 2013). However, there remains debate over the timing and nature of the assembly of the NAC, WAC and SAC (e.g. Myers et al., 1996; Betts and Giles, 2006; Cawood and Korsch, 2008; Payne et al., 2009; Ahmad and Scrimgeour, 2013; Smits et al., 2014). As a consequence, the configuration of these cratons in the Paleoproterozoic to Mesoproterozoic and in supercontinent Nuna is not fully understood.

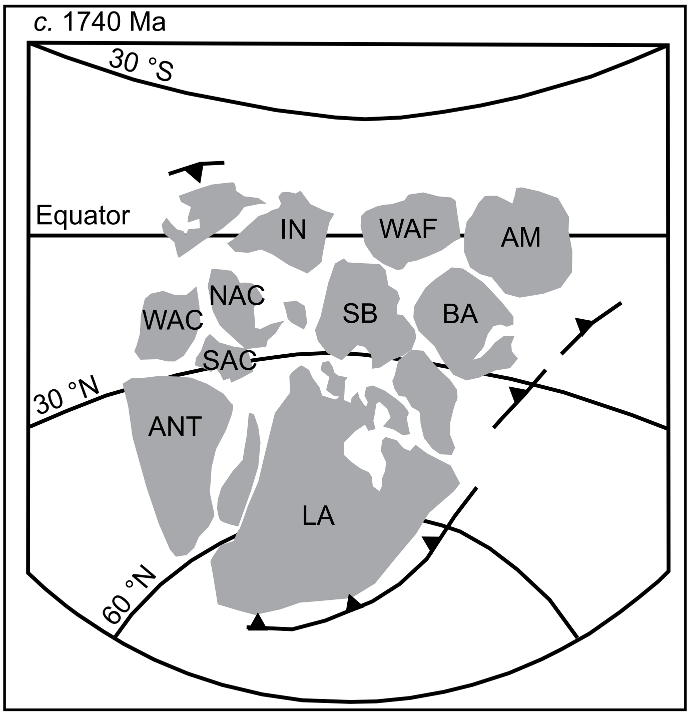

Fig. 1. Recent reconstruction of supercontinent Nuna for *c.* 1740 Ma (from Zhang et al., 2012). Reconstruction shows Proterozoic components of Australia in proposed close proximity, and following restored pre-Ediacaran fit of Australia by Li and Evans (2011). Abbreviations not discussed in text: AM−Amazonia, ANT− Antarctica, BA−Baltica, IN−India, LA−Laurentia, SB−Siberia, WAF−West Africa.

The NAC, WAC and SAC (Fig. 2) are composed largely of Archean–Paleoproterozoic components that have subsequently undergone either lateral crustal growth and/or reworking (e.g. Neumann and Fraser, 2007). Older components of the NAC and SAC share several geological similarities and have therefore been interpreted by some authors as being contiguous throughout most of their tectonic evolution (e.g. Payne et al., 2009). The WAC is commonly interpreted to have collided with the NAC at *c.* 1780 Ma, reflected by the medium- to high-pressure Yapungku Orogeny in the Rudall Province, eastern WAC (e.g. Smithies and Bagas, 1997; Bagas, 2004; see Fig. 2 for location of the Rudall Province). The *c.* 1780 Ma age for the collision of the WAC and NAC is based on crystallisation ages obtained from variably deformed orthogneisses that are inferred to have intruded the surrounding medium- to high-pressure rocks of the Rudall Province at that time (Smithies and Bagas, 1997; Bagas, 2004). In a number of Proterozoic reconstruction models, the NAC, SAC and WAC are interpreted to have been joined or in close proximity to each other since the late Paleoproterozoic (*c.* 1800-1600 Ma; e.g. Betts et al., 2006; Cawood and Korsch, 2008; Payne et al., 2009; Zhang et al., 2012). In a restored model of pre-Ediacaran Australia, Li and Evans (2011) proposed the NAC and WAC were in close proximity after *c.* 1800 Ma, with a ~40° rotation of the WAC–SAC relative to the NAC occurring at *c.* 650–550 Ma to account for discrepancies between paleopoles.

An alternative Mesoproterozoic timeline for the amalgamation of the major cratonic elements of Proterozoic Australia was proposed by Myers et al. (1996) and more recently in a U–Pb age and Hf zircon isotopic study by Smits et al. (2014). Major phases of Mesoproterozoic tectonism occur in the Albany Fraser Orogen (AFO; Fig. 2) on the eastern margin of the Yilgarn Craton (WAC) and Musgrave Province (MP; Fig. 2), central Australia (e.g. Myers et al., 1996; Giles et al., 2004; Betts and Giles, 2006; Cawood and Korsch, 2008; Wade et al., 2008; Aitken

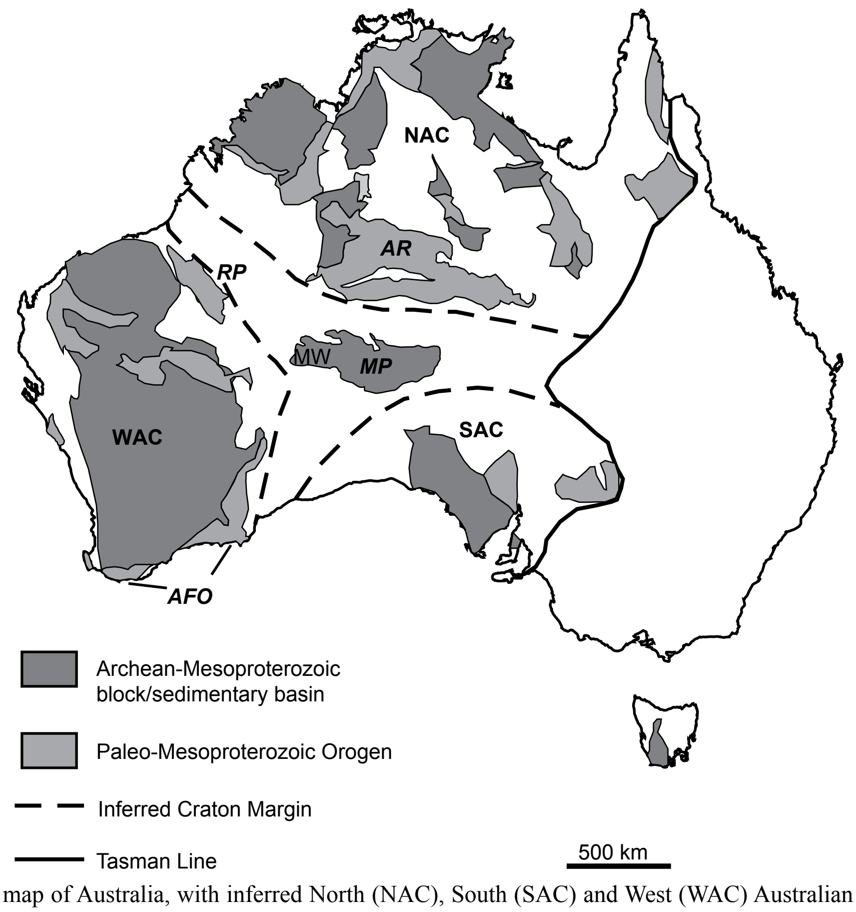

Fig. 2. Simplified map of Australia, with inferred North (NAC), South (SAC) and West (WAC) Australian Cratons indicated. AFO = Albany Fraser Orogen, AR = Arunta Region, MP = Musgrave Province, MW = Mount West Orogeny, RP = Rudall Province. Modified after Cawood and Korsch (2008) and Walsh et al. (2013).

and Betts, 2009; Spaggiari et al., 2009; Smithies et al., 2011). Stage I of the Albany Fraser Orogeny (*c.* 1340–1260 Ma) has been interpreted to be a response to the collision of the WAC with the SAC/Mawson Continent (e.g. Clark et al., 2000) and/or alternatively reflect the closure of a marginal ocean basin and accretion of the Loongana Magmatic Arc (east of the Albany Fraser Orogen) to the WAC, prior to the final convergence of the WAC and SAC/Mawson Continent (Spaggiari et al., 2014). Additional hints of the possibility of the operation of active plate margin processes in Australia during the Mesoproterozoic are reflected by the poorly preserved *c.* 1345–1292 Mount West Orogeny in the western Musgrave Province. The tectonic setting of the Mount West Orogeny remains uncertain. However, the Mount West Orogeny involved the emplacement of the metaluminous, calc to calc-alkaline granitoids of Wankanki Supersuite, which are geochemically similar to those that occur in modern day continental-arc settings (Smithies et al., 2010; Smithies et al., 2011).

Contention over the timing and configuration of cratons during Paleo−Mesoproterozoic Australia is arguably largely a consequence of the complex nature of many Precambrian Australian terrains and scarcity of available geological datasets from some key areas. This study specifically focuses on constraining the tectonic and thermal evolution of data poor, or debated areas of the southern NAC (Fig. 3) and Rudall Province (eastern WAC; Fig. 4), in order to gain further understanding into the evolution of Precambrian Australia, and its configuration in Nuna.

The aims of this project are to:

1. Quantify the tectonothermal regimes that define the southern Arunta region (Aileron Province) in a structural and temporal framework.

2. Quantify the tectonothermal events of the Rudall Province in a temporal framework

3. Characterise the crustal Hf isotopic signature of the Aileron Province during the late-Paleoproterozoic.

4. Present a revised tectonic model for the assembly of Proterozoic Australia using new and existing datasets.

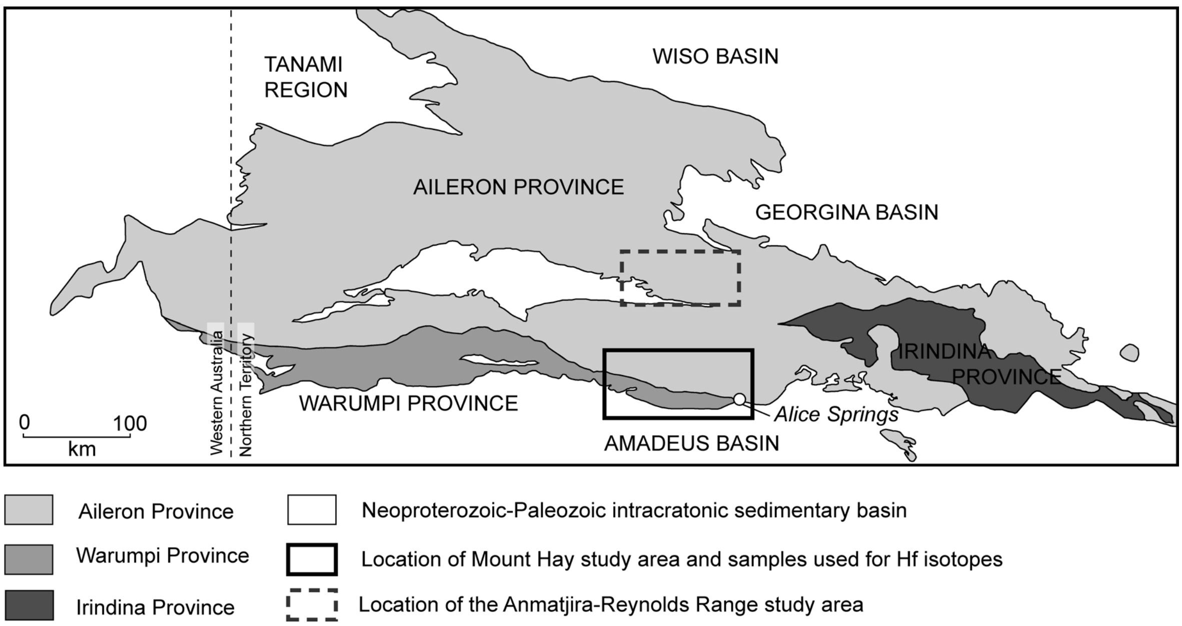

Fig 3. Simplified regional geology map of the Arunta Region, showing provinces, major structural boundaries and study areas (modified from Scrimgeour et al., 2005).

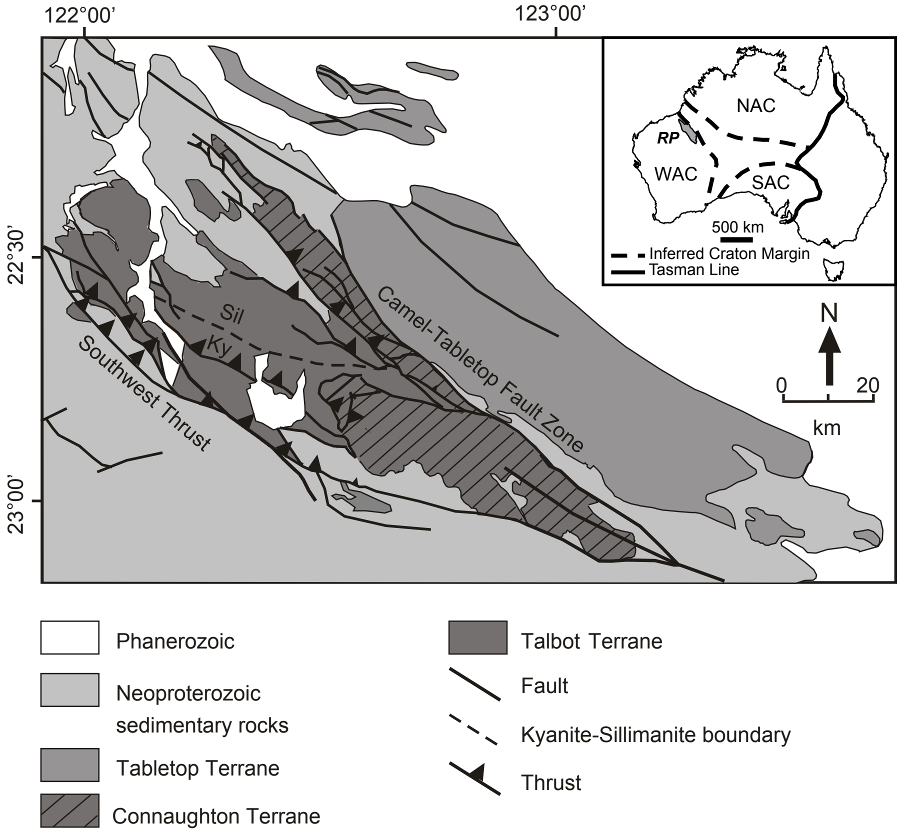

Fig 4. Map of the Rudall Province, showing lithological associations, major structures, and kyanite−sillimanite inferred isograd. Modified from Geological Survey of Western Australia (1999) and Smithies and Bagas (1997). Inset: simplified map of Australia showing the location of the Rudall Province (RP).

Thesis Outline

Chapter 1 provides metamorphic and geochronological constraints for the physical and temporal conditions of metamorphism in the Anmatjira Range, Arunta Region, central Australia. The high-thermal gradient metamorphosed rocks in the Anmatjira Range have been subject to substantial debate over the past 20 years involving the timing, nature, number of metamorphic events and thermal driver for metamorphism. Chapter 1 investigates the regional high-thermal gradient metamorphism in the Anmatjira Range using U−Pb monazite geochronology and $P-T$ pseudosections. Additionally, a new method for reintegrating melt into compositions for granulite facies rocks that have undergone melt loss is presented. This chapter is published as 'Anderson, J. R., Kelsey, D. E., Hand, M. and Collins W.J. 2013. Conductively driven, high-thermal gradient metamorphism in the Anmatjira Range, central Australia. *Journal of Metamorphic Geology*, 31(9): 1003–1026'.

Chapter 2 investigates the metamorphic evolution of the Mount Hay Block and Adla Domain, southern Arunta Region, central Australia. Sparse age and metamorphic data exists for the Mount Hay Bock and Adla Domain, key areas proximal to the postulated paleo-suture of the NAC during the Paleoproterozoic. Chapter 2 combines U−Pb monazite geochronology and $P-T$ pseudosection modelling in order to constrain the timing of metamorphism, and assess the thermal footprint within a km-scale structural architecture. This Chapter has been submitted to *Precambrian Research.*

Chapter 3 presents Hf zircon isotopic data on late Paleoproterozoic magmatic rocks from the Arunta Region (Fig. 3). These magmatic rocks are coeval with the proposed timing of the accretion of the Warumpi Province onto the Aileron Province (NAC) at *c.* 1640−1635 Ma during the Liebig Orogeny (Scrimgeour et al., 2005). The Hf isotopic signature of these rocks can therefore provide insight into crustal source interaction during late-Paleoproterozoic tectonism in the southern Arunta Region.

Chapter 4 investigates the timing and conditions of metamorphism the Yapungku Orogeny in the Rudall Province, eastern Pilbara margin, Western Australia. The Rudall Province is one of the few Precambrian terranes in Australia that records medium-P metamorphism similar to those found in continental collisional orogenic settings. The timing of metamorphism has been in recent years inferred to be broadly coeval with magmatism at *c.* 1780 Ma, however medium-P assemblages have not been directly age-constrained. Chapter 4 addresses this 'gap' by providing zircon and monazite U−Pb metamorphic age data on rocks were metamorphosed during and after the Yapungku Orogeny (D_2). In addition, $P-T$ pseudosection modelling of a garnet−diopside bearing amphibolite and staurolite-bearing metapelite is used constrain the conditions of metamorphism. This chapter is currently in preparation for submission to *Precambrian Research*.

References

Ahmad, M., Scrimgeour, I.R., 2013. Geological Framework, in: Ahmad, M., Munson, T.J. (Eds.), Geology and mineral resources of the Northern Territory, special publication 5. Northern Territory Geological Society.

Aitken, A.R.A., Betts, P.G., 2009. Constraints on the Proterozoic supercontinent cycle from the structural evolution of the south-central Musgrave Province, central Australia. Precambrian Research 168, 284-300.

Bagas, L., 2004. Proterozoic evolution and tectonic setting of the northwest Paterson Orogen, Western Australia. Precambrian Research 128, 475-496.

Bagas, L., Bierlein, F.P., Bodorkos, S., Nelson, D.R., 2008. Tectonic setting, evolution and orogenic gold potential of the late Mesoarchaean Mosquito Creek Basin, North Pilbara Craton, Western Australia. Precambrian Research 160, 227-244.

Betts, P.G., Giles, D., 2006. The 1800-1100 Ma tectonic evolution of Australia. Precambrian Research 144, 92-125.

Betts, P.G., Giles, D., Aitken, A., 2011. Palaeoproterozoic accretion processes of Australia and comparisons with Laurentia. International Geology Review 53, 1357-1376.

Betts, P.G., Giles, D., Mark, G., Lister, G.S., Goleby, B.R., Ailleres, L., 2006. Synthesis of the proterozoic evolution of the Mt Isa Inlier. Australian Journal of Earth Sciences 53, 187-211.

Betts, P.G., Giles, D., Schaefer, B.F., 2008. Comparing 1800-1600 Ma accretionary and basin processes in Australia and Laurentia: Possible geographic connections in Columbia. Precambrian Research 166, 81-92.

Cawood, P.A., Korsch, R.J., 2008. Assembling Australia: Proterozoic building of a continent. Precambrian Research 166, 1-38.

Clark, D.J., Hensen, B.J., Kinny, P.D., 2000. Geochronological constraints for a two-stage history of the Albany-Fraser Orogen, Western Australia. Precambrian Research 102, 155-183.

Etheridge, M.A., Rutland, R.W.R., Wyborn, L.A.I., 1987. Orogenesis and tectonic process in the Early to Middle Proterozoic of northern Australia, in: Kroner, A. (Ed.), Proterozoic Lithospheric Evolution. American Geophysical Union, Washington D.C., pp. 131-147.

Giles, D., Betts, P., Lister, G., 2002. Far-field continental backarc setting for the 1.80-1.67 Ga basins of northeastern Australia. Geology 30, 823-826.

Giles, D., Betts, P.G., Lister, G.S., 2004. 1.8-1.5 Ga links between the North and South Australian Cratons and the Early-Middle Proterozoic configuration of Australia. Tectonophysics 380, 27-41.

GSWA, 1999. Rudall Sheet SF 51-10, 1:250,000 map sheet, 2 ed. Geological Survey of Western Australia, Perth.

Li, Z.X., Evans, D.A.D., 2011. Late Neoproterozoic 40 degrees intraplate rotation within Australia allows for a tighter-fitting and longer-last ing Rodinia. Geology 39, 39-42.

Maidment, D.W., Hand, M., Williams, I.S., 2005. Tectonic cycles in the Strangways Metamorphic Complex, Arunta Inlier, central Australia: geochronological evidence for exhumation and basin formation between two high-grade metamorphic events. Australian Journal of Earth Sciences 52, 205-215.

Moores, E.M., 1991. Southwest U.S.-East Antarctica (SWEAT) connection: A hypothesis. Geology 19, 425-428.

Myers, J.S., Shaw, R.D., Tyler, I.M., 1996. Tectonic evolution of Proterozoic Australia. Tectonics 15, 1431-1446.

Neumann, N.L., Fraser, G.L., 2007. Geochronological synthesis and timespace plots for Proterozoic Australia. Geoscience Australia, Canber ra, p. 216.

Oliver, N.H.S., Holcombe, R.J., Hill, E.J., Pearson, P.J., 1991. Tectono-metamorphic evolution of the Mary Kathleen Fold Belt, northwest Queensland: a reflection of mantle plume processes? Austr. J. Earth. Sci. 38, 425-456.

Payne, J.L., Hand, M., Barovich, K.M., Reid, A., Evans, D.A.D., 2009. Correlations and reconstruction models for the 2500-1500 Ma evo lution of the Mawson Continent, in: Reddy, S.M., Mazumder, R., Evans, D.A.D., and Collins, A.S. (Ed.), Palaeoproterozoic Supercontinents and Global Evolution, pp. 319-355.

Pisarevsky, S.A., Elming, S.-Å., Pesonen, L.J., Li, Z.-X., 2014. Mesoproterozoic paleogeography: Supercontinent and beyond. Precambrian Research 244, 207-225.

Scrimgeour, I.R., Kinny, P.D., Close, D.F., Edgoose, C.J., 2005. High-T granulites and polymetamorphism in the southern Arunta Region, central Australia: Evidence for a 1.64 Ga accretional event. Precambrian Research 142, 1-27.

Smithies, R.H., Bagas, L., 1997. High pressure amphibolite-granulite facies metamorphism in the Paleoproterozoic Rudall Complex, central Western Australia. Precambrian Research 83, 243-265.

Smithies, R.H., Howard, H.M., Evins, P., Kirkland, C.L., Kelsey, D.E., Hand, M., Wingate, M.T.D., Collins, A.S., 2010. Geochemistry, geochronology, and pretrogenesis of Mesoproterozoic felsic rocks in the West Musgrave Province, central Australia, and implica tions for the Mesoproterozoic tectonic evolution of the region. Geological Survey of Western Australia, Perth.

Smithies, R.H., Howard, H.M., Evins, P.M., Kirkland, C.L., Kelsey, D.E., Hand, M., Wingate, M.T.D., Collins, A.S., Belousova, E., 2011. High-Temperature Granite Magmatism, Crust-Mantle Interaction and the Mesoproterozoic Intracontinental Evolution of the Mus grave Province, Central Australia. Journal of Petrology 52, 931-958.

Smits, R.G., Collins, W.J., Hand, M., Dutch, R., Payne, J., 2014. A Proterozoic Wilson cycle identified by Hf isotopes in central Australia: Implications for the assembly of Proterozoic Australia and Rodinia. Geology 42, 231-234.

Spaggiari, C.V., Bodorkos, S., Barquero-Molina, Tyler, I.M., Wingate, M.T.D., 2009. Interpreted Bedrock Geology of the South Yilgarn and central Albany-Fraser Orogen, Western Australia. Geological Survey of Western Australia, Perth.

Spaggiari, C.V., Kirkland, C.L., Smithies, R.H., Wingate, M.T.D., 2014. Tectonic links between Proterozoic sedimentary cycles, basin forma tion and magmatism in the Albany-Fraser Orogen, Western Austraia. Geological Survey of Western Australia, Perth.

Wade, B.P., Barovich, K.M., Hand, M., Scrimgeour, I.R., Close, D.F., 2006. Evidence for Early Mesoproterozoic Arc Magmatism in the Mus grave Block, Central Australia: Implications for Proterozoic Crustal Growth and Tectonic Reconstructions of Australia. Journal of Geology 114, 43-63.

Wade, B.P., Kelsey, D.E., Hand, M., Barovich, K.M., 2008. The Musgrave Province: Stitching north, west and south Australia. Precambrian Research 166, 370-386.

Wyborn, L.A.I., 1988. Petrology, geochemistry and origin of a major Australian 1880-1840 Ma felsic volcano-plutonic suite: amodel for intracontinental felsic magma generation. Precambrian Res. 40/41, 37-60.

Wyborn, L.A.I., Wyborn, D., Warren, R.G., Drummond, B.J., 1992. Proterozoic granite types in Australia: implications for lower crust com position, structure and evolution. Transactions of the Royal Society of Edinburgh 83, 201-210.

Zhang, S., Li, Z.-X., Evans, D.A.D., Wu, H., Li, H., Dong, J., 2012. Pre-Rodinia supercontinent Nuna shaping up: A global synthesis with new paleomagnetic results from North China. Earth and Planetary Science Letters 353, 145-155.

Chapter 1

This chapter has been published as:
Anderson, J. R., Kelsey, D. E., Hand, M. and Collins W.J. 2013. Conductively driven, high-thermal gradient metamorphism in the Anmatjira Range, central Australia. Journal of Metamorphic Geology, 31(9): 1003–1026.

Anderson, J. R., Kelsey, D. E., Hand, M. & Collins, W.J. (2013). Conductively driven, high-thermal gradient metamorphism in the Anmatjira Range, Arunta region, central Australia.
Journal of Metamorphic Geology, *31*(9): 1003–1026.

NOTE:
This publication is included on pages 3 - 32 in the print copy of the thesis held in the University of Adelaide Library.

It is also available online to authorised users at:

http://dx.doi.org/10.1111/jmg.12054

Chapter 2

This chapter is submitted as:

Anderson, J. R., Kelsey, D. E., Hand, M., Collins W.J. and Lawson-Wyatt, M. Submitted. Constraints on the timing and conditions of metamorphism on the Paleoproterozoic North Australian Craton margin. Precambrian Research.

Constraints on the timing and conditions of metamorphism of the Paleoproterozoic North Australian Craton margin

ABSTRACT

Granulites of the Mount Hay Block and surrounding regions in central Australia outcrop to the immediate north of the postulated southern paleo-margin of the North Australian Craton (NAC). As such, these granulites from the Mount Hay area potentially preserve the record of an ancient active margin. Monazite U−Pb dates obtained on metasedimentary granulites yield age populations at c. 1760−1740 Ma, and minor ages at c. 1570–1540 Ma. A kinematically late garnet-bearing pegmatite yields a single monazite population at c. 1540 Ma. Pressure−temperature (*P–T*) pseudosections calculated for garnet−sillimanite−plagioclase−K-feldspar−quartz−biotite ± rutile bearing assemblages yield peak metamorphic conditions of ~8–10 kbar, ~850−900 °C for Mount Hay and the adjacent Capricorn Ridge, and ~7–10 kbar, ~850−900 °C for prominent E–W structures of the Adla Domain. The timing of metamorphism is contemporaneous with the waning stages of arc-like magmatism (calcalkaline-trondhjemite magmatic suite) in the eastern and southern NAC, as well as bimodal magmatism and localised basin development.

The medium-*P* granulite facies metamorphism postdates a period of extensive basin development between c. 1805−1780 Ma associated with magmatism and localised high temperature–low pressure metamorphism (HTLP) in the southern part of the NAC, and was followed by further granulite facies metamorphism and mafic magmatism between c. 1730−1690 Ma. This history points to the development of a long-lived (>100 Ma) margin with an overall extensional character. The dominantly extensional margin was punctuated by at least one comparatively localised and short-lived period of thickening, which may record the arrival of a small scale 'collider' at a segment of the margin.

1. Introduction

The Arunta Region in central Australia comprises the southern North Australian Craton (NAC; Fig. 1) and is important to a number of Proterozoic Australia reconstruction models (e.g. Giles et al., 2004; Betts and Giles, 2006; Wade et al., 2006; Betts et al., 2008; Cawood and Korsch, 2008; Payne et al., 2009). The Arunta Region records multiple phases of late Paleoproterozoic-aged sedimentation, magmatism and episodic orogenesis, which have been interpreted in previous studies to represent an arc or back-arc environment of part of an evolving, long-lived (e.g. Betts and Giles, 2006; Betts et al., 2008) or intermittent convergent plate margin along the southern North Australian Craton (NAC) in the late Paleoproterozoic (Cawood and Korsch, 2008; Payne et al., 2009; Ahmad and Scrimgeour, 2013).

A postulated late-Paleoproterozoic plate margin on the southern NAC is supported by geochemical evidence from spatially restricted c. 1770–1750 Ma intrusive granitic to gabbroic rocks with arc-related geochemical signatures that occur in the south-eastern Arunta Region (Foden et al., 1988; Zhao and Bennett, 1995; Zhao and McCulloch, 1995). In addition, c. 1810, 1780 and 1635 Ma mafic−ultramafic rocks in the southern Arunta Region have been interpreted to have formed in a subduction or back-arc setting (Hoatson et al., 2005). A major system of shear zones, collectively called the Central Australian Suture in the southern Arunta Region have been interpreted as a suture between the NAC and the Warumpi Province to the south (Scrimgeour et al., 2005).

However, classic indicators of

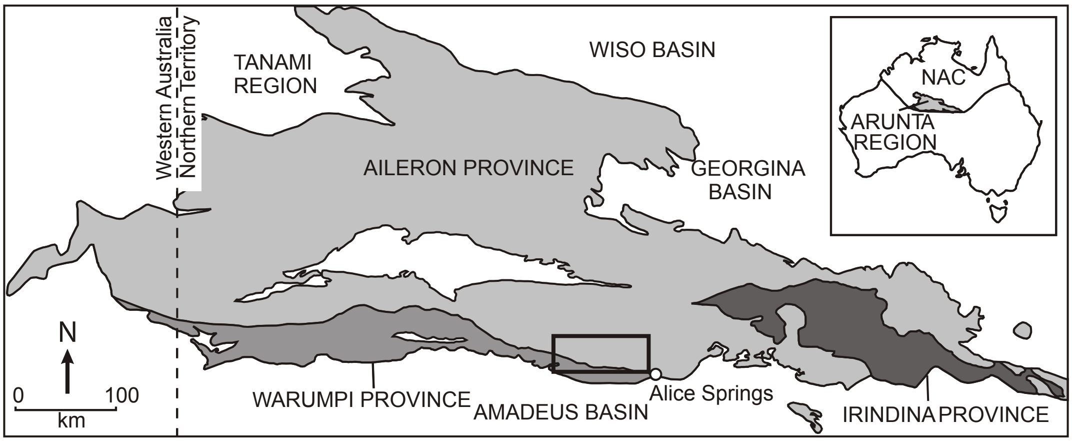

Fig. 1. Location map of the Arunta Region, showing the Aileron, Warumpi and Irindina Provinces, and location of the study area (rectangle) (after Scrimgeour et al., 2005).

contractional convergent margin processes, such as higher-*P* metamorphism have only been sparsely documented in the Arunta Region, and there is little evidence for areally extensive orogenic belts that commonly characterise active plate margins. Instead, the geological record in the Arunta Region during the late Paleoproterozoic is dominated by sedimentation and magmatism that commonly show a south to southeast younging trend. The Arunta Region also shows evidence for spatially and temporally restricted belts of deformation and typically high thermal gradient metamorphism (e.g. Scrimgeour, 2004; Claoue-Long et al., 2008a; Claoue-Long et al., 2008b; Ahmad and Scrimgeour, 2013). Additionally, the record of c. 1750−1745 Ma granitoid magmatism with 'A-type' geochemical characteristics (Cooper et al., 1988; Foden et al., 1988), contemporaneous with basin development (Maidment et al., 2005) and c. 1690 Ma aged dolerite dykes in the eastern Arunta Region (Claoue-Long and Hoatson, 2005) together suggest that the late Paleoproterozoic tectonic evolution of the Arunta Region may have involved a considerable component of extension.

Rare evidence for medium-*P* metamorphic conditions (~9−10 kbar) exists for the c. 1640−1635 Ma Liebig Orogeny in the Warumpi Province, which has been interpreted to record contractional tectonics and the accretion of the Warumpi Province as a formerly exotic terrane to the Aileron Province (NAC) (Scrimgeour et al., 2005). However, in a recent isotopic study, Hollis et al. (2013) proposed that the Warumpi Province was originally contiguous with the Aileron Province (NAC) based on distinctive provenance and inherited zircon affinities with the NAC, with the Liebig Orogeny marking the reattachment of the Warumpi Province to the Aileron Province following a phase of rifting. This interpretation, coupled with evidence for earlier extensional events lends support to the possibility that the late-Paleoproterozoic southern margin of the NAC was characterised by an overall extensional evolution, punctuated by short-lived contractional events, similar to that envisaged for the Paleozoic Tasmanides in eastern Australia (Collins, 2002; Smits et al., 2013). However, the complex and polydeformed nature of the Arunta Region and its comparatively large area means that substantial regions are poorly understood. At present there are limited constraints on the timing and conditions of the metamorphism, and the relationship between metamorphism, magmatism and basin development is not fully understood.

This study examines granulite facies gneisses of the Mount Hay area in the southern Arunta Region, for which existing quantitative constraints on the tectonic evolution are limited (e.g. Glikson, 1984). The Mount Hay area outcrops immediately north of the crustal scale Redbank Shear Zone (part of the proposed Central Australian Suture) and Warumpi Province (Fig. 2; Scrimgeour et al., 2005). In the Mount Hay area, much of the basement geology is obscured by recent sediments, but it includes mafic and felsic magmatic rocks as well as migmatised metasedimentary rocks. Distinct structural domains within the area can be distinguished using the First Vertical Derivative (1VD) of Total Magnetic Intensity (TMI) imagery, revealing a km-scale 'boudin', which comprises the Mount Hay Massif. The Mount Hay Massif is bound by a linear structural belt that extends ~100 km in an east–west direction (Fig. 2). Zircon U–Pb age data from metaigneous rocks provide the only existing published geochronology. The aims of this study are thus to: 1) provide *P–T–t* information for the timing of metamorphism from a data-poor, yet important part of the North Australian Craton; and 2) place the metamorphic history into the regional evolutionary framework in order to make inferences about the nature of the inferred Paleoproterozoic margin to the NAC.

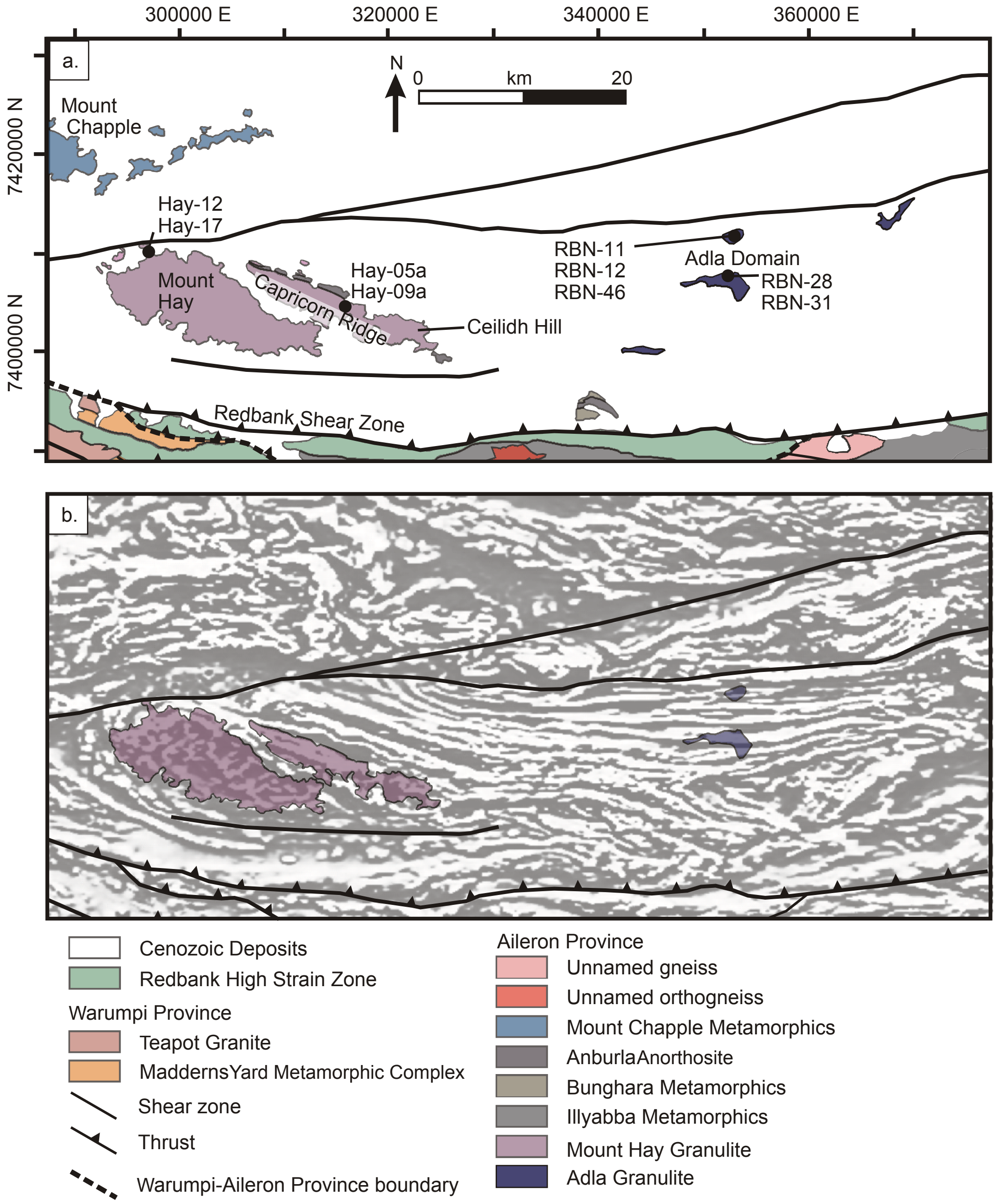

Fig. 2. (a) simplified geological map of the Mount Hay area and Adla Domain showing major structures, geological units and sample locations (modified from BMR, 1983; Shaw and Warren, 1995), (b) Total Magnetic Intensity (TMI) imagery of the area (Northern Territory Geological Survey, 1997a; 1997b).

2. Geological Background

2.1 The Arunta Region

The Arunta Region records a complex history involving multiple cycles of tectonism commencing before 1800 Ma and spanning over a c. 1500 Ma time-frame (e.g. Hand and Buick, 2001; Claoue-Long and Hoatson, 2005; Maidment et al., 2005; Claoue-Long et al., 2008a; Ahmad and Scrimgeour, 2013). The Arunta region has been divided into the Aileron, Warumpi and Irindina Provinces, which were defined based on differing protolith ages and tectonic histories (Ahmad and Scrimgeour, 2013). The Aileron Province is a metasedimentary and granitic rock dominated system. The metasedimentary protoliths have depositional ages largely between c. 1870 and 1740 Ma (Claoue-Long et al., 2008a; Bodorkos et al., 2013) that show a general younging to the south-southeast in the Aileron Province. The voluminous granitoids have intrusive ages largely within the age bracket of c. 1820–1700 Ma with some minor younger components (Collins and Williams, 1995; Claoue-Long and Hoatson, 2005; Maidment et al., 2005; Whelan et al., 2012). Intrusive rocks have been divided into three groups based on geochemical characteristics: 1) c. 1770−1750 Ma calc-alkaline trondhjemite suites (CAT group) with arc-related geochemical characteristics, limited to the southeast Aileron Province, 2) c. 1780−1570 Ma high K, Rb, Th, U, high-heat producing granitoids that occur largely in the central Aileron Province, and 3) volumetrically extensive c. 1820−1650 Ma deformed granitoids of the Main Group, which have geochemical characteristics between the CAT Group and HHP Group (Zhao and McCulloch, 1995). A number of tectonothermal events have been recognised in the Aileron Province and are summarised in Table 1.

Notably, the Proterozoic metamorphic events in the Aileron Province and greater Arunta Region are generally characterised by: 1) structural and metamorphic footprints that typically do not involve pervasive reworking of the entire province, but instead commonly occur as small belts or domains typically less than several thousand km^2, and 2) overall metamorphism dominated by high-thermal gradient with or without coeval magmatism (cf. Vry and Baker, 2006; Claoue-Long et al., 2008b; Ahmad and Scrimgeour, 2013; Anderson et al., 2013; Morrissey et al., 2014).

2.2 Geology of the Mount Hay Block and Adla Domain

2.2.1 Mount Hay Block

The Mount Hay Block contains the following areally dominant exposures: 1) the Mount Hay Massif, 2) Capricorn Ridge to the northeast and 3) Ceilidh Hill (Fig. 2; e.g. Waters-Tormey and Tikoff, 2007; Waters-Tormey et al., 2009; Bonamici et al., 2011). These exposures are volumetrically dominated by the Mount Hay Granulite Unit, which is composed of fine-to very-fine-grained mafic granulite (~60%), felsic and intermediate granulite (~25%), leucogabbro-anorthosite (~5%), other felsic igneous rocks (~5%) and granulite facies metasedimentary rocks (~5%, Shaw and Warren, 1995; Warren and Shaw, 1995; Hoatson and Stewart, 2001; Hoatson et al., 2005). The rare metasedimentary rocks at Mount Hay are comprised of quartzo-feldspathic and garnet−sillimanite-bearing lithologies (e.g. Fig. 3a), and wollastonite−scapolite-bearing calc-silicates (Glikson, 1984; Watt, 1992).

Several studies have focused on the structural character and deformation history of the Mount Hay Block. There is consensus among more recent studies that the Mount Hay Massif preserves an older deformation history than the Capricorn Ridge (Waters-Tormey and Tikoff, 2007; Waters-Tormey et al., 2009; Bonamici et al., 2011). However in detail, the interpreted structural history of the Mount Hay Block varies between studies (e.g. Collins and Sawyer, 1996; Hoatson et al., 2005; Waters-Tormey and Tikoff, 2007; Waters-Tormey et al., 2009). An outline of only the major structural characteristics of the

Table 1. Major Events in the Aileron Province

Event	Area affected	Geological Record	Deformation
Stafford Event (*c.* 1810–1790 Ma)	Widespread in Aileron Province (granitic more widespread in N and central Aileron)	Felsic and lesser mafic magmatism, volcanism, sedimentation, localised HTLP metamorphism	Localised ~N-S to NW-SW fabric, and subvertical foliation and folds, localised extensional shear zones
Yambah Event (*c.* 1780–1770 Ma)	Widespread in Aileron Province	Felsic and lesser mafic magmatism, sedimentation, localised HTLP metamorphism	localised, extent not well known
c. 1760–1740 Ma intrusive rocks and metamorphism	Southern and Eastern Aileron Province	Felsic, intermediate and mafic magmatism, sedimentation, metamorphism (up to 8–10 kbar, 850–900 °C in the southern Aileron Province)	S1-S3 in the Mount Hay Block, E-W trending fabric in the Adla Domain
Strangways Event (*c.* 1740–1690 Ma)	Most pervasive in Eastern Aileron Province	Felsic magmatism, metamorphism (~2.6–4 kbar, 750–800 °C in the Mopunga Range. In Strangways Range: M1 up to ~8–10 kbar, ~800–950 ° C, M2 ~6–7.5 kbar, ~670–720 ° C)	Evidence for multiple structural events and different structural characteristics in areas of the E Aileron Province. D1: development of migmatitic layering parallel to bedding. D2: a) non-co-axial strain, sheath fold development, transpressional, SSW-directed in Mt Pfitzner areas of the Strangways Region, b) NW vergent, isoclinal to open folding in the Ongeva Granulite, c) NE vergent folding in Wuluma Hills, reverse shear zones, d) steeply dipping N-S fabric in Jinka Domain and Albarta Metamorphics (for full summary see Scrimgeour, 2013)
		c. 1690 Ma Dolerite Dyke Swarms	
Chewings Event (*c.* 1600–1550 Ma)	Central Aileron Province, southern Aileron province	High thermal gradient metamorphism (up to 5–7 kbar, >850 °C), minor coeval magmatism in the central-western Aileron Province	Upright NW-SE trending folds, SSW-directed movement in central Aileron Province, inferred age of amphibolite facies thrusting along the Redbank Thrust.
Alice Springs Orogeny (*c.* 450–300 Ma)	Widespread in Aileron Province	Up to amphibolite facies metamorphism	Transpressional, crustal scale shear zones, N and S directed deformation

From Scrimgeour (2013) and references therein; this study; Morrissey et al. (2014); Anderson et al. (2013)

Fig. 3. Field photos from the Mount Hay Block and Adla Domain showing (a) metapelite with garnet-sillimanite rich and leucocratic domains in the NW Mount Hay Massif, (b) garnet-bearing metasediment from the Adla Domain, and (c) garnet-biotite bearing pegmatite from the Adla Domain, from which RBN-46 was sampled from (labelled), with foliation of host metasedimentary indicated by black dashed line, and mafic boudin in the bottom right corner.

Mount Hay Block as determined by previous studies is given here. The outcrop pattern and structural character of the Mount Hay Massif is largely controlled by a km-scale antiformal northeast-plunging sheath fold defined by compositional layering (Waters-Tormey and Tikoff, 2007; Waters-Tormey et al., 2009; Bonamici et al., 2011) and layer parallel foliation S_1 (Waters-Tormey et al., 2009). A moderate to steeply north-northeast to east dipping foliation (S_2) occurs throughout much of the massif and is axial planar to the km-scale sheath fold (Waters-Tormey et al., 2009; Bonamici et al., 2011). The Mount Hay Massif appears to reflect south-southwest directed movement during D_2 from kinematic indicators (Collins and Sawyer, 1996; Waters-Tormey et al., 2009; Bonamici et al., 2011). The above phases of deformation preserved within the Mount Hay Massif are interpreted to have occurred as a single progressive deformation event (Collins and Sawyer, 1996; Bonamici et al., 2011). Collins and Sawyer (1996) suggested that charnockitic magmatism occurred dominantly during the early phases of deformation, whereas the leucogranitic and tonalitic magmatism persisted throughout the deformation history.

To the northeast of the Mount Hay Massif, Capricorn Ridge is a ~4 km wide, high strain zone defined by a pervasive fabric (S_3) that is in areas planar, and is interpreted to be younger than the structural fabrics preserved in the Mount Hay Massif based on field relationships (Waters-Tormey and Tikoff, 2007; Waters-Tormey et al., 2009; Bonamici et al., 2011). The foliation on Capricorn Ridge is typically steeply southwest-dipping but transitions to north-dipping in the southwest of Capricorn Ridge (e.g. Waters-Tormey et al., 2009). The foliation on Capricorn Ridge is (sub)parallel to compositional layering and lithological boundaries, and interpreted to have formed via transposition of older foliations (Waters-Tormey and Tikoff, 2007; Waters-Tormey et al., 2009). Shear sense on Capricorn Ridge has been documented as mostly south-side up shear sense (Waters-Tormey and Tikoff, 2007; Waters-Tormey et al., 2009). Waters-Tormey et al. (2009) presented a restored model of the Mount Hay Massif and Capricorn Ridge to account for interpreted later rotation effects, in which the Capricorn Ridge restores to a moderately-dipping shear zone with normal kinematics.

Published age data from the Mount Hay Block indicate that emplacement of at least some igneous protoliths occurred during the c. 1810–1790 Mount Stafford Event (Claoue-Long and Hoatson, 2005; Scrimgeour, 2013). The protolith to the mafic and felsic granulite of the Mount Hay Granulite Unit has been suggested to have formed in a subduction (e.g. Hoatson et al., 2005) or back-arc (Bonnay et al., 2000) setting. No direct age constraints on the depositional age(s) of the protoliths to metasediments in the Mount Hay Block have been obtained; however, the metasediments are considered to pre-date the precursors to the mafic granulites based on the observation of relic mafic dykes (now 'pods') within the metasediments (Watt, 1992).

There is a paucity of published geochronological data directly constraining the timing of metamorphism and deformation in the Mount Hay Block and adjoining areas. The only published geochronological dataset constraining the timing of metamorphism at present is a SHRIMP zircon age from white CL, low-U overgrowths and recrystallised domains of zircon from the Mount Hay Massif that yield a $^{207}Pb/^{206}Pb$ age of 1700 ± 17 Ma (Claoue-Long and Hoatson, 2005). Some authors correlate this age to the timing of granulite facies peak metamorphism at the Mount Hay (Bonamici et al., 2011) and/or alternatively the granulite facies deformation on the Capricorn Ridge (Waters-Tormey et al., 2009). Available $P-T$ constraints on the conditions of peak metamorphism in the Mount Hay Massif give mean estimates in the range of ~670 to 930 °C and 6−8 kbar using different geothermobarometry techniques on mafic granulites, felsic granulites and meta-calcsilicates (Harley et al., 1994; Bonnay, 2001; Staffier, 2007). Published constraints on the metamorphic temperatures at Capricorn Ridge have been obtained via geothermometry on two samples of mafic granulite, resulting in a mean estimate of 776 °C at 8 kbar (Waters-Tormey et al., 2009).

The Mount Hay Block also contains evidence for deformation that post-dates the development of granulite facies fabrics on Capricorn Ridge. This deformation manifests as amphibolite facies, steeply-dipping, east to southeast striking mylonite and ultramylonite zones with south-side up shear sense. Additionally, greenschist facies north-side-up mylonite and ultramylonite zones are also present (Waters-Tormey and Tikoff, 2007; Waters-Tormey et al., 2009). There are no published age constraints from these mylonites and ultramylonites from Capricorn Ridge.

2.2.2 Adla Domain

A ~60 km long by ~10 km wide E–W trending structural belt can be identified via TMI–1VD magnetic imagery extending east of Mount Hay (Fig. 2). Outcrop is relatively sparse along the belt; however, the limited exposures are classified as part of the Adla Granulite and are assumed to be part of the Strangways Metamorphic Complex (Shaw and Warren, 1995), which lies further to the east (Maidment et al., 2005). Exposures of the Adla Granulite are comprised of migmatitic metasedimentary gneisses and less abundant granitic and mafic gneisses (e.g. Fig. 3b−c). In contrast to the Mount Hay Block, outcropping rock is dominated by metasedimentary rather than metaigneous lithologies. TMI imagery suggests that the Adla Domain 'wraps' around the Mount Hay massif, and is truncated by a buried ~east−west trending linear structure to the north, which is probably a shear zone.

In the northern part of the Adla Domain, rocks exhibit a planar east−west trending, steeply to vertically dipping foliation, and a steeply east plunging lineation. Outcrops in the central area also contain a steeply-dipping, east−west trending gneissic foliation, which is locally folded around open, upright, shallowly east-plunging folds. There are no published age or $P-T$ constraints on the Adla Domain.

3. Sample descriptions and petrography

3.1 Mount Hay Granulite (Capricorn Ridge and Mount Hay Massif samples)

Samples of garnet−sillimanite bearing metasedimentary gneisses were obtained from the Capricorn Ridge (Samples Hay-05a, Hay-09a) and northwest Mount Hay Massif (Sample Hay-12 and Hay-17, Fig. 2; mineral abbreviations in figures and text after Kretz, 1983). Sample Hay-12 and Hay-17 preserve steeply-dipping, northeast−southwest trending foliation ($S_{1A/B}$ of Collins and Sawyer, 1996), and in sample Hay-12, a moderately northeast-plunging mineral elongation lineation. Capricorn Ridge samples were obtained from a fabric domain with a steeply dipping, southeast−northwest trending foliation and steeply south-plunging mineral elongation lineation. The metasedimentary rocks at Capricorn Ridge contain stromatic, garnet-bearing leucosomes, and there is little evidence of structurally discordant leucosomes, suggesting that deformation (D_3) may have either post-dated or outlasted the bulk of partial melting.

In sillimanite−garnet rich metapelite Hay-17 (Fig. 4a−b), two distinct size and microstructural characteristics can be distinguished for garnet and sillimanite. Garnet$_1$ occurs as equant medium to coarse-grains (up to ~8 mm) containing rare, fine-grained sillimanite, quartz and K-feldspar inclusions. Garnet$_1$ grains are typically surrounded by fine-grained oriented and randomly oriented prismatic sillimanite$_2$ and randomly oriented, subhedral biotite (<1 mm), or in some areas by fine to medium-grained K-feldspar that partially enclose garnet. Garnet$_2$ typically occurs as 'clusters' of fine to medium grains (up to 2 mm), containing abundant fine-grained sillimanite inclusions. Recrystallised prismatic sillimanite$_1$ (up to 15 mm long) is also present in the rock and typically defines the foliation. Coarse sillimanite$_1$ contains fractures perpendicular to the long-axis of the grains, and is in contact with and is interpreted to be partly overgrown by fine-grained sillimanite$_2$ and fine-medium-grained garnet$_2$ (Fig. 4b). Typically, garnet$_1$ and sillimanite$_1$ are not in direct contact and are separated by biotite, garnet$_2$ and/or sillimanite$_2$. Lenses dominated by K-feldspar (up to ~3 mm), with lesser quartz and plagioclase (< 1 mm) are interpreted to be small-scale domains associated with melting. Elsewhere, quartz and plagioclase are present in low abundance as fine grains (< 1mm). Accessory phases include fine-grained, sub-to anhedral ilmenite and rare rutile−ilmenite intergrowths.

Sample Hay-17 is interpreted to record two generations of sillimanite and garnet growth (Fig. 4a−b). Garnet$_1$, sillimanite$_1$ and K-feldspar rich leucosomes are interpreted to have developed during high grade suprasolidus conditions (M_1). The peak M_1 assemblage is interpreted to be garnet−sillimanite−K-feldspar−quartz−ilmenite−melt ± biotite. Fine-grained sillimanite$_2$, unoriented biotite, and fine-medium-grained inclusion rich garnet$_2$ are interpreted to have grown at the expense of garnet$_1$, medium to coarse- grained sillimanite$_1$ and K-feldspar and may reflect a later phase of reworking.

Samples Hay-05a, Hay-09a and Hay-12 are essentially mineralogically identical, containing garnet, sillimanite, K-feldspar, plagioclase, quartz, ilmenite and rutile (Fig. 4c–d). Samples Hay-05a, Hay-09a and Hay-12 contain medium-to coarse-grained garnet (typically ~1−4 mm, but bimodal size in Hay-05, up to ~15 mm), with inclusions of fine-grained (<0.5 mm) biotite, quartz, K-feldspar, acicular oriented and unoriented sillimanite, rare rutile (sample Hay-05a and Hay-09a only) and rare ilmenite. Prismatic sillimanite grains (<0.5−4 mm) typically define the foliation, deflect around some garnet grains and are in direct contact with garnet and matrix minerals quartz, plagioclase, K-feldspar (<0.5−4 mm), biotite (up to ~2 mm) ± rutile (< 0.5 mm). Biotite occurs in the matrix as subhedral oriented grains parallel to the foliation, as anhedral unoriented grains and in contact with garnet, commonly in strain shadows. Ilmenite grains (<0.5 mm) in the matrix are anhedral and of low abundance. Ilmenite can also occur with biotite, on grain boundaries of garnet or rutile. Sample Hay-12 additionally contains sillimanite grains that commonly contain fractures perpendicular to the foliation (Fig. 4e). Fine-grained (<<0.5 mm) biotite and spinel occur in the fractures. Biotite and spinel are interpreted to have grown as reaction microstructures after peak metamorphism or during a later event at the expense of sillimanite. Rare poorly-preserved fine-grained kyanite (<1 mm) occurs in Capricorn Ridge samples Hay-05a and Hay-09a within the matrix in contact with K-feldspar, quartz, plagioclase, biotite. The peak assemblage for Hay-05a, Hay-09a and Hay-12 is interpreted to be garnet–sillimanite–plagioclase–K-feldspar–quartz–rutile–ilmenite–biotite and melt (based on the presence of abundant garnet-bearing leucosomes at outcrop scale). Rare kyanite is interpreted to have predated the growth of sillimanite in samples Hay-05a and Hay-09.

3.2 Adla Domain

Samples were obtained from the centre (RBN-28 and RBN-31) and northern part of the belt (RBN-11, RBN-12, RBN-46; Fig. 2).

3.2.1 Adla Granulite (samples RBN-11, RBN-12, RBN-28, and RBN-31)

Samples RBN-11, RN-12 and RBN-28 are mineralogically identical, containing garnet, sillimanite, K-feldspar, plagioclase, quartz, ilmenite and biotite. Garnet grains are ~0.5–10 mm in diameter and contain inclusions of fine to medium-grained, acicular sillimanite (<0.5–2 mm, Fig. 4f), fine-grained biotite (<0.5 mm), fine-grained quartz (< 1 mm) and rare fine-grained ilmenite (< 0.5 mm) inclusions. Biotite also commonly occurs in garnet fractures. Prismatic to bladed sillimanite grains (<0.5–5 mm) in the matrix are in areas in direct contact with garnet, are typically deflected around garnet grains and define the foliation of the rock. Quartz, K-feldspar (<0.5–4 mm), plagioclase (<0.5–2 mm), rare ilmenite (<0.5 mm) and biotite (<0.5–2 mm) also comprise the matrix. Ilmenite is commonly in contact with biotite. Biotite occurs as unoriented grains as well as oriented grains parallel to the foliation, commonly partially surrounding garnet in strain shadows. The abundance of biotite varies from ~5 area % in sample RBN-11 and RBN-12 to ~10% in sample RBN-28. The peak assemblages for the metapelitic Adla Granulites are interpreted to be garnet−sillimanite−quartz−K-feldspar−plagioclase−ilmenite−melt ± biotite for samples RBN-11, RBN12 and RBN-28. RBN-31 is a deformed fine to medium-grained (<2 mm) quartz−feldspar rich, garnet−biotite bearing psammitic gneiss obtained from the central Adla domain.

3.2.2 Pegmatite

Sample RBN-46 was obtained from a 30 cm wide garnet-bearing pegmatite in the northern area (Fig. 3c). Although the pegmatite is planar and transects the compositional layering by about 30°, it contains a well-developed structural fabric parallel to foliation in the host metasedimentary gneiss (sample RBN-12). The pegmatitic assemblage is K-feldspar, quartz, plagioclase (10–20 mm), euhedral tourmaline (~10 mm) and garnet, with a biotite-bearing selvage.

4. Analytical techniques

4.1 Monazite U−Pb geochronology

Monazite U−Pb geochronological data were obtained on nine samples from the Mount Hay Massif, Capricorn Ridge and Adla Domain to examine the timing of deformation and metamorphism. Monazite grains were analysed in situ for samples Hay-05a, Hay-09a, and Hay-12, and in grain mounts for all samples. Samples Hay-05a, Hay-09a

(Capricorn Ridge) and Hay-12 (Mount Hay Massif) were analysed in situ to investigate whether monazite records evidence for polymetamorphism and to link monazite ages to the silicate mineral evolution. Monazite grain mounts were prepared using panning, conventional magnet and Franz separation techniques using ~75−400 µm grain size fractions.

Monazite U−Pb analyses were obtained using the Laser Ablation Inductively Coupled Plasma Mass Spectrometer (LA−ICP−MS) at Adelaide Microscopy, University of Adelaide. Prior to laser ablation, monazite grains were imaged using a Phillips XL30 SEM. A beam accelerating voltage of 15 kV, and spot size of 5 µm was used to image the thin sections and grain mounts using a backscattered electron (BSE) detector.

U−Pb analyses of monazite were undertaken using an Agilent 7500cs ICP−MS with a New Wave 213 nm Nd-YAG laser in a helium ablation atmosphere. A laser spot size of 15 µm, repetition rate of 5 Hz and laser intensity of 75−80% was used for analyses. A 30 second gas blank was initially measured,

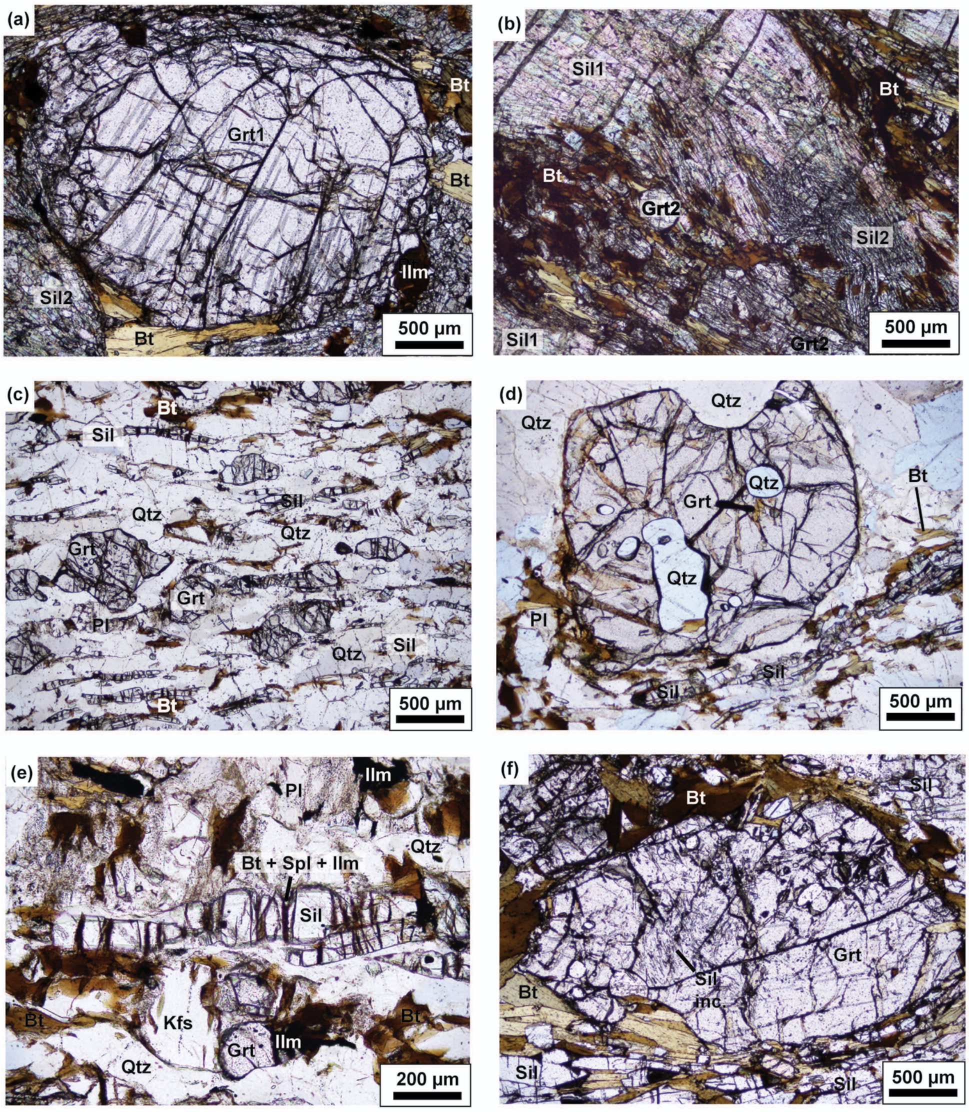

Fig. 4. Photomicrographs of samples from the Mount Hay area and Adla Domain, (a) sample Hay-17, showing equant garnet$_1$ surrounded by fine-grained sillimanite$_2$, biotite and ilmenite, (b) sample Hay-17 showing coarse-grained sillimanite$_1$, with fine grained biotite, garnet$_2$ and sillimanite$_2$, which are interpreted to have grown at the expense of sillimanite$_1$, (c) sample Hay-12 showing peak minerals garnet, sillimanite, quartz, K-feldspar, plagioclase and biotite grains, (d) sample Hay-09 showing garnet with quartz inclusions, sillimanite grains defining the fabric, mostly unoriented biotite in contact with garnet, sillimanite and matrix minerals quartz plagioclase and K-feldspar, (e) boudinaged sillimanite grains containing fine grained biotite, with and without spinel and ilmenite reaction microstructures in the boudin necks, and (f) sample RBN-28, showing garnet containing fine-grained sillimanite inclusions, and surrounded by biotite and in contact with sillimanite grains.

followed by 40 to 50 seconds of monazite sample ablation. The laser was fired for 10 seconds with the shutter closed prior to ablation in order to allow for beam and crystal stabilisation. Analyses measured isotopes ^{204}Pb, ^{206}Pb, ^{207} Pb and ^{238}U for 10, 15, 30 and 15 ms respectively. Corrections for common lead were not made due to an unresolvable interference of ^{204}Hg and ^{204}Pb peaks. However, apparent ^{204}Pb was monitored to assess the common lead of each analysis.

Monazite data was corrected for mass-bias and fractionation using the real-time correction program Glitter v. 4.23 (Griffin et al., 2008). Monazite standard MAdel was used to correct for mass bias and fractionation for monazite analyses (TIMS MAdel age: ^{207}Pb/^{206}Pb = 490.0 Ma, ^{206}Pb/^{238}U = 518.37 Ma and ^{207}Pb/^{235}U = 513.13 Ma; Payne et al., 2008, updated with additional TIMS data). A 1% uncertainty was given to the age of the MAdel standard for sample age error calculations. Accuracy was monitored by analysing the 222 (c. 450 Ma; Maidment, 2005) and 44069 (TIMS data: ^{206}Pb/^{238}U = 426 ± 3 Ma; Aleinikoff et al., 2006) monazite standards prior to and throughout unknown analysis runs. Average 222 ages obtained throughout this study were ^{207}Pb/^{235}U = 452.3 ± 1.3 Ma (95 %, n = 131, MSWD = 1.3), ^{207}Pb/^{206}Pb = 461.1 ± 5.1 Ma (MSWD = 0.6) and ^{206}Pb/^{238}U = 450.5 ± 1.4 Ma (MSWD = 1.3). Average 44069 monazite ages obtained throughout this study were ^{207}Pb/^{235}U = 412.8 ± 2.2 Ma (95 %, n = 25, MSWD = 0.46), ^{207}Pb/^{206}Pb = 403 ± 11 Ma (MSWD = 0.65) and ^{206}Pb/^{238}U = 414.7 ± 2.5 Ma (MSWD = 0.29). Conventional concordia, weighted averages, and probability distribution plots were generated using Isoplot version 4.11 (Ludwig, 2008).

4.2 Mineral Chemistry

Mineral chemical composition analyses were obtained using a Cameca SX51 electron microprobe at the University of Adelaide using a beam current of 20 nA and accelerating voltage of 15 kV. See Table 2 for representative mineral chemistry and Appendix 1 for results.

4.3 Mineral equilibria modelling

Bulk chemical compositions of samples Hay-17, Hay-05a, Hay-09a and RBN-28 were determined using whole-rock geochemical analyses (Table 3). Major element concentrations were determined by X-ray fluorescence (XRF), using a Panalytical 2404 XRF unit at Franklin and Marshall College. Samples were prepared for analysis by fusion of the milled sample with lithium tetraborate. A small amount of Fe was estimated as Fe_2O_3 (2–4 %) by taking into account that the samples contain ilmenite ± rutile, and are not magnetite-bearing. H_2O content for all samples was estimated by taking into account the abundance of hydrous phases (estimated 3.5 wt.% H_2O in biotite), on the assumption that the estimated H_2O in biotite is a reasonable approximation for the whole rock abundance of H_2O in the residual composition at peak metamorphic conditions after melt loss. The $P-T$ pseudosections were calculated using THERMOCALC v3.33 (October 2009 update of Powell and Holland, 1988), with the internally consistent dataset of Holland and Powell (1998; tc-ds55, Nov. 2003 update). The model chemical system NCKFMASHTO ($Na_2O-CaO-K_2O-FeO-MgO-Al_2O_3-SiO_2-H_2O-TiO_2-Fe_2O_3$) was used for $P-T$ pseudosection calculations using $a-x$ relationships of White et al. (2007) for biotite, garnet and silicate melt, White et al. (2000) for ilmenite, Holland and Powell (2003) for K-feldspar and plagioclase, Holland and Powell (1998) for cordierite, and White et al. (2002) for magnetite, spinel and orthopyroxene.

5. Results

5.1 U−Pb Geochronology

For all samples, monazites typically range in size between 20 and 200 μm (Fig. 5). In most samples, monazite grains show irregular (patchy) zoning, regular zoning and/or no zoning when imaged using BSE. Sample RBN-31 additionally contains monazite grains that show oscillatory zoning. Apart from where noted below, there is no correspondence between monazite morphology and age.

Monazite age data is presented in Figures 6−8 and in Appendix 2. All monazite age data shown in linear probability plots, weighted averages and discussed in text are $^{207}Pb/^{206}Pb$ ages. Error ellipses on concordia plots and error boxes on linear probability plots are plotted at 1 σ uncertainty. Only 100 ± 10 % concordant data are included in weighted averages and linear probability plots. Weighted average ages have been calculated using data that are considered to comprise a population. An age population is defined by analyses that plot along the same slope in linear probability plots and are representative of a normal distribution of data. Monazite data excluded from plots due to variable or poor isotopic signal are shown in Appendix 2.

5.1.1 Mount Hay Massif Sample Hay-12: garnet−sillimanite-Rutile metapelite

Fifty-four analyses were obtained in situ and from a grain mount. Forty-eight monazite analyses (21 in situ, 27 grain mount, Fig. 6a−b) are within 100 ± 10 % concordancy and yield a $^{207}Pb/^{206}Pb$ age range between c. 1770−1520 Ma. Rare monazite grains that occur as inclusions in garnet preserve ages of c. 1770−1708 Ma, whereas monazite located at grain boundaries in the matrix gives an age range of 1756−1520 Ma. A group of analyses defines a linear slope with ages ranging from 1758 ± 15 Ma (n = 9, MSWD = 0.03, 95 % confidence; Fig. 6b). Three monazite grains contained darker cores and lighter rims that were large enough to be analysed, which yielded ages between c. 1756–1720 Ma from cores and c. 1735–1535 Ma from rims.

5.1.2 Mount Hay Massif Sample Hay-17: garnet−sillimanite metapelite

Forty-one analyses were obtained from a monazite grain mount. All analyses are within 100 ± 10 % concordancy and record an age range between 1783 and 1536 Ma (Fig. 6c–d). Age data was obtained from darker cores, lighter rims, patchy domains and unzoned grains under BSE. One major age population from darker cores, lighter rims, patchy domains and homogenous regions yields a weighted average age of 1740 ± 7 Ma (n = 37, MSWD = 0.91). Some monazite grains yield older ages from darker cores and younger ages from lighter rims. These ages are variable (cores: 1753–1715 Ma, rims: 1752–1657 Ma).

5.1.3 Capricorn Ridge Sample Hay-05a: garnet−sillimanite−rutile metapelite

Forty three analyses were obtained in situ and from a grain mount. Forty-one analyses are within 100 ± 10 % concordance and yield an age range between c. 1805 and 1400 Ma (Fig. 6e–f). Two analyses of monazite included in garnet yield ages of c. 1743 Ma. There is no correspondence between age data and microstructural location of analysed monazite grains located in the matrix. One dominant age grouping yields a weighted average of 1756 ± 8 Ma (n = 26, MSWD = 0.97). One analysis also yielded an older spot age of c. 1805 Ma.

5.1.4 Capricorn Ridge Sample Hay-09a: garnet−sillimanite metapelite

Fifty-one analyses were obtained in situ in thin section and from a grain mount. Forty-nine monazite analyses are within 100 ± 10 % concordance and yield ages between c. 1810 and 1575 Ma (Fig. 7a−b). Four analyses of monazite included in garnet yield ages ranging between 1790−1750 Ma, whereas monazite grains in the matrix yield ages over a range of c. 1800 to 1575 Ma. Forty-six analyses yield a weighted average of 1756.7 ± 6 Ma (MSWD = 0.93, 95 % confidence). One analysis gives an older age of c. 1810 Ma.

5.1.5 Adla Domain- Sample RBN-11: garnet−sillimanite metapelite

Ninety-eight analyses were obtained from monazite grain mounts, all of which fall within 100 ± 10 concordance and range from c. 1790 to 1465 Ma (Fig. 7c–d). Using

Table 2. EPMA representative mineral analyses

Sample	Hay-05									Hay-09								
Mineral	Grt-Core	Grt-Rim	Bt	Ilm- inc Grt	Pl	Kfs	Rt	Qtz	Sil	Grt-Core	Grt-Rim	Ilm	Pl	Kfs	Rt	Qtz	Sil	Bt
ID number	223	208	256	197	204	189	195	200	309	46	27	179	181	186	178	65	68	1
SiO_2	38.06	38.59	36.79	0.02	57.12	64.18	0.07	100.12	35.92	38.33	38.09	0.05	57.71	64.00	0.08	99.55	36.78	36.74
TiO_2	0.25	0.00	4.82	53.98	0.04	0.03	98.87	0.00	0.00	0.03	0.00	52.41	0.04	0.00	99.37	0.01	0.00	4.23
Al_2O_3	21.55	21.78	16.32	0.00	26.58	18.63	0.00	0.05	61.35	21.62	21.43	0.00	25.91	18.62	0.00	0.00	60.83	16.06
Cr_2O_3	0.30	0.40	0.11	0.16	0.20	0.00	0.05	0.10	0.47	0.38	0.55	0.09	0.15	0.03	0.31	0.03	0.48	0.06
FeO	27.89	27.75	12.16	43.21	0.00	0.00	0.41	0.03	0.42	28.11	28.29	44.82	0.09	0.05	0.24	0.08	0.41	13.12
MnO	0.45	0.43	0.02	0.12	0.06	0.00	0.00	0.02	0.00	0.47	0.37	0.20	0.00	0.01	0.00	0.02	0.00	0.00
MgO	9.11	9.02	14.72	1.64	0.00	0.00	0.02	0.01	0.01	8.70	8.58	0.27	0.01	0.00	0.00	0.01	0.00	14.76
ZnO	0.10	0.00	0.13	0.00	0.07	0.00	0.04	0.00	0.00	0.02	0.13	0.10	0.00	0.00	0.02	0.11	0.05	0.06
CaO	1.63	1.83	0.00	0.00	8.52	0.08	0.00	0.04	0.01	1.46	1.62	0.09	8.25	0.05	0.10	0.01	0.00	0.01
Na_2O	0.00	0.00	0.10	0.01	7.05	1.35	0.01	0.00	0.01	0.03	0.01	0.01	7.06	1.25	0.00	0.00	0.01	0.05
K_2O	0.00	0.00	9.03	0.00	0.07	14.75	0.00	0.01	0.01	0.00	0.00	0.06	0.22	14.70	0.02	0.00	0.00	9.84
Total	99.33	99.81	94.18	99.15	99.72	99.02	99.48	100.37	98.19	99.15	99.08	98.09	99.44	98.71	100.14	99.82	98.56	94.93
No. Oxygens	12	12	11	3	8	8	2	2	5	12	12	3	8	8	2	2	5	11
Si	2.96	2.98	2.74	0.00	2.57	2.98	0.00	1.00	0.99	2.99	2.98	0.00	2.60	2.98	0.00	1.00	1.01	2.74
Ti	0.01	0.00	0.27	1.01	0.00	0.00	1.00	0.00	0.00	0.00	0.00	1.01	0.00	0.00	0.99	0.00	0.00	0.24
Al	1.98	1.99	1.43	0.00	1.41	1.02	0.00	0.00	1.99	1.99	1.98	0.00	1.38	1.02	0.00	0.00	1.97	1.41
Cr	0.02	0.02	0.01	0.00	0.01	0.00	0.00	0.00	0.01	0.02	0.03	0.00	0.01	0.00	0.00	0.00	0.01	0.00
Fe^{2+}	1.82	1.79	0.76	0.90	0.00	0.00	0.00	0.00	0.01	1.83	1.85	0.96	0.00	0.00	0.00	0.00	0.01	0.82
Mn^{2+}	0.03	0.03	0.00	0.00	0.00	0.00	0.00	0.00	0.00	0.03	0.02	0.00	0.00	0.00	0.00	0.00	0.00	0.00
Mg	1.06	1.04	1.63	0.06	0.00	0.00	0.00	0.00	0.00	1.01	1.00	0.01	0.00	0.00	0.00	0.00	0.00	1.64
Zn	0.01	0.00	0.01	0.00	0.00	0.00	0.00	0.00	0.00	0.00	0.01	0.00	0.00	0.00	0.00	0.00	0.00	0.00
Ca	0.14	0.15	0.00	0.00	0.41	0.00	0.00	0.00	0.00	0.12	0.14	0.00	0.40	0.00	0.00	0.00	0.00	0.00
Na	0.00	0.00	0.01	0.00	0.62	0.12	0.00	0.00	0.00	0.00	0.00	0.00	0.62	0.11	0.00	0.00	0.00	0.01
K	0.00	0.00	0.86	0.00	0.00	0.87	0.00	0.00	0.00	0.00	0.00	0.00	0.01	0.87	0.00	0.00	0.00	0.94
Total Cations	8	8	8	2	5	5	1	1	3	8	8	2	5	5	1	1	3	8
XMg (Mg/(Fe+Mg))	0.37	0.37	0.68							0.36	0.35							0.67
XFe (Fe/(Fe+Mg))	0.63	0.63	0.32							0.64	0.65							0.33
X(alm)	0.60	0.60								0.61	0.61							
X(py)	0.35	0.34								0.34	0.33							
X(grs)	0.04	0.05								0.04	0.05							
X(spss)	0.01	0.01								0.01	0.01							
XAn (Ca/(Ca+Na+K)					0.40	0.00							0.39	0.00				
XOr (K/(Na+Ca+K)					0.00	0.87							0.01	0.88				

Table 2. EPMA representative mineral analyses continued

Sample					Hay-12										Hay-17			
Mineral	Grt-Core	Grt-Rim	Bt	Ilm	Kfs	Pl	Rt	Qtz	Sil	Grt-core	Grt-rim	Sil	Bt	Ilm	Kfs	Pl	Qtz	Rt
ID number	150	141	166	84	122	126	169	86	70	8	3	27	31	50	54	59	25	49
SiO_2	37.86	37.78	35.62	0.03	63.72	57.66	0.08	99.76	36.57	37.79	37.92	36.08	37.01	0.00	64.69	62.09	98.44	0.02
TiO_2	0.03	0.01	4.99	51.92	0.01	0.00	98.69	0.00	0.01	0.00	0.01	0.02	4.09	52.37	0.03	0.00	0.01	97.41
Al_2O_3	21.55	21.68	16.76	0.00	18.51	26.11	0.00	0.00	62.32	20.86	21.10	60.25	16.30	0.01	18.72	24.75	0.11	0.05
Cr_2O_3	0.06	0.04	0.08	0.03	0.00	0.00	0.57	0.02	0.00	0.02	0.00	0.00	0.03	0.04	0.02	0.02	0.00	0.03
FeO	31.42	31.19	14.91	44.72	0.09	0.02	0.13	0.12	0.61	28.74	29.79	0.22	13.54	42.78	0.02	0.28	0.51	0.26
MnO	0.43	0.53	0.03	0.12	0.00	0.00	0.02	0.00	0.03	0.63	0.61	0.01	0.00	0.14	0.01	0.00	0.00	0.02
MgO	7.01	7.11	13.05	0.55	0.02	0.00	0.00	0.00	0.03	7.40	7.79	0.00	14.81	1.44	0.00	0.00	0.00	0.00
ZnO	0.00	0.01	0.00	0.08	0.02	0.01	0.00	0.01	0.08	0.00	0.06	0.03	0.05	0.01	0.00	0.00	0.01	0.02
CaO	1.46	1.63	0.00	0.03	0.03	8.39	0.01	0.00	0.00	2.66	1.35	0.00	0.00	0.02	0.05	5.86	0.03	0.00
Na_2O	0.00	0.00	0.08	0.04	1.14	6.95	0.01	0.01	0.00	0.00	0.03	0.00	0.15	0.01	1.52	8.47	0.00	0.02
K_2O	0.01	0.00	9.87	0.00	14.65	0.26	0.04	0.00	0.02	0.01	0.00	0.01	9.65	0.00	14.35	0.06	0.00	0.00
Total	99.83	99.98	95.40	97.51	98.19	99.39	99.55	99.92	99.67	98.11	98.66	96.62	95.64	96.85	99.41	101.54	99.12	97.84
No. Oxygens	12	12	11	3	8	8	2	2	5	12	12	5	11	3	8	8	2	2
Si	2.98	2.97	2.67	0.00	2.98	2.60	0.00	1.00	0.99	3.00	3.00	1.01	2.74	0.00	2.99	2.72	1.00	0.00
Ti	0.00	0.00	0.28	1.00	0.00	0.00	0.99	0.00	0.00	0.00	0.00	0.00	0.23	1.01	0.00	0.00	0.00	1.00
Al	2.00	2.01	1.48	0.00	1.02	1.39	0.00	0.00	2.00	1.95	1.97	1.98	1.42	0.00	1.02	1.28	0.00	0.00
Cr	0.00	0.00	0.00	0.00	0.00	0.00	0.01	0.00	0.00	0.00	0.00	0.00	0.00	0.00	0.00	0.00	0.00	0.00
Fe^{2+}	2.07	2.05	0.93	0.96	0.00	0.00	0.00	0.00	0.01	1.91	1.97	0.01	0.84	0.92	0.00	0.01	0.00	0.00
Mn^{2+}	0.03	0.03	0.00	0.00	0.00	0.00	0.00	0.00	0.00	0.04	0.04	0.00	0.00	0.00	0.00	0.00	0.00	0.00
Mg	0.82	0.83	1.46	0.02	0.00	0.00	0.00	0.00	0.00	0.88	0.92	0.00	1.63	0.06	0.00	0.00	0.00	0.00
Zn	0.00	0.00	0.00	0.00	0.00	0.00	0.00	0.00	0.00	0.00	0.00	0.00	0.00	0.00	0.00	0.00	0.00	0.00
Ca	0.12	0.14	0.00	0.00	0.00	0.41	0.00	0.00	0.00	0.23	0.11	0.00	0.00	0.00	0.00	0.27	0.00	0.00
Na	0.00	0.00	0.01	0.00	0.10	0.61	0.00	0.00	0.00	0.00	0.00	0.00	0.02	0.00	0.14	0.72	0.00	0.00
K	0.00	0.00	0.94	0.00	0.88	0.01	0.00	0.00	0.00	0.00	0.00	0.00	0.91	0.00	0.85	0.00	0.00	0.00
Total Cations	8	8	8	2	5	5	1	1	3	8	8	3	8	2	5	5	1	1
XMg (Mg/(Fe+Mg))	0.28	0.29	0.61							0.31	0.32		0.66					
XFe (Fe/(Fe+Mg))	0.72	0.71	0.39							0.69	0.68		0.34					
X(alm)	0.68	0.67								0.62	0.65							
X(py)	0.27	0.27								0.29	0.30							
X(grs)	0.04	0.04								0.07	0.04							
X(spss)	0.01	0.01								0.01	0.01							
XAn (Ca/(Ca+Na+K)					0.00	0.39									0.00	0.28		
XOr (K/(Na+Ca+K)					0.89	0.01									0.86	0.00		

Table 2. EPMA representative mineral analyses continued

Sample				RBN-28				
Mineral	Grt-Core	Grt-Rim	Bt	Ilm	Kfs	Pl	Qtz	Sil
ID number	283	295	297	315	302	59.1042	321	305
SiO_2	37.80	38.00	36.51	0.34	64.31	0.07	99.82	36.72
TiO_2	0.02	0.01	4.66	52.37	0.00	24.85	0.00	0.02
Al_2O_3	21.75	21.06	16.19	0.00	18.55	0.07	0.01	61.74
Cr_2O_3	0.00	0.00	0.06	0.00	0.00	0.00	0.00	0.05
FeO	31.47	32.56	14.18	42.99	0.04	0.02	0.00	0.61
MnO	0.36	0.34	0.10	0.05	0.00	0.00	0.04	0.00
MgO	7.47	6.36	14.20	0.21	0.01	0.14	0.02	0.00
ZnO	0.05	0.00	0.15	0.08	0.00	6.83	0.00	0.01
CaO	1.29	1.26	0.02	0.00	0.06	7.56	0.01	0.00
Na_2O	0.03	0.02	0.12	0.00	2.35	0.17	0.01	0.00
K_2O	0.02	0.02	9.47	0.04	13.45	0.17	0.00	0.00
Total	100.23	99.64	95.64	96.08	98.77	98.81	99.91	99.16
No. Oxygens	12	12	11	3	8	8	2	5
Si	2.96	3.01	2.71	0.01	2.98	2.67	1.00	1.00
Ti	0.00	0.00	0.26	1.02	0.00	0.00	0.00	0.00
Al	2.01	1.96	1.42	0.00	1.01	1.32	0.00	1.99
Cr	0.00	0.00	0.00	0.00	0.00	0.00	0.00	0.00
Fe^{2+}	2.06	2.15	0.88	0.93	0.00	0.00	0.00	0.01
Mn^{2+}	0.02	0.02	0.01	0.00	0.00	0.00	0.00	0.00
Mg	0.87	0.75	1.57	0.01	0.00	0.00	0.00	0.00
Zn	0.00	0.00	0.01	0.00	0.00	0.00	0.00	0.00
Ca	0.11	0.11	0.00	0.00	0.00	0.33	0.00	0.00
Na	0.00	0.00	0.02	0.00	0.21	0.66	0.00	0.00
K	0.00	0.00	0.90	0.00	0.80	0.01	0.00	0.00
Total Cations	8	8	8	2	5	5	1	3
XMg (Mg/(Fe+Mg))	0.30	0.26	0.64					
XFe (Fe/(Fe+Mg))	0.70	0.74	0.36					
X(alm)	0.67	0.71						
X(py)	0.28	0.25						
X(grs)	0.04	0.04						
X(spss)	0.01	0.01						
XAn (Ca/(Ca+Na+K)					0.00	0.33		
XOr (K/(Na+Ca+K)					0.79	0.01		

a linear probability diagram, analyses for which error boxes lie on the same slope yield a weighted average age of 1737 ± 7 Ma (95 % confidence, *n* = 48, MSWD = 0.3). Grey analyses are interpreted not to comprise the above population and were excluded from weighted average calculations.

5.1.6 Adla Domain- Sample RBN-12: garnet−sillimanite metapelite

Sixty-nine monazite analyses were obtained from a grain mount (Fig. 7e−f). The dominant population yields a weighted average of 1743 ± 6 Ma (95 % confidence, *n* = 61, MSWD = 0.44). A minor younger age grouping at c. 1580 Ma also exists for this sample. Five monazite rims that typically have a brighter response under BSE imaging yield ages between c. 1731−1570 Ma.

5.1.7 Adla Domain- Sample RBN-28: garnet−sillimanite metapelite

Forty analyses were obtained from monazite from a grain mount, and yield an age range between 1765 and 1652 Ma (Fig. 8a−b). Thirty-eight analyses that lie along the same slope in Fig. 8b constitute one age population. The weighted average for this age population is 1738 ± 7 Ma (95 % confidence, *n* = 38, MSWD = 0.53).

5.1.8 Adla Domain- Sample RBN-31: garnet−biotite psammite

Thirty-nine analyses were obtained from monazite within a grain mount (Fig. 8c−d). Thirty-eight analyses are within 100 ± 10 % concordancy and yield ages between c. 1920 and 1489 Ma. Whereas unzoned domains and cores yield an age range of c. 1920 to 1649 Ma, 4 rims that appear lighter using BSE imaging yield age range between c. 1677 and 1489 Ma. One main age population is evident (Fig. 8d), which was obtained from unzoned domains, and oscillatory and regularly zoned cores. This population yields a weighted average of 1751 ± 8 Ma (95 % confidence, *n* = 27, MSWD = 0.65). A single older c. 1920 Ma

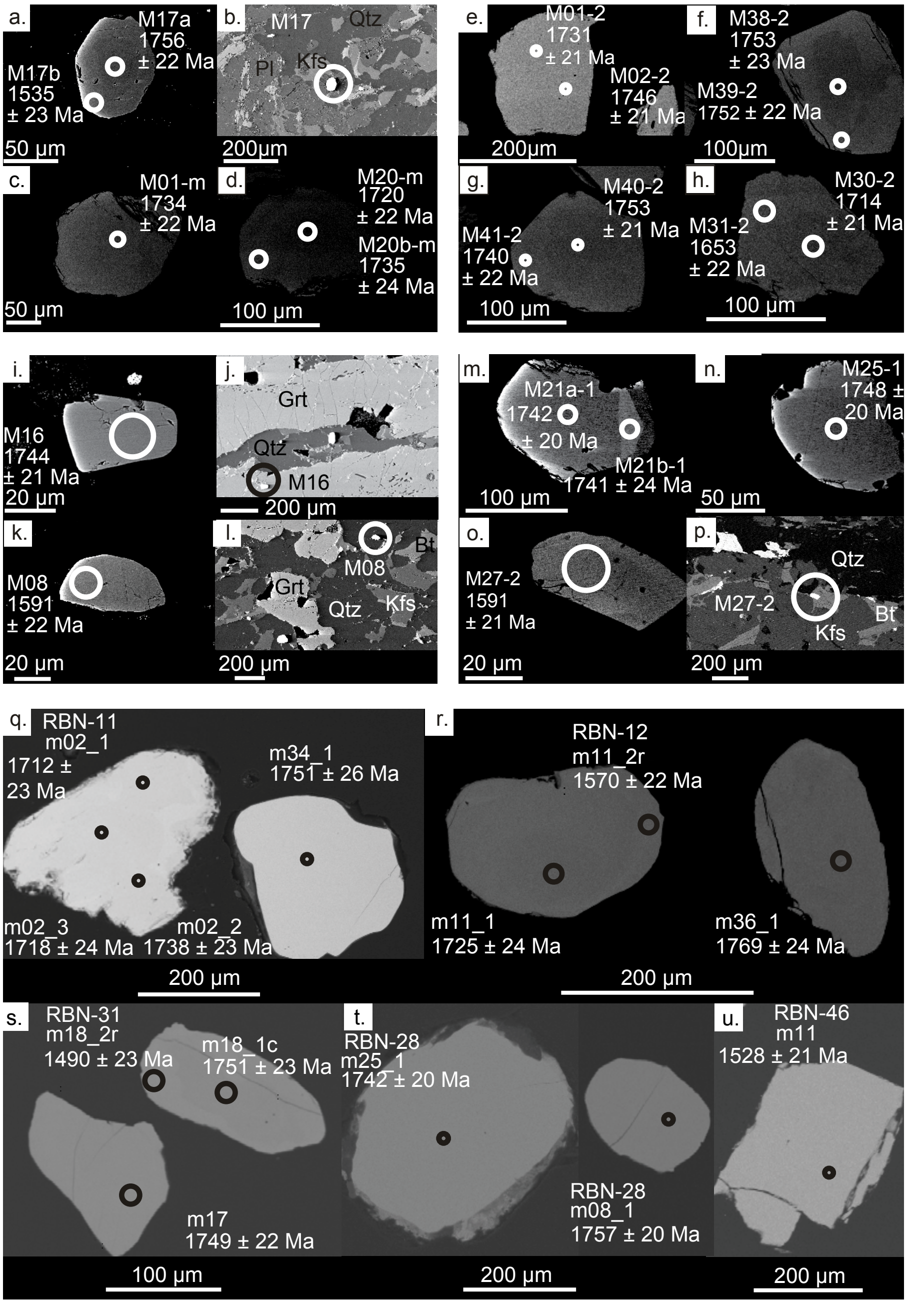

Fig. 5. Representative monazite BSE images for Mount Hay Massif samples Hay-12 (a–d), Hay-17 (e–h), Capricorn Ridge samples Hay-05a (i–l), Hay-09a (m–p) and Adla Domain samples RBN-11 (q), RBN-12 (r), RBN-31 (s), RBN-28 (t) and RBN-46 (u).

age was also obtained.

5.1.9 Adla Domain- Sample RBN-46: garnet-bearing pegmatite

Forty analyses were obtained from a grain mount. Thirty-nine analyses are within 100 ± 10 % concordancy and yield an age range between c. 1586 and 1331 Ma. Excluding one outlier (M22), analyses show one age population (Fig. 8e–f) and yield a weighted average of 1542 ± 7 Ma (95 % confidence, *n* = 38, MSWD = 0.78).

5.2 *P*−*T* results

The *P*−*T* pseudosection calculated for the Mount Hay Massif sample Hay-17 has a stability field corresponding to the interpreted peak assemblage garnet−sillimanite−K-feldspar−quartz−ilmenite−biotite−melt at ~7–10 kbar, ~850–900 °C (Fig. 9a). X_{Grs} garnet compositional isopleths were calculated for pseudosections in order to further investigate

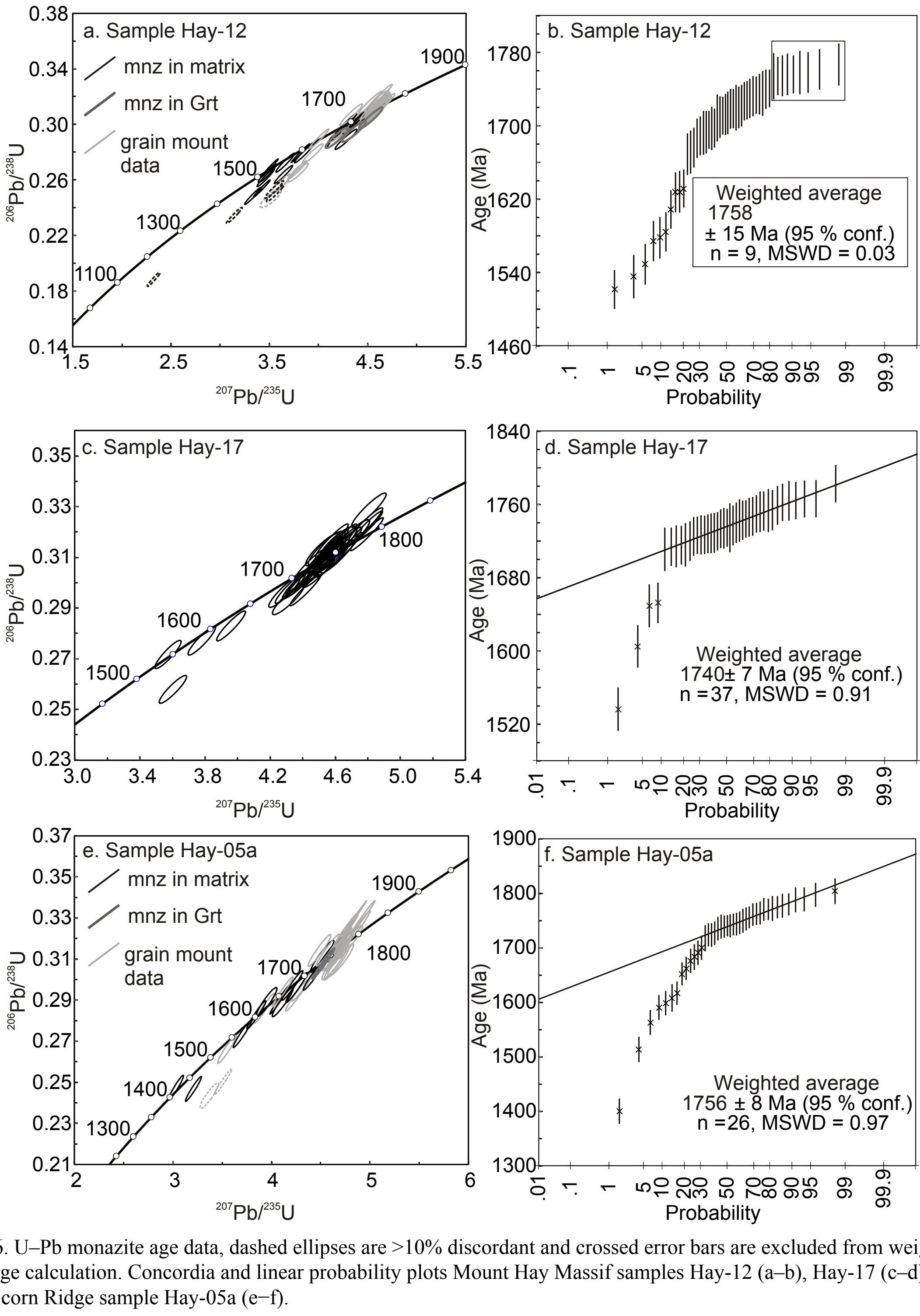

Fig. 6. U–Pb monazite age data, dashed ellipses are >10% discordant and crossed error bars are excluded from weighted average calculation. Concordia and linear probability plots Mount Hay Massif samples Hay-12 (a–b), Hay-17 (c–d), and Capricorn Ridge sample Hay-05a (e−f).

the conditions of metamorphism. Calculated X_{Grs} isopleths do not take into account Mn or Fe^{3+} (pseudosection $X_{Grs} = Ca/(Fe^{2+}+Mg+Ca)$). However EPMA chemical analyses of garnet have low calculated X_{Spss} values of ~0.01, and samples have reduced whole rock compositions (96–98% FeO from total Fe). Calculated X_{Grs} contours are therefore considered to be comparable to X_{Grs} garnet values. X_{Grs} isopleths compositions from EPMA analyses from cores of coarse-grained garnet$_1$ (up to ~0.08) are higher than those calculated for the peak stability field (~0.03−0.04). Calculated X_{Grs} isopleths do not correspond to X_{Grs} garnet$_1$ core compositions of ~0.08, whereas X_{Grs} compositions from fine-grained garnet$_2$ and rims on coarse-grained garnet$_1$ have values which lie within the peak stability field at

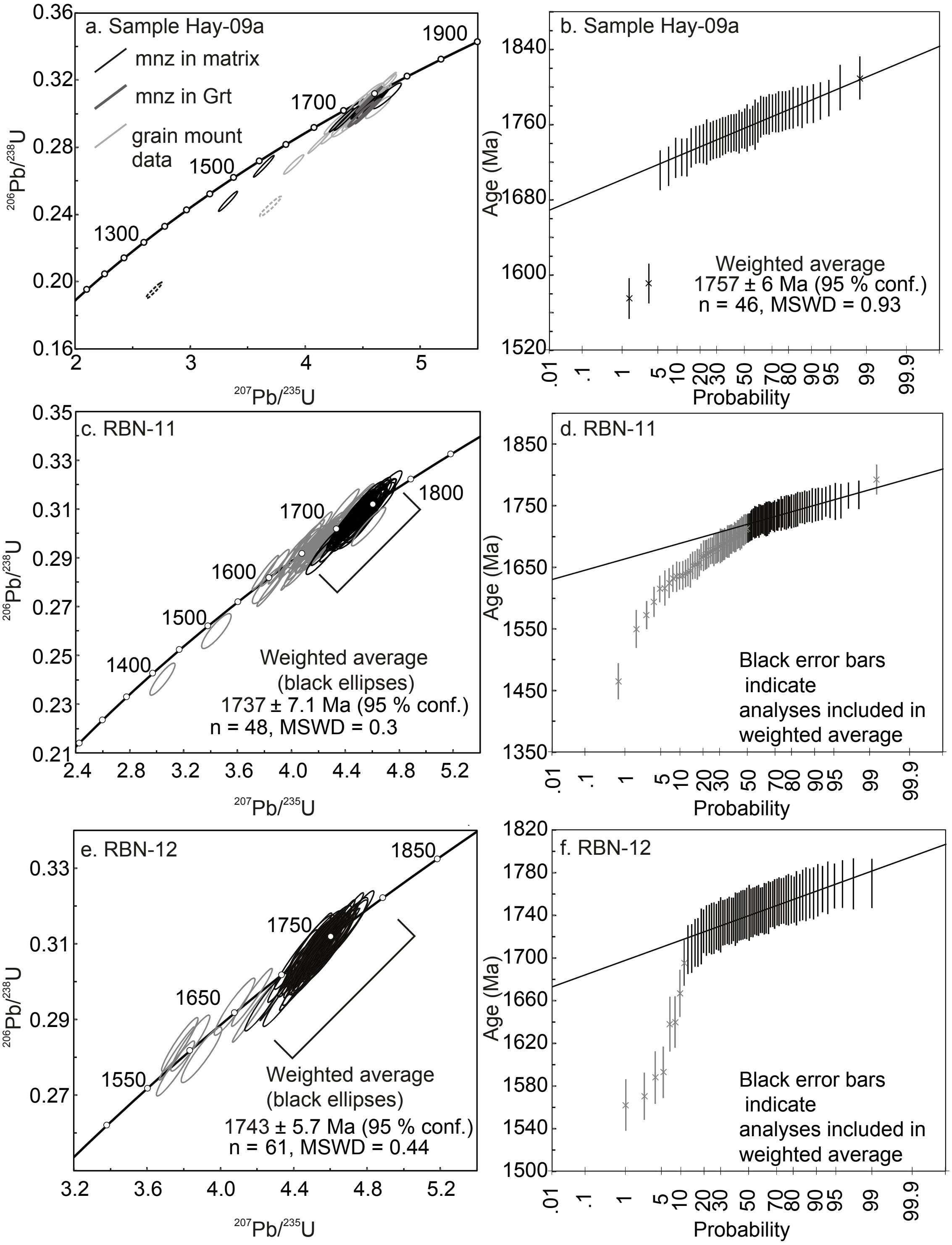

Fig. 7. Monazite U–Pb data continued. Concordia and linear probability plots for Capricorn Ridge sample Hay-09a (a–b), and Adla Domain samples RBN-11 (c–d) and RBN-12 (e–f). Dashed ellipses are >10% discordant.

~8−10 kbar, ~870 °C.

Capricorn Ridge samples Hay-05a and Hay-09a have the peak assemblage garnet−sillimanite−plagioclase−K-feldspar−quartz−ilmenite−rutile−biotite−melt, which is calculated to occur at ~7−11 kbar, ~840–880 °C for Hay-05a and ~7–11 kbar, ~850–880 °C for Hay-09a (Fig. 9b−c). X_{Grs} garnet core values of ~0.04 in samples Hay-05a and Hay-09a occur within the peak assemblage fields at ~8 kbar, ~850–880 °C for Hay-05a and ~10 kbar, ~850–880 °C for sample Hay-09a. Using combined peak stability fields and X_{Grs} contours, the peak conditions of metamorphism recorded at Capricorn Ridge

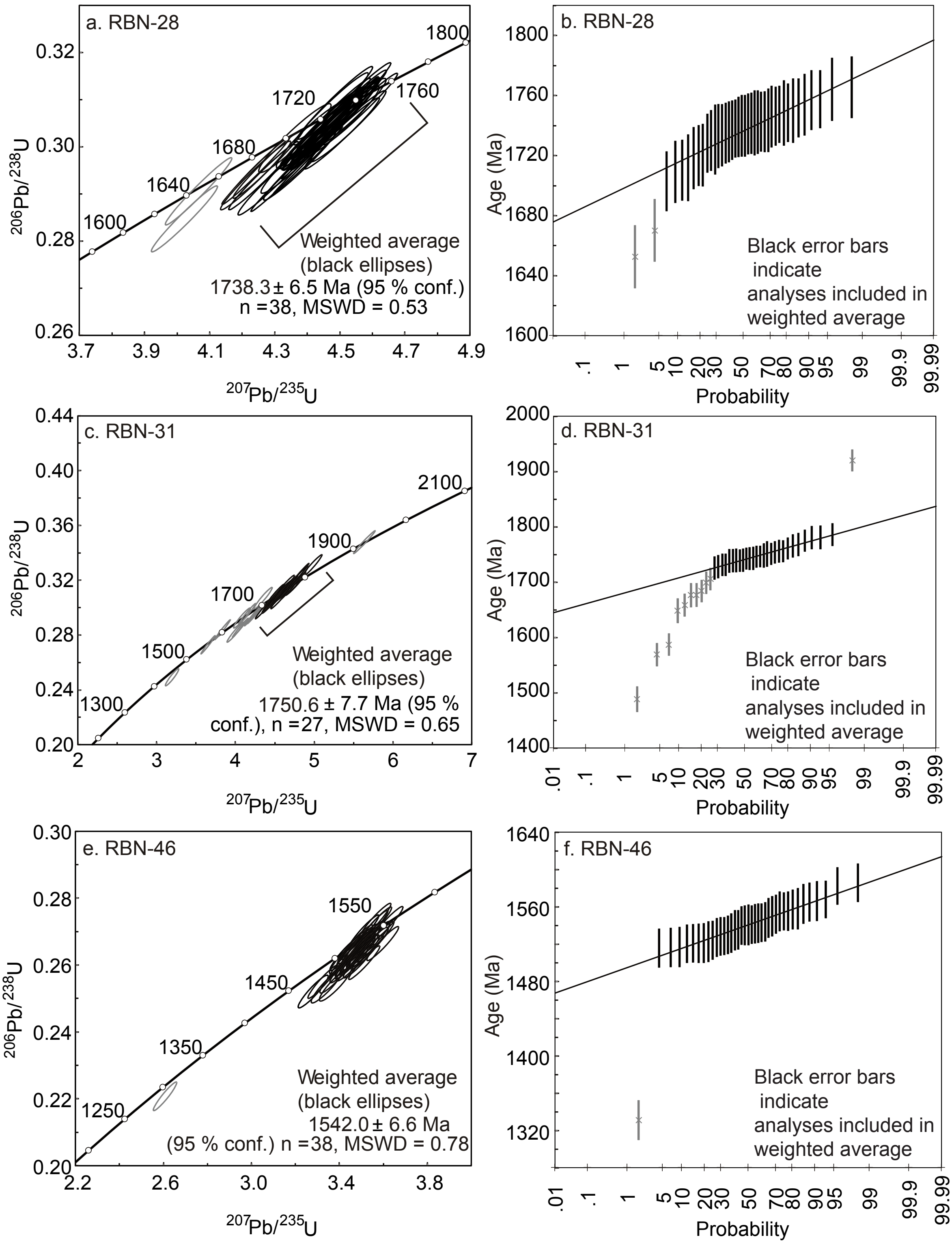

Fig. 8. Monazite U–Pb data continued. Concordia and linear probability plots for Adla Domain samples RBN-28 (a–b), RBN-31 (c–d) and RBN-46 (e–f).

are interpreted to be ~8−10 kbar, ~850 °C.

Sample RBN-28 (Adla Domain), contains the interpreted peak assemblage garnet−sillimanite−plagioclase−K-feldspar−quartz−ilmenite−biotite−melt at $P−T$ conditions of ~7−10 kbar and ~850–890 °C (Fig. 9d). X_{Grs} compositions of garnet cores range between 0.03 and 0.04, which lie within the calculated stability field of the interpreted peak assemblage between ~7−9 kbar.

Table 3. Whole rock geochemistry of samples used for *P-T* pseudosections (wt.%)

	SiO_2	TiO_2	Al_2O_3	MnO	MgO	CaO	Na_2O	K2O	P_2O_5	Fe_2O_3T	Total
Hay-11-5a	68.71	0.62	16.62	0.1	2.06	0.65	0.56	3.78	0.06	6.58	100.29
Hay-11-09	68.04	0.61	15.63	0.1	2.12	2.43	2.07	3.2	0.07	5.48	100.27
Hay-11-17	43.51	1.16	35.29	0.21	4.06	0.53	0.18	2.81	0.09	12.2	100.45
RBN-28	49.08	0.96	27.48	0.15	4.18	0.62	0.75	5.47	0.08	10.87	100.03

6. Discussion

The aim of this study is to provide constraints on the timing and conditions of metamorphism from the poorly characterised southern margin of the North Australian Craton, in order to place the metamorphic evolution into the regional tectonic framework to make inferences about the nature of the inferred Paleoproterozoic margin to the NAC. A summary of age and $P-T$ data from this study is shown in Table 4.

6.1 Timing of high grade metamorphism

The U–Pb age data from Mount Hay and Capricorn Ridge show major age populations at c. 1760–1740 Ma. Texturally, the c. 1760–1740 Ma age populations were obtained from monazite located within garnet and the enclosing matrix, which therefore provide a textural context for similarly aged analyses obtained from grain mounts. With the exception of one analysis (M44B, Hay-12, c. 1708 Ma), monazite grains included in garnet yield ages between c. 1790−1740 Ma. In contrast, monazite located in the matrix typically yield a larger age range, extending from c. 1800 Ma to c. 1520 Ma (excluding one younger c. 1400 Ma possible outlier in Hay-05a, Fig. 6e–f). We attribute the above age range differences to greater chemical communication in the matrix and more restricted chemical communication with external reservoirs for monazite in garnet (cf. Stuwe, 1997). Monazite grain mount age data obtained from the central and northern Adla Domain show similar age populations at c. 1750–1738 Ma (samples RBN-11, RBN-12, RBN-28 and RBN-31). These samples also show variable younger ages that in some samples extend down to c. 1650−1500 Ma, with one younger c. 1465 Ma age from monazite from sample RBN-11.

Several studies have discussed the growth−dissolution behaviour of monazite during high-grade metamorphism (e.g. Rubatto et al., 2006; Kelsey et al., 2008; Brown and Korhonen, 2009; Stepanov et al., 2012; Korhonen et al., 2013; Rubatto et al., 2013; Yakymchuk and Brown, 2014). Phase equilibria modelling coupled with experimental data has been used to argue that in average metapelite or metagreywacke rocks that have melted, monazite may commonly (but not always) record an age along the high-T part of the retrograde path (Kelsey et al., 2008; Yakymchuk and Brown, 2014; but see also Stepanov et al., 2012). Additionally, monazite may approximate the age at which the rock cools through its elevated solidus (e.g. Brown and Korhonen, 2009; Kali et al., 2010; Reno et al., 2012; Korhonen et al., 2013; Morrissey et al., 2014). On this basis, we tentatively interpret the main c. 1760−1740 Ma monazite age populations from Mount Hay, Capricorn Ridge and the Adla Domain to record monazite growth and/or recrystallisation predominantly during cooling, and close to the elevated solidus. The c. 20 Ma weighted average age range that samples from Mount Hay, Capricorn Ridge and the Adla Domain yield may be related to local-scale differences in composition or melt abundance, resulting in local differences in the temperature of the elevated solidus. We consider c. 1760−1740 Ma to be the best estimate for the timing of granulite facies metamorphism and partial melting.

Rare monazite grains that preserve ages between 1920−1805 Ma from samples Hay-05a, Hay-09a and RBN-31 are probably detrital (e.g. equivalent to the Lander Rock Beds; Claoue-Long et al., 2008a), or for the grains with c. 1810 Ma ages, may record contact metamorphism from the protolith to the nearby mafic and felsic Mount Hay granulite (c. 1803 Ma; Claoue-Long and

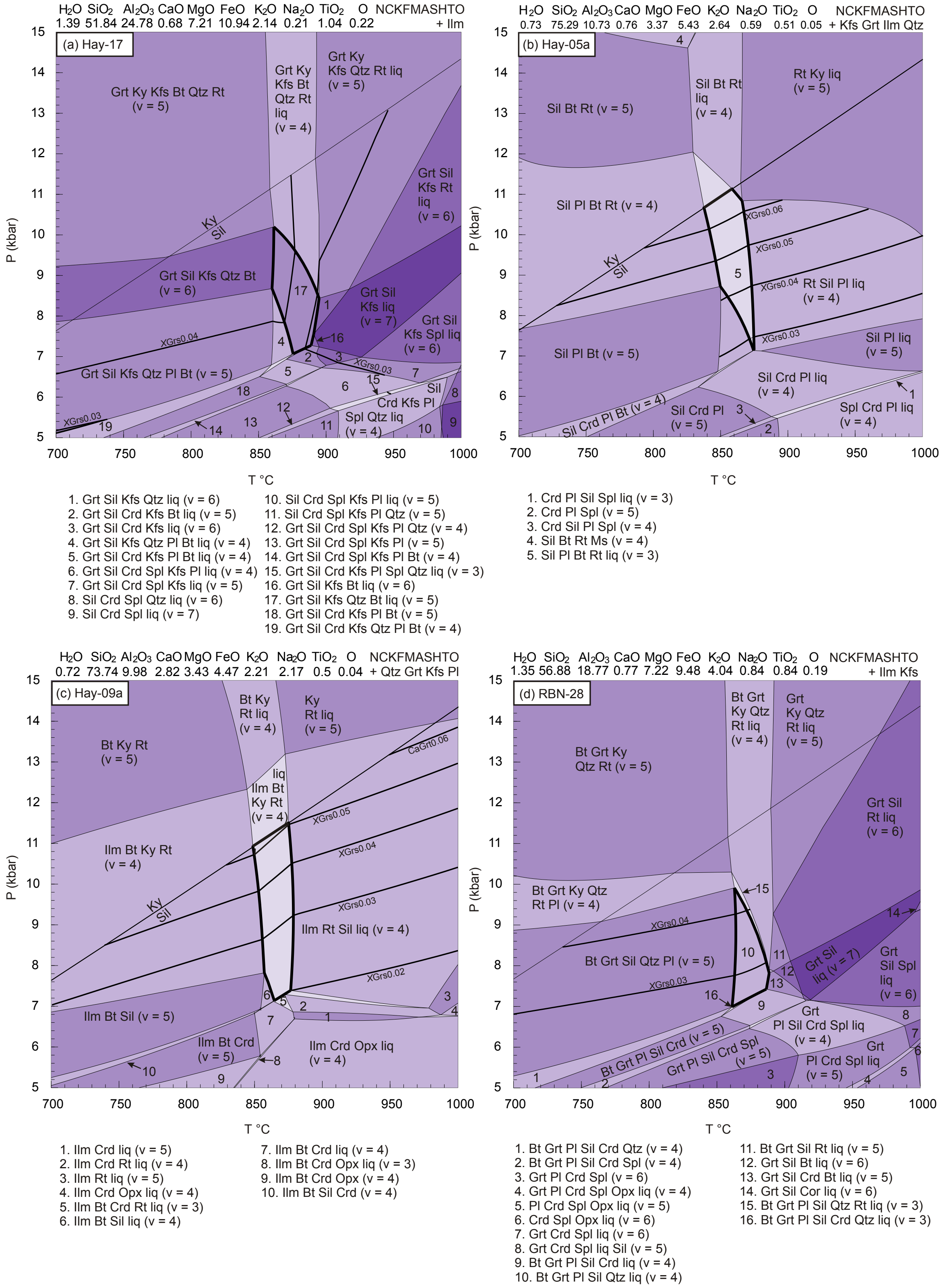

Fig. 9. $P-T$ pseudosections calculated for (a) Sample Hay-17, (b) Hay-05a, (c) Hay-09a and (d) RBN-28. Bold lines outline interpreted peak stability fields. + phases label above pseudosection indicates phases that are stable throughout the respective pseudosections.

Hoatson, 2005). These rare preserved grains with older ages provide support for the notion that not all monazite had completely dissolved into melt by the metamorphic peak (Stepanov et al., 2012).

As documented by a number of studies, the Mount Hay Massif records an earlier phase of deformation relative to Capricorn Ridge (Waters-Tormey and Tikoff, 2007; Waters-Tormey et al., 2009; Bonamici et al., 2011). Using aeromagnetic imagery of the Mount Hay area, the fabrics of the Adla Domain are inferred to be younger than the fabrics on the Mount Hay Massif as they appear to envelop magnetic trends at Mount Hay. The age data in this study reveals no discernible age differences between the major age populations from Mount Hay, Capricorn Ridge or the Adla Domain. Consequently, the lack of discernible age differences from different structural domains suggests that the main event was responsible for: 1) the development of S_1−S_2 preserved in the Mount Hay Massif; 2) the subsequent transposition of S_1−S_2 fabrics and generation of S_3 on Capricorn Ridge, and 3) development of the east−west trending fabric in the Adla Domain. Thus, all of these fabrics developed within a timespan shorter than the resolution of the age data.

Claoue-Long and Hoatson (2005) obtained a c. 1700 Ma U−Pb zircon weighted average age from low-U overgrowths and recrystallised zircon domains from the Mount Hay Massif, which is younger than most of the calculated weighted averages obtained in this study. Some samples from the Mount Hay Massif, Capricorn Ridge and Adla Domain (Hay-12, Hay-05a, RBN-11 and RBN-12) record younger ages that overlap with c. 1700 Ma weighted average age obtained by Claoue-Long and Hoatson (2005). It is possible that these younger, variably recorded ages represent minor Strangways Event-aged (c. 1740−1690 Ma) reworking. However, the majority of the above samples also yield younger monazite ages that extend to at least as young as c.1600−1540 Ma, which corresponds to the timing of the c. 1600−1560 Ma Chewings Orogeny in the Arunta Region (e.g. Vry et al., 1996; Ahmad and Scrimgeour, 2013; Anderson et al., 2013; Morrissey et al., 2014). Our preferred interpretation is that monazite ages younger than the c. 1760−1740 Ma populations represent partially to fully recrystallised monazite grains (or domains in monazite grains) as a result of Chewings Orogeny-aged reworking.

A garnet-bearing pegmatite from the northern Adla Domain that contains a fabric parallel to the main foliation yields a single monazite population of c. 1542 Ma (RBN-46). The single late Chewings Orogeny-aged population (e.g. Morrissey et al., 2014) for the pegmatite is supportive of the presence of late stage melts in this area of southern Aileron Province. In addition, it may suggest that the fabric at least in the northern Adla Domain may be composite or reworked. The pegmatite is located ~2 km south of a major shear zone that does not outcrop but is evident in the TMI–1VD image (Fig. 2), and may record the timing of deformation associated with displacement of this shear zone. The nature and physical conditions of the Chewings Orogeny in this area of the southern Aileron Province remain relatively unknown. However, the absence of significant large and/or pervasive Chewings Orogeny-aged (c. 1600–1550 Ma) monazite populations in the studied samples, and minor scattered c. 1640−1560 Ma zircon ages from the Mount Hay Granulite from previous work (Claoue-Long and Hoatson, 2005) could indicate that Chewings Orogeny-aged reworking did not pervasively affect the Hay area. Instead, Chewings Orogeny-aged reworking may be restricted to localised discrete zones, such as shear zones, within a largely residual granulite facies belt of c. 1760−1740 Ma age.

6.2 P−T conditions of metamorphism in and east of the Mount Hay Block

Rocks at Mount Hay, Capricorn Ridge and the Adla Domain are interpreted to have undergone granulite facies metamorphism and partial melting at c. 1760−1740 Ma.

Table 4. Summary of data from this study

Sample	Location	Location Zone 53 K (Easting)	(Southing)	Rock type	Monazite U−Pb age weighted average (Ma, 95 % conf.)	*P−T* results
Hay-05a	Capricorn Ridge	315701	7405322	Grt-Sil metapelitic gneiss	1756 ± 8	~8 kbar,~850−880 °C
Hay-09a	Capricorn Ridge	315827	7405246	Grt-Sil metapelitic gneiss	1757 ± 6	~10 kbar, ~850−880 °C
Hay-12	Mount Hay Massif	296989	7410728	Grt-Sil metapelitic gneiss	1758 ± 15	
Hay-17	Mount Hay Massif	297115	7410517	Grt-Sil metapelitic gneiss	1740 ± 7	~7−10 kbar, ~850−900 °C
RBN-11	Northern Adla Domain	353106	7412191	Grt-Sil metapelitic gneiss	1738 ± 7	
RBN-12	Northern Adla Domain	352135	7412382	Grt-Sil metapelitic gneiss	1743 ± 6	
RBN-28	Central Adla Domain	351666	7408488	Grt-Sil metapelitic gneiss	1738 ± 7	~7−10 kbar, ~850−900 °C
RBN-31	Central Adla Domain	351661	7408408	Grt-Bt psammitic gneiss	1751 ± 8	
RBN-46	Northern Adla Domain	352139	7412379	Pegmatite	1542 ± 7	

Calculated garnet X_{Grs} isopleths were used to further investigate the peak $P-T$ conditions of metamorphism. In implementing this approach, an assumption is made that Ca diffusion in garnet is sufficiently slow, such that garnet X_{Grs} core values have not been appreciably modified post-peak metamorphism (cf. Pattison and Bégin, 1994). For sample Hay-17, the interpreted peak stability field occurs at ~7−10 kbar, 850−900 °C. X_{Grs} isopleths for the interpreted peak field for Hay-17 (~0.03−0.04) correspond to measured X_{Grs} values of coarse garnet$_1$ rims and fine-to-medium-grained garnet$_2$ but are lower than coarse garnet$_1$ core values (~0.07−0.08). It is possible that the coarse garnet$_1$ cores grew at lower temperatures when the rock was more Ca rich (e.g. greater abundance of plagioclase), whereas the coarse garnet$_1$ rims and garnet$_2$ may have either grown after most melt loss had occurred, or alternatively were able to equilibrate with the effective bulk composition. For Capricorn Ridge samples (Hay-05a and Hay-09a) and Adla Domain sample RBN-28, Ca compositional isopleths correspond to the core X_{Grs} values of garnet (~0.04), at ~8−10 kbar, which are interpreted to be the best P estimates of peak metamorphism. Together, the $P-T$ estimates of peak metamorphism for Mount Hay Massif, Capricorn Ridge and the central Adla Domain are similar (~7–10 kbar, ~850–900 °C). These $P-T$ estimates overlap but are somewhat higher P compared to previous estimates (in the range of ~700−900 °C, ~6−8 kbar; Glikson, 1984; Harley et al., 1994; Bonnay, 2001; Staffier, 2007), which may be related to differences in methodology in this study compared to previous studies. Existing $P-T$ estimates on the conditions of metamorphism in the Mount Hay area have been calculated using conventional thermobarometry methods, in which individual mineral chemistry is the primary compositional input for calculations (compared to bulk composition in phase diagrams). Conventional thermobarometry and pseudosection thermobarometry methods for estimating $P-T$ have been reviewed and discussed by Powell and Holland (2008). Commonly, forward modelling pseudosection thermobarometry is considered to be the most effective thermobarometry for granulite facies rocks (Powell and Holland, 2008). We therefore favour the $P-T$ range obtained in this study as the best estimates on peak metamorphic conditions in the Mount Hay area. The occurrence of garnet-bearing mafic granulites in the Mount Hay Block and as boudins in metasediments in the Adla Domain also provides qualitative circumstantial support for the attainment of medium-P conditions (cf. Spear, 1993; Pitra et al., 2010). Taken together, the presence of garnet-bearing mafic granulites and elevated pressures obtained from metapelitic samples is a significant finding as elevated pressures are distinctly rare for the Arunta Region.

Spinel−biotite reaction microstructures are present in boudinaged peak metamorphic sillimanite grains in sample Hay-12 (Mount Hay Massif). These reaction microstructures are similar to Chewings Orogeny-aged reaction microstructures in garnet-sillimanite bearing metapelites in the Anmatjira Range, central Aileron Province (Anderson et al., 2013). In addition, Hay-17 contains evidence for two generations of garnet and sillimanite growth. It is possible, given the spread of monazite ages down to c. 1530 Ma in nearby sample Hay-12 that the fine-grained reaction spinel-biotite microstructures and generation of garnet−sillimanite−biotite development in Hay-17 may be c. 1600–1550 Ma Chewings Orogeny-aged (or possibly c. 1740–1690 Ma Strangways Event-aged) rather than c. 1760−1740 Ma. As a consequence of a lack of reaction microstructures that can confidently be attributed to the same c. 1760−1740 Ma event; a retrograde *P−T* path cannot be confidently surmised for any sample.

6.3 Broader context of c. 1760−1740 Ma metamorphism in the Arunta Region

The identified occurrence of c. 1760−1740 Ma metamorphism elsewhere in the Arunta Region is limited. The only other reports of similar-aged metamorphism are c. 1770−1740 Ma ages from the south-eastern Arunta (e.g. Wade et al., 2008; Carson et al., 2009; Whelan et al., 2012; Bodorkos et al., 2013; Kositcin et al., 2013), and c. 1780−1770 Ma monazite ages obtained from a metasedimentary gneiss further west of Mount Hay (Biermeier et al., 2003). In the eastern Arunta, Whelan et al. (2012) obtained peak *P−T* estimates of 5.2–7.4 kbar, 730–810 °C from the Albarta Metamorphics, for which they obtained monazite U−Pb ages of c. 1770−1750 Ma from the same outcrop. To the west of Mount Hay around the Mount Heughlin area, Biermeier et al. (2003) obtained estimates of ~10 kbar, ~780 °C for the same sample as that in which a c. 1770 Ma monazite age grouping was obtained. Although the spatial distribution of c. 1770–1740 Ma metamorphosed rocks in the Arunta Region is still uncertain, age data from previous work and this study together suggest that this event may have an east−west trending footprint across ~300 km of the present day southern Aileron Province.

The c. 1770–1740 Ma timing of metamorphism in the southern Aileron Province overlaps with a c. 1770−1750 Ma magmatic suite (CAT suite) of arc-related or Cordilleran-type geochemical signatures in the southeast Arunta region (Foden et al., 1988; Zhao and Bennett, 1995; Zhao and McCulloch, 1995). The CAT suite magmatic rocks have been used as evidence for the operation of active margin processes in the late-Paleoproterozoic in the southern NAC (e.g. Zhao and McCulloch, 1995). However, the metamorphic record of orogenesis with a postulated plate margin at this time has remained enigmatic. Identification of ancient plate margins is assisted greatly by the presence of high-pressure metamorphic rocks (e.g. Möller et al., 1995). Whereas eclogites have not been identified in the Arunta Region, pressures of ~8−10 kbar (this study; Biermeier et al., 2003) for the c. 1780−1740 Ma timeline are unusually high for the Arunta Region. These pressures broadly equate to crustal depths of about 25 to 35 km, and by themselves do not imply significantly thick crust. However, in the context of high-thermal gradient metamorphism that characterises much of the tectonothermal evolution of the Arunta Region (pressures of <~7 kbar at similar temperatures; e.g. Morrissey et al., 2011; Anderson et al., 2013; Morrissey et al., 2014), pressures of ~8−10 kbar are somewhat anomalous. The *P−T* estimates obtained in this study correspond to an apparent thermal gradient of ~85−110 °C $kbar^{-1}$ for Mount Hay and Capricorn Ridge, and ~ 90−130 °C $kbar^{-1}$ for the central Adla Domain. Although these thermal gradients can be classified as ‘warmer than normal’, they still fall within the Barrovian realm of metamorphism (Stuwe, 2007). In this context, the *P−T* constraints may provide support for thickened crust (Jamieson et al., 1998).

Metamorphosed mafic and intermediate intrusive rocks volumetrically dominate exposures in the Mount Hay Block and adjacent Mount Chapple Hills. In addition, Collins and Sawyer (1996) argued that granitoid magmatism accompanied at least the early stages of granulite facies deformation in the Mount Hay Block (e.g. charnockitic magmatism). This interpretation is supported by reported U−Pb zircon ages of

c. 1783−1774 Ma obtained from granitoids inferred to be syntectonic with metamorphism and deformation on Mount Hay (Bonnay et al., 2000). The tectonic setting in which the above rocks were metamorphosed remains uncertain to some extent, however: 1) the proximity both temporally and spatially to the c. 1770−1750 Ma CAT suite magmatic rocks, 2) the apparently discrete tectonothermal footprint in only the southern Arunta Region, 3) the moderate to medium-*P*, warmer than normal apparent thermal gradient, and 4) lack of high-*P* rocks suggests that if metamorphism was related to an active margin it did not develop or did not preserve evidence for a large orogenic plateaux, and did not preserve, exhume or even generate high-*P* rocks.

The Paleoproterozoic evolution of the Arunta Region between c. 1820−1640 Ma is characterised by episodic tectonothermal events, deep (turbiditic) to shallow marine and volcaniclastic sedimentation, and felsic to mafic magmatism with a younging pattern broadly to the south−south east (e.g. Scrimgeour, 2004; Betts and Giles, 2006; Claoue-Long et al., 2008a; Ahmad and Scrimgeour, 2013). Evidence for the earliest tectonic events recognised in the Arunta Region— the c. 1810–1790 Ma Stafford Event and c. 1780–1770 Ma Yambah Events are widespread in the Aileron Province, predominantly involving bimodal magmatism and localised high-thermal gradient metamorphism and deformation, contemporaneous with, and bracketed temporally by sedimentation (Scrimgeour, 2003; Claoue-Long and Hoatson, 2005; Hoatson et al., 2005; Rubatto et al., 2006; Wade et al., 2008). Bonnay et al. (2000) proposed that protolith to the interlayered mafic and felsic Mount Hay granulite may have formed via basaltic magma injection into a silicic magma chamber at shallow (<2 kbar) depth, based on field relationships and phase equilibria modelling. This probably implies the lithosphere was relatively thin at the time of intrusion of basaltic magma, constrained at c. 1803 Ma by Claoue-Long and Hoatson (2005). A back-arc environment has been proposed for the Aileron Province during the Stafford Event, on the basis of volcanic and volcaniclastic sedimentation and bimodal magmatism (Scrimgeour, 2006; Ahmad and Scrimgeour, 2013). However, upright fabrics have also been attributed to the Stafford Event in the central and northern Aileron Province (Scrimgeour, 2006; Ahmad and Scrimgeour, 2013), implying there may have been compressional as well as extensional components during the Stafford Event. The event also affected the Tanami Region, where it is associated with upright fabrics and mineralisation, and Tennant Region, where it is known as the c. 1820–1800 Ma Murchison Event and is associated with extension (Scrimgeour, 2003; Ahmad and Scrimgeour, 2013).

The c. 1770–1750 Ma intrusive rocks in the Aileron Province were considered to have developed during north-dipping subduction or underthrusting of oceanic crust to the south–southeast of the Aileron Province (Betts and Giles, 2006; Scrimgeour, 2006; Ahmad and Scrimgeour, 2013). However, evidence for compressional deformation of this age in the Arunta Region outside of the Mount Hay area appears to be relatively limited. Compressional fabrics inferred to be of 1780–1770 Ma in the Reynolds and Anmatjira Range are now recognised to be 1600–1550 Ma Chewings Orogeny-aged (e.g. Vry et al., 1996; Anderson et al., 2013; Morrissey et al., 2014). The c. 1770–1750 Ma intrusive rocks were also approximately coeval with basin development in the Arunta Region (Maidment et al., 2005; Ahmad and Scrimgeour, 2013) and are temporally and spatially proximal to the protolith of the c. 1750–1745 Bruna Gneiss in the eastern Arunta. The Bruna Gneiss has ‘A-type’ or anorogenic geochemical characteristics (Cooper et al., 1988; Foden et al., 1988). Together, in the c. 50 Ma preceding deformation and metamorphism in the Mount Hay area, the Arunta Region appears to be dominated by extensional processes.

Following 1760–1740 Ma deformation and metamorphism in the Mount Hay area and southern Aileron Province, areas of the Arunta

Region underwent up to granulite facies metamorphism and magmatism during the c. 1740–1690 Ma Strangways Event, which is most pervasive in the eastern Aileron Province (Möller et al., 2003; Claoue-Long et al., 2008b; Bodorkos et al., 2013). This event is complex, and despite a number of studies, remains not fully understood. The Strangways Event was coeval with the deposition of the sedimentary protolith of unnamed pelitic gneiss in the eastern Aileron Province (Bodorkos et al., 2013). Geochronological constraints on the timing of the Strangways Event suggest it was a prolonged event (e.g. Claoue-Long et al., 2008b), potentially involving at least two tectonothermal phases (Norman and Clarke, 1990; Goscombe, 1992; Diener et al., 2008). *P–T* conditions of up to ~8–10 kbar, ~800–950 º C have been estimated for M_1 in the Strangways Metamorphic Complex, for which both clockwise and anticlockwise *P–T* paths have been advocated (Goscombe, 1992; Ballevre et al., 1997; Möller et al., 2003; Diener et al., 2008). More recent *P–T* pseudosection modelling on M_2 assemblages suggest peak *P–T* conditions of ~6–7.5 kbar, ~670–720 ºC with little change in *P* throughout M_2 (Diener et al., 2008). Very high thermal gradient conditions (~2.6–4.0 kbar, 750–800 ºC) have also been estimated in the Mopunga Range in the eastern Arunta Region at c. 1730 Ma, attributed to magmatically driven, thermal sources (Scrimgeour et al., 2001). The Strangways Event has been reported to involve a component of east−west compression (Payne et al., 2009; Ahmad and Scrimgeour, 2013); however, structural evidence for northeast extension and granite emplacement at c. 1730 Ma has also been documented (Lafrance et al., 1995). Some Proterozoic reconstruction models have attributed the Strangways Event to be related to an active margin to the south of the Arunta Region (Betts and Giles, 2006; Scrimgeour, 2006). By contrast, other models have argued that the east-west compressional component of the Strangways Event may be associated with the postulated accretion of Laurentia to eastern Paleoproterozoic Australia (Payne et al., 2009). The termination of the Strangways Event is marked by the intrusion of dolerite dykes, constrained by Claoue-Long and Hoatson (2005) to be c. 1690 Ma, implying extensional processes were active at this time at least on a local scale.

After the Strangways Event, the record of tectonism in the Arunta Region largely shifted to the Warumpi Province, involving c. 1690–1650 Ma magmatism, (sub)aerial volcanism and sedimentation (Scrimgeour et al., 2005; Hollis et al., 2013). The c. 1640–1635 Ma Liebig Orogeny in the Warumpi Province is interpreted to record the accretion of the exotic Warumpi Province onto the Aileron Province (southern NAC) via south-dipping subduction (Scrimgeour et al., 2005). However, recently, U–Pb age and Hf isotopic data were used to propose that the Warumpi Province may have originally been a segment of the Aileron Province (NAC), which rifted from the Aileron Province after 1780–1760 Ma and then reaccreted during the Liebig Orogeny (Hollis et al., 2013).

Further insights into the evolution of the southern margin of the NAC during the late-Paleoproterozoic were provided through U–Pb and Hf isotopic work by Smits et al. (2013). Zircon U−Pb age and Lu−Hf isotopic data on igneous and sedimentary protoliths sampled from Pine Creek in the northern NAC through to the Arunta Region were used to argue for a long-lived, southwards migrating retreating margin during the late-Paleoproterozoic.

We suggest that the southern Aileron Province underwent c. 1760−1740 Ma aged granulite facies metamorphism and deformation, which was associated spatially and temporally with magmatism and basin development to the east as part of the long-lived retreating margin setting as proposed by Smits et al. (2013) and consistent with evidence for a considerable component of extension in the Arunta Region between 1820–1640 Ma. Structural data on the Mount Hay Block has been used to propose that deformation preserved on the Mount Hay Massif developed in a contractional setting, whereas the development of the Capricorn

Ridge subsequently occurred in an oblique-divergent setting (Waters-Tormey et al., 2009; Bonamici et al., 2011). If this is the case, the age data obtained in this study suggests that the switch from contractional to extensional tectonics was relatively rapid. In the context of an envisaged retreating margin setting, the Mount Hay area may have been situated in a back-arc environment in which the deformation and metamorphism preserved on the Mount Hay Massif occurred during a short-lived compressional phase, potentially as a result of the arrival of more buoyant oceanic crust/plateaux, followed by renewed extension (e.g. Collins, 2002; Betts et al., 2011). Such a scenario is one way in which deformation and orogenesis could be localised into narrow belts (< 100 km wide), such as the Mount Hay area and Adla Domain. Short-lived compressional phases in an otherwise extension-dominated setting could possibly also be recorded by the c. 1740−1690 Ma Strangways Event further east.

7. Conclusion

The Mount Hay area, in the southern Aileron Province underwent moderate-*P*, granulite facies metamorphism at c. 1760−1740 Ma. Monazite ages ranging as young as c. 1600−1520 Ma and pegmatite crystallisation at c. 1542 Ma suggest cryptic non-pervasive reworking of the area during the Chewings Orogeny. Combined with previously identified 1770−1750 Ma magmatism with arc-related geochemical characteristics, the Mount Hay area is interpreted to record the tectonothermal evolution of a comparatively short-lived compressional phase along the southern margin of the NAC. The envisaged tectonic setting of the central–southern Arunta Region in a back-arc environment during the late-Paleoproterozoic, as part of a long-lived retreating margin could allow for the generation of short-lived compressional phases leading to hot, narrow deformation belts such as the Mount Hay area.

Acknowledgements

We would like to thank B. Wade and A. Netting at Adelaide Microscopy for their assistance with analytical instruments. This work was funded by ARC discovery grant DP1095456 and ARC Linkage Grant LP100200127.

8. References

Northern Territory Geological Survey, 1997a. Alcoota/Alice Springs: magnetics and radiometric survey. Northern Territory Geological Survey, Darwin.

Northern Territory Geological Survey, 1997b. Napperby/Hermannsburg: magnetic and radiometric survey, Darwin.

Ahmad, M., Scrimgeour, I.R., 2013. Geological Framework, in: Ahmad, M., Munson, T.J. (Eds.), Geology and mineral resources of the Northern Territory, special publication 5. Northern Territory Geological Society.

Aleinikoff, J., Schenck, W., Plank, M., Srogi, L., Fanning, C., Kamo, S., Bosbyshell, H., 2006. Deciphering igneous and metamorphic events in high-grade rocks of the Wilmington Complex, Delaware: Morphology, cathodoluminescence and backscattered electron zoning, and SHRIMP U-Pb geochronology of zircon and monazite. Geological Society of America Bulletin 118, 39-64.

Anderson, J., Kelsey, D.E., Hand, M., Collins, W.J., 2013. Conductively driven, high-thermal gradient metamorphism in the Anmatjira Range, Arunta region, central Australia. Journal of Metamorphic Geology 31, 1003-1026.

Ballevre, M., Hensen, B.J., Reynard, B., 1997. Orthopyroxene-andalusite symplectites replacing cordierite in granulites from the Strangways Range (Arunta block, central Australia): A new twist to the pressure-temperature history. Geology 25, 215-218.

Betts, P.G., Giles, D., 2006. The 1800-1100 Ma tectonic evolution of Australia. Precambrian Research 144, 92-125.

Betts, P.G., Giles, D., Aitken, A., 2011. Palaeoproterozoic accretion processes of Australia and comparisons with Laurentia. International Geology Review 53, 1357-1376.

Betts, P.G., Giles, D., Schaefer, B.F., 2008. Comparing 1800-1600 Ma accretionary and basin processes in Australia and Laurentia: Possible geographic connections in Columbia. Precambrian Research 166, 81-92.

Biermeier, C., Stuwe, K., Foster, D.A., Finger, F., 2003. Thermal evolution of the Redbank thrust system, central Australia: Geochronological and phase-equilibrium constraints. Tectonics 22, 1-23.

BMR, 1983. Alice Springs, Northern Territory: sheet SF5314, 2nd ed. Bureau of Mineral Resources, Geology and Geophysics, Canberra.

Bodorkos, S., Beyer, E.E., Edgoose, C.J., Whelan, J.A., Webb, G., Vandenberg, L.C., Hallet, L., 2013. Summary of results: Joint NTGS-GA geochronology project: Central and eastern Arunta Region, January 2008-June 2011, p. 74.

Bonamici, C.E., Tikoff, B., Goodwin, L.B., 2011. Anatomy of a 10 km scale sheath fold, Mount Hay ridge, Arunta Region, central Australia: The structural record of deep crustal flow. Tectonics 30, 19.

Bonnay, M., 2001. Felsic characterization and transfer of the magmas in the average crust to deep. Example: The Hay Mount in central Australia (Translated title). University of Quebec–Chicoutimi, Chicoutimi, Canada, p. 522.

Bonnay, M., Collins, W.J., Sawyer, E.W., Wiebe, R.A., 2000. Mt Hay: Granite magma transfer through the deep crust or a buried high-level plutonic complex?, in: Collins, W.J. (Ed.), Granite magma seggregation and transfer during compressional deformation in the deep crust? Proterozoic Arunta Inlier, central Australia. Geological Society of Australia Incorporated, Sydney, p. 104.

Brown, M., Korhonen, F.J., 2009. Some remarks on melting and extreme metamorphism of crustal rocks, Physics and Chemistry of the Earth's Interior. Springer New York, pp. 67-87.

Carson, C., Claoue-Long, J., Stern, R.A., Close, D., Scrimgeour, I., Glass, L.M., 2009. Summary of results. Joint NTGS-GA geochronology project: Arunta and Pine Creek regions, July 2006–May 2007. Northern Territory Geological Survey, Darwin.

Cawood, P.A., Korsch, R.J., 2008. Assembling Australia: Proterozoic building of a continent. Precambrian Research 166, 1-38.

Claoue-Long, J., Edgoose, C., Worden, K., 2008a. A correlation of Aileron Province stratigraphy in central Australia. Precambrian Research 166, 230-245.

Claoue-Long, J., Maidment, D., Hussey, K., Huston, D., 2008b. The duration of the Strangways Event in central Australia: Evidence for prolonged deep crust processes. Precambrian Research 166, 246-262.

Claoue-Long, J.C., Hoatson, D.M., 2005. Proterozoic mafic-ultramafic intrusions in the Arunta Region, central Australia Part 2: Event chronology and regional correlations. Precambrian Research 142, 134-158.

Collins, W.J., 2002. Hot orogens, tectonic switching, and creation of continental crust. Geology 30, 535-538.

Collins, W.J., Sawyer, E.W., 1996. Pervasive granitoid magma transfer through the lower-middle crust during non-coaxial compressional deformation. Journal of Metamorphic Geology 14, 565-579.

Collins, W.J., Williams, I.S., 1995. SHRIMP ionprobe dating of short-lived Proterozoic tectonic cycles in the northern Arunta Inlier, central Australia. Precambrian Research 71, 69-89.

Cooper, J.A., Mortimer, G.E., James, P.R., 1988. Rate of Arunta Inlier evolution at the eastern margin of the Entia Dome, central Australia. Precambrian Research 40-41, 217-231.

Diener, J.F.A., White, R.W., Powell, R., 2008. Granulite facies metamorphism and subsolidus fluid-absent reworking, Strangways Range, Arunta Block, central Australia. Journal of Metamorphic Geology 26, 603-622.

Foden, J.D., Buick, I.S., Mortimer, G.E., 1988. The petrology and geochemistry of granitic gneisses from the east Arunta Inlier, central Australia - Implications for Proterozoic crustal development. Precambrian Research 40-1, 233-259.

Giles, D., Betts, P.G., Lister, G.S., 2004. 1.8-1.5 Ga links between the North and South Australian Cratons and the Early-Middle Proterozoic configuration of Australia. Tectonophysics 380, 27-41.

Glikson, A.Y., 1984. Granulite-gneiss terranes of the southwestern Arunta block, central Australia: Glen Helen, Narwietooma, and Amburla. Bureau of Mineral Resourses, Canberra.

Goscombe, B., 1992. High-Grade Reworking of central Australian Granulites - Metamorphic evolution of the Arunta Complex. Journal of Petrology 33, 917-962.

Griffin, W.L., Powell, W.J., Pearson, N.J., O'Reilly, S.Y., 2008. GLITTER: data reduction software for laser ablation ICP-MS, in: Sylvester, P. (Ed.), Laser Ablation ICP-MS in the Earth Sciences: Current Practices and Outstanding Issues. Mineralogical Association of Canada. Shourt Course Series 40, pp. 308-311.

Hand, M., Buick, I.S., 2001. Tectonic evolution of the Reynolds-Anmatjira Ranges: a case study in terrain reworking from the Arunta Inlier, central Australia, in: Miller, J., Holdsworth, R.E., Buick, I.S., Hand, M. (Eds.), Continental Reactivation and Reworking, pp. 237-260.

Harley, S.L., Fitzsimons, I.C.W., Buick, I.S., 1994. Reactions and textures in wollastonite scapolite granulites and their significance for pressure temperature fluid histories of high-grade terranes. Precambrian Research 66, 309-323.

Hoatson, D.M., Stewart, A.J., 2001. Field investigations of Proterozoic mafic-ultramafic intrusions in the Arunta Province, central Australia. Geoscience Australia, Canberra.

Hoatson, D.M., Sun, S.S., Claoue-Long, J.C., 2005. Proterozoic mafic-ultramafic intrusions in the Arunta Region, central Australia Part 1: Geological setting and mineral potential. Precambrian Research 142, 93-133.

Holland, T., Powell, R., 2003. Activity–composition relations for phases in petrological calculations: an asymmetric multicomponent formulation. Contributions to Mineralogy and Petrology 145, 492-501.

Holland, T.J.B., Powell, R., 1998. An internally consistent thermodynamic data set for phases of petrological interest. Journal of Metamorphic Geology 16, 309-343.

Hollis, J.A., Kirkland, C.L., Spaggiari, C.V., Tyler, I.M., Haines, P.W., Wingate, M.T.D., Belousova, E., Murphy, R.C., 2013. Zircon U-Pb-Hf isotope evidence for links between the Warumpi and Aileron Provinces, West Arunta Region. Geological Survey of Western Australia, Perth.

Jamieson, R.A., Beaumont, C., Fullsack, P., Lee, B., 1998. Barrovian regional metamorphism: where's the heat?, in: Taylor, P.J., Obrien, P.J. (Eds.), What Drives Metamorphism and Metamorphic Reactions? Geological Soc Publishing House, Bath, pp. 23-51.

Kali, E., Leloup, P.H., Arnaud, N., Mahéo, G., Liu, D., Boutonnet, E., Van der Woerd, J., Liu, X., Liu-Zeng, J., Li, H., 2010. Exhumation history of the deepest central Himalayan rocks, Ama Drime range: Key pressure-temperature-deformation-time constraints on orogenic models. Tectonics 29, TC2014.

Kelsey, D.E., Clark, C., Hand, M., 2008. Thermobarometric modeling of zircon and monazite growth in melt-bearing systems: examples using model metapelitic and metapsammitic granulites. Journal of Metamophic Geology 26, 199-212.

Korhonen, F.J., Clark, C., Brown, M., Bhattacharya, S., Taylor, R., 2013. How long-lived is ultrahigh temperature (UHT) metamorphism? Constraints from zircon and monazite geochronology in the Eastern Ghats orogenic belt, India. Precambrian Research 20, 764-781.

Kositcin, N., Beyer, E.E., Whelan, J.A., Close, D.F., Hallet, L., Dunkley, D., 2013. Summary of results: Joint NTGS-GA geochronology project: Arunta Region, Ngalia Basin, Tanami Region and Murphy Province, July 2011-June 2012, in: Survey, N.T.G. (Ed.), p. 45.

Kretz, R., 1983. Symbols for rock-forming minerals. American Mineralogist 68, 277-279.

Lafrance, B., Clarke, G.L., Collins, W.J., Williams, I.S., 1995. The emplacement of the Wuluma granite: melt generation and migration along steeply dipping extensional fractures at the close of the Late Strangways orogenic event, Arunta Block, central Australia. Precambrian Research 72, 43-67.

Ludwig, K.R., 2008. Isoplot: A Geochronological Toolkit for Microsoft Excel, 3.7 ed. Berkeley Geochronology Centre, Berkeley.

Maidment, D., 2005. Paleozoic high-grade metamorphism within the Centralian Superbasin, Harts Range region, central Australia (PhD thesis). Australian National University, Canberra, p. 422.

Maidment, D.W., Hand, M., Williams, I.S., 2005. Tectonic cycles in the Strangways Metamorphic Complex, Arunta Inlier, central Australia: geochronological evidence for exhumation and basin formation between two high-grade metamorphic events. Australian Journal of Earth Sciences 52, 205-215.

Möller, A., Appel, P., Mezger, K., Schenk, V., 1995. Evidence for a 2 Ga subduction zone - Eclogites in the Usagaran Belt of Tanzania. Geology 23, 1067-1070.

Möller, A., Hensen, B., Armstrong, R., Mezger, K., Ballèvre, M., 2003. U–Pb zircon and monazite age constraints on granulite-facies metamorphism and deformation in the Strangways Metamorphic Complex (central Australia). Contributions to Mineralogy and Petrology 145, 406-423.

Morrissey, L., Payne, J.L., Kelsey, D.E., Hand, M., 2011. Grenvillian-aged reworking in the North Australian Craton, central Australia: constraints from geochronology and modelled phase equilibria. Precambrian Research 191, 141-165.

Morrissey, L.J., Hand, M., Raimondo, T., Kelsey, D.E., 2014. Long-lived high-T, low-P granulite facies metamorphism in the Arunta Region, central Australia. Journal of Metamorphic Geology 32, 25-47.

Norman, A.R., Clarke, G.L., 1990. A barometric response to late compression in the Strangways Metamorphic Complex, Arunta Block, central Australia. Journal of Structural

Geology 12, 667-684.

Pattison, D.R.M., Bégin, N.J., 1994. Zoning patterns in orthopyroxene and garnet in granulites: implications for geothermometry. Journal of Metamorphic Geology 12, 387-410.

Payne, J.L., Hand, M., Barovich, K.M., Reid, A., Evans, D.A.D., 2009. Correlations and reconstruction models for the 2500-1500 Ma evolution of the Mawson Continent, in: Reddy, S.M., Mazumder, R., Evans, D.A.D., and Collins, A.S. (Ed.), Palaeoproterozoic Supercontinents and Global Evolution, pp. 319-355.

Payne, J.L., Hand, M., Barovich, K.M., Wade, B.P., 2008. Temporal constraints on the timing of high-grade metamorphism in the northern Gawler Craton; implications for assembly of the Australian Proterozoic. Australian Journal of Earth Sciences 55, 623-640.

Pitra, P., Kouamelan, A.N., BallÈVre, M., Peucat, J.J., 2010. Palaeoproterozoic high-pressure granulite overprint of the Archean continental crust: evidence for homogeneous crustal thickening (Man Rise, Ivory Coast). Journal of Metamorphic Geology 28, 41-58.

Powell, R., Holland, T.J.B., 1988. An internally consistent thermodynamic dataset with uncertainties and correlations: 3. Applications to geobarometry, worked examples and a computer program. J. Metamorphic Geol. 6, 173-204.

Powell, R., Holland, T.J.B., 2008. On thermobarometry. Journal of Metamorphic Geology 26, 155-179.

Reno, B.L., Piccoli, P.M., Brown, M., Trouw, R.A.J., 2012. In situ monazite (U–Th)–Pb ages from the Southern Brasília Belt, Brazil: constraints on the high-temperature retrograde evolution of HP granulites. Journal of Metamorphic Geology 30, 81-112.

Rubatto, D., Chakraborty, S., Dasgupta, S., 2013. Timescales of crustal melting in the Higher Himalayan Crystallines (Sikkim, Eastern Himalaya) inferred from trace element-constrained monazite and zircon chronology. Contributions to Mineralogy and Petrology 165, 349-372.

Rubatto, D., Hermann, J., Buick, I.S., 2006. Temperature and bulk composition control on the growth of monazite and zircon during low-pressure anatexis (Mount Stafford, central Australia). Journal of Petrology 47, 1973-1996.

Scrimgeour, I., 2003. Developing a revised framework for the Arunta Region, Annual Geoscience Exploration Seminar (AGES) Record of Abstracts, Darwin.

Scrimgeour, I., 2006. The Arunta Region: Links between Tectonics and mineralisation, Annual Geoscience Exploration Seminar (AGES). Northern Territory Geological Survey, Alice Springs, pp. 7-8.

Scrimgeour, I., 2013. Ch. 12 Aileron Province, Geology and mineral resources of the Northern Territory. Northern Territory Geological Survey, Special Publications 5, pp. 1-75.

Scrimgeour, I., Smith, J.B., Raith, J.G., 2001. Palaeoproterozoic high-T, low-P metamorphism and dehydration melting in metapelites from the Mopunga Range, Arunta Inlier, central Australia. Journal of Metamorphic Geology 19, 739-757.

Scrimgeour, I.E., 2004. A revised province definition and Palaeoproterozoic framework for the Arunta Region, central Australia., Geological Society of Australia (Abstracts), p. 173.

Scrimgeour, I.R., Kinny, P.D., Close, D.F., Edgoose, C.J., 2005. High-T granulites and polymetamorphism in the southern Arunta Region, central Australia: Evidence for a 1.64 Ga accretional event. Precambrian Research 142, 1-27.

Shaw, R.D., Warren, R.G., 1995. Hermannsburg (1:250 000 scale map). Australia Geological Survey Association, Canberra.

Smits, R.G., Collins, W.J., Hand, M., 2013. The North Australian Craton: A Palaeoproterozoic accretionary orogen, Mineralogical Magazine, p. 2230.

Spear, F.S., 1993. Metamorphic Phase Equilibria and Pressure-Temperature-Time Paths. Mineralogical Society of America, Washington D.C.

Staffier, K., 2007. Field and microstructural investigation of plagioclase deformation behaviour in granulite facies rocks, Mt. Hay, central Australia. University of Wisconsin-Madison, Madison, U.S., p. 87.

Stepanov, A.S., Hermann, J., Rubatto, D., Rapp, R.P., 2012. Experimental study of monazite/melt partitioning with implications for the REE, Th and U geochemistry of crustal rocks. Chemical Geology 300, 200-220.

Stuwe, K., 1997. Effective bulk composition changes due to cooling: a model predicting complexities in retrograde reaction textures. Contributions to Mineralogy and Petrology 129, 43-52.

Stuwe, K., 2007. Geodynamics of the Lithosphere. Springer, Berlin.

Vry, J., Compston, W., Cartwright, I., 1996. SHRIMP II dating of zircons and monazites: Reassessing the timing of high-grade metamorphism and fluid flow in the Reynolds Range, northern Arunta Block, Australia. Journal of Metamorphic Geology 14, 335-350.

Vry, J.K., Baker, J.A., 2006. LA-MC-ICPMS Pb–Pb dating of rutile from slowly cooled granulites: Confirmation of the high closure temperature for Pb diffusion in rutile. Geochimica Et Cosmochimica Acta 70, 1807-1820.

Wade, B.P., Barovich, K.M., Hand, M., Scrimgeour, I.R., Close, D.F., 2006. Evidence for Early Mesoproterozoic Arc Magmatism in the Musgrave Block, Central Australia: Implications for Proterozoic Crustal Growth and Tectonic Reconstructions of Australia. Journal of Geology 114, 43-63.

Wade, B.P., Hand, M., Maidment, D.W., Close, D.F., Scrimgeour, I.R., 2008. Origin of metasedimentary and igneous rocks from the Entia Dome, eastern Arunta region, central Australia: a U - Pb LA-ICPMS, SHRIMP and Sm - Nd isotope study. Australian Journal of Earth Sciences 55, 703-719.

Warren, R.G., Shaw, R.D., 1995. Hermannsburg, Northern Territory - 1: 250 000 Geological series, Explanatory Notes. Northern Territory Geological Survey.

Waters-Tormey, C., Goodwin, L.B., Tikoff, B., Staffier, K., Kelso, P., 2009. A granulite-facies normal shear zone exposed in the Arunta inlier of central Australia: Implications for deep-crustal deformation during oblique divergence. Geological Society of America Special Papers 456, 267-286.

Waters-Tormey, C., Tikoff, B., 2007. Characteristics of a kilometer-scale high strain zone in the lower continental crust: Mt. Hay block, central Australia. Journal of Structural Geology 29, 562-582.

Watt, G., 1992. Geology of Mount Hay - Mount Chapple massif (Arunta Block, Hermannburg 1:250 000 Sheet area, central Australia) Field report, 1990., A contribution to the Kimberley-Arunta NGMA Project. University of Edinburgh.

Whelan, J., Webb, G., Close, D., Kositcin, N., Bodorkos, S., Maas, R., 2012. New copper-gold discoveries in the eastern Arunta Region: Implications for Cu-Au mineralisation in the Arunta, Annual Geoscience Exploration Seminar (AGES). Record of abstracts. Northern Territory Geological Survey, Alice Springs, pp. 38-42.

White, Powell, Holland, Worley, 2000. The effect of TiO_2 and Fe_2O_3 on metapelitic assemblages at greenschist and amphibolite facies conditions: mineral equilibria calculations in the system K_2O–FeO–MgO–Al_2O_3–SiO_2–H_2O–TiO_2–Fe_2O_3. Journal of Metamorphic Geology 18, 497-511.

White, R.W., Powell, R., Clarke, G.L., 2002. The interpretation of reaction textures in Fe-rich metapelitic granulites of the Musgrave Block, central Australia: constraints from mineral equilibria calculations in the system K_2O-FeO-MgO-Al_2O_3-SiO_2-H_2O-TiO_2-Fe_2O_3. Journal of Metamorphic Geology 20, 41-55.

White, R.W., Powell, R., Holland, T.J.B., 2007. Progress relating to calculation of partial melting equilibria for metapelites. Journal of Metamorphic Geology 25, 511-527.

Yakymchuk, C., Brown, M., 2014. Behaviour of zircon and monazite during crustal melting. Journal of the Geological Society,

London 171, 465-479.
Zhao, J.X., Bennett, V.C., 1995. SHRIMP U-Pb zircon geochronology of granites in the Arunta-Inlier, central Australia - Implications for Proterozoic crustal evolution. Precambrian Research 71, 17-43.
Zhao, J.X., McCulloch, M.T., 1995. Geochemical and Nd isotopic systematics of granites from the Arunta-Inlier, central Australia - implications for Proterozoic crustal evolution. Precambrian Research 71, 265-299.

Supporting Information

Appendix 1: Mineral Chemistry

Garnet

In sample Hay-05a, X_{Alm} (= Fe/(Fe+Mg+Ca+Mn) and X_{Py} (= Mg/(Fe+Mg+Ca+Mn) values range from ~0.59–0.62 and 0.32–0.35 respectively. Garnet grains generally exhibit a small increase in X_{Alm} values and decrease in X_{Py} values from core to rim. X_{Grs} (= Ca/(Fe+Mg+Ca+Mn) values increase slightly from core (~0.04) to rim (~0.05). Garnet grains in sample Hay-09a have relatively flat X_{Alm} and X_{Py} profiles and range from ~0.61 to 0.63 and ~0.31 to 0.34 respectively. Some garnet grains show a small increase in X_{Alm} values and decrease in X_{Py} values from core to rim. X_{Grs} values increase from core (~0.04) to rim (~0.05). For samples Hay-05a and Hay-09a, X_{Spss} (= Mn/(Fe+Mg+Ca+Mn) content is ~0.01 and does not display any zonation.

In sample Hay-17 X_{Alm} and X_{Py} ranges between 0.63–0.68 and 0.26–0.30 respectively. In coarse grained garnet, X_{Alm} increases slightly from core to rim, whereas X_{Py} decreases from core to rim. X_{Grs} values in fine grained garnet are ~0.04, and decrease from core to rim in coarse grained garnet (~0.08–0.04). X_{Spss} content in Hay-17 is ~0.01–0.02 and does not display zonation. In sample RBN-28, X_{Alm} increases from core to rim (~0.66–0.73) and X_{Py} decreases from core to rim (~0.29–0.22). X_{Grs} and X_{Spss} do not show zonation (~0.03–0.04 and ~0.01 respectively).

Feldspar

Alkali feldspar in Mount Hay and Capricorn Ridge samples are orthoclase rich (X_{Or} values of 0.85–0.88 for Hay-05a, 0.88–0.90 for Hay-09a, 0.88–0.90 for Hay-12 and 0.80–0.86 for Hay-17, where X_{Or} = K/(K+Na+Ca). X_{An} (=Ca/(Ca+Na+K)) content is 0 for the four samples. Sample RBN-28 contains alkali feldspar with X_{Or} values of 0.83–0.88 and X_{An} values of 0.

Plagioclase has X_{An} values of 0.39–0.40 for samples Hay-05a and Hay-12, 0.38–0.39 for sample Hay-09a, ~0.27 for sample Hay-17 and ~0.29–0.33 for RBN-28. X_{Or} in plagioclase is ~0.01 for all five samples.

Ilmenite

The MnO wt % in ilmenite grains is 0.11–0.30 in Hay-05a, ~0.20 in Hay09a, 0.05–0.17 in Hay-12, 0.12–0.22 in Hay-17 and ~0.04–0.10 in RBN-28. Recalculated wt % Fe_2O_3 is 0.00 in Hay-05a, Hay-09a, Hay-17 and RBN-28, and ranges from 0 to 0.64 in Hay-12 (method of Droop, 1987).

Biotite

X_{Mg} (X_{Mg} = Mg/(Mg+Fe^{2+})) ranges from 0.59 to 0.67 in Hay-12, ~0.66–0.68 in Hay-05a, sample Hay-09a and Hay-17, and ~0.62–0.65 in RBN-28. TiO_2 wt % content is 4.05−5.25 in Hay-12, ~4.82 in Hay-05a, ~4.22 in Hay-09a, 3.58–4.11 in Hay-17 and ~3.99–4.45 in RBN-28.

References

Droop, G.T.R., 1987. A General equation for estimating Fe^{3+} concentrations in ferromagnesian silicates and oxides from Microprobe analyses, using stoichiometric criteria. Mineralogical Magazine 51, 431-435.

Sample Hay-12 U–Pb monazite data

Analysis	Pb^{207}/Pb^{206}		Pb^{207}/U^{235}		Pb^{206}/U^{238}		Rho	Conc.	Pb^{207}/Pb^{206}		Pb^{206}/U^{238}		Pb^{207}/U^{235}		Pb^{204}	Pb^{206}	Pb^{207}	U^{238}	
14	0.10258	0.0013	3.94196	0.06986	0.27885	0.00467	0.944996	95	1671.3	23.22	1585.6	23.6	1622.3	14.4	8	13314	1394	78408	Mount
15	0.10341	0.00172	3.514	0.07094	0.24659	0.00423	0.849719	84	1686.2	30.4	1420.8	21.9	1530.4	16	0	9339	983	61219	Mount
16	0.10498	0.00133	4.30603	0.07569	0.29765	0.0049	0.936545	98	1713.9	23.17	1679.6	24.4	1694.5	14.5	17	36700	3920	199400	Mount
17	0.10473	0.00128	4.35432	0.07586	0.30171	0.00499	0.949332	99	1709.5	22.39	1699.8	24.7	1703.7	14.4	0	32585	3470	175982	Mount
18	0.104	0.00134	4.21988	0.07466	0.29444	0.00487	0.934855	98	1696.7	23.47	1663.7	24.2	1677.9	14.5	0	21764	2300	119718	Mount
19	0.10531	0.00142	4.33842	0.07872	0.29897	0.00497	0.916168	98	1719.6	24.56	1686.2	24.7	1700.7	15	6	28643	3060	155459	Mount
20	0.10531	0.00129	4.59162	0.07972	0.31639	0.00521	0.948448	103	1719.8	22.38	1772.1	25.5	1747.7	14.5	7	35505	3805	182117	Mount
14B	0.10215	0.0014	3.62263	0.06647	0.25734	0.00433	0.91702	89	1663.6	25.1	1476.2	22.2	1554.5	14.6	7	12621	1310	80176	Mount
15B	0.10375	0.00134	3.7917	0.06738	0.26519	0.00439	0.931559	90	1692.3	23.67	1516.3	22.4	1591	14.3	2	25961	2739	158763	Mount
19B	0.10543	0.00131	4.34248	0.0757	0.29889	0.00492	0.944269	98	1721.9	22.57	1685.8	24.4	1701.5	14.4	12	50331	5392	273024	Mount
20B	0.1062	0.00141	4.60403	0.08272	0.31459	0.00522	0.923535	102	1735.2	24.15	1763.2	25.6	1750	15	2	16189	1749	83419	Mount
M01	0.10615	0.00128	4.60654	0.07999	0.31492	0.00527	0.963717	102	1734.4	21.94	1764.8	25.8	1750.5	14.5	7	30047	3265	156991	Mount
M02	0.10245	0.00126	4.33286	0.07555	0.3069	0.00512	0.956783	103	1669	22.49	1725.5	25.3	1699.6	14.4	4	23383	2449	124840	Mount
M02B	0.10653	0.00118	4.5085	0.07538	0.30711	0.00505	0.983498	99	1740.8	20.22	1726.5	24.9	1732.5	13.9	0	58739	6385	312052	Mount
M03	0.10283	0.00121	3.78455	0.06456	0.26707	0.00442	0.97017	91	1675.8	21.5	1525.9	22.5	1589.5	13.7	8	24817	2610	151710	Mount
M04	0.10609	0.00117	4.58127	0.0763	0.31337	0.00515	0.986759	101	1733.2	20.07	1757.3	25.3	1745.9	13.9	4	82745	8969	430847	Mount
M05	0.10741	0.00122	4.6244	0.07817	0.31242	0.00517	0.978965	100	1756	20.62	1752.6	25.4	1753.7	14.1	4	38267	4201	200434	Mount
M05B	0.1048	0.00119	4.6322	0.07811	0.32074	0.00529	0.9781	105	1710.9	20.69	1793.3	25.8	1755.1	14.1	2	59218	6348	301853	Mount
M05C	0.10731	0.00123	4.62338	0.07823	0.31261	0.00516	0.975513	100	1754.3	20.76	1753.6	25.3	1753.5	14.1	0	64149	7048	335169	Mount
M06	0.10576	0.00121	4.54561	0.0769	0.31188	0.00515	0.97608	101	1727.6	20.81	1750	25.3	1739.4	14.1	2	54396	5892	285419	Mount
M06B	0.10379	0.0013	4.25165	0.07484	0.29726	0.00496	0.947914	99	1692.9	22.97	1677.7	24.6	1684.1	14.5	10	19177	2037	105562	Mount
M07	0.10775	0.00131	4.59855	0.07979	0.30972	0.00517	0.962041	99	1761.6	22.03	1739.3	25.4	1749	14.5	5	16697	1842	88302	Mount
M07B	0.10732	0.00131	4.59143	0.07974	0.31045	0.00517	0.958894	99	1754.4	22.14	1742.9	25.4	1747.7	14.5	6	17237	1895	90815	Mount
M08	0.10752	0.00131	4.65499	0.08092	0.31416	0.00524	0.959496	100	1757.9	22.08	1761.1	25.7	1759.2	14.5	5	18048	1986	94123	Mount
M09	0.10588	0.00124	4.54063	0.07749	0.3112	0.00516	0.971584	101	1729.7	21.26	1746.6	25.4	1738.4	14.2	12	30859	3341	162295	Mount
M10†	0.1035	0.00132	4.30718	0.07585	0.30199	0.005	0.940188	101	1687.9	23.36	1701.2	24.8	1694.7	14.5	0	31150	3297	167332	Mount
M11†	0.10896	0.00158	4.75311	0.08906	0.31655	0.00532	0.896942	99	1782.1	26.18	1772.9	26.1	1776.7	15.7	3	20417	2268	104607	Mount
M11B	0.10646	0.00124	4.59436	0.07875	0.31316	0.00519	0.966887	101	1739.7	21.25	1756.3	25.5	1748.2	14.3	1	47430	5149	248318	Mount
M12	0.10039	0.00112	4.00374	0.06748	0.28941	0.00478	0.979953	100	1631.3	20.6	1638.6	23.9	1635	13.7	0	217125	22225	1230785	Mount
M13	0.10752	0.0014	4.53733	0.0813	0.30623	0.00512	0.933108	98	1757.8	23.54	1722.1	25.3	1737.8	14.9	4	17093	1870	91266	Mount
M13B	0.10405	0.00119	4.52793	0.07712	0.31579	0.00522	0.970521	104	1697.5	20.88	1769.1	25.6	1736.1	14.2	6	172061	18229	894656	Mount
M01	0.08946	0.00104	2.32111	0.03891	0.18828	0.00307	0.9726771	79	1413.9	22.12	1112.1	16.65	1218.8	11.9	16	54076	4990	462892	in situ matrix
M12	0.10317	0.00123	3.56102	0.0604	0.25048	0.0041	0.9650466	86	1681.9	21.88	1440.9	21.13	1540.9	13.45	13	44054	4675	283671	in situ matrix
M13	0.10571	0.00119	4.42657	0.07338	0.30388	0.00495	0.9826361	99	1726.7	20.59	1710.5	24.5	1717.3	13.73	3	82885	9035	440517	in situ matrix
M16	0.1018	0.00129	3.55015	0.06197	0.25308	0.00418	0.9462016	88	1657.1	23.33	1454.3	21.48	1538.5	13.83	15	26486	2773	169095	in situ matrix
M17A	0.10741	0.00132	4.28087	0.0739	0.28921	0.00477	0.9554164	93	1755.9	22.32	1637.6	23.83	1689.7	14.21	0	32505	3587	181867	in situ matrix
M17B	0.09538	0.00119	3.4797	0.06017	0.26475	0.00432	0.943647	99	1535.5	23.36	1514.1	22.04	1522.6	13.64	3	67700	6633	410636	in situ matrix
M18†	0.0876	0.00151	0.18314	0.00317	2.21087	0.04605	0.8310165	79	1373.7	32.85	1084.1	17.25	1184.5	14.56	8	16898	1515	150877	in situ matrix
m21	0.09917	0.00112	3.81505	0.06177	0.27915	0.00448	0.9912039	99	1608.5	20.84	1587.1	22.56	1595.9	13.03	0	63268	6537	359511	in situ matrix
M25	0.10804	0.00136	4.53213	0.07909	0.3044	0.00503	0.9469	97	1766.6	22.79	1713.1	24.88	1736.9	14.52	3	30444	3376	162200	in situ gt
M26	0.09606	0.00113	3.46334	0.05881	0.26162	0.0043	0.9679245	97	1548.9	21.86	1498.1	21.97	1518.9	13.38	1	72609	7167	451165	in situ matrix
M28	0.10488	0.00127	4.19651	0.07212	0.29036	0.00478	0.9579077	96	1712.2	22.07	1643.3	23.9	1673.3	14.09	7	51450	5545	287715	in situ matrix
M30	0.09736	0.00113	3.33451	0.05692	0.24852	0.00412	0.9711873	91	1574.2	21.63	1430.8	21.27	1489.2	13.33	11	71646	7148	472801	in situ matrix
M30B	0.10018	0.00118	3.85558	0.06573	0.27928	0.00462	0.9703496	98	1627.4	21.68	1587.7	23.29	1604.4	13.75	0	52522	5412	307431	in situ matrix

m33	0.09789	0.00112	3.42323	0.05584	0.25375	0.00408	0.9857001	92	1584.3	21.25	1457.8	20.99	1509.7	12.82	0	53980	5516	338025	in situ matrix
m34	0.10522	0.00124	4.42592	0.07268	0.30521	0.00491	0.979651	100	1718.2	21.48	1717.1	24.23	1717.2	13.6	15	54684	6030	283532	in situ matrix
m36	0.09466	0.00107	3.5037	0.05701	0.26856	0.00432	0.9885947	101	1521.4	21.14	1533.5	21.96	1528	12.85	10	72655	7167	430716	in situ matrix
m38	0.10392	0.00116	4.26598	0.06903	0.29786	0.00479	0.9938121	99	1695.3	20.47	1680.7	23.8	1686.8	13.31	0	83695	9087	447416	in situ matrix
m39†	0.10185	0.00131	4.00363	0.06877	0.28521	0.00465	0.9491681	98	1658.1	23.7	1617.6	23.31	1634.9	13.96	10	83744	9031	467806	in situ matrix
m41	0.09733	0.00117	3.14479	0.05244	0.23444	0.00379	0.9694747	86	1573.6	22.38	1357.7	19.8	1443.7	12.85	14	50428	5145	342246	in situ matrix
m42†	0.15401	0.00428	0.28969	0.00601	6.1482	0.1728	0.738151	69	2391	46.51	1640	30.06	1997.1	24.55	23	7408	1200	40916	in situ matrix
M44	0.10729	0.00149	4.35976	0.07984	0.29485	0.00498	0.9222959	95	1753.9	25.08	1665.7	24.77	1704.7	15.13	10	15033	1662	83244	in situ gt
M44B	0.10466	0.00145	4.18835	0.07658	0.29037	0.00489	0.9210532	96	1708.4	25.3	1643.4	24.42	1671.7	14.99	1	16970	1835	95272	in situ gt
M47	0.10602	0.00127	4.467	0.07637	0.30573	0.00505	0.9661543	99	1732.1	21.79	1719.7	24.95	1724.9	14.19	0	66457	7288	354443	in situ matrix
M47B	0.09756	0.00117	3.66259	0.06307	0.27243	0.00452	0.9634939	98	1577.9	22.27	1553.1	22.91	1563.3	13.74	0	60297	6062	362616	in situ matrix
M48†	0.09244	0.00114	3.21596	0.05616	0.25246	0.0042	0.9526651	98	1476.2	23.33	1451.1	21.61	1461	13.52	18	57853	5499	375524	in situ matrix
m50	0.10341	0.00121	4.28083	0.07092	0.30039	0.00488	0.9806039	100	1686.1	21.45	1693.2	24.17	1689.7	13.64	0	52644	5694	280448	in situ matrix
m50b	0.10356	0.00119	4.2092	0.06945	0.29491	0.00478	0.9823488	99	1688.9	21.13	1666	23.81	1675.8	13.54	0	74138	8020	402830	in situ matrix
m50c	0.1002	0.00122	3.64336	0.06162	0.26384	0.00431	0.9658663	93	1627.8	22.49	1509.4	21.98	1559.1	13.47	2	37645	3942	228945	in situ matrix
m50d	0.10524	0.00123	4.35852	0.07261	0.3005	0.00489	0.976803	99	1718.5	21.34	1693.8	24.26	1704.5	13.76	7	72900	8004	390002	in situ matrix

† indicates analysis was discarded due to variable isotopic signal

Isotope measurements are in cps

Sample Hay-17 U–Pb monazite data

Analysis	Pb^{207}/Pb^{206}		Pb^{207}/U^{235}		Pb^{206}/U^{238}		Rho	Conc.	Pb^{207}/Pb^{206}		Pb^{206}/U^{238}		Pb^{207}/U^{235}		Pb^{204}	Pb^{206}	Pb^{207}	U^{238}
M01-2	0.10594	0.00122	4.53315	0.06407	0.31049	0.00418	0.95252	101	1730.7	20.91	1743.1	20.6	1737.1	11.76	7	49192	5321	209796
M02-2	0.10681	0.00124	4.51924	0.0645	0.30702	0.00415	0.947081	99	1745.7	20.97	1726	20.5	1734.5	11.87	0	47075	5116	203854
M03-2	0.10777	0.0012	4.58209	0.06413	0.3085	0.00416	0.963475	98	1762.1	20.17	1733.3	20.5	1746	11.66	0	76832	8444	332228
M04-2	0.10532	0.00124	4.32501	0.0623	0.29797	0.00404	0.941256	98	1720	21.5	1681.3	20.1	1698.1	11.88	1	31388	3371	140321
M05-2	0.10703	0.0012	4.5616	0.06392	0.30925	0.00416	0.959984	99	1749.5	20.25	1737	20.5	1742.3	11.67	11	161823	17638	696689
M06-2	0.10615	0.00119	4.63367	0.06509	0.31675	0.00427	0.95967	102	1734.4	20.38	1773.8	20.9	1755.4	11.73	0	163313	17653	687763
M07-2	0.1061	0.00122	4.39607	0.06258	0.30066	0.00405	0.946255	98	1733.4	20.97	1694.6	20.1	1711.6	11.78	0	145569	15738	643857
M08-2	0.10662	0.00135	4.31193	0.06477	0.29344	0.00398	0.902946	95	1742.5	23.01	1658.7	19.9	1695.6	12.38	1	59334	6448	267717
M09-2	0.10581	0.00124	4.3703	0.06283	0.29971	0.00404	0.937615	98	1728.4	21.4	1689.9	20	1706.7	11.88	11	126160	13629	558811
M10-2	0.10578	0.00122	4.40955	0.06304	0.3025	0.00408	0.943437	99	1727.9	21.1	1703.7	20.2	1714.1	11.83	0	138355	14936	609377
M11-2	0.10899	0.00121	4.79391	0.06665	0.31918	0.00429	0.966744	100	1782.6	20.11	1785.7	21	1783.8	11.68	16	89625	10000	373667
M12-2	0.09897	0.00123	3.77987	0.05597	0.27714	0.00376	0.916242	98	1604.8	22.95	1576.9	19	1588.5	11.89	9	33024	3337	157806
M13-2	0.09542	0.00121	3.57217	0.05327	0.27169	0.00367	0.90582	101	1536.3	23.65	1549.4	18.6	1543.4	11.83	0	40409	3944	195433
M14-2	0.10499	0.00132	4.28796	0.06389	0.29636	0.00402	0.910383	98	1714.1	22.93	1673.2	20	1691.1	12.27	2	37238	3995	165974
M15-2	0.10571	0.00121	4.39103	0.06211	0.30144	0.00406	0.952204	98	1726.7	20.81	1698.4	20.1	1710.7	11.7	0	147087	15900	648830
M16-2	0.10506	0.00121	4.44313	0.0628	0.30692	0.0041	0.945122	101	1715.4	21.07	1725.5	20.2	1720.4	11.72	3	256490	27580	1102124
M17-2	0.10728	0.00129	4.49803	0.06511	0.30431	0.00408	0.926229	98	1753.7	21.76	1712.6	20.2	1730.6	12.02	0	118072	12957	511432
M18-2	0.1056	0.00121	4.58062	0.06521	0.31477	0.00426	0.950662	102	1724.8	20.91	1764.1	20.9	1745.7	11.87	6	125027	13510	530688
M19-2	0.10482	0.00135	4.52127	0.0683	0.31308	0.00422	0.892271	103	1711.1	23.53	1755.8	20.7	1734.9	12.56	8	146474	15728	615173
M20-2	0.10613	0.00128	4.80641	0.07028	0.32867	0.00445	0.925953	106	1733.9	21.97	1831.9	21.6	1786	12.29	0	93409	10129	377863
M21-2	0.10802	0.00121	4.78829	0.06772	0.3217	0.00438	0.96269	102	1766.2	20.3	1798	21.4	1782.8	11.88	12	138915	15292	581426
M22-2	0.10584	0.00126	4.53072	0.06599	0.31067	0.00422	0.932615	101	1728.9	21.63	1744	20.8	1736.6	12.12	0	134537	14485	578603
M23-2	0.108	0.0012	4.66301	0.06615	0.31333	0.00429	0.965143	100	1765.9	20.17	1757.1	21.1	1760.6	11.86	3	81260	8926	351689
M24-2	0.1079	0.00121	4.41726	0.06291	0.29709	0.00407	0.961922	95	1764.3	20.31	1676.8	20.2	1715.6	11.79	8	95532	10498	435119
M25-2	0.10672	0.00118	4.48135	0.06351	0.30474	0.00418	0.967862	98	1744.1	20.08	1714.8	20.6	1727.5	11.76	0	132271	14364	589768
M26-2	0.10758	0.00125	4.78603	0.06955	0.32285	0.00444	0.946369	103	1758.9	20.97	1803.6	21.7	1782.5	12.2	10	109910	12068	462192
M27-2	0.10688	0.00123	4.55857	0.06596	0.3095	0.00425	0.949022	100	1746.9	20.8	1738.2	20.9	1741.7	12.05	0	139856	15239	613213
M28-2	0.10629	0.00125	4.56572	0.06729	0.31174	0.00431	0.938088	101	1736.7	21.5	1749.3	21.2	1743	12.28	0	78737	8531	343867
M29-2	0.10789	0.00128	4.61345	0.06814	0.3103	0.00428	0.933868	99	1764.1	21.49	1742.2	21.1	1751.7	12.33	0	101438	11124	443646
M30-2	0.10496	0.0012	4.57963	0.06638	0.31662	0.00437	0.952218	103	1713.6	20.88	1773.2	21.4	1745.6	12.08	13	133441	14310	575023
M31-2	0.10154	0.00122	3.95975	0.05863	0.28296	0.0039	0.9308666	97	1652.5	22.06	1606.2	19.58	1626	12	19	162530	16820	778387
M32-2	0.10568	0.00117	4.56234	0.06488	0.31328	0.00432	0.9696788	102	1726.2	20.13	1756.8	21.19	1742.4	11.84	4	141803	15274	618315
M33-2	0.1057	0.00123	4.51425	0.06608	0.30995	0.00431	0.949951	101	1726.6	21.13	1740.5	21.2	1733.6	12.17	27	133617	14446	591385
M34-2	0.10616	0.00154	4.61736	0.0769	0.3156	0.00447	0.8504287	102	1734.5	26.39	1768.2	21.91	1752.4	13.9	0	80021	8748	344557
M35-2	0.10664	0.00125	4.55461	0.06664	0.30995	0.00428	0.9437747	100	1742.8	21.32	1740.4	21.04	1741	12.18	3	80154	8711	351441
M36-2	0.10136	0.00128	3.60239	0.05563	0.25792	0.00363	0.9113879	90	1649.2	23.27	1479.2	18.58	1550.1	12.27	0	57241	5903	305022
M37-2	0.10508	0.00136	4.54055	0.0704	0.31363	0.0044	0.9048381	102	1715.7	23.54	1758.5	21.61	1738.4	12.9	12	24438	2619	106240
M38-2	0.10726	0.00137	4.70164	0.07216	0.31815	0.00443	0.9072451	102	1753.3	23.2	1780.7	21.66	1767.5	12.85	6	51732	5694	220460
M39-2	0.10718	0.0013	4.58695	0.06836	0.31057	0.0043	0.9290325	100	1752	21.94	1743.5	21.16	1746.9	12.42	0	48891	5346	213942
M40-2	0.10721	0.00126	4.65973	0.06828	0.31541	0.00435	0.9411981	101	1752.6	21.21	1767.3	21.32	1760	12.25	4	124753	13627	538387
M41-2	0.10646	0.00128	4.56587	0.06773	0.31122	0.00429	0.9292493	100	1739.8	21.94	1746.7	21.07	1743.1	12.36	14	109375	11877	476122

† indicates analysis was discarded due to variable isotopic signal

Sample Hay-05a U–Pb monazite data

Analysis	Pb^{207}/Pb^{206}		Pb^{207}/U^{235}		Pb^{206}/U^{238}		Rho	Conc.	Pb^{207}/Pb^{206}		Pb^{206}/U^{238}		Pb^{207}/U^{235}		Pb^{204}	Pb^{206}	Pb^{207}	U^{238}	
M03†	0.10074	0.00134	3.73255	0.06464	0.26877	0.00437	0.93887	94	1637.7	24.41	1534.6	22.22	1578.4	13.87	3	54728	5824	322420	Grt
M07B	0.08883	0.00108	3.03007	0.05089	0.24741	0.00398	0.95782	102	1400.4	23.14	1425.1	20.56	1415.2	12.82	19	69929	6440	447114	Matrix
M07	0.09427	0.00115	3.20806	0.0537	0.24683	0.00398	0.96328	94	1513.5	22.91	1422.1	20.55	1459.1	12.96	7	36183	3557	231762	Matrix
M08	0.09821	0.00118	3.7052	0.06165	0.27361	0.0044	0.96649	98	1590.5	22.31	1559.1	22.27	1572.5	13.3	15	64330	6585	372035	Matrix
M10	0.09865	0.00118	3.8465	0.06378	0.28281	0.00454	0.96815	100	1598.8	22.2	1605.5	22.82	1602.5	13.36	12	66003	6799	368938	Matrix
M13	0.09915	0.00135	3.95055	0.06958	0.28901	0.00471	0.92530	102	1608.1	25.13	1636.6	23.58	1624.1	14.27	10	28263	2929	154610	Matrix
M26	0.10207	0.00116	4.08532	0.06666	0.29029	0.00467	0.98593	99	1662.1	20.92	1643	23.32	1651.4	13.31	17	85952	9132	470796	Matrix
M06	0.10284	0.00123	4.21349	0.06965	0.29717	0.00477	0.97103	100	1676	21.85	1677.3	23.72	1676.7	13.57	0	81920	8807	435931	Matrix
M28	0.10325	0.00133	4.11536	0.07112	0.28909	0.00472	0.94477	97	1683.3	23.55	1637	23.61	1657.4	14.12	6	39191	4208	216122	Matrix
M14	0.1042	0.00127	4.25407	0.07099	0.29612	0.00477	0.96529	98	1700.2	22.21	1672	23.7	1684.5	13.72	26	57271	6229	305856	Matrix
M20†	0.10488	0.00131	4.43862	0.07485	0.307	0.00494	0.95421	101	1712.2	22.86	1725.9	24.38	1719.6	13.98	35	126378	13973	651027	Matrix
M29B	0.10518	0.00137	4.51579	0.07829	0.31139	0.0051	0.94470	102	1717.4	23.72	1747.6	25.06	1733.9	14.41	14	39279	4323	201335	Matrix
M21	0.10621	0.00122	4.54626	0.07473	0.31044	0.00499	0.97787	100	1735.4	21	1742.9	24.55	1739.5	13.68	26	121681	13389	622577	Matrix
M29	0.10641	0.00127	4.4341	0.0742	0.30221	0.0049	0.96892	98	1738.8	21.68	1702.3	24.25	1718.7	13.86	30	41029	4521	216586	Matrix
M27	0.10664	0.00113	4.59845	0.07343	0.31275	0.00502	0.99485	101	1742.7	19.35	1754.2	24.64	1749	13.32	12	325787	36031	1663030	Grt
M16	0.1067	0.00121	4.52578	0.07324	0.30766	0.00491	0.98618	99	1743.8	20.58	1729.2	24.23	1735.7	13.46	13	91031	10116	467716	Grt
M32B	0.10723	0.00124	4.67823	0.07724	0.3164	0.0051	0.97628	101	1752.9	20.95	1772.1	24.99	1763.4	13.81	29	129946	14477	655091	Matrix
M32A†	0.10755	0.00129	4.59972	0.07695	0.31019	0.00503	0.96931	99	1758.3	21.76	1741.6	24.74	1749.2	13.95	23	106000	11943	545593	Matrix
M31†	0.11062	0.00157	4.80159	0.08786	0.31482	0.00524	0.90963	98	1809.6	25.56	1764.4	25.67	1785.2	15.38	20	17108	1947	86985	Grt
M01	0.10651	0.00113	4.84683	0.07911	0.33024	0.00538	0.99811	106	1740.5	19.34	1839.5	26.09	1793.1	13.74	11	303925	33159	1494145	Mount
M02	0.10554	0.00121	4.57072	0.07615	0.31427	0.00509	0.97214	102	1723.8	20.99	1761.7	24.97	1743.9	13.88	0	68596	7411	349712	Mount
M03	0.10554	0.00124	4.31791	0.07277	0.29688	0.00484	0.96735	97	1723.8	21.35	1675.8	24.04	1696.8	13.89	0	47706	5145	258481	Mount
M04	0.10854	0.00119	4.66386	0.07705	0.3118	0.00509	0.98813	99	1775	19.88	1749.6	24.99	1760.8	13.81	2	141109	15655	733719	Mount
M05	0.10641	0.00117	4.74441	0.07895	0.32354	0.00531	0.98627	104	1738.9	20.09	1807	25.85	1775.1	13.96	0	103902	11310	523321	Mount
M05B	0.10367	0.00124	4.48799	0.07644	0.31416	0.00511	0.95500	104	1690.8	21.96	1761.2	25.08	1728.8	14.14	7	78646	8328	402092	Mount
M06	0.10176	0.00116	3.50906	0.05919	0.25024	0.00412	0.97607	87	1656.4	20.94	1439.7	21.24	1529.3	13.33	0	58227	6057	379546	Mount
M06B	0.10153	0.00115	4.11293	0.06933	0.29397	0.00484	0.97673	101	1652.3	20.83	1661.3	24.09	1656.9	13.77	5	111376	11548	618391	Mount
M071	0.10788	0.00125	4.64301	0.07869	0.31233	0.00511	0.96536	99	1763.9	21.01	1752.2	25.09	1757	14.16	2	142035	15626	736983	Mount
M07B	0.10772	0.00121	4.64091	0.07819	0.31262	0.00514	0.97588	100	1761.3	20.41	1753.6	25.26	1756.7	14.07	1	70414	7734	367679	Mount
M08	0.10829	0.00116	4.9256	0.0823	0.33007	0.00547	0.99184	104	1770.8	19.42	1838.7	26.49	1806.7	14.1	7	247744	27245	1238159	Mount
M08B	0.10743	0.00116	4.6955	0.07885	0.31718	0.00526	0.98755	101	1756.2	19.6	1776	25.77	1766.4	14.06	0	152352	16637	793382	Mount
M09†	0.10656	0.00141	5.58275	0.1032	0.38023	0.00651	0.92620	119	1741.4	24.08	2077.4	30.4	1913.4	15.92	4	32168	3473	141473	Mount
M10	0.10778	0.00119	4.63491	0.07846	0.31206	0.00519	0.98248	99	1762.2	19.91	1750.8	25.5	1755.6	14.14	4	140741	15396	745733	Mount
M10B	0.10869	0.0013	4.6732	0.0818	0.312	0.00522	0.95582	98	1777.5	21.65	1750.5	25.63	1762.5	14.64	7	103134	11371	546783	Mount
M11	0.09962	0.00115	3.92668	0.06762	0.28603	0.00478	0.97044	100	1617	21.29	1621.7	23.96	1619.2	13.94	0	49370	5002	285705	Mount
M12	0.10828	0.00122	4.71999	0.0806	0.3163	0.00526	0.97385	100	1770.7	20.52	1771.7	25.75	1770.8	14.31	0	161295	17734	841583	Mount
M12B	0.10705	0.00129	4.67991	0.08124	0.31724	0.00522	0.94787	102	1749.8	21.84	1776.2	25.53	1763.7	14.52	4	163502	17696	838160	Mount
M13	0.10931	0.00136	4.63546	0.08184	0.30772	0.00511	0.94057	97	1787.9	22.59	1729.5	25.18	1755.7	14.75	6	55652	6163	295550	Mount
M14	0.10838	0.00134	4.70538	0.08283	0.31504	0.00522	0.94126	100	1772.2	22.37	1765.5	25.61	1768.2	14.74	3	110796	12161	575515	Mount
M15	0.10881	0.0012	4.87639	0.0833	0.3252	0.00545	0.98107	102	1779.6	19.95	1815.1	26.51	1798.2	14.39	0	213882	23551	1096354	Mount
M16	0.10652	0.0012	4.75945	0.08265	0.32424	0.0055	0.97681	104	1740.7	20.51	1810.4	26.75	1777.8	14.57	0	61694	6655	320007	Mount
M16B	0.10682	0.0012	4.67969	0.08126	0.3179	0.00538	0.97461	102	1745.9	20.4	1779.5	26.34	1763.6	14.53	0	73659	7965	389596	Mount
M17†	0.10132	0.00118	3.35856	0.0587	0.24054	0.00405	0.96335	84	1648.5	21.47	1389.5	21.03	1494.8	13.68	1	87913	9005	609229	Mount
M18A	0.10572	0.00122	4.25616	0.07511	0.29217	0.005	0.96974	96	1726.9	20.96	1652.4	24.94	1684.9	14.51	3	89157	9550	517945	Mount

M18B	0.09679	0.00116	3.5485	0.06315	0.26605	0.00452	0.95466	97	1563.1	22.27	1520.7	23.01	1538.1	14.1	6	65282	6388	412417	Mount
M19	0.10938	0.00132	4.79522	0.086	0.31816	0.00545	0.95513	100	1789	21.78	1780.7	26.67	1784.1	15.07	0	39281	4346	209097	Mount
M19B	0.10988	0.00133	4.65879	0.08348	0.30771	0.00524	0.95034	96	1797.3	21.93	1729.4	25.82	1759.9	14.98	6	107492	11950	587995	Mount
M19C	0.11028	0.00144	4.70201	0.0864	0.30945	0.00525	0.92329	96	1804	23.61	1738	25.87	1767.6	15.39	4	49110	5466	264588	Mount
M20	0.10041	0.00136	3.37013	0.06235	0.24355	0.00411	0.91215	86	1631.8	24.9	1405.1	21.33	1497.5	14.49	0	46001	4678	312532	Mount

† indicates analysis was discarded due to variable isotopic signal

Sample Hay-09a U–Pb monazite data

Analysis	Pb^{207}/Pb^{206}		Pb^{207}/U^{235}		Pb^{206}/U^{238}		Rho	Conc.	Pb^{207}/Pb^{206}		Pb^{206}/U^{238}		Pb^{207}/U^{235}		Pb^{204}	Pb^{206}	Pb^{207}	U^{238}	
M01	0.10643	0.00115	4.50606	0.06703	0.30701	0.00451	0.9875333	99	1739.1	19.75	1726	22.27	1732.1	12.36	3	101615	11136	482911	mount
M02	0.10822	0.00117	4.45574	0.06605	0.29854	0.00438	0.9897343	95	1769.7	19.62	1684.1	21.74	1722.8	12.29	4	134153	14945	654557	mount
M03	0.1082	0.0012	4.45115	0.06607	0.2983	0.00434	0.9801768	95	1769.3	20.08	1682.9	21.53	1721.9	12.31	0	157908	17581	762636	mount
M04A	0.10559	0.00123	4.43959	0.06801	0.30486	0.0045	0.9635675	99	1724.6	21.17	1715.4	22.21	1719.8	12.69	0	36386	3948	173336	mount
M04B	0.10562	0.00115	4.11618	0.06098	0.28259	0.00412	0.9841184	93	1725.1	19.86	1604.4	20.72	1657.5	12.1	3	164004	17806	840362	mount
M05	0.1076	0.00123	4.46358	0.06753	0.30078	0.0044	0.9669194	96	1759.3	20.66	1695.2	21.83	1724.2	12.55	0	50425	5574	242377	mount
M06	0.10675	0.0012	4.40869	0.0659	0.29947	0.00436	0.9739963	97	1744.6	20.4	1688.7	21.61	1714	12.37	1	86547	9486	416020	mount
M07A	0.10669	0.00118	4.50906	0.06712	0.30644	0.00446	0.9777402	99	1743.6	20.12	1723.2	22.01	1732.6	12.37	0	109550	11995	515882	mount
M07B	0.10744	0.00148	4.33678	0.07116	0.29274	0.00428	0.8910317	94	1756.4	24.9	1655.2	21.37	1700.4	13.54	13	26306	2904	126399	mount
M08	0.10647	0.00122	4.23366	0.06336	0.28833	0.00415	0.9617431	94	1739.8	20.79	1633.2	20.79	1680.6	12.29	4	131430	14345	649697	mount
M09	0.11062	0.0014	4.6336	0.07212	0.30374	0.00433	0.9159014	94	1809.6	22.8	1709.8	21.43	1755.3	13	0	124227	14060	571328	mount
M10	0.10698	0.00115	4.68736	0.06815	0.31775	0.00455	0.9848913	102	1748.5	19.51	1778.7	22.24	1765	12.17	3	131067	14330	586025	mount
M11	0.10914	0.00119	4.56736	0.06688	0.30348	0.00435	0.9788771	96	1785.1	19.76	1708.6	21.53	1743.3	12.2	9	106111	11835	497607	mount
M12	0.10876	0.00122	4.52882	0.06596	0.30201	0.00426	0.9684845	96	1778.7	20.28	1701.3	21.11	1736.3	12.11	0	154553	17245	715058	mount
M13	0.10711	0.00119	4.45443	0.06575	0.30164	0.00434	0.9747588	97	1750.7	20.06	1699.4	21.49	1722.5	12.24	0	85145	9335	402171	mount
M14	0.10837	0.00118	4.6023	0.06727	0.30801	0.00441	0.9795515	98	1772.1	19.8	1730.9	21.74	1749.7	12.19	7	139348	15462	643100	mount
M14B	0.10897	0.00123	4.54192	0.06751	0.30229	0.00434	0.9659115	96	1782.2	20.5	1702.7	21.49	1738.7	12.37	5	57280	6385	268870	mount
M15†	0.10372	0.0012	3.49131	0.05209	0.24414	0.00348	0.9553761	83	1691.7	21.23	1408.2	18.04	1525.3	11.78	4	69453	7395	399919	mount
M16	0.10484	0.0012	3.89988	0.0576	0.26979	0.00382	0.9586637	90	1711.5	20.91	1539.8	19.41	1613.7	11.94	13	143081	15417	742658	mount
M17	0.1083	0.00127	4.42013	0.0661	0.29606	0.00421	0.9509024	94	1770.9	21.27	1671.7	20.93	1716.1	12.38	0	95388	10613	451293	mount
M18	0.10507	0.0012	4.26099	0.06365	0.29414	0.00421	0.9581646	97	1715.6	20.89	1662.2	20.97	1685.9	12.28	3	118467	12727	570128	mount
M19	0.10714	0.00116	4.51172	0.06531	0.30549	0.00434	0.9814206	98	1751.3	19.62	1718.5	21.44	1733.1	12.03	0	121561	13314	561175	mount
M20	0.10714	0.00118	4.54979	0.06574	0.30808	0.00433	0.972716	99	1751.4	20.02	1731.2	21.31	1740.1	12.03	10	128556	14064	580118	mount
M21A	0.10661	0.00118	4.56133	0.06719	0.31035	0.00444	0.971221	100	1742.3	20.23	1742.4	21.86	1742.2	12.27	0	88017	9592	401896	mount
M21B	0.10655	0.00141	4.5747	0.07262	0.31152	0.00445	0.8998714	100	1741.3	23.98	1748.2	21.89	1744.7	13.23	6	29159	3167	129097	mount
M22	0.10765	0.00158	4.49072	0.07729	0.30262	0.00452	0.8678276	97	1760.1	26.53	1704.3	22.34	1729.3	14.29	0	15666	1720	73226	mount
M23	0.10849	0.00128	4.5326	0.06749	0.30312	0.00426	0.94385	96	1774.1	21.35	1706.7	21.06	1737	12.39	0	110719	12250	505073	mount
M24†	0.09962	0.00128	3.83421	0.06042	0.27923	0.004	0.9090611	98	1617.1	23.71	1587.5	20.15	1600	12.69	0	39051	3953	194943	mount
M25	0.10692	0.0012	4.56285	0.06771	0.30955	0.00444	0.966575	99	1747.6	20.29	1738.5	21.84	1742.5	12.36	0	97966	10673	449129	mount
M26	0.10681	0.00121	4.37002	0.06536	0.29679	0.00426	0.9596917	96	1745.7	20.61	1675.4	21.16	1706.7	12.36	1	107892	11738	515758	mount
M27	0.10719	0.00136	4.566	0.07127	0.30909	0.00439	0.9099315	99	1752.2	22.96	1736.2	21.6	1743.1	13	0	100333	10938	450313	mount
MA28	0.10839	0.00122	4.64286	0.06845	0.31072	0.00441	0.962679	98	1772.5	20.4	1744.3	21.7	1757	12.32	5	93479	10279	422655	mount
M29A	0.10738	0.00126	4.68805	0.06946	0.31669	0.00444	0.9462504	101	1755.5	21.19	1773.6	21.72	1765.1	12.4	5	93419	10199	406971	mount
M29B	0.10816	0.00131	4.49068	0.06823	0.30119	0.00426	0.9309059	96	1768.5	22.07	1697.2	21.12	1729.2	12.62	2	44953	4934	206867	mount
M30	0.1062	0.00122	4.33491	0.06475	0.29609	0.00424	0.9586993	96	1735.2	20.84	1671.9	21.07	1700	12.32	9	61095	6602	291545	mount
M31†	0.10372	0.00137	4.09922	0.06481	0.28674	0.00403	0.8889472	96	1691.7	24.1	1625.2	20.19	1654.1	12.91	0	109112	11459	520771	mount
M32	0.10846	0.0013	4.62663	0.06972	0.30942	0.00436	0.935073	98	1773.7	21.69	1737.9	21.48	1754.1	12.58	7	88767	9780	398146	mount
M33	0.10778	0.00126	4.50796	0.06757	0.30337	0.0043	0.9456316	97	1762.3	21.2	1708	21.24	1732.4	12.46	0	98894	10827	455342	mount
M34	0.10853	0.00124	4.58391	0.06823	0.30634	0.00436	0.9561884	97	1774.9	20.69	1722.7	21.52	1746.3	12.41	4	165766	18293	762620	mount
M35A	0.10877	0.00134	4.58552	0.07104	0.30579	0.00437	0.922452	97	1778.9	22.38	1719.9	21.59	1746.6	12.91	0	70904	7830	325626	mount
M35B†	0.10941	0.0018	4.35271	0.0795	0.28857	0.00427	0.8101572	91	1789.5	29.77	1634.4	21.34	1703.4	15.08	9	14341	1593	68020	mount
M01	0.1073	0.00115	4.50695	0.07221	0.30466	0.00485	0.9936003	98	1754.1	19.43	1714.4	23.97	1732.3	13.31	6	193392	21245	1005412	in situ Grt
M01B	0.1071	0.00114	4.55506	0.07329	0.30847	0.00494	0.9953215	99	1750.7	19.31	1733.2	24.32	1741.1	13.4	8	193421	21154	998526	in situ Grt
M04†	0.09835	0.00115	3.52504	0.0587	0.25996	0.00418	0.9655965	94	1593.1	21.68	1489.6	21.41	1532.8	13.17	16	43720	4395	267132	matrix

M08	0.10932	0.00117	4.54466	0.07295	0.30151	0.00481	0.9938468	95	1788.1	19.33	1698.8	23.82	1739.2	13.36	0	471706	52667	2484979	in situ Grt
M10†	0.10692	0.00119	4.23792	0.06903	0.28751	0.0046	0.9822448	93	1747.5	20.1	1629.1	23.05	1681.4	13.38	11	70878	7723	390960	matrix
M13†	0.10532	0.00112	4.41513	0.07053	0.30407	0.00484	0.9964176	100	1719.9	19.36	1711.5	23.92	1715.2	13.22	6	138607	14893	721702	matrix
M13B†	0.099	0.0011	3.72962	0.06105	0.27325	0.0044	0.9837198	97	1605.4	20.5	1557.3	22.27	1577.7	13.11	6	75171	7587	439014	matrix
M16	0.10638	0.00117	4.35977	0.07093	0.29727	0.00476	0.9842139	97	1738.2	20.05	1677.7	23.66	1704.7	13.44	0	111585	12115	596691	matrix
M18	0.10563	0.00117	4.31512	0.06975	0.2963	0.00471	0.9834175	97	1725.3	20.17	1672.9	23.41	1696.3	13.32	1	152178	16440	809740	matrix
M20	0.10963	0.00132	3.70273	0.06167	0.24497	0.00391	0.9583231	79	1793.3	21.72	1412.5	20.23	1572	13.32	39	63513	7128	407021	in situ Grt
M22	0.1086	0.00122	4.48516	0.07321	0.29955	0.00478	0.9776111	95	1776	20.39	1689.1	23.72	1728.2	13.55	10	101845	11294	537691	in situ Grt
M23	0.10902	0.00115	2.68662	0.0445	0.195	0.00311	0.9628797	71	1622.8	21.64	1148.4	16.79	1324.8	12.26	13	68406	6982	552998	matrix
M23B†	0.11006	0.00165	5.46589	0.10191	0.36019	0.00593	0.8830131	110	1800.4	26.97	1983.1	28.1	1895.3	16	7	22624	2536	98525	matrix
M24†	0.10902	0.00115	4.45426	0.07051	0.29636	0.00469	0.9997194	94	1783	19.11	1673.2	23.31	1722.5	13.13	0	240669	26825	1278555	in situ Grt
M255	0.09741	0.00113	3.329	0.05467	0.24788	0.00394	0.9678754	91	1575.1	21.53	1427.5	20.38	1487.9	12.82	10	70608	7031	447524	matrix
M26	0.10747	0.00117	4.50705	0.07229	0.3042	0.00483	0.9899245	97	1756.9	19.73	1712.1	23.85	1732.3	13.33	0	111290	12221	575833	matrix
M26B	0.10891	0.00119	4.61302	0.07409	0.30721	0.00487	0.987005	97	1781.3	19.81	1726.9	24.04	1751.6	13.4	3	120546	13406	617729	matrix
M26C	0.11	0.00146	4.71132	0.08235	0.31065	0.00505	0.9300344	97	1799.4	23.93	1743.9	24.83	1769.3	14.64	4	21583	2428	109344	matrix
M26D	0.10871	0.00132	4.56583	0.07676	0.30464	0.0049	0.95674	96	1777.8	22.08	1714.3	24.21	1743.1	14	0	32309	3592	167141	matrix
M27	0.09824	0.00111	3.64017	0.05924	0.26875	0.00427	0.9763061	96	1591	20.97	1534.4	21.71	1558.4	12.96	10	87781	8815	513736	matrix

† indicates analysis was discarded due to variable isotopic signal

Sample RBN-11 U–Pb monazite data

Analysis	Pb^{207}/Pb^{206}		Pb^{207}/U^{235}		Pb^{206}/U^{238}		Rho	Conc.	Pb^{207}/Pb^{206}		Pb^{206}/U^{238}		Pb^{207}/U^{235}		Pb^{204}	Pb^{206}	Pb^{207}	U^{238}	
11A_M01	0.10809	0.00136	4.52948	0.08105	0.30404	0.0052	0.955802	97	1767.5	22.9	1711.3	25.71	1736.4	14.88	0	30367	3405	167750	Mount
11A_M01_2	0.10413	0.00133	4.19661	0.07566	0.29243	0.00501	0.9502723	97	1698.9	23.33	1653.7	24.97	1673.4	14.78	4	40292	4347	231670	Mount
11A_M01_3	0.10957	0.00145	4.57235	0.08394	0.30277	0.00522	0.9391353	95	1792.3	23.98	1705	25.84	1744.2	15.3	4	25099	2853	139741	Mount
11A_M02_1	0.10491	0.00133	4.30055	0.07752	0.29745	0.00511	0.9530532	98	1712.7	23.06	1678.7	25.37	1693.5	14.85	3	56586	6158	321402	Mount
11A_M02_2	0.10635	0.00133	4.43671	0.07995	0.30271	0.00521	0.9551103	98	1737.7	22.84	1704.7	25.77	1719.2	14.93	0	70472	7784	394638	Mount
11A_M02_3	0.10519	0.00137	4.42161	0.08122	0.30502	0.00528	0.9423735	100	1717.6	23.86	1716.1	26.06	1716.4	15.21	0	53340	5826	296991	Mount
11A_M03_1	0.10243	0.00139	4.19042	0.07835	0.29685	0.00516	0.9296751	100	1668.6	24.8	1675.7	25.65	1672.1	15.33	2	42637	4537	244406	Mount
11A_M03_2	0.10695	0.00147	4.47089	0.08457	0.30333	0.0053	0.9237153	98	1748.1	24.96	1707.8	26.22	1725.6	15.7	4	35055	3896	197301	Mount
11A_M04_1	0.1065	0.00156	4.48134	0.08749	0.30535	0.00538	0.9024722	99	1740.2	26.63	1717.8	26.57	1727.5	16.21	9	24627	2726	137856	Mount
11A_M04_2	0.10456	0.00151	4.28958	0.08322	0.2977	0.00524	0.9072762	98	1706.6	26.28	1679.9	26.03	1691.4	15.98	0	34198	3717	196884	Mount
11A_M05_1	0.10551	0.00147	4.23051	0.08076	0.29095	0.00514	0.9254249	96	1723.3	25.42	1646.3	25.64	1680	15.68	4	27103	2973	160387	Mount
11A_M05_2	0.10607	0.00148	4.46085	0.08511	0.30518	0.00538	0.9239814	99	1732.9	25.33	1717	26.6	1723.7	15.83	0	32014	3532	180727	Mount
11A_M05_3	0.10722	0.00151	4.64024	0.08907	0.31404	0.00555	0.9206976	100	1752.8	25.43	1760.5	27.21	1756.5	16.04	0	34691	3862	190482	Mount
11A_M06_1	0.10308	0.00138	4.27182	0.08043	0.30071	0.00528	0.9325689	101	1680.4	24.51	1694.8	26.18	1687.9	15.49	5	105650	11292	606749	Mount
11A_M06_2	0.1035	0.00146	4.25655	0.08223	0.29844	0.00528	0.9158078	100	1687.8	25.78	1683.6	26.2	1685	15.88	4	44105	4722	255492	Mount
11A_M06_3	0.10338	0.00148	4.26522	0.08304	0.29938	0.00529	0.9075843	100	1685.7	26.19	1688.2	26.24	1686.7	16.01	4	89342	9560	515662	Mount
11A_M07_1†	0.10334	0.00158	4.1897	0.08425	0.29419	0.00525	0.8874511	99	1685	27.89	1662.4	26.14	1672	16.48	1	29573	3159	173967	Mount
11A_M07_2	0.10468	0.00179	4.37771	0.094	0.30347	0.0055	0.8440459	100	1708.7	31.1	1708.5	27.22	1708.1	17.75	11	29843	3235	170881	Mount
11A_M08_1	0.10672	0.00164	4.5703	0.09262	0.31077	0.00554	0.8796514	100	1744.1	27.86	1744.5	27.25	1743.9	16.88	5	54316	5978	302801	Mount
11A_M08_2	0.10653	0.00162	4.6016	0.09284	0.31343	0.00558	0.8824038	101	1740.9	27.57	1757.6	27.39	1749.6	16.83	0	85087	9351	470707	Mount
11A_M08_3	0.10498	0.00134	4.26498	0.0794	0.29479	0.00522	0.9511615	97	1713.9	23.36	1665.4	26.01	1686.6	15.31	9	51162	5558	302733	Mount
11A_M08_4	0.10633	0.00133	4.50456	0.08308	0.3074	0.00544	0.9595131	99	1737.4	22.78	1727.9	26.82	1731.8	15.32	0	79968	8820	454220	Mount
11A_M09_1	0.10601	0.00141	4.52797	0.08576	0.30993	0.00553	0.9420637	100	1731.9	24.28	1740.4	27.2	1736.1	15.75	3	31208	3434	175982	Mount
11A_M09_2	0.10574	0.00143	4.45182	0.08505	0.30551	0.00546	0.9354713	100	1727.1	24.62	1718.6	26.95	1722	15.84	7	39458	4325	226130	Mount
11A_M10_1	0.10375	0.00147	4.27666	0.08353	0.2991	0.00538	0.9209331	100	1692.3	25.89	1686.9	26.69	1688.9	16.07	7	27660	2976	162220	Mount
11A_M10_2	0.10654	0.00155	4.56433	0.09036	0.31086	0.00561	0.9115885	100	1741.2	26.3	1744.9	27.59	1742.8	16.49	2	28342	3132	160128	Mount
11A_M10_3	0.10702	0.0015	4.56444	0.08892	0.30949	0.00556	0.9221811	99	1749.3	25.41	1738.2	27.4	1742.8	16.22	5	37049	4118	210395	Mount
11A_M11_1	0.09958	0.00154	3.82733	0.07813	0.27889	0.00507	0.8905393	98	1616.3	28.48	1585.8	25.55	1598.5	16.43	6	22438	2321	141546	Mount
11A_M12_1	0.1072	0.00158	4.51752	0.0902	0.30578	0.00553	0.9057526	98	1752.4	26.7	1719.9	27.32	1734.2	16.6	0	29823	3325	171728	Mount
11A_M12_2	0.10578	0.00152	4.39247	0.08665	0.30133	0.00543	0.9134772	98	1727.9	26.08	1697.9	26.9	1710.9	16.32	3	69536	7653	406665	Mount
11A_M13_1	0.10744	0.00142	4.64565	0.08789	0.31377	0.00565	0.9517964	100	1756.5	23.84	1759.2	27.72	1757.5	15.81	7	31151	3492	175336	Mount
11A_M13_2	0.10621	0.00149	4.60035	0.08933	0.31432	0.0057	0.9338914	102	1735.3	25.43	1761.9	27.94	1749.3	16.2	0	20511	2273	115274	Mount
11A_M13_3	0.10439	0.00133	4.48657	0.08383	0.31189	0.00558	0.9575197	103	1703.5	23.31	1750	27.44	1728.5	15.51	4	98821	10765	559414	Mount
11A_M14_1	0.10526	0.00143	4.49142	0.08618	0.30964	0.00558	0.9391919	101	1718.9	24.81	1738.9	27.46	1729.4	15.93	0	33251	3652	189500	Mount
11A_M14_2	0.10607	0.00138	4.40112	0.08275	0.3011	0.00539	0.9520795	98	1732.9	23.6	1696.8	26.72	1712.6	15.56	0	112997	12512	662290	Mount
11A_M15_1	0.10594	0.00155	4.47009	0.0888	0.3062	0.00555	0.9124122	100	1730.6	26.67	1722	27.41	1725.4	16.48	4	24526	2706	141279	Mount
11A_M15_2	0.10666	0.0016	4.52746	0.09088	0.308	0.00559	0.9041644	99	1743.2	27.1	1730.9	27.56	1736	16.7	0	27733	3081	158849	Mount
11A_M15_3	0.10581	0.0016	4.50661	0.09084	0.30906	0.00561	0.9005191	100	1728.4	27.57	1736.1	27.64	1732.2	16.75	0	23101	2550	131681	Mount
11A_M16_1	0.09189	0.0014	3.04252	0.06165	0.24025	0.00435	0.8935651	95	1465.1	28.79	1388	22.62	1418.4	15.48	0	41979	4016	307916	Mount
11A_M16_2	0.0961	0.00158	3.44269	0.07243	0.25996	0.00473	0.8648366	96	1549.7	30.55	1489.6	24.2	1514.2	16.55	0	54068	5412	365787	Mount
11A_M17_1	0.10168	0.00138	4.13951	0.07807	0.29542	0.00522	0.9369046	101	1655	24.9	1668.6	25.99	1662.1	15.42	0	38610	4098	226170	Mount
11A_M17_2	0.10342	0.00139	4.15518	0.07853	0.29157	0.00517	0.9382141	98	1686.3	24.6	1649.4	25.79	1665.2	15.47	13	42314	4544	252117	Mount
11A_M17_3	0.10325	0.00138	4.1455	0.07788	0.29137	0.00515	0.9408348	98	1683.3	24.4	1648.4	25.7	1663.3	15.37	2	44794	4808	266526	Mount

11A_M18_1	0.10485	0.00141	4.33994	0.08158	0.30035	0.0053	0.9387463	99	1711.8	24.59	1693.1	26.25	1701	15.51	7	38945	4258	224013	Mount
11A_M18_2	0.10639	0.00156	4.53239	0.08898	0.30916	0.00552	0.9094748	100	1738.4	26.72	1736.6	27.17	1736.9	16.33	8	25610	2840	143563	Mount
11A_M19_1	0.10584	0.00159	4.42966	0.08767	0.3037	0.00542	0.9017245	99	1728.9	27.31	1709.7	26.8	1717.9	16.39	0	20074	2214	114220	Mount
11A_M19_2	0.10643	0.00163	4.52624	0.09107	0.3086	0.00553	0.890618	100	1739.1	27.73	1733.8	27.23	1735.8	16.73	0	24298	2676	136518	Mount
11A_M19_3	0.10691	0.00158	4.45808	0.088	0.30258	0.00538	0.9007562	98	1747.5	26.84	1704.1	26.63	1723.2	16.37	0	38468	4273	219978	Mount
11A_M20_1†	0.1075	0.00168	4.47151	0.09043	0.30185	0.0054	0.8845945	97	1757.4	28.22	1700.5	26.75	1725.7	16.78	3	21591	2413	123671	Mount
11A_M20_2	0.10644	0.00171	4.26945	0.08682	0.29109	0.00518	0.8750938	95	1739.3	29.09	1647	25.89	1687.5	16.73	2	17493	1948	102918	Mount
11A_M20_3	0.10688	0.00149	4.43011	0.08516	0.30079	0.00537	0.9287306	97	1746.9	25.27	1695.2	26.63	1718	15.92	13	20836	2315	120526	Mount
11A_M21_1	0.10269	0.0013	4.08506	0.07503	0.28869	0.00509	0.959952	98	1673.3	23.16	1635	25.44	1651.3	14.98	2	77510	8304	466231	Mount
11A_M21_2	0.10394	0.00135	4.19983	0.07855	0.29322	0.0052	0.9481898	98	1695.6	23.71	1657.6	25.92	1674	15.34	15	55883	6027	332580	Mount
11A_M21_3	0.10313	0.00138	4.0631	0.07728	0.2859	0.00509	0.9360392	96	1681.3	24.44	1621	25.54	1646.9	15.5	7	63657	6794	389827	Mount
11A_M22_1	0.10412	0.00141	4.21906	0.08072	0.29405	0.00525	0.9331956	98	1698.9	24.7	1661.7	26.13	1677.7	15.7	1	60513	6526	360355	Mount
11A_M23_1	0.10372	0.00147	4.2312	0.08287	0.29602	0.00532	0.9176072	99	1691.8	25.85	1671.5	26.45	1680.1	16.09	0	38567	4134	228802	Mount
11A_M24_1	0.10747	0.00157	4.51958	0.08991	0.30519	0.0055	0.9059046	98	1756.9	26.43	1717	27.19	1734.6	16.54	0	30980	3444	178373	Mount
11A_M24_2	0.10709	0.00166	4.57178	0.09393	0.30979	0.00563	0.8845492	99	1750.5	28.02	1739.7	27.7	1744.1	17.12	8	31293	3457	177930	Mount
11A_M25_1	0.10633	0.00165	4.56759	0.09375	0.31171	0.00567	0.8862335	101	1737.5	28.04	1749.1	27.87	1743.4	17.1	7	22631	2492	127946	Mount
11A_M25_2	0.10747	0.00176	4.62332	0.09795	0.31217	0.00573	0.8663891	100	1757	29.53	1751.4	28.15	1753.5	17.69	8	20137	2233	114030	Mount
11A_M26_1	0.10652	0.00141	4.5311	0.08629	0.30868	0.00559	0.9509255	100	1740.6	24.05	1734.2	27.52	1736.7	15.84	17	28919	3209	166303	Mount
11A_M27_1	0.10686	0.00145	4.5656	0.08796	0.31004	0.00563	0.9425476	100	1746.5	24.63	1740.9	27.69	1743	16.05	0	24797	2762	141971	Mount
11A_M28_1	0.1025	0.00132	4.14598	0.07812	0.29351	0.00529	0.9565281	99	1669.9	23.69	1659.1	26.36	1663.4	15.41	0	53577	5732	323808	Mount
11A_M29_1	0.10545	0.00135	4.42387	0.08272	0.30442	0.00547	0.9609615	99	1722.2	23.4	1713.2	27.06	1716.8	15.49	3	69020	7651	401625	Mount
11A_M30_1	0.10441	0.00147	4.4113	0.08577	0.30658	0.00556	0.9327433	101	1704	25.74	1723.8	27.44	1714.5	16.09	0	24588	2700	141930	Mount
11A_M31_1	0.10563	0.00156	4.40943	0.08756	0.30293	0.00551	0.91598	99	1725.3	26.83	1705.8	27.26	1714.1	16.44	0	26388	2929	154010	Mount
11A_M32_1	0.10551	0.0015	4.54535	0.08902	0.3126	0.00567	0.926134	102	1723.3	25.94	1753.5	27.84	1739.3	16.3	1	33731	3735	191053	Mount
11A_M33_1	0.10295	0.00147	4.18647	0.08176	0.29507	0.00534	0.9266662	99	1678.1	26.06	1666.8	26.58	1671.4	16.01	11	44015	4773	263877	Mount
11A_M34_1	0.10713	0.00155	4.67912	0.09272	0.31695	0.00574	0.9139278	101	1751.1	26.2	1774.8	28.09	1763.5	16.58	0	125287	14019	700152	Mount
11A_M35_1	0.10109	0.00149	4.09591	0.08136	0.29402	0.00534	0.9143319	101	1644.2	27.09	1661.6	26.59	1653.5	16.21	0	41261	4395	248365	Mount
11B_M01_1	0.10402	0.00118	4.31994	0.0715	0.30137	0.00495	0.9923774	100	1697	20.68	1698.1	24.52	1697.2	13.65	1	67583	7341	364527	Mount
11B_M01_2R	0.09728	0.00117	3.80559	0.06486	0.28387	0.0047	0.9714566	102	1572.5	22.29	1610.8	23.59	1593.9	13.7	4	67097	6813	385694	Mount
11B_M02_1	0.10803	0.00123	4.61023	0.07736	0.30966	0.00512	0.985351	98	1766.4	20.76	1739	25.21	1751.1	14	0	130236	14646	688794	Mount
11B_M03_1	0.09952	0.00115	3.92906	0.06643	0.28646	0.00476	0.982805	101	1615.2	21.39	1623.8	23.84	1619.7	13.68	0	102367	10625	587244	Mount
11B_M04_1	0.10289	0.00117	4.02453	0.06779	0.28382	0.00472	0.9872986	96	1676.9	20.91	1610.6	23.69	1639.2	13.7	0	281341	30219	1633439	Mount
11B_M05_1	0.10354	0.00123	4.24572	0.07318	0.29756	0.00498	0.9709877	99	1688.5	21.75	1679.2	24.75	1682.9	14.17	6	96549	10385	536689	Mount
11B_M06_1	0.10086	0.00121	4.01269	0.0695	0.28869	0.00485	0.9699756	100	1640	22.02	1635	24.27	1636.8	14.08	6	91239	9578	524558	Mount
11B_M07_1	0.10097	0.00124	4.1901	0.07352	0.30111	0.00509	0.9634108	103	1642	22.6	1696.8	25.2	1672.1	14.38	10	79814	8411	441286	Mount
11B_M08_1	0.10393	0.00132	4.41102	0.07894	0.30797	0.00524	0.9507466	102	1695.5	23.26	1730.7	25.82	1714.4	14.81	13	48771	5279	264567	Mount
11B_M09_1	0.10558	0.00135	4.49923	0.08069	0.30921	0.00527	0.9503325	101	1724.5	23.23	1736.8	25.93	1730.8	14.9	0	57271	6310	309941	Mount
11B_M10_1	0.10287	0.0012	4.17101	0.07304	0.29422	0.00506	0.982107	99	1676.5	21.48	1662.6	25.21	1668.3	14.34	0	64409	6890	372367	Mount
11B_M11_1	0.10232	0.00118	4.17109	0.07259	0.29579	0.00508	0.9868542	100	1666.7	21.21	1670.4	25.25	1668.4	14.25	0	127118	13543	730566	Mount
11B_M12_1	0.10066	0.00122	3.84635	0.06799	0.27728	0.00477	0.9732033	96	1636.2	22.33	1577.7	24.09	1602.5	14.24	10	61051	6421	373778	Mount
11B_M13_1	0.10179	0.00121	4.08795	0.07189	0.2914	0.00501	0.9776542	99	1657.1	21.85	1648.5	25.02	1651.9	14.35	3	104620	11115	610525	Mount
11B_M14_1	0.10502	0.00131	4.46133	0.07965	0.30824	0.00532	0.9667211	101	1714.8	22.68	1732.1	26.23	1723.8	14.81	0	48714	5358	268479	Mount
11B_M15_1	0.1061	0.00134	4.32838	0.07808	0.29603	0.00513	0.9606545	96	1733.4	22.93	1671.6	25.53	1698.8	14.88	14	46137	5109	265628	Mount
11B_M16_1	0.10607	0.00129	4.49234	0.07996	0.30733	0.00531	0.9707098	100	1732.9	22.11	1727.6	26.2	1729.6	14.78	18	99321	11000	551656	Mount
11B_M17_1	0.10441	0.0013	4.24794	0.0767	0.29523	0.00512	0.9604892	98	1704	22.67	1667.6	25.5	1683.3	14.84	4	68041	7375	394372	Mount

11B_M18_1	0.10576	0.00133	4.3801	0.0794	0.30053	0.00522	0.958178	98	1727.6	22.94	1693.9	25.9	1708.6	14.99	11	42430	4671	241455	Mount
11B_M19_1R	0.0984	0.00126	3.87609	0.07086	0.28585	0.00497	0.9510665	102	1594	23.81	1620.7	24.93	1608.7	14.76	12	77246	7939	462430	Mount
11B_M19_2C	0.10162	0.00121	4.10647	0.07281	0.29322	0.00512	0.9848135	100	1653.9	21.96	1657.6	25.53	1655.6	14.48	0	60760	6501	357349	Mount
11B_M20_1	0.10157	0.00122	4.10925	0.07299	0.29357	0.00513	0.9837956	100	1653	22.02	1659.3	25.59	1656.1	14.51	0	68357	7320	402177	Mount
11B_M21_1	0.10466	0.00129	4.43004	0.07971	0.30714	0.00539	0.9753202	101	1708.4	22.45	1726.6	26.6	1718	14.91	23	48632	5361	273976	Mount
11B_M22_1	0.10042	0.00118	4.03356	0.07156	0.29145	0.00511	0.9882687	101	1632	21.65	1648.7	25.5	1641	14.43	0	124757	13171	742893	Mount
11B_M23_1	0.10575	0.00132	4.4284	0.08048	0.30385	0.00536	0.9706539	99	1727.4	22.71	1710.4	26.5	1717.7	15.05	0	49851	5548	285048	Mount
11B_M24_1	0.1007	0.00124	4.13176	0.07484	0.29773	0.00525	0.9735046	103	1637	22.65	1680.1	26.09	1660.6	14.81	7	80122	8494	468606	Mount
11B_M25_1	0.10258	0.00131	4.38014	0.08063	0.30986	0.00549	0.9624943	104	1671.2	23.42	1740	27.02	1708.6	15.22	25	59314	6413	333706	Mount
11B_M26_1	0.10477	0.00143	4.49346	0.08509	0.31122	0.00555	0.9417331	102	1710.3	24.94	1746.7	27.28	1729.8	15.73	25	35618	3944	199436	Mount
11B_M27_1	0.10003	0.00131	4.01688	0.07445	0.2914	0.00516	0.955398	101	1624.6	24.09	1648.5	25.74	1637.6	15.07	0	117537	12452	702231	Mount
11B_M27_2	0.10059	0.00134	4.10368	0.07725	0.29605	0.00527	0.9456285	102	1635	24.53	1671.7	26.21	1655	15.37	14	117409	12458	693793	Mount

† indicates analysis was discarded due to variable isotopic signal

Sample RBN-12 U–Pb monazite data

Analysis	Pb^{207}/Pb^{206}		Pb^{207}/U^{235}		Pb^{206}/U^{238}		Rho	Conc.	Pb^{207}/Pb^{206}		Pb^{206}/U^{238}		Pb^{207}/U^{235}		Pb^{204}	Pb^{206}	Pb^{207}	U^{238}	
12_M01_1	0.10625	0.00118	4.48519	0.0727	0.3063	0.00495	0.9970218	99	1736	20.16	1722.5	24.45	1728.2	13.46	13	119715	13301	626872	Mount
12_M02_1	0.10586	0.00125	4.50618	0.07506	0.30889	0.00503	0.9776066	100	1729.3	21.46	1735.2	24.79	1732.1	13.84	0	45621	5049	237248	Mount
12_M03_1	0.10561	0.00117	4.32218	0.07023	0.29695	0.00481	0.9968778	97	1725	20.13	1676.2	23.91	1697.6	13.4	20	359667	39695	1948061	Mount
12_M04_1	0.10676	0.00126	4.61789	0.07725	0.31386	0.00513	0.9770718	101	1744.9	21.4	1759.7	25.16	1752.5	13.96	15	53328	5952	273723	Mount
12_M05_1	0.10608	0.00123	4.47555	0.07439	0.30615	0.00499	0.9806141	99	1733.1	21.09	1721.7	24.64	1726.4	13.8	15	115274	12778	607464	Mount
12_M06_1	0.10792	0.00128	4.60834	0.07756	0.30987	0.00507	0.9721542	99	1764.6	21.5	1740.1	24.96	1750.8	14.04	0	80125	9033	417761	Mount
12_M07_1	0.09673	0.00125	3.77813	0.0658	0.2834	0.00468	0.9481936	103	1562	24.05	1608.5	23.49	1588.1	13.98	19	38832	3956	221239	Mount
12_M08_1	0.10744	0.00131	4.63242	0.07895	0.31285	0.00514	0.9640127	100	1756.5	22.1	1754.7	25.26	1755.1	14.23	1	75818	8543	392485	Mount
12_M09_1	0.10616	0.00131	4.50589	0.07756	0.30803	0.00508	0.9581058	100	1734.6	22.46	1731	25.05	1732.1	14.3	10	63297	7015	333749	Mount
12_M10_1	0.10642	0.00131	4.50836	0.07723	0.30741	0.00507	0.9627699	99	1739	22.44	1728	25	1732.5	14.24	0	82183	9215	434095	Mount
12_M11_1	0.10566	0.00137	4.45776	0.07867	0.30618	0.00513	0.9493975	100	1725.7	23.65	1721.9	25.33	1723.1	14.64	7	20871	2305	111442	Mount
12_M11_2R	0.09716	0.00115	3.76219	0.06345	0.28099	0.00465	0.9812308	102	1570.4	21.93	1596.4	23.42	1584.7	13.53	0	54930	5613	319563	Mount
12_M12_1C	0.10615	0.00124	4.54349	0.0762	0.31063	0.00514	0.98663	101	1734.3	21.27	1743.8	25.3	1739	13.96	16	57082	6388	300405	Mount
12_M12_2R	0.10577	0.00139	4.50158	0.08042	0.30886	0.0052	0.9424158	100	1727.7	24.01	1735.1	25.6	1731.3	14.84	0	21805	2403	115817	Mount
12_M13_1	0.10719	0.00129	4.65994	0.07991	0.3155	0.00526	0.9722223	101	1752.2	21.82	1767.7	25.78	1760.1	14.34	0	47870	5370	249329	Mount
12_M14_1C	0.1071	0.00137	4.53265	0.07964	0.30715	0.00514	0.952431	99	1750.6	23.22	1726.7	25.37	1737	14.62	0	31834	3579	169938	Mount
12_M14_2R	0.11165	0.00142	4.79587	0.0838	0.31175	0.0052	0.9545974	96	1826.5	22.81	1749.3	25.56	1784.2	14.68	34	76302	8964	401111	Mount
12_M15_1C	0.10591	0.00135	4.43146	0.07837	0.30364	0.00509	0.9478853	99	1730.1	23.25	1709.3	25.18	1718.2	14.65	16	44795	4942	242879	Mount
12_M16_1C	0.10662	0.00153	4.58509	0.08573	0.31206	0.00532	0.9117769	100	1742.4	25.97	1750.8	26.12	1746.6	15.59	0	16960	1883	89502	Mount
12_M17_1C	0.10768	0.00144	4.61277	0.08343	0.31087	0.00523	0.9301702	99	1760.5	24.12	1745	25.7	1751.6	15.09	0	53305	5960	282174	Mount
12_M18_1	0.1061	0.00123	4.44969	0.07549	0.30433	0.00509	0.9858557	99	1733.4	21.06	1712.8	25.17	1721.6	14.07	8	116867	12985	636147	Mount
12_M19_1	0.10573	0.0013	4.46484	0.07788	0.30643	0.00516	0.9653802	100	1727.1	22.41	1723.1	25.45	1724.5	14.47	0	55153	6085	298180	Mount
12_M20_1	0.10725	0.00125	4.59961	0.07858	0.31119	0.00522	0.9818697	100	1753.2	21.15	1746.6	25.64	1749.2	14.25	0	135759	15208	723558	Mount
12_M21_1	0.10652	0.00132	4.52719	0.07968	0.3084	0.0052	0.9580063	100	1740.7	22.61	1732.8	25.61	1736	14.64	27	64696	7156	347986	Mount
12_M22_1	0.1082	0.00133	4.59489	0.08027	0.30813	0.00519	0.9641736	98	1769.3	22.29	1731.5	25.58	1748.3	14.57	0	74617	8430	402047	Mount
12_M23_1	0.10784	0.00145	4.57524	0.08363	0.30784	0.00524	0.9312323	98	1763.3	24.38	1730.1	25.85	1744.8	15.23	16	30444	3410	164348	Mount
12_M24_1	0.1065	0.00135	4.52729	0.0803	0.30848	0.00521	0.9522116	100	1740.2	23.04	1733.2	25.69	1736	14.75	12	102952	11450	555155	Mount
12_M25_1	0.10533	0.00151	4.49306	0.08448	0.30953	0.00533	0.9158256	101	1720	26.05	1738.4	26.22	1729.7	15.62	15	21324	2347	114793	Mount
12_M26_1R	0.10085	0.00132	4.07718	0.07353	0.29336	0.00499	0.9431808	101	1639.8	24.04	1658.3	24.86	1649.8	14.71	7	54349	5726	309034	Mount
12_M26_2C	0.10657	0.00141	4.55459	0.08268	0.3101	0.00529	0.9397292	100	1741.7	23.86	1741.2	26.01	1741	15.11	0	51606	5750	277964	Mount
12_M27_1	0.10618	0.00126	4.53715	0.07874	0.31006	0.00526	0.9775247	100	1734.8	21.64	1741	25.86	1737.8	14.44	4	56952	6293	307245	Mount
12_M28_1	0.1081	0.00124	4.63968	0.07927	0.31143	0.00526	0.9885633	99	1767.6	20.86	1747.7	25.88	1756.4	14.27	16	106485	12031	572317	Mount
12_M29_1	0.10501	0.0013	4.48832	0.07894	0.31013	0.00527	0.96617	102	1714.5	22.58	1741.4	25.95	1728.8	14.6	16	41443	4551	223391	Mount
12_M30_1	0.10709	0.00126	4.51797	0.07812	0.30612	0.00518	0.9786314	98	1750.5	21.24	1721.6	25.55	1734.3	14.37	17	139795	15568	764384	Mount
12_M31_1	0.10823	0.00137	4.71063	0.08395	0.31583	0.00538	0.9558444	100	1769.8	22.97	1769.3	26.37	1769.1	14.93	1	44364	5002	235073	Mount
12_M32_1	0.10648	0.00135	4.52795	0.08079	0.30856	0.00526	0.9554108	100	1740	23.07	1733.6	25.93	1736.1	14.84	3	45366	5031	246360	Mount
12_M33_1	0.10733	0.00141	4.58549	0.08334	0.31001	0.00531	0.9424343	99	1754.6	23.86	1740.8	26.12	1746.6	15.15	15	34443	3849	186115	Mount
12_M34_1	0.10627	0.00145	4.54663	0.08396	0.31045	0.00534	0.9314655	100	1736.4	24.85	1742.9	26.26	1739.5	15.37	1	24062	2666	129838	Mount
12_M35_1	0.1073	0.00136	4.55086	0.0812	0.30776	0.00523	0.9524166	99	1754.1	22.94	1729.7	25.8	1740.3	14.85	4	65753	7351	357585	Mount
12_M36_1	0.10822	0.00142	4.67476	0.08481	0.31347	0.00535	0.940741	99	1769.5	23.81	1757.8	26.27	1762.7	15.18	11	46862	5279	250321	Mount
12_M37_1	0.10734	0.00127	4.43824	0.07657	0.30004	0.00508	0.9813788	96	1754.7	21.39	1691.5	25.2	1719.5	14.3	0	40932	4585	227897	Mount
12_M38_1	0.10675	0.00124	4.53905	0.07796	0.30854	0.00521	0.9831491	99	1744.6	21.06	1733.5	25.68	1738.2	14.29	2	61538	6839	333177	Mount
12_M39_1	0.10672	0.0013	4.46394	0.07819	0.30352	0.00516	0.9705759	98	1744.1	22.14	1708.7	25.51	1724.3	14.53	4	33009	3673	181744	Mount

12_M40_1	0.1076	0.0014	4.51086	0.08112	0.30421	0.00521	0.9523479	97	1759.1	23.59	1712.1	25.76	1733	14.95	6	17998	2024	98900	Mount
12_M41_1	0.105	0.00128	4.373	0.0758	0.30221	0.00509	0.971671	99	1714.2	22.21	1702.3	25.21	1707.3	14.33	10	53403	5883	293301	Mount
12_M42_1	0.10469	0.00131	4.41227	0.07788	0.30581	0.00519	0.9615056	101	1708.9	22.77	1720.1	25.63	1714.6	14.61	0	36553	3991	199406	Mount
12_M43_1	0.10673	0.0014	4.53064	0.0815	0.30801	0.00525	0.9475376	99	1744.4	23.75	1730.9	25.86	1736.6	14.96	21	27028	3017	146090	Mount
12_M44_1	0.10663	0.00131	4.55615	0.07969	0.31006	0.00524	0.9662283	100	1742.5	22.39	1741	25.77	1741.3	14.56	0	57480	6413	308477	Mount
12_M45_1	0.10766	0.00138	4.52294	0.0809	0.30484	0.00518	0.9500142	97	1760.2	23.16	1715.3	25.61	1735.2	14.87	12	44068	4940	241302	Mount
12_M46_1	0.10672	0.00136	4.34989	0.07774	0.29576	0.00503	0.9516172	96	1744.2	23.15	1670.2	25.03	1702.9	14.76	22	41746	4649	235837	Mount
12_M47_1	0.10392	0.00121	4.17288	0.07129	0.29137	0.0049	0.9843704	97	1695.3	21.32	1648.4	24.48	1668.7	13.99	17	81207	8829	463717	Mount
12_M48_1	0.10728	0.00126	4.54642	0.07839	0.30751	0.0052	0.980738	99	1753.8	21.24	1728.5	25.64	1739.5	14.35	0	68099	7609	370083	Mount
12_M49_1	0.10705	0.00124	4.53954	0.07791	0.30771	0.0052	0.9846466	99	1749.8	21	1729.4	25.65	1738.2	14.28	8	78088	8719	424516	Mount
12_M50_1	0.10734	0.00134	4.45898	0.07884	0.30145	0.00513	0.9624784	97	1754.7	22.55	1698.5	25.43	1723.4	14.66	4	33236	3720	184476	Mount
12_M51_1	0.10232	0.00123	4.17156	0.07347	0.29583	0.00505	0.969254	100	1666.7	22.11	1670.6	25.1	1668.5	14.42	0	66982	7097	381312	Mount
12_M52_1	0.10684	0.00141	4.51242	0.08191	0.30648	0.00522	0.9382984	99	1746.2	23.89	1723.4	25.78	1733.3	15.09	16	46146	5127	251252	Mount
12_M53_1	0.10074	0.0014	3.89636	0.0732	0.28065	0.00485	0.9198663	97	1637.8	25.53	1594.7	24.4	1612.9	15.18	1	32910	3421	197386	Mount
12_M53_2R	0.10464	0.0013	4.24761	0.0758	0.29455	0.00502	0.9550368	97	1708.1	22.68	1664.2	24.97	1683.3	14.67	0	158802	17191	905999	Mount
12_M54_1	0.10723	0.00134	4.49788	0.08032	0.30437	0.00519	0.9548819	98	1752.9	22.58	1712.9	25.65	1730.6	14.83	0	138917	15456	767739	Mount
12_M55_1	0.10799	0.00145	4.67403	0.08615	0.31406	0.00538	0.9294068	100	1765.7	24.34	1760.7	26.38	1762.6	15.42	0	75668	8475	404407	Mount
12_M56_1	0.10685	0.00138	4.56494	0.08295	0.31001	0.00534	0.9479474	100	1746.3	23.48	1740.8	26.3	1742.9	15.14	8	40250	4475	219418	Mount
12_M57_1	0.09809	0.00129	3.83567	0.07036	0.28374	0.00489	0.939515	101	1588.1	24.42	1610.1	24.53	1600.3	14.77	3	69492	7077	413788	Mount
12_M58_1	0.10663	0.00136	4.52138	0.08165	0.30768	0.0053	0.9538749	99	1742.6	23.09	1729.3	26.13	1734.9	15.02	16	51501	5721	283338	Mount
12_M59_1	0.1069	0.00145	4.51447	0.08406	0.30645	0.00533	0.9340819	99	1747.2	24.49	1723.2	26.31	1733.6	15.48	5	25779	2859	142862	Mount
12_M60_1	0.09834	0.00127	3.75439	0.06875	0.27704	0.0048	0.9461619	99	1592.8	23.97	1576.4	24.22	1583.1	14.68	4	39454	4018	242240	Mount
12_M61_1	0.10633	0.00137	4.5546	0.08308	0.31082	0.00538	0.9489145	100	1737.4	23.47	1744.7	26.45	1741	15.19	0	46046	5091	251795	Mount
12_M62_1	0.10576	0.00139	4.48268	0.08268	0.30757	0.00533	0.9395513	100	1727.5	23.93	1728.7	26.28	1727.8	15.31	4	61407	6736	339765	Mount
12_M63_1	0.10741	0.0015	4.52576	0.08567	0.30574	0.00532	0.9192256	98	1755.9	25.35	1719.7	26.28	1735.7	15.74	8	40598	4538	225443	Mount
12_M64_1	0.10763	0.00149	4.5822	0.08657	0.30893	0.00539	0.9234966	99	1759.7	25.02	1735.4	26.56	1746	15.75	9	35001	3908	193102	Mount
12_M64_2R	0.10596	0.00151	4.53397	0.08666	0.31049	0.00544	0.9166662	101	1731	25.96	1743.1	26.74	1737.2	15.9	0	23037	2545	126254	Mount

Sample RBN-28 U–Pb monazite data

Analysis	Pb^{207}/Pb^{206}		Pb^{207}/U^{235}		Pb^{206}/U^{238}		Rho	Conc.	Pb^{207}/Pb^{206}		Pb^{206}/U^{238}		Pb^{207}/U^{235}		Pb^{204}	Pb^{206}	Pb^{207}	U^{238}	
28_M01_1	0.10691	0.00112	4.42727	0.07054	0.30047	0.00477	0.9963635	97	1747.5	19.02	1693.6	23.65	1717.5	13.2	2	315233	34302	1660174	Mount
28_M02_1	0.10631	0.00115	4.43053	0.07161	0.3024	0.00483	0.9882057	98	1737.1	19.71	1703.2	23.9	1718.1	13.39	0	75981	8222	398775	Mount
28_M03_1	0.10579	0.00113	4.42573	0.07133	0.30354	0.00485	0.9913762	99	1728.2	19.48	1708.8	23.98	1717.2	13.35	0	158748	17099	831748	Mount
28_M04_1	0.10647	0.0012	4.29097	0.06859	0.29242	0.00455	0.9734172	95	1739.8	20.52	1653.6	22.68	1691.6	13.16	22	390470	42521	2060361	Mount
28_M05_1	0.10698	0.00115	4.45935	0.07256	0.30245	0.00487	0.9895771	97	1748.6	19.53	1703.4	24.08	1723.4	13.5	0	175341	19107	927911	Mount
28_M06_1	0.10624	0.00118	4.54293	0.07501	0.31028	0.00502	0.9798663	100	1735.8	20.2	1742.1	24.71	1738.9	13.74	4	68487	7412	354641	Mount
28_M07_1	0.10591	0.00117	4.48173	0.07407	0.30704	0.00498	0.9813812	100	1730.2	20.12	1726.1	24.56	1727.6	13.72	0	102743	11088	539123	Mount
28_M08_1	0.10747	0.00119	4.56255	0.07576	0.30804	0.00502	0.9814412	99	1757	20	1731	24.73	1742.5	13.83	0	132660	14529	697027	Mount
28_M09_1	0.10477	0.00116	4.28013	0.07141	0.29642	0.00485	0.9806909	98	1710.3	20.21	1673.5	24.11	1689.5	13.73	0	193672	20680	1061961	Mount
28_M10_1	0.10534	0.0012	4.4729	0.07554	0.30809	0.00506	0.97249	101	1720.3	20.78	1731.3	24.92	1726	14.02	11	83115	8927	439124	Mount
28_M11_1	0.10155	0.00115	4.06609	0.06754	0.29057	0.00472	0.9779286	99	1652.7	20.88	1644.4	23.56	1647.5	13.54	3	62118	6457	343801	Mount
28_M12_1	0.10683	0.00121	4.49565	0.07498	0.30541	0.00497	0.9757087	98	1746	20.57	1718.1	24.53	1730.2	13.85	7	78175	8523	412649	Mount
28_M13_1	0.10656	0.0012	4.50895	0.07546	0.30708	0.00503	0.9787574	99	1741.5	20.38	1726.3	24.81	1732.6	13.91	20	65635	7133	347365	Mount
28_M14_1	0.10487	0.00128	4.36193	0.07341	0.30186	0.00483	0.9507471	99	1712	22.2	1700.5	23.94	1705.2	13.9	23	169686	18290	888537	Mount
28_M15_1	0.10649	0.00119	4.52914	0.0753	0.30868	0.00503	0.9801223	100	1740	20.45	1734.2	24.77	1736.3	13.83	3	122352	13311	641045	Mount
28_M16_1	0.10611	0.0012	4.42745	0.07349	0.30281	0.00492	0.9788594	98	1733.6	20.58	1705.2	24.37	1717.5	13.75	21	75771	8247	403502	Mount
28_M17_1	0.10662	0.00124	4.50776	0.07588	0.30683	0.00501	0.9700037	99	1742.3	21.1	1725.1	24.71	1732.4	13.99	0	57489	6273	302760	Mount
28_M18_1	0.10607	0.00123	4.4608	0.07475	0.3052	0.00496	0.9698369	99	1732.9	21.2	1717	24.48	1723.7	13.9	6	77593	8443	408633	Mount
28_M19_1	0.10659	0.00126	4.36803	0.07287	0.29738	0.00478	0.9635028	96	1741.9	21.47	1678.3	23.76	1706.3	13.78	0	157288	17244	841391	Mount
28_M20_1	0.10594	0.00135	4.42029	0.07618	0.30279	0.00488	0.9351647	99	1730.7	23.22	1705.1	24.15	1716.1	14.27	5	69192	7527	361902	Mount
28_M21_1	0.10684	0.00116	4.45733	0.07319	0.30273	0.00493	0.9917781	98	1746.3	19.65	1704.8	24.41	1723.1	13.62	0	90467	9898	484059	Mount
28_M22_1	0.10654	0.00118	4.45751	0.07388	0.30361	0.00495	0.9836816	98	1741.1	20.21	1709.2	24.49	1723.1	13.75	1	58983	6429	314364	Mount
28_M23_1	0.10716	0.00116	4.33459	0.07122	0.29351	0.00478	0.9911766	95	1751.7	19.53	1659.1	23.82	1700	13.56	7	319261	34939	1763389	Mount
28_M24_1	0.10532	0.00117	4.26579	0.07078	0.29389	0.00479	0.9822898	97	1720	20.16	1661	23.89	1686.8	13.65	0	95863	10310	528518	Mount
28_M25_1	0.10663	0.00118	4.45807	0.07388	0.30338	0.00495	0.9845511	98	1742.6	20.2	1708	24.46	1723.2	13.74	2	92718	10115	494754	Mount
28_M26_1	0.10252	0.00116	4.02254	0.0671	0.28472	0.00463	0.9748569	97	1670.2	20.77	1615.1	23.25	1638.8	13.57	4	93763	9816	531743	Mount
28_M27_1	0.10668	0.00123	4.50066	0.07555	0.30612	0.00499	0.9710701	99	1743.5	21	1721.6	24.61	1731.1	13.95	0	60044	6551	316364	Mount
28_M28_1	0.10729	0.00121	4.37648	0.07318	0.296	0.00483	0.975861	95	1753.9	20.45	1671.4	24	1707.9	13.82	13	238126	26067	1302273	Mount
28_M29_1	0.10697	0.00128	4.52575	0.07683	0.30701	0.00498	0.9555129	99	1748.4	21.6	1726	24.58	1735.7	14.12	10	73400	8007	383660	Mount
28_M30_1	0.10705	0.00127	4.50477	0.07688	0.30534	0.00499	0.9575823	98	1749.9	21.47	1717.7	24.64	1731.9	14.18	2	94404	10291	500063	Mount
28_M31_1	0.10751	0.00113	4.40134	0.07061	0.29707	0.00475	0.9966749	95	1757.6	19.11	1676.8	23.61	1712.6	13.27	0	248352	27224	1331535	Mount
28_M32_1	0.10637	0.00113	4.50757	0.07262	0.30747	0.00493	0.9952459	99	1738.1	19.34	1728.2	24.32	1732.4	13.39	0	154491	16785	802668	Mount
28_M33_1	0.10436	0.00113	4.24238	0.06912	0.29497	0.00475	0.9883747	98	1703	19.89	1666.3	23.67	1682.3	13.39	9	72371	7719	392965	Mount
28_M34_1	0.10643	0.00117	4.43595	0.07297	0.30243	0.0049	0.9849485	98	1739.2	20.06	1703.3	24.23	1719.1	13.63	1	67767	7358	360136	Mount
28_M35_1	0.10663	0.00117	4.50601	0.07408	0.30663	0.00497	0.9859001	99	1742.6	19.94	1724.1	24.54	1732.1	13.66	2	83454	9098	438645	Mount
28_M36_1	0.1062	0.00118	4.46212	0.07381	0.30489	0.00495	0.9814949	99	1735.1	20.2	1715.5	24.45	1724	13.72	12	99291	10762	524912	Mount
28_M37_1	0.1079	0.00124	4.52608	0.07632	0.3044	0.00498	0.9702163	97	1764.2	20.83	1713.1	24.59	1735.8	14.02	5	53467	5879	284226	Mount
28_M38_1	0.10471	0.00119	4.24124	0.0712	0.29393	0.00482	0.9768232	97	1709.2	20.71	1661.1	24	1682	13.79	12	64357	6894	355732	Mount
28_M39_1	0.10797	0.00122	4.50653	0.07594	0.30287	0.00499	0.9777233	97	1765.5	20.43	1705.5	24.67	1732.2	14	0	94072	10389	507366	Mount
28_M40_1	0.10523	0.00119	4.48601	0.07573	0.30935	0.0051	0.9765901	101	1718.4	20.62	1737.5	25.11	1728.4	14.02	8	128030	13790	677095	Mount

Sample RBN-31 U–Pb monazite data

Analysis	Pb^{207}/Pb^{206}		Pb^{207}/U^{235}		Pb^{206}/U^{238}		Rho	Conc.	Pb^{207}/Pb^{206}		Pb^{206}/U^{238}		Pb^{207}/U^{235}		Pb^{204}	Pb^{206}	Pb^{207}	U^{238}	
31_M01_1	0.10598	0.00116	4.49574	0.07198	0.30779	0.00486	0.9862139	100	1731.4	19.9	1729.8	23.97	1730.2	13.3	5	58418	6319	297564	Mount
31_M02_1	0.11761	0.00129	5.63738	0.09056	0.3478	0.00552	0.9879851	100	1920.2	19.54	1924.1	26.38	1921.8	13.85	8	49625	5969	224344	Mount
31_M03_1	0.10664	0.00117	4.55205	0.0727	0.3097	0.00488	0.986623	100	1742.7	19.9	1739.2	24	1740.5	13.29	25	87685	9562	442635	Mount
31_M04_1	0.10685	0.00114	4.62705	0.0737	0.31419	0.00499	0.9971142	101	1746.4	19.3	1761.3	24.47	1754.2	13.3	13	173920	19072	874601	Mount
31_M051	0.10713	0.00115	4.53936	0.07286	0.30743	0.00491	0.9950404	99	1751.2	19.47	1728	24.19	1738.2	13.36	4	134582	14802	694855	Mount
31_M06_1	0.10681	0.00115	4.5985	0.07423	0.31237	0.00501	0.9935853	100	1745.8	19.64	1752.3	24.6	1749	13.46	9	127618	14001	651258	Mount
31_M07_1	0.10329	0.00112	4.06206	0.06631	0.28536	0.00461	0.9896352	96	1684	19.92	1618.3	23.12	1646.7	13.3	7	148238	15692	834311	Mount
31_M08_1C	0.10414	0.00115	4.21772	0.06814	0.29384	0.0047	0.9900624	98	1699.2	20.19	1660.7	23.41	1677.5	13.26	0	80774	8701	436131	Mount
31_M08_2R	0.09709	0.00107	3.65212	0.0598	0.27292	0.00441	0.9868408	99	1569	20.49	1555.6	22.35	1561	13.05	10	135246	13523	795901	Mount
31_M09_1	0.10566	0.00121	4.50524	0.07595	0.3094	0.00508	0.973943	101	1725.8	20.9	1737.7	25.01	1731.9	14.01	21	53170	5766	279320	Mount
31_M10_1	0.10728	0.00118	4.55439	0.07475	0.30806	0.00501	0.9908808	99	1753.7	19.96	1731.1	24.68	1741	13.67	0	136617	15101	715940	Mount
31_M11_1	0.10643	0.00117	4.48549	0.07328	0.30581	0.00497	0.9947848	99	1739.2	19.98	1720.1	24.51	1728.3	13.56	9	118221	13002	623229	Mount
31_M12_1	0.10742	0.00117	4.58805	0.07445	0.30993	0.00501	0.9961794	99	1756.1	19.77	1740.3	24.67	1747.1	13.53	0	103558	11523	536723	Mount
31_M13_1	0.10642	0.00122	4.4585	0.07394	0.30401	0.00493	0.9778413	98	1739	20.93	1711.2	24.37	1723.3	13.75	0	86353	9495	455743	Mount
31_M14_1	0.10643	0.00123	4.45032	0.07511	0.30341	0.00496	0.9686018	98	1739.2	21.08	1708.2	24.55	1721.8	13.99	1	124362	13552	664331	Mount
31_M15_1	0.10667	0.00121	4.52392	0.07551	0.30774	0.00502	0.9773052	99	1743.3	20.61	1729.6	24.77	1735.4	13.88	0	145262	15902	764488	Mount
31_M16_1	0.1058	0.00119	4.36363	0.07307	0.29928	0.00491	0.979744	98	1728.2	20.47	1687.7	24.38	1705.5	13.83	14	237066	25727	1291648	Mount
31_M17_1	0.10133	0.00123	4.08399	0.07098	0.29246	0.00484	0.9521986	100	1648.7	22.26	1653.8	24.16	1651.1	14.18	10	151281	15665	846933	Mount
31_M18_1C	0.10712	0.00137	4.60612	0.08346	0.312	0.00528	0.933977	100	1751.1	23.24	1750.5	25.96	1750.4	15.12	0	46219	5035	246663	Mount
31_M18_2R	0.09303	0.00115	3.1952	0.05597	0.24922	0.00412	0.9437502	96	1488.5	23.23	1434.5	21.24	1456	13.55	7	111816	10596	731599	Mount
31_M19_1D	0.10856	0.00116	4.6996	0.07919	0.31412	0.00526	0.9937582	99	1775.4	19.43	1761	25.83	1767.2	14.11	0	155373	17199	825448	Mount
31_M20_1D	0.10452	0.00114	4.2608	0.07205	0.29582	0.00496	0.9915424	98	1705.9	19.86	1670.5	24.66	1685.8	13.91	0	99984	10666	563325	Mount
31_M21_1D	0.1119	0.00133	5.84149	0.10168	0.37881	0.00636	0.9645479	113	1830.5	21.45	2070.7	29.75	1952.6	15.09	0	26917	3075	117601	Mount
31_M22_1D	0.10648	0.00123	4.47497	0.0768	0.30498	0.00508	0.9705575	99	1739.9	21.14	1716	25.09	1726.3	14.24	0	62636	6800	338512	Mount
31_M23_1D	0.10289	0.00119	3.99995	0.07077	0.28211	0.00483	0.967685	96	1676.8	21.16	1602	24.31	1634.2	14.37	0	142092	14827	856526	Mount
31_M23_2R†	0.07569	0.00101	1.95956	0.03537	0.18789	0.00312	0.9199716	102	1086.8	26.62	1109.9	16.91	1101.7	12.14	4	44331	3444	383230	Mount
31_M234_1C	0.10887	0.00123	4.7686	0.08204	0.31785	0.00533	0.9746984	100	1780.5	20.58	1779.2	26.07	1779.4	14.44	1	123761	13714	648060	Mount
31_M234_2C	0.10919	0.00125	4.96993	0.08578	0.33028	0.00554	0.9718332	103	1786	20.74	1839.7	26.83	1814.2	14.59	6	129401	14380	651714	Mount
31_M234_3C	0.10813	0.00125	4.79636	0.0834	0.32186	0.00542	0.9684518	102	1768.1	20.99	1798.8	26.43	1784.3	14.61	0	94172	10357	488466	Mount
31_M234_4R	0.10287	0.0012	4.35149	0.07609	0.30694	0.00517	0.9632687	103	1676.6	21.41	1725.6	25.49	1703.2	14.44	0	237081	24763	1289838	Mount
31_M25_1C	0.10599	0.00114	4.46904	0.07659	0.30594	0.00519	0.9898588	99	1731.5	19.6	1720.7	25.64	1725.2	14.22	0	192637	20733	1064679	Mount
31_M25_2R	0.09803	0.00106	3.8357	0.06563	0.28391	0.0048	0.9881043	102	1587	20.08	1611	24.12	1600.3	13.78	12	219928	21905	1305234	Mount
31_M26_1	0.1077	0.00117	4.80761	0.08277	0.32391	0.00552	0.9898537	103	1760.8	19.64	1808.8	26.89	1786.2	14.47	0	134550	14748	704724	Mount
31_M27_1	0.10188	0.00113	4.14876	0.07195	0.29546	0.00504	0.9836019	101	1658.7	20.42	1668.7	25.06	1664	14.19	0	95696	9919	548642	Mount
31_M28_1	0.10799	0.00123	4.57128	0.08018	0.30716	0.00527	0.9781776	98	1765.6	20.68	1726.7	25.98	1744	14.61	0	53650	5902	297019	Mount
31_M29_1	0.1089	0.00128	4.76123	0.08485	0.31725	0.00547	0.9675045	100	1781.1	21.38	1776.3	26.79	1778.1	14.95	10	43421	4822	233545	Mount
31_M30_1	0.10741	0.00121	4.66548	0.0818	0.31517	0.00541	0.9790287	101	1756	20.47	1766.1	26.53	1761.1	14.66	0	88447	9691	478462	Mount
31_M31_1	0.10639	0.00124	4.62609	0.08142	0.3155	0.00538	0.9688709	102	1738.5	21.23	1767.7	26.37	1754	14.69	0	79077	8584	423446	Mount
31_M32_1	0.10694	0.00127	4.59477	0.08151	0.31175	0.00534	0.9655787	100	1748	21.47	1749.3	26.25	1748.3	14.79	0	55217	6036	300174	Mount
31_M33_1	0.10665	0.00121	4.52746	0.07933	0.30803	0.00529	0.9801213	99	1742.9	20.59	1731	26.07	1736	14.57	18	184911	20186	1024101	Mount

† indicates analysis was discarded due to variable isotopic signal

Sample RBN-46 U–Pb monazite data

Analysis	Pb^{207}/Pb^{206}		Pb^{207}/U^{235}		Pb^{206}/U^{238}		Rho	Conc.	Pb^{207}/Pb^{206}		Pb^{206}/U^{238}		Pb^{207}/U^{235}		Pb^{204}	Pb^{206}	Pb^{207}	U^{238}	
46_M01	0.09638	0.00105	3.61706	0.0478	0.27229	0.00343	0.9532136	100	1555.3	20.32	1552.4	17.4	1553.3	10.51	9	299061	28650	1375980	Mount
46_M02	0.09559	0.00105	3.49446	0.04632	0.26523	0.00334	0.9500257	98	1539.8	20.5	1516.5	17.02	1526	10.46	4	458190	43511	2160818	Mount
46_M03	0.09797	0.00107	3.59744	0.0477	0.26641	0.00336	0.9511827	96	1585.9	20.31	1522.6	17.11	1549	10.53	92	599303	58324	2820122	Mount
46_M04	0.09566	0.00105	3.53549	0.04712	0.26816	0.00339	0.9485277	99	1541	20.59	1531.4	17.21	1535.2	10.55	0	560305	53225	2619196	Mount
46_M05	0.09575	0.00106	3.42671	0.0459	0.25964	0.00328	0.9431199	96	1542.9	20.74	1488	16.8	1510.5	10.53	51	347543	33041	1678550	Mount
46_M06	0.0958	0.00107	3.4737	0.04675	0.26306	0.00333	0.9405895	98	1543.9	20.85	1505.5	17	1521.3	10.61	0	459359	43675	2193047	Mount
46_M07	0.09519	0.00107	3.50485	0.04733	0.26711	0.00338	0.9370429	100	1531.9	20.98	1526.1	17.21	1528.3	10.67	8	663044	62608	3117695	Mount
46_M08	0.09639	0.0011	3.45765	0.04709	0.26024	0.0033	0.9310912	96	1555.4	21.17	1491.1	16.9	1517.6	10.73	4	418476	40010	2020983	Mount
46_M09	0.09562	0.00109	3.38134	0.04626	0.25654	0.00326	0.9288503	96	1540.3	21.34	1472.1	16.72	1500.1	10.72	0	466559	44229	2287014	Mount
46_M10	0.09648	0.00111	3.50953	0.04822	0.26389	0.00335	0.9239397	97	1557.1	21.44	1509.7	17.1	1529.4	10.86	40	673579	64409	3208380	Mount
46_M11	0.09501	0.00104	3.54985	0.04687	0.27112	0.00343	0.9581811	101	1528.3	20.55	1546.5	17.39	1538.4	10.46	0	484425	46015	2236165	Mount
46_M12	0.09438	0.00104	3.50931	0.04652	0.2698	0.00341	0.9534424	102	1515.8	20.73	1539.8	17.33	1529.3	10.47	11	537609	50705	2492772	Mount
46_M13	0.09689	0.00108	3.57643	0.04756	0.26785	0.00339	0.9517348	98	1565.1	20.66	1529.9	17.26	1544.3	10.55	54	444172	43013	2077361	Mount
46_M14	0.0948	0.00106	3.45716	0.04623	0.26462	0.00336	0.9495377	99	1524.1	20.92	1513.4	17.13	1517.5	10.53	2	411247	38956	1948858	Mount
46_M15	0.09695	0.0011	3.48929	0.04705	0.26116	0.00332	0.9427767	96	1566.2	21.09	1495.8	16.97	1524.8	10.64	20	436885	42292	2097381	Mount
46_M16	0.09601	0.00109	3.45169	0.04665	0.26087	0.00332	0.9416599	97	1548	21.16	1494.3	16.98	1516.3	10.64	7	611597	58620	2944000	Mount
46_M16A	0.09466	0.00108	3.46306	0.04703	0.26548	0.00339	0.9402708	100	1521.2	21.35	1517.8	17.25	1518.8	10.7	17	701655	66255	3323432	Mount
46_M17	0.0961	0.00111	3.49042	0.04771	0.26354	0.00337	0.9355169	97	1549.8	21.47	1507.9	17.19	1525.1	10.79	5	611120	58600	2918073	Mount
46_M18	0.09473	0.0011	3.42638	0.04714	0.26246	0.00336	0.9305123	99	1522.6	21.73	1502.4	17.17	1510.5	10.81	0	508521	48024	2440900	Mount
46_M19	0.09444	0.0011	3.28088	0.04515	0.25207	0.00323	0.9311378	96	1516.9	21.73	1449.2	16.64	1476.5	10.71	0	412278	38827	2061805	Mount
46_M20	0.09503	0.00102	3.42221	0.04527	0.26128	0.00333	0.9634612	98	1528.7	20.16	1496.4	17	1509.5	10.39	67	286887	27178	1389410	Mount
46_M21	0.09703	0.00104	3.52923	0.04666	0.26391	0.00336	0.9629831	96	1567.8	20.02	1509.8	17.13	1533.8	10.46	14	637348	61653	3057434	Mount
46_M21A	0.09779	0.00106	3.51326	0.04671	0.26069	0.00332	0.9578867	94	1582.4	20.1	1493.4	17	1530.2	10.51	10	736188	71706	3581238	Mount
46_M22	0.08569	0.00095	2.60711	0.03523	0.22077	0.00283	0.9486218	97	1331.1	21.39	1286	14.93	1302.6	9.92	4	133277	11373	766387	Mount
46_M23	0.09463	0.00104	3.56218	0.04783	0.27315	0.00349	0.9515677	102	1520.7	20.55	1556.7	17.69	1541.1	10.65	4	406680	38350	1890965	Mount
46_M24	0.09495	0.00105	3.45836	0.0466	0.26428	0.00338	0.949154	99	1527.2	20.62	1511.7	17.26	1517.8	10.61	10	623242	58985	2998423	Mount
46_M24A	0.09464	0.00105	3.48017	0.04718	0.26683	0.00342	0.94544	100	1520.9	20.8	1524.7	17.42	1522.7	10.69	0	452331	42633	2157864	Mount
46_M25	0.09623	0.00107	3.50418	0.04767	0.26423	0.00339	0.9431024	97	1552.3	20.79	1511.4	17.31	1528.2	10.75	3	581454	55727	2803656	Mount
46_M26	0.09536	0.00107	3.47534	0.04754	0.26444	0.0034	0.9399178	99	1535.2	21	1512.5	17.35	1521.6	10.79	16	554881	52718	2676376	Mount
46_M27	0.09534	0.0011	3.49032	0.04835	0.26566	0.00342	0.9293273	99	1534.8	21.5	1518.7	17.41	1525	10.93	5	320540	30445	1535147	Mount
46_M27	0.09509	0.00104	3.56481	0.04816	0.27203	0.00351	0.955081	101	1529.9	20.46	1551.1	17.79	1541.7	10.71	0	341178	32287	1607632	Mount
46_M28	0.09831	0.00108	3.09726	0.04189	0.22861	0.00295	0.9541004	83	1592.3	20.36	1327.2	15.47	1432	10.38	106	236167	23117	1323203	Mount
46_M29	0.09462	0.00104	3.32483	0.04483	0.25499	0.00328	0.9540066	96	1520.5	20.5	1464.1	16.85	1486.9	10.53	14	644110	60656	3228732	Mount
46_M30	0.0957	0.00107	3.51365	0.04807	0.26642	0.00344	0.9437914	99	1541.9	20.81	1522.6	17.53	1530.3	10.81	13	301917	28703	1453231	Mount
46_M31	0.09441	0.00105	3.42825	0.04689	0.26349	0.0034	0.9434242	99	1516.4	20.92	1507.6	17.34	1510.9	10.75	16	630967	59165	3065358	Mount
46_M32	0.09573	0.00108	3.45312	0.04764	0.26175	0.00339	0.9387564	97	1542.4	21.04	1498.8	17.31	1516.6	10.86	10	480260	45580	2354838	Mount
46_M33	0.09639	0.0011	3.55705	0.04937	0.26778	0.00347	0.9336373	98	1555.3	21.22	1529.5	17.64	1540	11	7	410242	39218	1965903	Mount
46_M34	0.09678	0.0011	3.54854	0.04937	0.26606	0.00345	0.9320218	97	1563	21.26	1520.7	17.56	1538.1	11.02	4	566964	54346	2735598	Mount
46_M35	0.09564	0.00111	3.34314	0.04706	0.25364	0.00329	0.9214691	95	1540.8	21.76	1457.2	16.91	1491.2	11	11	436250	41323	2204867	Mount
46_M36	0.09653	0.00114	3.38198	0.04833	0.25424	0.00332	0.9137943	94	1558	22.05	1460.3	17.06	1500.2	11.2	53	541532	51744	2746717	Mount

Chapter 3

This chapter has been written in publication style format as:
Anderson, J. R., Hand, M., Kelsey, D. E., and Collins W.J. Hf isotopic characterisation of late Paleoproterozoic granitoids from the southern Arunta Region, central Australia

Hf isotopic characterisation of late Paleoproterozoic granitoids from the southern Arunta Region, central Australia

ABSTRACT

LA−MC−ICP−MS zircon Lu−Hf isotopic data has been collected from five late Paleoproterozoic (*c.* 1649–1626 Ma) granitoids from the southern Aileron Province, Arunta Region. These magmatic rocks provide insights into the crustal evolution of the Arunta Region during the *c.* 1640−1635 Ma Liebig Orogeny, which was proposed to record the (re)accretion of the Warumpi Province to the Aileron Province via south-dipping subduction. The analysed granites have isotopic compositions near and below CHUR (εHf -6.2 to +1.5) and crustal model ages (T_{DMc}) between 2.2–2.7 Ga. This isotopic range is similar to existing Hf isotopic data from the Arunta Region, with the εHf range suggesting the granitoids were probably derived from dominantly Aileron Province crust (North Australian Craton). The Liebig Orogeny-aged magmatism in the Aileron Province suggests that the magmatic and thermal footprint of Liebig Orogeny-aged tectonism may be larger than previously known. We interpret, in agreement with other recent isotopic work, that the rocks of the Warumpi Province are unlikely to be exotic to the NAC. The occurrence of *c.* 1640−1635 Ma mafic-ultramafic magmatism of and deposition of approximately coeval sedimentary packages leading up to and post-dating the Liebig-Orogeny may indicate the operation of extensional processes during the late Paleoproterozoic in the southern Arunta Region.

A geophysically modelled, lithospheric-scale structure in the southern Arunta Region has previously been interpreted to be the remnants of a late Paleoproterozoic, south-dipping subduction zone. This modelled structure has not been directly age constrained, and consequently it is possible that the structure is instead related to Grenvillian-aged subduction. If true, it negates the requirement for Liebig-aged tectonism to be related to the (re)accretion of the Warumpi Province via south-dipping subduction. Instead, Liebig-aged tectonism may reflect the continuation of a long-lived (>150 Myr) north-dipping, retreating subduction system on the southern margin of the NAC in a dominantly extensional setting.

Introduction

In a number of recent Proterozoic Australia plate reconstruction models, the Arunta Region is commonly considered to record plate margin processes during the late-Paleoproterozoic as part of the amalgamation of Proterozoic Australia (e.g. Betts and Giles, 2006; Betts et al., 2008; Cawood and Korsch, 2008; Payne et al., 2009; Ahmad and Scrimgeour, 2013; Aitken et al., in press). Throughout this time, evidence of classical indicators for collisional orogenesis in the Arunta Region are notably rare from the geological record (e.g. Collins and Shaw, 1995; Betts et al., 2011; Anderson et al., 2013; Morrissey et al., 2014). Instead, the Arunta Region is dominated by generally south-east younging sedimentation, high thermal gradient metamorphism and granitoid-dominated magmatism (e.g. Ahmad and Scrimgeour, 2013; Anderson et al., 2013; Scrimgeour, 2013a; Morrissey et al., 2014). This geological record has led some workers to propose the Arunta Region was situated at a long-lived, southward migrating margin, involving cycles of accretion and extension related to subduction roll-back between *c.* 1800–1640 Ma (e.g. Betts et al., 2008; Betts et al., 2011).

One of the few documented occurrences of medium-*P* metamorphism of Proterozoic age in the Arunta Region is preserved in the Warumpi Province of the southern Arunta Region (9–10 kbar, >800 °C; Scrimgeour et al., 2005b). This medium-*P* metamorphism occurred at *c.* 1640–1635 Ma during the Liebig Orogeny and has been considered to reflect the docking of the Warumpi Province as an exotic terrane to the North Australian Craton (NAC; Scrimgeour et al., 2005b), via south dipping subduction (Scrimgeour et al., 2005b; Selway et al., 2009; Ahmad and Scrimgeour, 2013). However, in a recent isotopic study, Hollis et al. (2013) proposed the Warumpi Province formed an originally contiguous terrane with the Aileron Province (of the southern NAC), based on distinctive provenance affinities with the NAC. In the model proposed by Hollis et al. (2013), the Liebig Orogeny is interpreted to mark the reconvergence of the Warumpi Province to the Aileron Province following a phase of rifting. The tectonic and crustal evolution of the *c.* 1640 Ma timeline in the Arunta Region is yet to be fully understood due to: 1) the complex geological nature of the polycyclic Arunta Region; and 2) the paucity of data constraining the timing, isotopic evolution and spatial footprint of Liebig Orogeny-aged tectonism. In order to gain further insight to the crustal evolution of the Arunta Region during the latest Paleoproterozoic, this study investigates the Hf isotopic signature of late Paleoproterozoic granitoids in the southern Arunta Region. These granitoids have zircon U–Pb crystallisation ages of *c.* 1649–1626 Ma, and therefore intruded at a similar time to the medium-*P* Liebig Orogeny (Scrimgeour et al., 2005b).

Geological Background

The Arunta Region, central Australia (Fig. 1) is a poly-deformed and poly-metamorphosed terrain that has experienced a complex tectonic history from the Paleoproterozoic to Paleozoic (e.g. Hand and Buick, 2001; Claoue-Long and Hoatson, 2005; Maidment et al., 2005; Claoue-Long et al., 2008a; Ahmad and Scrimgeour, 2013). The Arunta Region has been divided into the Aileron, Warumpi and Irindina Provinces (Fig. 1), which were defined based on differing protolith ages and tectonic histories (e.g. Scrimgeour, 2003; Scrimgeour, 2004; Ahmad and Scrimgeour, 2013). The majority of the rocks in the Aileron Province are variably deformed metasedimentary and granitic rocks. The metasedimentary protoliths have depositional ages mostly between *c.* 1870 and at least 1740 Ma (Claoue-Long et al., 2008a; Bodorkos et al., 2013) that show a general younging to the south-southeast across the Aileron Province. Granitoids have intrusive ages mostly within the age bracket of *c.* 1820–1700 Ma, with some minor younger components (Collins and Williams, 1995; Claoue-Long and Hoatson, 2005; Maidment et al., 2005; Whelan et al., 2012). A number of identified tectonothermal cycles have been identified in the Aileron Province, which are: 1) *c.* 1810−1790 Ma Stafford Event; 2) *c.* 1780−1770 Ma Yambah Event; 3) *c.* 1760–1740 Ma metamorphism and magmatism in the south eastern Aileron Province (Inkamulla Event); 4) *c.* 1735−1690 Ma Strangways Event; 5) *c.* 1600−1570 Ma Chewings Event; and 6) *c.* 450−300 Ma Alice Springs Orogeny (e.g. Claoue-Long and Hoatson, 2005; Huston et al., 2006; Neumann and Fraser, 2007; Claoue-Long et al., 2008b; Scrimgeour, 2013a).

A series of major faults and shear zones collectively known as the Central Australian Suture define the boundary between the Aileron and Warumpi Province (e.g. Scrimgeour et al., 2005b; Scrimgeour, 2013b). The Warumpi Province contains protolith sedimentary and igneous rocks largely in the age range of *c.* 1700–1600 Ma (Scrimgeour, 2013b). The Warumpi Province is further divided into three fault-bound sub-domains, distinguished based on discrete protolith differences and metamorphic characteristics (Scrimgeour et al., 2005b). These sub-domains are: 1) the Haasts Bluff Domain, which is metamorphosed to amphibolite facies and is characterised by dominantly *c.* 1690–1660 Ma igneous and sedimentary protoliths and a *c.* 1630–1600 Ma cover sequence; 2) the typically granulite facies metamorphosed Yaya Domain, dominantly comprised of the *c.* 1660–1640 Ma supracrustal succession of the Yaya Metamorphic Complex, and 3) the Kintore Domain, metamorphosed to greenschist facies, and containing *c.* 1690–1655 Ma granitoids and a younger supracrustal succession (Scrimgeour et al., 2005b; Scrimgeour, 2013b). Several major tectonothermal events

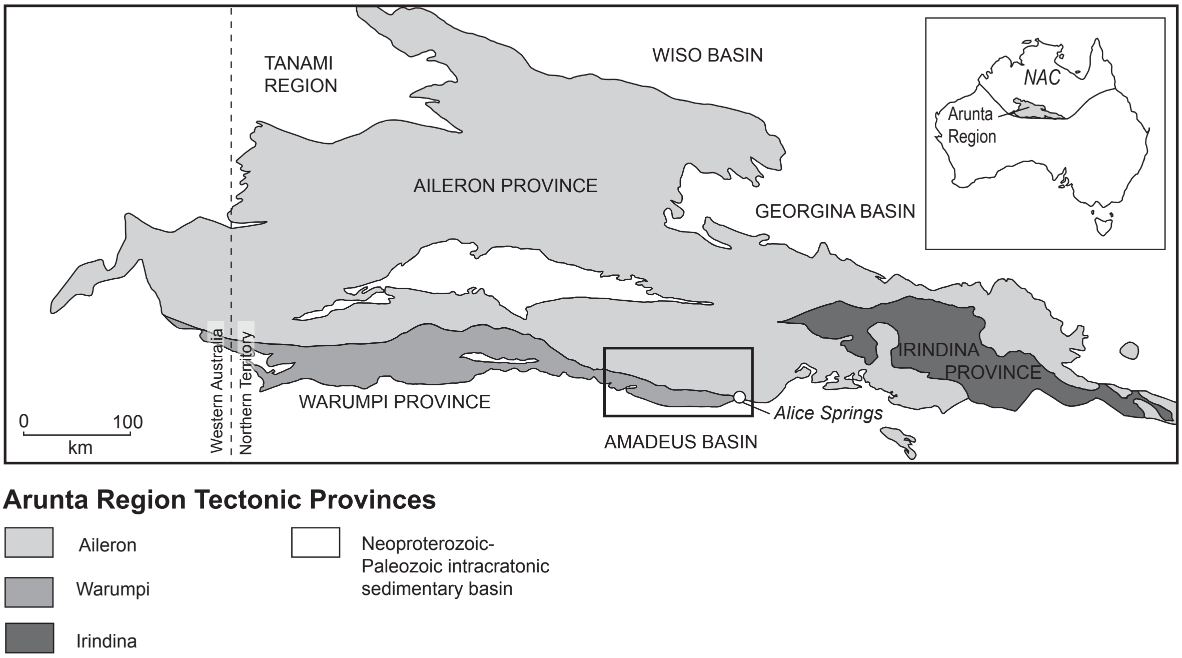

Fig. 1. Simplified regional geology map of the Arunta Region, showing provinces, major structural boundaries and study area (modified from Scrimgeour et al., 2005b). Inset, location of the Arunta Region in Australia.

are recognised in the Warumpi Province, which are: 1) *c.* 1690−1660 Ma Argilke Event (e.g. Collins and Shaw, 1995; Hollis et al., 2013); 2) the *c.* 1640–1635 Ma Liebig Orogeny, which resulted in estimated peak *P–T* conditions of ~9–10 kbar, >800 °C, followed by an interpreted steeply decompressive post-peak evolution (Scrimgeour et al., 2005b); 3) the *c.* 1590–1560 Ma Chewings Event; 4) *c.* 1150–1100 Ma Teapot Event and Grenvillian-aged reworking (Morrissey et al., 2011; Scrimgeour, 2013b; Wong et al., submitted); and 5) *c.* 450–300 Ma Alice Springs Orogeny (e.g. Shaw et al., 1992; McLaren et al., 2009).

Sample Descriptions

Samples of granitoid were collected from the Aileron Province in the south-eastern Arunta Region (Fig. 2). U–Pb zircon age data for the samples were collected by Wong (2011), Fields (2012) and Lawson-Wyatt (2012) using LA–ICP–MS, at the University of Adelaide using methodology and standards outlined in Payne et al. (2006; Fig. 3). Sample descriptions and a summary of U–Pb age data are provided in Table 1.

Analytical Methods

Lu–Hf isotopes

Lu–Hf spot analyses were conducted on zircon grains with pre-analysed spot U–Pb age data (100 ± 10 % concordant data) on domains that exhibit oscillatory and concentric zoning in Cathodoluminescence (CL) imagery, typical of zircon growth during igneous crystallisation (Wong, 2011; Fields, 2012; Lawson-Wyatt, 2012). Lu–Hf spot analyses were conducted over or in the same Cathodoluminescence domain as U–Pb age spots using a New Wave 213 nm laser, attached to a ThermoScientific Neptune Multicollector (LA–MC−ICP–MS) equipped with Faraday detectors and 10^{11} Ω amplifiers at CSIRO, Adelaide. Analyses used a dynamic measurement routine with: ten 0.524 s integrations on ^{171}Yb, ^{173}Yb, ^{175}Lu, ^{176}Hf (+Lu + Yb), ^{177}Hf, ^{178}Hf, ^{179}Hf and ^{180}Hf; one 0.524 s integration on ^{160}Gd, ^{163}Dy, ^{164}Dy, ^{165}Ho, ^{166}Er, ^{167}Er, ^{168}Er, ^{170}Yb and ^{171}Yb, and one 0.524 s integration of Hf oxides with masses ranging from 187 to 196 amu. An idle time of 1.5 s was included between each mass change to allow for magnet settling and to negate any potential effects of signal decay. This measurement cycle is repeated 15 times to provide a total

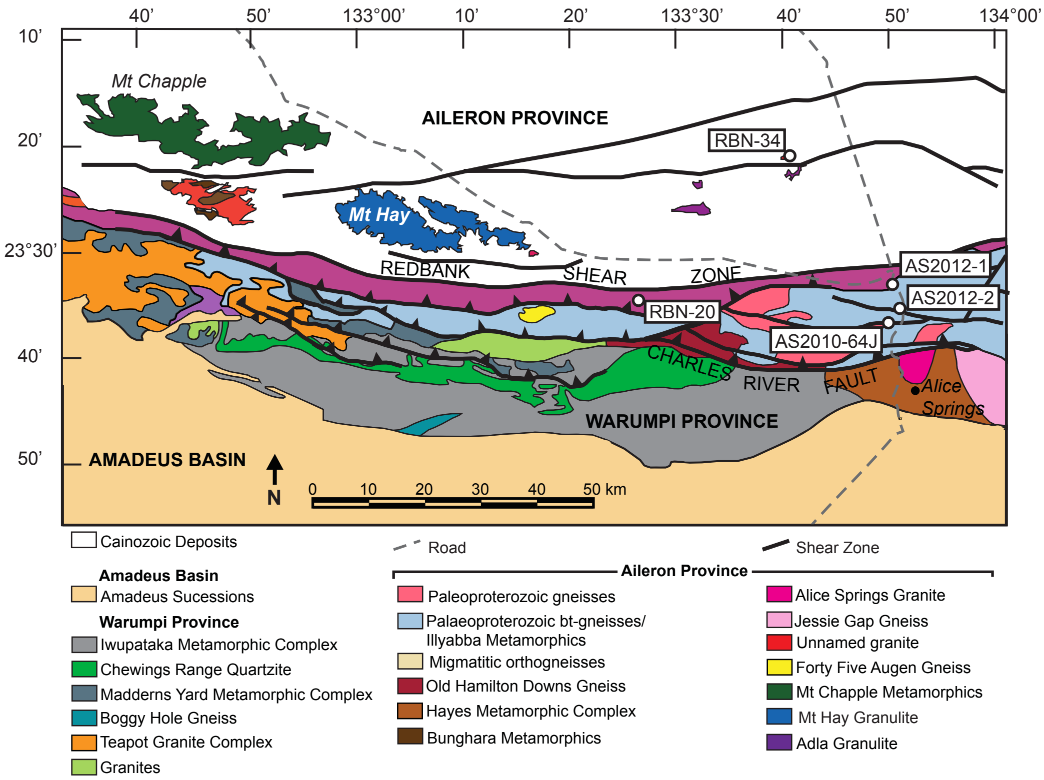

Fig. 2. Simplified geological map of the study area and locations of samples used in this study. Specific location of samples are provided in Table 1.

maximum measurement time of 3.75 min including an off-peak baseline measurement. A 35 µm spot size and repetition rate of 5 Hz was used, with ablation time of 120 s. Data was normalised to $^{179}Hf/^{177}Hf = 0.7325$, using exponential correction for mass bias.

Correction of isobaric interferences of ^{176}Lu and ^{176}Yb on ^{176}Hf are required for measurement of accurate $^{176}Hf/^{177}Hf$. Interference of ^{176}Lu on ^{176}Hf was corrected by measuring the intensity of the interference-free ^{172}Yb isotope using a $^{176}Lu/^{175}Lu$ value of 0.02655 (Vervoort et al., 2004) assuming the same mass bias behaviour as Yb. Yb interference on ^{176}Hf was corrected for using a Yb mass bias factor calculated from $^{171}Yb/^{173}Yb$ and Yb isotopic composition of Segal et al. (2003). Yb and Lu correction accuracy has been verified by repeated analysis of standard zircons with a range in $^{176}Yb/^{177}Hf$ and $^{176}Lu/^{177}Hf$ (Griffin et al., 2004).

The Mud Tank (Griffin et al., 2004) and Plesovice (Sláma et al., 2008) zircon standards were used as a measure of accuracy of the analytical technique. Mud Tank standard analyses obtained throughout this study have a corrected weighted average $^{176}Hf/^{177}Hf$ value of 0.282497 ± 0.0000044 (n = 9), and are within uncertainty of the long-term average of 0.282507 ± 6 (Woodhead et al., 2004). Plesovice standard analyses obtained during this study have weighted average $^{176}Hf/^{177}Hf$ value of 0.282463 ± 0.000007, which is comparable to the published value of 0.282482 ± 0.000013 (2 σ) by Sláma et al. (2008). εHf(T) and crustal model ages were calculated using ^{176}Lu decay constant after Scherer et al. (2001). εHf(T) represents the deviation of $^{176}Hf/^{177}Hf$ ratio from the $^{176}Hf/^{177}Hf$ ratio of CHUR (in parts per 10,000). Crustal model ages, otherwise known as two stage model ages (T_{DMc}) were calculated using the methods of Griffin et al. (2002) with an average crustal composition of $^{176}Lu/^{177}Hf = 0.015$.

Lu-Hf isotopic results

Hf isotopic results are presented in Table 2.

Sample AS2012-1 Migmatitic granitic gneiss

Twenty-one analyses were obtained on

zircons ~100 µm to >200 µm in size with aspect ratios of 1:1–1:3. Analyses were obtained from moderately luminescent, oscillatory and concentric zoned domains. The $^{176}Hf/^{177}Hf$ isotopic range varies from εHf -6.2 to -1.7 over the 1608–1662 Ma $^{207}Pb/^{206}Pb$ age range, and form a cluster that is slightly more evolved than CHUR (Chondritic Uniform Reservoir; Fig. 4). Hf crustal model ages (T_{DMc}) for this sample are mostly between 2500–2700 Ma. One zircon analysis yields a *c.*1762 Ma age, plotting slightly above CHUR (εHf 0.6, T_{DMc} = 2400 Ma).

Sample AS-2012-2 Migmatitic Orthogneiss

Eighteen analyses were obtained on zircon grains ~100–200 µm in size with aspect rations of 1:1 to 1:3, from moderately luminescent oscillatory and concentric zoned domains. The $^{176}Hf/^{177}Hf$ isotopic range varies from εHf -5.0 to 0.0 over the $^{207}Pb/^{206}Pb$ age spectrum of 1608–1662 Ma, and plots on and below CHUR. Hf crustal model ages (T_{DMc}) for the age population are between 2300–2600 Ma.

Sample RBN-34 Granitic gneiss

Eleven analyses were obtained from zircon grains ~100 µm in size, with aspect ratios of 1:1 to 1:2. Analyses were obtained from weakly to strongly luminescent domains, with oscillatory, concentric or no visible zoning. The $^{176}Hf/^{177}Hf$ isotopic range varies from εHf -0.9 to 1.5 over the $^{207}Pb/^{206}Pb$ age spectrum of 1623–1671 Ma, and forms a cluster around CHUR. Hf crustal model ages (T_{DMc}) for the age population are between 2200–2400 Ma.

Sample RBN-20 Folded migmatitic granitic gneiss

Twenty analyses were obtained from zircon grains ~100–300 µm in size, with aspect ratios of 1:1 to 1:3. Analyses were obtained on one strongly luminescent zircon core, moderately to weakly luminescent oscillatory and concentric zoned domains and one moderately luminescent unzoned domain. The $^{176}Hf/^{177}Hf$ isotopic range varies from εHf -4.7 to -1.9 over the $^{207}Pb/^{206}Pb$ age spectrum of 1556–1654 Ma, and forms a cluster below CHUR. Hf crustal model ages for the age population are between 2400–2500 Ma.

Sample AS-2010-64D Granitic augen gneiss

Twenty-three analyses were obtained from zircon grains 100–400 µm in size, with aspect ratios of 1:1 to 1:4. Analyses were obtained from moderately luminescent, oscillatory zoned domains. The $^{176}Hf/^{177}Hf$ isotopic range varies from εHf -5.1 to -0.7 over the $^{207}Pb/^{206}Pb$ age spectrum of 1625–1690 Ma, and plots near and below CHUR. Hf crustal model ages (T_{DMc}) for the age population are between 2400–2700 Ma.

Discussion

Interpretation of Hf isotopic data from late-Paleoproterozoic granitoids

Zircon Hf isotope data for the five magmatic protoliths of *c.* 1649–1626 Ma age have εHf values near and typically slightly more evolved than CHUR, with one older (*c.* 1762 Ma) inherited grain yielding a εHf value slightly more juvenile than CHUR (Fig. 4). All analysed zircons are interpreted to record the crystallisation ages of respective granitoids (Wong, 2011; Fields, 2012; Lawson-Wyatt, 2012) and have T_{DMc} ages in the range of 2200–2700 Ma. The results indicate that the igneous protoliths of the samples were derived from either: 1) melting of a Paleoproterozoic to Neoarchean crustal reservoir, or 2) via extensive mixing of juvenile crust and older sources. Existing magmatic and inherited zircon Hf isotopic data from igneous samples from the Aileron Province have crustal model ages between ~2100−3200 Ma (Fig. 5; Hollis et al., 2010; Beyer et al., 2013; Hollis et al., 2013). The Hf zircon crustal model ages of granitoid samples in this study are consistent with the range of existing crustal model ages obtained from the Aileron Province crust of the NAC. Given this similarity, and

Table 1. Sample descriptions and existing U–Pb age data

Sample	Easting, Zone, 53K	Southing, Zone 53K	Location	Unit	Rock type	LA-ICP-MS crystallisation Age-U-Pb age weighted average (Ma)	Source
AS2012-1	384435	7394616	Aileron Province	Unnamed Paleoproterozoic gneiss (Illyabba Metamorphics)	Migmatitic granitic gneiss	1633 ± 9 Ma (n = 33)	Fields (2012)
AS2012-2	385668	7389949	Aileron Province	Unnamed Paleoproterozoic gneiss (Illyabba Metamorphics)	Migmatitic orthogneiss	1628 ± 8 (n = 44)	Fields (2012)
RBN-20	342330	7391309	Aileron Province	Unnamed Paleoproterozoic gneiss (Illyabba Metamorphics)	Folded porphyroclastic granitic gneiss	1627 ± 7 (n = 43)	Fields (2012)
RBN-34	367471	7417565	Aileron Province	Unnamed lithology	Granitic gneiss	1641 ± 10 (n = 26)	Lawson-Wyatt (2012)
AS-2010-64J	385454	7389461	Aileron Province (Wigley Block)	Unnamed Paleoproterozoic biotite-bearing gneiss	Augen gneiss	1649 ± 6.8 (n = 32)	Wong (2011)

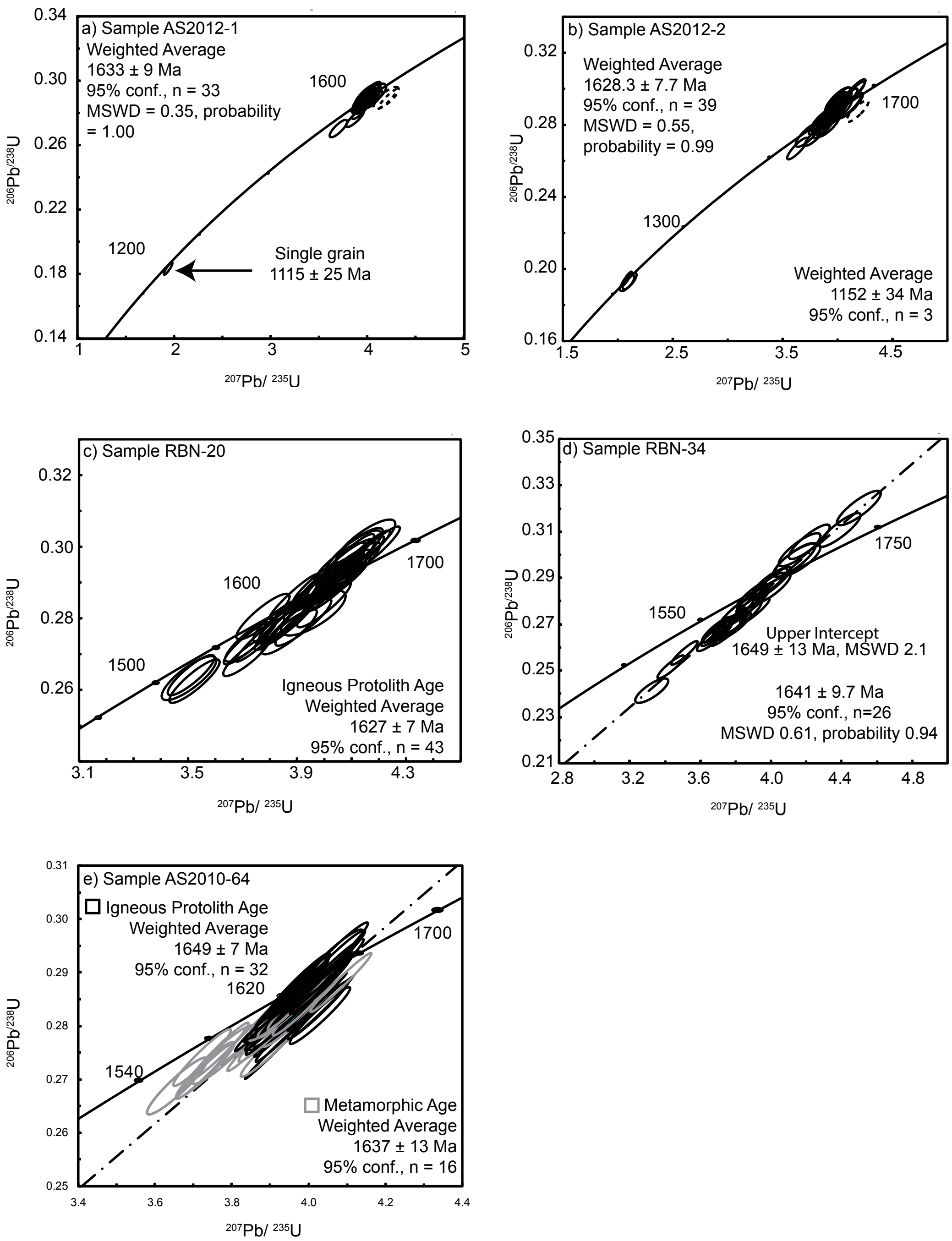

Fig. 3. Concordia plots of zircon U–Pb age data (from Wong, 2011; Fields, 2012; Lawson-Wyatt, 2012).

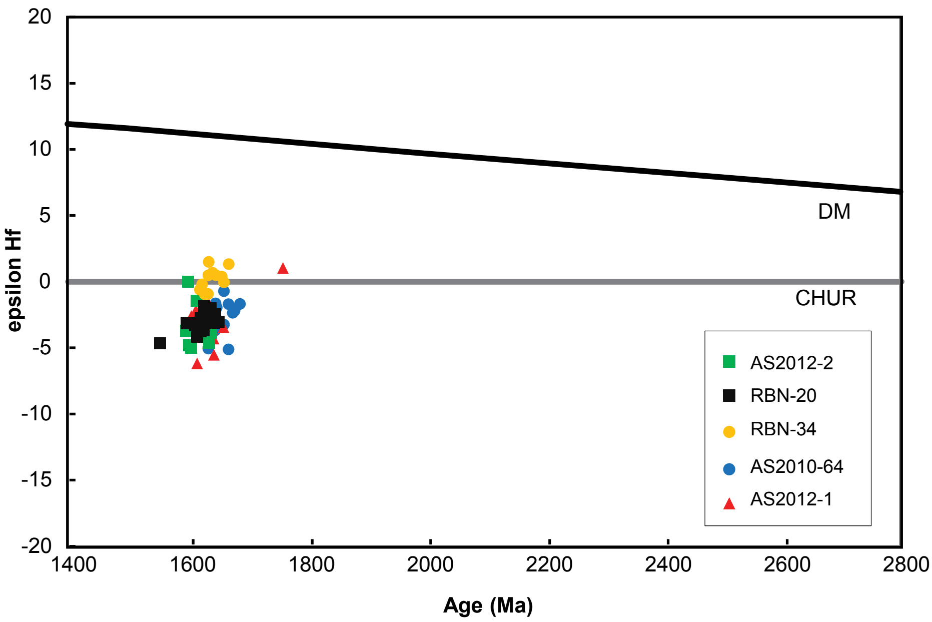

Fig. 4. εHf vs. age (Ma) plots for samples in this study.

the reconnaissance nature of this study, we interpret that the studied rocks are derived mostly from the melting of the pre-existing Aileron Province crust.

Evolution of the Paleoproterozoic to early Mesoproterozoic Aileron and Warumpi Province crust

The Paleo- to early Mesoproterozoic crustal evolution of the Aileron and Warumpi Provinces can be partly constrained by the magmatic rocks forming during this time. Zhao and McCulloch (1995) noted an overall increase in εNd trend with decreasing crystallisation ages of the granitoids, suggesting an increasing proportion of juvenile mantle addition to crust at the time. More recently, Hollis et al. (2013) used U−Pb and Lu−Hf igneous, detrital and inherited zircon isotopic signatures from the Warumpi and Aileron Provinces to suggest: 1) derivation of >1850 Ma and *c.* 1775 Ma magmatic zircon in the Aileron Province from early Archean to Paleoproterozoic sources, 2) that a component of Liebig Orogeny-aged (*c.* 1640−1635 Ma) volcanic and igneous rocks from the Warumpi Province were derived either from a homogenous crustal source or efficient source mixing, 3) a component of mantle derived sources as reflected by Hf vertical arrays for Argilke Event-aged (*c.* 1690−1675 Ma) magmatic and volcanic rocks from the Warumpi Province, and 4) that the Warumpi Province crust was derived in part from the mixing of older crustal sources of Archean age, similar to the crustal sources of the Aileron Province.

Zircon Hf data from the late Paleoproterozoic-aged magmatic samples of this study lie within the main isotopic range for the Aileron Province and less juvenile zircon analyses for the Warumpi Province (Fig. 5). Earlier work favoured the origin of the Warumpi Province as an exotic terrane to the Aileron Province (southern NAC), based on distinct protolith ages and the less evolved isotopic character of the Warumpi Province crust (Scrimgeour et al., 2005a; Scrimgeour et al., 2005b). However, based on isotopic work, Hollis et al. (2013) suggested that the Warumpi and Aileron Province were rifted apart and an oceanic basin developed between them at *c.* 1700 Ma. Following this phase of rifting, Hollis et al. (2013) proposed the closure of the rift basin and reattachment of the formerly contiguous Warumpi Province at *c.* 1640−1635 Ma via south-dipping subduction (Fig. 6a). Evidence for a south-dipping subduction system during the late-Paleoproterozoic is largely based on magnetotelluric imaging of a sub-vertical, crustal-scale structure between

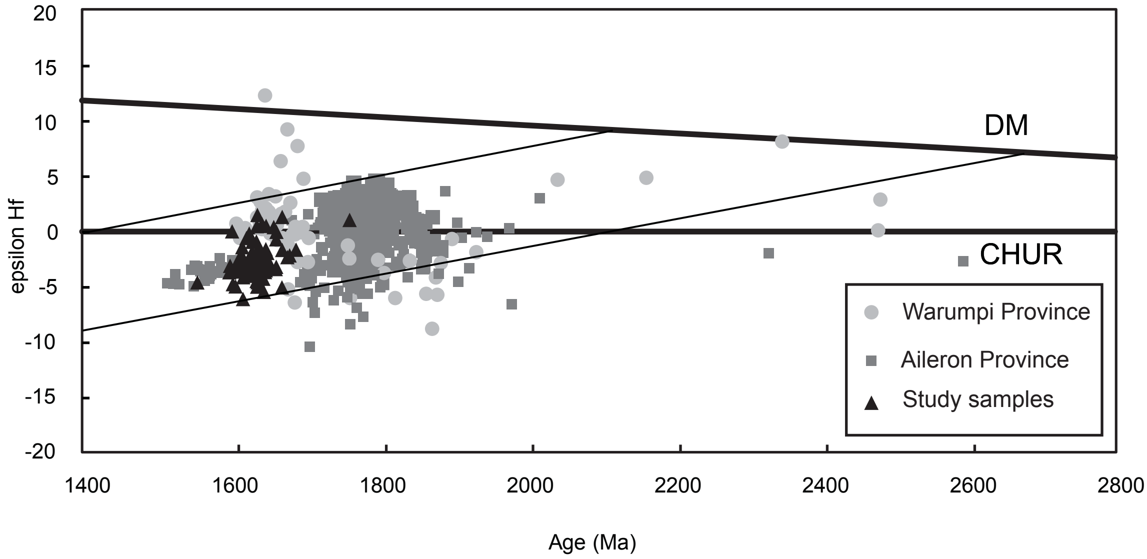

Fig. 5. εHf vs. age (Ma) for samples from this study and for the Arunta Region (data sources for the Arunta Region are: Hollis et al., 2010; Beyer et al., 2013; Hollis et al., 2013).

the Aileron and Warumpi Provinces that dips-southwards to modelled depths of ~150 km into the mantle (e.g. Selway et al., 2009), and the occurrence of late-Paleoproterozoic pre- and syn-tectonic magmatism mostly within the Warumpi Province rather than the Aileron Province (Scrimgeour et al., 2005b). The absolute timing of the modelled lithospheric scale structure between the Warumpi and Aileron Province is unknown. Recent work in the southern Arunta Region has demonstrated that the southern Aileron Province and Warumpi Province underwent Grenvillian-aged reworking between *c.* 1140 and 1100 Ma (e.g. Morrissey et al., 2011; Wong, 2011; Wong et al., submitted). This reworking occurs E−W along strike over at least ~100 km and proximal to the interface of the lithospheric scale, south-dipping, modelled structure (Selway et al., 2009). Taking the recent identification of this Grenvillian reworking into consideration, the possibility that the lithospheric scale structure transecting the crust in the southern Arunta Region (Selway et al., 2009) is Grenvillian-aged rather than late-Paleoproterozoic-aged should not be discounted.

The *c.* 1640−1635 Ma Liebig Orogeny was preceded by the deposition of sedimentary packages, magmatism and volcanism in the age bracket *c.* 1700−1640 Ma in the Warumpi Province (e.g. Scrimgeour et al., 2005a; Scrimgeour, 2013b). The Liebig Orogeny involved the generation of medium-*P*, high-*T* conditions, interpreted to be associated with the rapid burial and exhumation of sediments (Scrimgeour et al., 2005b; Scrimgeour, 2013b). Coeval occurrence of *c.* 1640−1635 Ma-aged mafic and ultramafic intrusions in the Warumpi Province and southern Aileron Province (Claoue-Long and Hoatson, 2005; Hoatson et al., 2005) implies that the Liebig Orogeny involved at least some component of extension, coeval with medium-*P* granulite facies conditions.

We support the general concept of rifting and re-accretion of the Warumpi to the Aileron Province. However, if the modelled lithospheric scale structure transecting the crust in the southern Arunta Region (Selway et al., 2009) is Grenvillian rather than Paleoproterozoic, it suggests the re-accretion of the Warumpi Province could have occurred in the Grenvillian rather than during the *c.* 1640–1635 Ma Liebig Orogeny. We tentatively present an alternate model for the southern Arunta Region during the *c.* 1640–1635 Ma ‘Liebig Orogeny’ in Fig. 6b, whereby the Warumpi and southern Aileron Provinces are placed in an extensional setting (back-arc) at *c.* 1640−1635 Ma, consistent with coeval mafic and ultramafic intrusions in the area (Claoue-Long and Hoatson, 2005). In this scenario, the island arc is not present in the outcropping part of the Warumpi Province. Feasibly at least some metasedimentary units of the Iwupataka Metamorphic Complex (Haasts Bluff Domain; Scrimgeour et al. 2005a) were deposited in the back-arc setting as part of a proposed long-lived (>150 M. y.), north-dipping subduction system along the southern NAC (e.g. Betts and Giles, 2006). Tucker et al. (submitted) and Maidment et al. (2013) recently argued that the development of medium-*P* assemblages is not necessarily indicative of compressional thickening of the crust, and can occur in extensional, rift-style settings. As such, it is possible that the Liebig-aged medium-*P* metamorphic conditions (Scrimgeour et al., 2005b) were generated in an overall extensional setting. Although more work is required to decipher the tectonic evolution of the southern Arunta during the late-Paleoproterozoic, and both the model of Hollis et al (2013) and the extensional setting proposed in Fig. 6 are consistent with magmatism occurring mostly in the Warumpi Province; we favour the latter extension dominated setting based on: 1) the proximal occurrence *c.* 1640−1635 Ma mafic and ultramafic intrusions (e.g. Claoue-Long and Hoatson, 2005); 2) the deposition of sedimentary packages in the age bracket of *c.* 1700−1600 Ma (e.g. Ahmad and Scrimgeour, 2013); and 3) a lack of identified compressional structures that can be confidently related to the medium-*P* assemblages. If this interpretation is correct, the Warumpi Province was likely to be separated from the NAC for *c.* 500 Ma, until it re-accreted during the Grenvillian.

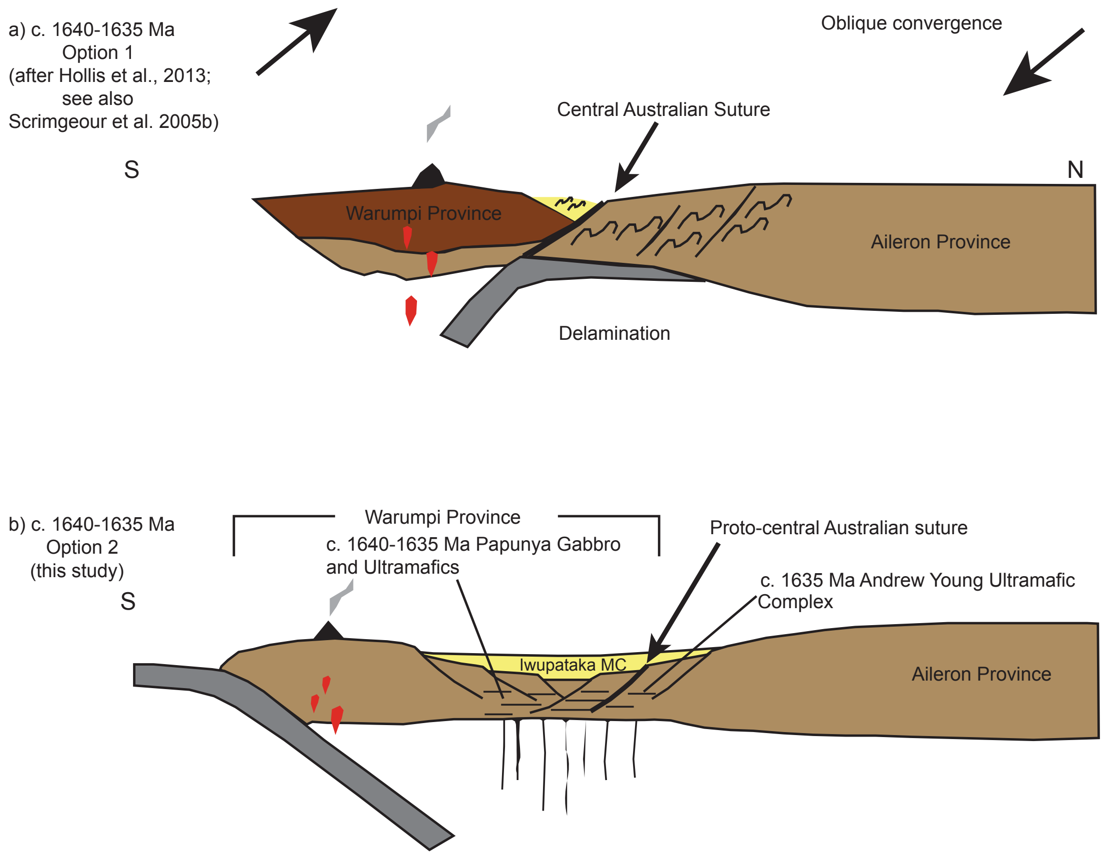

Fig. 6. Schematic diagram a) after Hollis et al. (2013) involving the reattachment of the Warumpi Province onto the Aileron Province following a phase of rifting, and b) an alternative tectonic scenario for the southern Arunta Region. In this alternate scenario, the Warumpi and southern Aileron Provinces are placed in a dominantly extensional regime, producing coeval mafic and ultramafic complexes as part of a long-lived (>150 Myr) southwards retreating margin on the southern NAC. In this postulated scenario, the Warumpi Province rifted from the NAC at or just after c. 1640–1635 Ma, and reattached to the NAC during the Mesoproterozoic.

Conclusions

The Hf isotopic signature of late-Paleoproterozoic granitoids in the southern Aileron Province suggests the granitoids were derived from the NAC. Recent zircon Hf isotopic studies in the Arunta Region, combined with the deposition of sedimentary packages and mafic-ultramafic intrusions in the Warumpi Province at a similar time to the Liebig Orogeny suggests that the Warumpi Province may have been originally contiguous with the NAC and underwent extension in the latest-Paleoproterozoic. If so, the *c.* 1640–1635 Ma Liebig Orogeny reflects an overall extensional/back-arc setting rather than compressional setting, with the reattachment of the Warumpi occurring during the Grenvillian, contemporaneous with major phases of tectonism in Australia.

References

Ahmad, M., Scrimgeour, I.R., 2013. Geological Framework, in: Ahmad, M., Munson, T.J. (Eds.), Geology and mineral resources of the Northern Territory, special publication 5. Northern Territory Geological Society.

Aitken, A.R.A., Betts, P.G., Young, D.A., Blankenship, D.D., Roberts, J.L., Siegert, M.J., in press. The Australo-Antarctic Columbia to Gondwana transition. Gondwana Research.

Anderson, J., Kelsey, D.E., Hand, M., Collins, W.J., 2013. Conductively driven, high-thermal gradient metamorphism in the Anmatjira Range, Arunta region, central Australia. Journal of Metamorphic Geology 31, 1003-1026.

Betts, P.G., Giles, D., 2006. The 1800-1100 Ma tectonic evolution of Australia. Precambrian Research 144, 92-125.

Betts, P.G., Giles, D., Aitken, A., 2011. Palaeoproterozoic accretion processes of Australia and comparisons with Laurentia. International Geology Review 53, 1357-1376.

Betts, P.G., Giles, D., Schaefer, B.F., 2008. Comparing 1800-1600 Ma accretionary and basin processes in Australia and Laurentia: Possible geographic connections in Columbia. Precambrian Research 166, 81-92.

Beyer, E., Hollis, J.A., Whelan, J., Glass, L.M., Donnellan, N., Yaxley, G., Armstrong, R., Allen, C.M., Schersten, A., 2013. Summary of results. NTGS laser ablation ICPMS and SHRIMP U-Pb, Hf and O geochronology project: Pine Creek Orogen, Arunta Region, Georgina Basin and McArthur Basin, July 2008–May 2011. Northern Territory Geological Survey, Darwin.

Bodorkos, S., Beyer, E.E., Edgoose, C.J., Whelan, J.A., Webb, G., Vandenberg, L.C., Hallet, L., 2013. Summary of results: Joint NTGS-GA geochronology project: Central and eastern Arunta Region, January 2008-June 2011, p. 74.

Cawood, P.A., Korsch, R.J., 2008. Assembling Australia: Proterozoic building of a continent. Precambrian Research 166, 1-38.

Claoue-Long, J., Edgoose, C., Worden, K., 2008a. A correlation of Aileron Province stratigraphy in central Australia. Precambrian Research 166, 230-245.

Claoue-Long, J., Maidment, D., Hussey, K., Huston, D., 2008b. The duration of the Strangways Event in central Australia: Evidence for prolonged deep crust processes. Precambrian Research 166, 246-262.

Claoue-Long, J.C., Hoatson, D.M., 2005. Proterozoic mafic-ultramafic intrusions in the Arunta Region, central Australia Part 2: Event chronology and regional correlations. Precambrian Research 142, 134-158.

Collins, W.J., Shaw, R.D., 1995. Geochronoogical constraints on orogenic events in the Arunta Inlier: a review. Precambrian Research 71, 315-346.

Collins, W.J., Williams, I.S., 1995. SHRIMP ionprobe dating of short-lived Proterozoic tectonic cycles in the northern Arunta Inlier, central Australia. Precambrian Research 71, 69-89.

Fields, C., 2012. Liebig-aged (c. 1640 Ma) magmatism and metamorphism in c. 1760 Ma crust in the Warumpi and southern Aileron Province, central Australia: a case for revising the tectonic framework of Proterozoic Australia, Geology and Geophysics. University of Adelaide, Adelaide, p. 70.

Griffin, W.L., Belousova, E.A., Shee, S.R., Pearson, N.J., O'Reilly, S.Y., 2004. Archaean crustal evolution in the northern Yilgarn craton, U-Pb and Hf-isotope evidence from detrital zircons. Precambrian Research 131, 231-282.

Griffin, W.L., Wang, X., Jackson, S.E., Pearson, N.J., O'Reilly, S.Y., Xu, X., Zhou, X., 2002. Zircon chemistry and magma mixing, SE China: In-situ analysis of Hf isotopes, Tonglu and Pingtan igneous complexes. Lithos 61, 237-269.

Hand, M., Buick, I.S., 2001. Tectonic evolution of the Reynolds-Anmatjira Ranges: a case study in terrain reworking from the Arunta Inlier, central Australia, in: Miller, J., Holdsworth, R.E., Buick, I.S., Hand, M. (Eds.), Continental Reactivation and Reworking, pp. 237-260.

Hoatson, D.M., Sun, S.S., Claoue-Long, J.C., 2005. Proterozoic mafic-ultramafic intrusions in the Arunta Region, central Australia Part 1: Geological setting and mineral potential. Precambrian Research 142, 93-133.

Hollis, J.A., Beyer, E.E., Whelan, J.A., Kemp, A.I.S., Scherstén, A., Greig, A., 2010. Summary of results. NTGS laser U-Pb and Hf geochronology project: Pine Creek Orogen, Murphy Inlier, McArthur Basin and Arunta Region, July 2007–June 2008. Northern Territory Geological Survey, Darwin.

Hollis, J.A., Kirkland, C.L., Spaggiari, C.V., Tyler, I.M., Haines, P.W., Wingate, M.T.D., Belousova, E., Murphy, R.C., 2013. Zircon U-Pb-Hf isotope evidence for links between the Warumpi and Aileron Provinces, West Arunta Region. Geological Survey of Western Australia, Perth.

Huston, D.L., Larson, R., E., G., 2006. Archive of results from the North Australia and Tanami National Geoscience Accord Projects. Geoscience Australia, Canberra.

Lawson-Wyatt, M., 2012. Regional Inkamulla-aged (ca. 1740–1755 Ma) tectonism along strike of the Mt Hay-Redbank Hill region, southern Aileron Province, central Australia, Geology and Geophysics. University of Adelaide.

Maidment, D.W., Hand, M., Williams, I.S., 2005. Tectonic cycles in the Strangways Metamorphic Complex, Arunta Inlier, central Australia: geochronological evidence for exhumation and basin formation between two high-grade metamorphic events. Australian Journal of Earth Sciences 52, 205-215.

Maidment, D.W., Hand, M., Williams, I.S., 2013. High grade metamorphism of sedimentary rocks during Palaeozoic rift basin formation in central Australia. Gondwana Research 24, 865-885.

McLaren, S., Sandiford, M., Dunlap, W.J., Scrimgeour, I., Close, D., Edgoose, C., 2009. Distribution of Palaeozoic reworking in the Western Arunta Region and northwestern Amadeus Basin from (40)Ar/(39)Ar thermochronology: implications for the evolution of intracratonic basins. Basin Research 21, 315-334.

Morrissey, L., Payne, J.L., Kelsey, D.E., Hand, M., 2011. Grenvillian-aged reworking in the North Australian Craton, central Australia: constraints from geochronology and modelled phase equilibria. Precambrian Research 191, 141-165.

Morrissey, L.J., Hand, M., Raimondo, T., Kelsey, D.E., 2014. Long-lived high-T, low-P granulite facies metamorphism in the Arunta Region, central Australia. Journal of Metamorphic

Geology 32, 25-47.
Neumann, N.L., Fraser, G.L., 2007. Geochronological synthesis and timespace plots for Proterozoic Australia. Geoscience Australia, Canberra, p. 216.
Payne, J.L., Barovich, K.M., Hand, M., 2006. Provenance of metasedimentary rocks in the northern Gawler Craton, Australia; implications for Palaeoproterozoic reconstructions. Precambrian Research 148, 275-291.
Payne, J.L., Hand, M., Barovich, K.M., Reid, A., Evans, D.A.D., 2009. Correlations and reconstruction models for the 2500-1500 Ma evolution of the Mawson Continent, in:
Reddy, S.M., Mazumder, R., Evans, D.A.D., and Collins, A.S. (Ed.), Palaeoproterozoic Supercontinents and Global Evolution, pp. 319-355.
Scherer, E., Münker, C., Mezger, K., 2001. Calibration of the lutetium-hafnium clock. Science 293, 683-687.
Scrimgeour, I., 2003. Developing a revised framework for the Arunta Region, Annual Geoscience Exploration Seminar (AGES) Record of Abstracts, Darwin.
Scrimgeour, I., 2013a. Ch. 12 Aileron Province, Geology and mineral resources of the Northern Territory. Northern Territory Geological Survey, Special Publications 5, pp. 1-75.
Scrimgeour, I., 2013b. Chapter 13: The Warumpi Province, in: Ahmad, M., Munson, T.J. (Eds.), Geology and mineral resources of the Northern Territory. Northern Territory Geological Survey, Darwin, p. 21.
Scrimgeour, I., Close, D., Edgoose, C., 2005a. Mount Liebig SF 52-16, 1:250 000 Geological Map Series Explanatory Notes. Northern Territory Geological Survey, Darwin, p. 71.
Scrimgeour, I.E., 2004. A revised province definition and Palaeoproterozoic framework for the Arunta Region, central Australia., Geological Society of Australia (Abstracts), p. 173.
Scrimgeour, I.R., Kinny, P.D., Close, D.F., Edgoose, C.J., 2005b. High-T granulites and polymetamorphism in the southern Arunta Region, central Australia: Evidence for a 1.64 Ga accretional event. Precambrian Research 142, 1-27.
Segal, I., Halicz, L., Platzner, I.T., 2003. Accurate isotope ratio measurements of ytterbium by multiple collection inductively coupled plasma mass spectrometry applying erbium and hafnium in an improved double external normalization procedure. Journal of Analytical Atomic Spectrometry 18, 1217-1223.
Selway, K., Hand, M., Heinson, G.S., Payne, J.L., 2009. Magnetotelluric constraints on subduction polarity: Reversing reconstruction models for Proterozoic Australia. Geology 37, 799-802.
Shaw, R.D., Zeitler, P.K., Mcdougall, I., Tingate, P.R., 1992. The Paleozoic history of an unusual intracratonic thrust belt in central australia based on ^{40}Ar-^{39}Ar, K-Ar and fission-track dating. Journal of the Geological Society 149, 937-954.
Sláma, J., Kosler, J., Condon, D.J., Crowley, J.L., Gerdes, A., Hanchar, J.M., Horstwood, M.S.A., Morris, G.A., Nasdala, L., Norberg, N., Schaltegger, U., Schoene, B., Tubrett, M.N., Whitehouse, M.J., 2008. Plesovice zircon -- A new natural reference material for U-Pb and Hf isotopic microanalysis. Chemical Geology 249, 1-35.
Tucker, N.M., Hand, M., Payne, J.L., submitted. A rift-related origin for regional medium-pressure, high-temperature metamorphism. Earth and Planetary Science Letters.
Vervoort, J.D., Patchett, P.J., Söderlund, U., Baker, M., 2004. Isotopic composition of Yb and the determination of Lu concentrations and Lu/Hf ratios by isotope dilution using MC-ICPMS. Geochemistry, Geophysics, Geosystems 5, Q11002.
Whelan, J., Webb, G., Close, D., Kositcin, N., Bodorkos, S., Maas, R., 2012. New copper-gold discoveries in the eastern Arunta Region: Implications for Cu-Au mineralisation in the Arunta, Annual Geoscience Exploration Seminar (AGES). Record of abstracts. Northern Territory Geological Survey, Alice Springs, pp. 38-42.
Wong, B., 2011. Grenvillian-aged reworking of late Paleoproterozoic crust in the southern Aileron Province, central Australia: Implications for the assembly of Mesoproterozoic Australia, Geology and Geophysics. University of Adelaide, Adelaide, p. 80.
Wong, B.L., Morrissey, L.J., Hand, M., Fields, C.E., Kelsey, D.E., submitted. Grenvillian-aged reworking of late Paleoproterozoic crust of the southern North Australian Craton, central Australia: implications for the assembly of Mesoproterozoic Australia. Precambrian Research.
Woodhead, J., Hergt, J., Shelley, M., Eggins, S., Kemp, R., 2004. Zircon Hf-isotope analysis with an excimer laser, depth profiling, ablation of complex geometries, and concomitant age estimation. Chemical Geology 209, 121-135.
Zhao, J.X., McCulloch, M.T., 1995. Geochemical and Nd isotopic systematics of granites from the Arunta-Inlier, central Australia - implications for Proterozoic crustal evolution. Precambrian Research 71, 265-299.

Table 2. Hf isotopic data for samples in this study.

Sample and analysis number	$^{207}Pb/^{206}Pb$ age (Ma)*	Concordancy %	Hf^{176}/Hf^{177} measured	2 σ uncertainty	Lu176/Hf177	Yb176/Hf177	Hf^{176}/Hf^{177} initital	εHf	1 σ uncertainty	*TDM* (Ga)	*TDMc* (Ga)
AS2012_1_01c	1626.2	100	0.281661	0.000032	0.000701	0.024695	0.281639	-3.9	1.1	2.2	2.6
AS2012_1_02_01c	1617.3	101	0.281676	0.000031	0.000621	0.022139	0.281657	-3.5	1.1	2.2	2.5
AS2012_1_05_02c	1662.3	98	0.281648	0.000031	0.000571	0.020529	0.281630	-3.4	1.1	2.2	2.6
AS2012_1_07_02c	1647.2	97	0.281673	0.000029	0.000528	0.018763	0.281657	-2.8	1.0	2.2	2.5
AS2012_1_09_02c	1762.4	92	0.281702	0.000033	0.000652	0.022631	0.281681	0.6	1.2	2.2	2.4
AS2012_1_11_01c	1654.2	95	0.281663	0.000024	0.000494	0.018190	0.281648	-3.0	0.8	2.2	2.5
AS2012_1_12_01c	1637.9	97	0.281717	0.000032	0.000748	0.021863	0.281694	-1.7	1.1	2.1	2.4
AS2012_1_14_01c	1645.5	98	0.281636	0.000045	0.000648	0.023679	0.281616	-4.3	1.6	2.2	2.6
AS2012_1_16_01c	1612	96	0.281704	0.000045	0.000596	0.017958	0.281686	-2.6	1.6	2.1	2.5
AS2012_1_17_02c	1646.3	100	0.281612	0.000058	0.000993	0.029855	0.281581	-5.5	2.0	2.3	2.7
AS2012_1_18_02c	1621.3	100	0.281669	0.000034	0.000607	0.022479	0.281651	-3.6	1.2	2.2	2.5
AS2012_1_20_01c	1635.3	95	0.281737	0.000053	0.001972	0.064561	0.281676	-2.4	1.8	2.2	2.5
AS2012_1_21_04r	1608.2	102	0.281674	0.000018	0.000543	0.020222	0.281658	-3.7	0.6	2.2	2.5
AS2012_1_21_03c	1637.9	101	0.281660	0.000029	0.000523	0.020031	0.281643	-3.5	1.0	2.2	2.5
AS2012_1_26_01c	1624.8	101	0.281656	0.000035	0.000691	0.026773	0.281635	-4.1	1.2	2.2	2.6
AS2012_1_27_01c	1608.3	102	0.281684	0.000034	0.000491	0.014945	0.281669	-3.3	1.2	2.2	2.5
AS2012_1_28_01c	1617.9	101	0.281596	0.000033	0.000506	0.018766	0.281581	-6.2	1.1	2.3	2.7
AS2012_1_29_01c	1643.6	99	0.281729	0.000037	0.001596	0.061920	0.281680	-2.1	1.3	2.2	2.5
AS2012_1_31_01c	1624.3	101	0.281708	0.000057	0.001195	0.035778	0.281672	-2.8	2.0	2.2	2.5
AS2012_1_32_01c	1636.5	103	0.281648	0.000052	0.001046	0.032471	0.281615	-4.5	1.8	2.3	2.6
AS2012_1_35_01c	1643.4	99	0.281651	0.000021	0.000451	0.017004	0.281637	-3.6	0.8	2.2	2.5
AS2012_1_37_01c	1621.9	102	0.281662	0.000017	0.000444	0.016692	0.281649	-3.7	0.6	2.2	2.5
AS2012_2z01c	1636.1	100	0.281646	0.000027	0.000522	0.018379	0.281630	-4.0	1.0	2.2	2.6
AS2012_2z04c	1626.6	101	0.281666	0.000033	0.000512	0.017285	0.281650	-3.5	1.2	2.2	2.5
AS2012_2z06c	1626.8	100	0.281658	0.000031	0.000594	0.021134	0.281640	-3.9	1.1	2.2	2.6
AS2012_2z10c	1599.6	100	0.281678	0.000031	0.000539	0.018714	0.281662	-3.7	1.1	2.2	2.5
AS2012_2z11c	1608.1	103	0.281634	0.000032	0.000480	0.017218	0.281620	-5.0	1.1	2.2	2.6
AS2012_2z14	1603.3	103	0.281787	0.000069	0.000748	0.021308	0.281764	0.0	2.4	2.0	2.3
AS2012_2z22_02c	1641.2	96	0.281652	0.000032	0.000667	0.024981	0.281631	-3.9	1.1	2.2	2.6
AS2012_2z24	1642	99	0.281651	0.000040	0.000494	0.017463	0.281635	-3.7	1.4	2.2	2.6
AS2012_2z29_02c	1632.9	98	0.281652	0.000032	0.000667	0.024981	0.281631	-4.0	1.1	2.2	2.6
AS2012_2z32_01c	1631.9	101	0.281674	0.000040	0.000463	0.017049	0.281660	-3.1	1.4	2.2	2.5
AS2012_2z37_01c	1624.9	101	0.281676	0.000040	0.000482	0.017558	0.281661	-3.2	1.4	2.2	2.5
AS2012_2z38_01c	1639.4	103	0.281658	0.000029	0.000475	0.017118	0.281643	-3.5	1.0	2.2	2.5
AS2012_2z39_01c	1637.8	100	0.281631	0.000042	0.000613	0.020180	0.281612	-4.6	1.5	2.2	2.6
AS2012_2z41_01c	1637.8	100	0.281630	0.000039	0.000364	0.012801	0.281619	-4.4	1.4	2.2	2.6
AS2012_2z46_01c	1616.9	101	0.281733	0.000055	0.000596	0.017186	0.281715	-1.4	1.9	2.1	2.4
AS2012_2z47_01c	1604.3	99	0.281658	0.000039	0.000987	0.031037	0.281628	-4.8	1.4	2.2	2.6
AS2012_2z48_01c	1632.5	99	0.281687	0.000047	0.000745	0.021441	0.281664	-2.9	1.6	2.2	2.5
AS2012_2z51_01c	1626.9	101	0.281670	0.000025	0.000809	0.029607	0.281645	-3.7	0.9	2.2	2.5
rbn-34-13	1671.2	104	0.281821	0.000061	0.001972	0.066988	0.281758	1.3	2.1	2.1	2.3
rbn-34-15	1622.7	105	0.281782	0.000062	0.001538	0.051017	0.281735	-0.6	2.2	2.1	2.4
rbn-34-16	1659.5	108	0.281819	0.000054	0.002543	0.067829	0.281739	0.4	1.9	2.1	2.3
rbn-34-19	1636.9	96	0.281834	0.000068	0.002496	0.080705	0.281756	0.5	2.4	2.1	2.3
rbn-34-21	1643.9	99	0.281794	0.000037	0.001190	0.041933	0.281757	0.7	1.3	2.1	2.3
rbn-34-24	1626.3	106	0.281831	0.000070	0.002826	0.103953	0.281744	-0.2	2.4	2.1	2.3
rbn-34-26	1637.5	103	0.281828	0.000042	0.001418	0.047675	0.281784	1.5	1.5	2.0	2.2

Sample and analysis number	$^{207}Pb/^{206}Pb$ age (Ma)*	Concordancy %	Hf^{176}/Hf^{177} measured	2 σ uncertainty	Lu176/Hf177	Yb176/Hf177	Hf^{176}/Hf^{177} initital	εHf	1 σ uncertainty	*TDM* (Ga)	*TDMc* (Ga)
rbn-34-28	1649.3	96	0.281784	0.000049	0.001115	0.038058	0.281749	0.5	1.7	2.1	2.3
rbn-34-29	1663.2	94	0.281774	0.000072	0.001559	0.059401	0.281725	0.0	2.5	2.1	2.3
rbn-34-30	1636.3	93	0.281758	0.000040	0.001341	0.046088	0.281717	-0.9	1.4	2.1	2.4
rbn-34-33	1630.8	96	0.281780	0.000058	0.001951	0.059918	0.281720	-0.9	2.0	2.1	2.4
rbn-20-01c	1640.7	106	0.281705	0.000026	0.000691	0.024894	0.281684	-2.0	0.9	2.2	2.4
rbn-20-02c	1628.8	99	0.281669	0.000019	0.000780	0.028930	0.281644	-3.7	0.7	2.2	2.5
rbn-20-03c	1625.1	106	0.281681	0.000022	0.000706	0.026382	0.281659	-3.2	0.8	2.2	2.5
rbn-20-04	1618.5	97	0.281649	0.000020	0.000404	0.015493	0.281637	-4.2	0.7	2.2	2.6
rbn-20-05-02c	1614.8	98	0.281681	0.000018	0.000560	0.021489	0.281664	-3.3	0.6	2.2	2.5
rbn-20-z10	1556.2	103	0.281676	0.000027	0.000454	0.018344	0.281663	-4.7	0.9	2.2	2.5
rbn-20-z11	1620	97	0.281684	0.000019	0.000583	0.022660	0.281666	-3.1	0.7	2.2	2.5
rbn-20-z12	1600.7	103	0.281688	0.000015	0.000353	0.012976	0.281677	-3.1	0.5	2.2	2.5
rbn-20-z16	1617.6	102	0.281672	0.000026	0.000540	0.021161	0.281656	-3.5	0.9	2.2	2.5
rbn-20-z17	1648.7	100	0.281681	0.000018	0.000506	0.019418	0.281665	-2.5	0.6	2.2	2.5
rbn-20-z18	1627.3	97	0.281681	0.000021	0.000578	0.021741	0.281663	-3.1	0.7	2.2	2.5
rbn-20-z19	1623.8	96	0.281665	0.000028	0.000628	0.024690	0.281646	-3.7	1.0	2.2	2.5
rbn-20-z20-c01	1639.7	100	0.281690	0.000020	0.000529	0.020368	0.281673	-2.4	0.7	2.2	2.5
rbn-20-z21	1646.8	100	0.281667	0.000020	0.000554	0.021445	0.281649	-3.1	0.7	2.2	2.5
rbn-20-z24	1654.2	105	0.281664	0.000021	0.000587	0.022619	0.281646	-3.0	0.8	2.2	2.5
rbn-20-z25_01c	1630.3	101	0.281709	0.000022	0.000483	0.018796	0.281694	-1.9	0.8	2.1	2.4
rbn-20-z27	1631.1	98	0.281674	0.000020	0.000528	0.020359	0.281657	-3.2	0.7	2.2	2.5
rbn-20-z29	1633.4	103	0.281678	0.000018	0.000604	0.022959	0.281660	-3.0	0.6	2.2	2.5
rbn-20-z30	1622.1	99	0.281673	0.000017	0.000613	0.023465	0.281654	-3.5	0.6	2.2	2.5
rbn-20-z31	1623.9	99	0.281694	0.000025	0.000663	0.022093	0.281673	-2.8	0.9	2.2	2.5
AS2010-64_z01	1670.8	97	0.281615	0.000052	0.001209	0.035796	0.281577	-5.1	1.8	2.3	2.7
AS2010-64_z02	1629	100	0.281699	0.000049	0.000626	0.019791	0.281680	-2.4	1.7	2.2	2.5
AS2010-64_z06-1	1629	99	0.281693	0.000048	0.000884	0.030334	0.281666	-2.9	1.7	2.2	2.5
AS2010-64_z06-2	1681	96	0.281673	0.000042	0.000653	0.019725	0.281653	-2.2	1.5	2.2	2.5
AS2010-64_z10	1678	93	0.281686	0.000030	0.001130	0.043346	0.281650	-2.4	1.1	2.2	2.5
AS2010-64_z13	1654	99	0.281676	0.000042	0.001024	0.033986	0.281644	-3.1	1.5	2.2	2.5
AS2010-64_z14	1637	101	0.281618	0.000035	0.000564	0.020679	0.281600	-5.1	1.2	2.3	2.6
AS2010-64_z17	1636	98	0.281690	0.000033	0.000811	0.029830	0.281665	-2.8	1.1	2.2	2.5
AS2010-64_z18	1641	101	0.281645	0.000025	0.000584	0.020900	0.281627	-4.0	0.9	2.2	2.6
AS2010-64_z21	1649	100	0.281652	0.000027	0.000557	0.019947	0.281635	-3.6	1.0	2.2	2.6
AS2010-64_z23	1652	98	0.281668	0.000040	0.000583	0.018899	0.281650	-2.9	1.4	2.2	2.5
AS2010-64_z24	1649	96	0.281709	0.000040	0.000651	0.020896	0.281689	-1.6	1.4	2.1	2.4
AS2010-64_z26	1690	95	0.281674	0.000022	0.000408	0.015225	0.281661	-1.7	0.8	2.2	2.5
AS2010-64_z27	1650	99	0.281668	0.000032	0.000913	0.030878	0.281639	-3.4	1.1	2.2	2.5
AS2010-64_z35	1625	100	0.281655	0.000033	0.000524	0.018108	0.281638	-4.0	1.2	2.2	2.6
AS2010-64_z37	1628	100	0.281694	0.000038	0.000669	0.024099	0.281674	-2.7	1.3	2.2	2.5
AS2010-64_z40	1671	95	0.281690	0.000028	0.000542	0.018924	0.281673	-1.7	1.0	2.2	2.5
AS2010-64_z41	1651	97	0.281693	0.000025	0.000470	0.016858	0.281679	-2.0	0.9	2.2	2.5
AS2010-64_z42	1631	98	0.281693	0.000030	0.000581	0.020904	0.281675	-2.6	1.0	2.2	2.5
AS2010-64_z44	1631	98	0.281697	0.000027	0.000637	0.022737	0.281678	-2.4	0.9	2.2	2.5
AS2010-64_z45	1663	96	0.281727	0.000050	0.000656	0.023750	0.281706	-0.7	1.7	2.1	2.4
AS2010-64_z46	1663	96	0.281662	0.000030	0.000861	0.030713	0.281635	-3.2	1.0	2.2	2.5
AS2010-64_z49	1648	97	0.281666	0.000055	0.001097	0.040274	0.281631	-3.7	1.9	2.2	2.6

* U-Pb data collected by Wong (2011), Lawson-Wyatt (2012) and Fields (2012)

Chapter 4

This chapter is in preparation to be submitted to Precambrian Research as:
Anderson, J. R., Kelsey, D. E., Hand, M., and Collins, W.J. Mesoproterozoic metamorphism in the Rudall Province: revising the timeline of the Yapungku Orogeny and implications for cratonic Australia assembly.

Mesoproterozoic metamorphism in the Rudall Province: revising the timeline of the Yapungku Orogeny and implications for cratonic Australia assembly

ABSTRACT

LA−ICP−MS U−Pb zircon and monazite geochronology from metasedimentary rocks from the Connaughton and Talbot Terranes in the western Rudall Province, North Australia provides evidence for two metamorphic events at *c.* 1665 Ma and between *c.* 1380−1275 Ma. $P-T$ (*pressure−temperature*) pseudosection modelling of a staurolite–biotite bearing assemblage from the Talbot Terrane suggests peak $P-T$ conditions of ~5.5−8.5 kbar, ~600−650 °C were attained at *c.* 1285 Ma. $P-T$ modelling of on garnet−clinopyroxene-bearing mafic amphibolite from the Rudall Province shows that peak metamorphic conditions of ~8–11 kbar, and minimum ~620–650 °C were attained at *c.* 1380 Ma and followed a clockwise retrograde evolution. The geochronology and $P-T$ modelling suggest that the age of regional metamorphism (M_2, Yapungku Orogeny) is Mesoproterozoic rather than *c.* 1800−1765 Ma. If regional metamorphism in the Rudall Province does reflect the collision of the North and West Australian Cratons, it occurred during the Mesoproterozoic and not the Paleoproterozoic as has previously long been assumed. Metamorphic age data and physical conditions of metamorphism from the Rudall Province may reflect a stage-wise tectonic evolution, involving the accretion of ribbons, and outboard migration of subduction and the back-arc over time, producing both medium-*P*, and high-thermal gradient conditions. In this proposed scenario, the system was closed during the final amalgamation of the North Australian Craton to the accreted ribbons (West Australian Craton) during the Mesoproterozoic.

1. Introduction

The Rudall Province occurs at the north-eastern margin of the West Australian Craton (WAC) and has long been recognised as occupying a critical location for understanding the Australian continent assembly (e.g. Clarke, 1991; Smithies and Bagas, 1997; Bagas, 2004; Betts et al., 2006; Cawood and Korsch, 2008; Payne et al., 2009). The Rudall Province is one of the few localities in Australia where Proterozoic-aged medium to high pressure metamorphic assemblages are preserved (minimum apparent thermal gradients of ~60–80 °C). Evidence for regional, moderate-thermal gradient conditions (corresponding to eclogite-high pressure granulite thermal gradients of Brown, 2007), combined with evidence for thrust stacking and magmatism has led to the proposal that the Rudall Province records crustal thickening associated with the collision of the WAC and North Australian Craton (NAC) at *c.* 1830−1765 Ma (e.g. Bagas, 2004; Cawood and Korsch, 2008).

Despite its apparent importance in the assembly of Proterozoic Australia, the Rudall Province is an understudied region, and as a consequence, the tectonic evolution of the Rudall Province and its implications for the assembly of Proterozoic Australia is still notional rather than demonstrated (e.g. Maidment, 2007, 2014). The Rudall Province is considered to have a protracted tectonic history spanning at least *c.* 1300 M. y. from the Paleoproterozoic to the late Neoproterozoic–Cambrian (e.g. Bagas et al., 2000; Bagas, 2004; Kirkland et al., 2013). U–Pb zircon geochronology from voluminous felsic magmatic rocks of the Kalkan Supersuite comprises the largest dataset for constraining the absolute timing of tectonism in the Rudall Province (Nelson, 1995, 1996; Kirkland et al., 2013). However, the Kalkan Supersuite, and consequently the majority of the geochronological dataset, is restricted to the time interval *c.* 1800–1765 Ma, which comprises only the oldest part of the history (Nelson, 1995, 1996; Kirkland et al., 2013). At present, absolute time-related interpretations for metasedimentary rocks of the Rudall Province are largely based on extrapolation of magmatic rock geochronology to fit structural and metamorphic constraints. Metasediments comprise approximately 10−60 % of the terranes within the outcropping Rudall Province (Bagas et al., 2000) and therefore present an effectively untapped opportunity to understand the fuller tectonic—including metamorphic and temporal—history.

In this contribution we present an integrated metamorphic and U−Pb monazite and zircon geochronology study on metamorphic rocks of the Talbot and Connaughton Terranes of the Rudall Province. The aim of this study is to more completely understand the metamorphic evolution of the Yapungku Orogeny (M_2) and its implications for the timing of assembly of the WAC and NAC.

2. Geological Background

The Paleo- to Mesoproterozoic Rudall Province is located within the approximately 2000 km long, north-west trending, late Neoproterozoic to Cambrian-aged Paterson Orogen, which is exposed along the eastern margin of the Pilbara Craton in north-western Australia. The Paterson Orogen continues into the Musgrave Province in central Australia (Fig. 1) where it is known as the Petermann Orogen (e.g. Bagas and Smithies, 1998; Camacho and McDougall, 2000; Wade et al., 2005; Raimondo et al., 2009, 2010; Walsh et al., 2013).

The Rudall Province contains Paleoproterozoic–Mesoproterozoic metaigneous rocks and metasedimentary rocks with Paleoproterozoic protolith depositional ages (Nelson, 1995, 1996; Smithies and Bagas, 1997; Bagas and Smithies, 1998; Bagas, 2004; Kirkland et al., 2013). The Rudall Province has experienced a number of phases of tectonism, which have been assigned to the following events: a) the Yapungku Orogeny (D_1−D_2) spanning *c.* 1800−1765 Ma and corresponding to the emplacement of voluminous felsic magmatic rocks of the Kalkan Supersuite; b) the Miles Orogeny (D_3−D_4) at *c.* 650 Ma; c) the Blake Movement (D_5), a poorly constrained Neoproterozoic

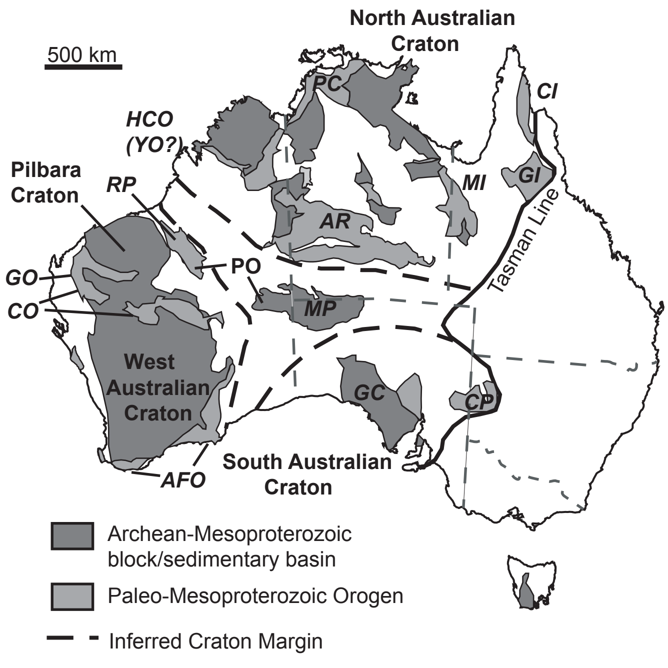

Fig. 1. Simplified map of Australia showing Archean-Mesoproterozoic geological components. AFO = Albany Fraser Orogen, AR = Arunta Region, CI = Coen Inlier, CO = Capricorn Orogen, CP = Curnamona Province, GC = Gawler Craton, GO = Gascoyne Orogen, HCO = Halls Creek Orogen, MI = Mount Isa Inlier, MP = Musgrave Province, PC = Pine Creek Orogen, PO = Paterson Orogen, RP = Rudall Province, YO = Yampi Orogen. Modified after Cawood and Korsch (2008) and Walsh et al. (2013).

deformation; and d) the Paterson Orogeny (D6; c. ≥550 Ma; Smithies and Bagas, 1997; Bagas and Smithies, 1998; Bagas et al., 2000; Bagas, 2004; Czarnota et al., 2009; Kirkland et al., 2013). Earlier work ascribed D_2 and M_2 to a *c.* 1300 Ma event based on Rb–Sr ages obtained from felsic magmatic rocks (Chin and de Laeter, 1981; Clarke, 1991). This timeline is broadly contemporaneous with the crystallisation of interpreted post- D_2 intrusive rocks and minor evidence for metamorphic zircon growth between *c.* 1310 and 1220 Ma (Nelson, 1995, 1996; Bagas, 2004; Kirkland et al., 2013). However, subsequent studies have favoured a Paleoproterozoic *c.* 1800−1760 Ma age for D_2 and M_2 based on zircon U−Pb data for magmatic crystallisation ages from the Kalkan Supersuite that were interpreted to be syn-deformational with regional medium to high-*P* metamorphism (Nelson, 1995, 1996; Smithies and Bagas, 1997; Bagas, 2004). This event has been interpreted to record the amalgamation of the NAC with the WAC (e.g. Li, 2000; Bagas, 2004) and has been adopted by virtually all recent paleo-tectonic reconstructions of Proterozoic Australia (e.g. Betts et al., 2002; Betts and Giles, 2006; Cawood and Korsch, 2008; Payne et al., 2009; Huston et al., 2012; Johnson, 2013). As a result, the regional significance of *c*. 1300 Ma ages has diminished somewhat.

Unconformably overlying the Rudall Province are deformed but poorly age-constrained late Mesoproterozoic to early Neoproterozoic sedimentary rocks of the Yeneena Supergroup, which are overlain by Phanerozoic cover sequences (Bagas and Smithies, 1998; Williams and Bagas, 1999; Bagas, 2004). Rocks of the Rudall Province have variably undergone retrogression to greenschist facies (Bagas and Smithies, 1998), which may be related to the Miles (D_4) and/or *c*. 550 Ma Paterson (D_6) orogenies.

Three terranes have been distinguished in the Rudall Province. To the southwest, the Talbot and Connaughton Terranes record similar poly-deformation histories but are distinguished on lithological differences, with the exception of the voluminous orthogneisses that occur in both terranes (Fig. 2). The Talbot and Connaughton Terranes are separated by an east-dipping thrust, interpreted to have formed during or before the Yapungku Orogeny and are commonly interpreted to have undergone similar tectonic histories thereafter (D_1 or D_2; Smithies and Bagas, 1997; Bagas, 2004). A kyanite−sillimanite isograd in the Connaughton and Talbot Terranes is interpreted to have formed during M_2 (Smithies and Bagas, 1997). To the north-east, the poorly outcropping Tabletop Terrane contains early Mesoproterozoic granitoids and is separated from the Talbot and Connaughton Terranes by the Camel–Tabletop Fault Zone (Smithies and Bagas, 1997). The relationship between the Tabletop Terrane and the Talbot and Connaughton Terranes is uncertain. The geology of the Connaughton, Talbot and Tabletop Terranes are described below, and existing constraints on the tectonic evolution of the Rudall Province are summarised in Table 1.

2.1 Talbot Terrane

The Talbot Terrane is composed of sedimentary derived and granitoid rocks that have been multiply deformed and metamorphosed to amphibolite facies (Smithies and Bagas, 1997; Bagas and Smithies, 1998; Bagas, 2004). Clarke (1991) divided the metasedimentary rocks of the Talbot Terrane into: 1) an older Yandagooge Formation, which appears to record a poorly preserved, high-thermal gradient M_1–D_1 event; and 2) the younger Tjingkulatjatjarra Formation, inferred to post-date D_1–M_1 and the majority of the emplacement of orthogneisses. Both formations and many of the orthogneisses of the Kalkan Supersuite are considered to record the M_2–D_2 Yapungku Orogeny, associated with crustal thickening (Watarra Orogeny of Clarke, 1991). There are no direct age data on the timing of D_1–M_1; however, two orthogneiss samples reported to contain S_1 and S_2 fabrics yield zircon U–Pb magmatic crystallisation ages of *c.* 2015 Ma (Sample 104932; Nelson, 1995; Hickman and Bagas, 1998) and *c.* 1801 Ma (Sample 112310; Nelson, 1995; Kirkland et al., 2013). A major phase of felsic magmatism occurred at *c.* 1800–1765 Ma, based on U–Pb zircon age data from orthogneisses assigned to the Kalkan Supersuite. These granitoids are

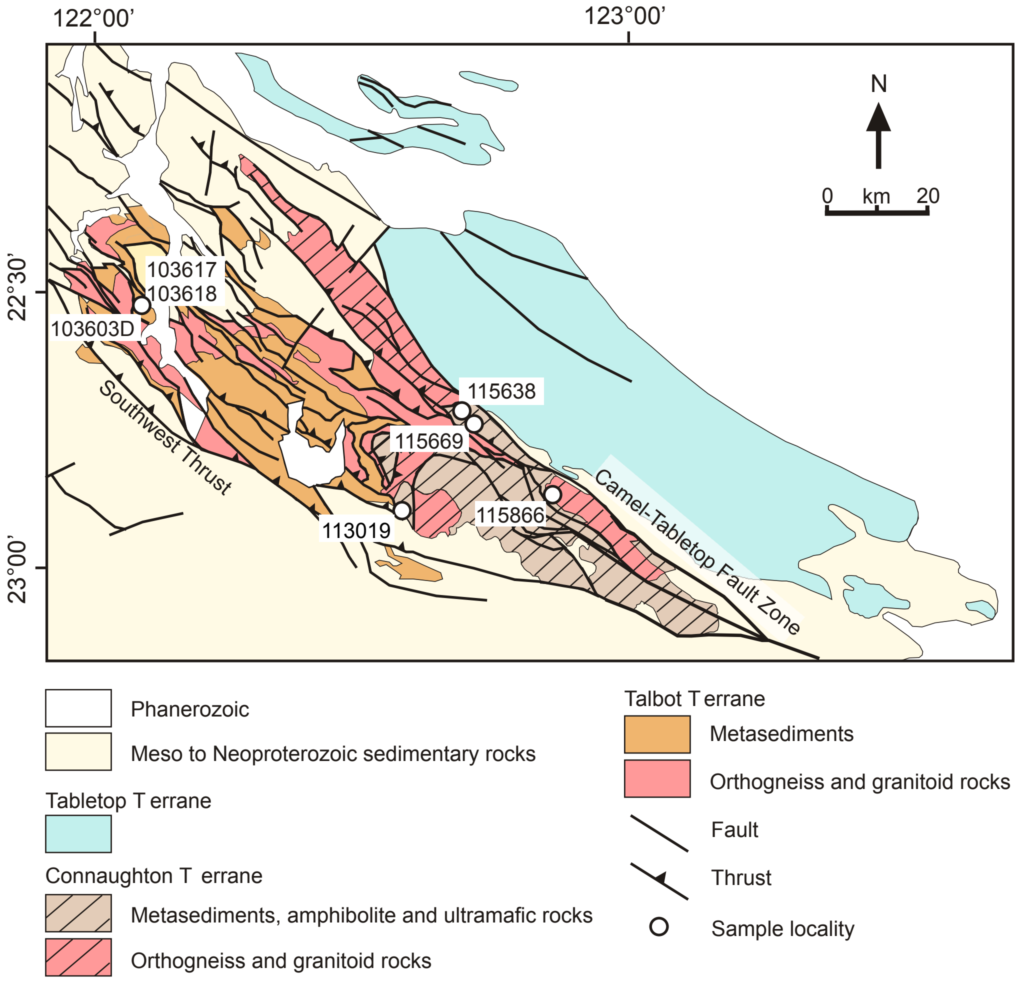

Fig. 2. Map of the Rudall Province, showing lithological associations, major structures and sample locations. Modified from Geological Survey of Western Australia (1999).

interpreted to be coeval with M_2–D_2 and have been variably deformed during D_2 (cf. Nelson, 1995; Bagas, 2004; Kirkland et al., 2013). The younger age limit on the timing of D_2–M_2 is interpreted to be *c.* 1765 Ma, based on U–Pb zircon age data from an aplite dyke considered to cross-cut the S_2 foliation (Nelson, 1995; Bagas, 2004). Evidence for a major phase of Mesoproterozoic tectonism in the Talbot Terrane is limited, though a monzogranite that cuts D_2 fabrics yields a U–Pb zircon age of *c.* 1476 Ma (Nelson, 1996; Bagas, 2004). Qualitative $P-T$ conditions for the M_2 event were previously estimated to have reached approximately ≥5 kbar and 600 °C, based on the presence of kyanite–staurolite and garnet–staurolite bearing assemblages (Clarke, 1991). However, these metamorphic mineral assemblages, and therefore $P–T$ conditions, have not been temporally quantified to have grown during D_2–M_2.

2.2 Connaughton Terrane

The Connaughton Terrane contains multiply deformed banded iron-formation, metasediments, metachert, orthogneiss and metagranitoids and voluminous deformed mafic rocks that have been metamorphosed at amphibolite to granulite facies conditions (Bagas and Smithies, 1998; Bagas et al., 2000). Available zircon U−Pb geochronology of two samples of the voluminous orthogneisses and metagranitoids of the Kalkan Supersuite yield U−Pb zircon magmatic crystallisation ages of *c.* 1780−1770 Ma and are interpreted to be coeval with D_2, similar to the Talbot Terrane (Nelson, 1995, 1996; Bagas, 2004). A garnet-bearing microgneiss and pegmatite, both interpreted to post-date D_2 yield U−Pb zircon magmatic crystallisation ages of *c.* 1222 and *c.* 1291 Ma respectively (Nelson, 1995, 1996). Recently, Kirkland et al (2013) reinterpreted a *c.* 1200 Ma U–Pb zircon analysis from the

Table 1. Geological history of the Rudall Province

Events	Talbot Terrane	Connaughton Terrane	Tabletop Terrane	Constraining data	Reference
<*c.* 2800 Ma			Sedimentation: Maximum depositional age for quartzite	U-Pb zircon geochronology	Maidment, (2007)
>1800 Ma	Sedimentation of older turbiditic succession	Sedimentation		Minimum age defined by pre D1 intrusives	Hickman and Bagas, (1998); Bagas, (2004)
c. 2015* Ma, 1800 Ma	Pre D1 granitoids	?		Crystallisation ages of banded orthogneiss interpreted to contain early foliations.	Nelson, (1995); Hickman and Bagas, (1998); Kirkland et al. (2013)
***c.* 1800 Ma Yapungku Orogeny (D1-M1)**	D1: Layer parallel shear, layer parallel schistosity	D1: Poorly preserved but inferred S1 inclusion trails in some garnet grains in amphibolite	?	Age inferred based on pre and post D1 intrusives of *c.* 1800 Ma, no direct age constraints	Nelson, (1995); Bagas, (2004); see Kirkland et al. (2013) for reinterpretation of U-Pb data
	M1: Amphibolite facies metamorphism, andalusite bearing assemblages (high apparent thermal gradients)	M1: Poorly preserved but inferred assemblage of garnet, epidote, hornblende, apatite in mafic amphibolite			
c. 1790 Ma	Sedimentation (deposition of Fingoon Quartzite)			Maximum depositional age of protolith to Fingoon Quartzite	Nelson, (1995)
***c.* 1800-1760 Ma Yapungku Orogeny (D2-M2)^**	D2: N-NW trending isoclinal folds, E to NE dipping thrusts with younger thrusts to the E-NE, W to SW movement, S2 commonly defined by alignment of micas and quartz	D2: N-NW trending isoclinal folds, E to NE dipping thrusts with younger thrusts to the E- NE, W to SW movement	?	Age constrained by crystallisation ages of interpreted pre, syn and post granitoids	Bagas (2004); Bagas et al, (2000)
	M2: amphibolite facies metamorphism, ~ > 5 kbar, 600 ° C	M2: amphibolite-granulite facies, peak conditions ~12 kbar, up to ~800 °C, followed by steep decompression		thermobarometry on amphibolite and biotite-garnet gneiss samples	Clarke (1991); Smithies and Bagas (1997)
c. 1800-1765 Ma	Emplacement of the Kalkan Supersuite	Emplacement of the Kalkan Supersuite			Kirkland et al. (2013); Nelson, (1995; 1996)
post- D2		Inferred metamorphism of orthopyroxene-garnet gneiss ('charnockite'), ~2.4−3.7 kbar, 770−860 °C		thermobarometry	Smithies and Bagas (1997)
c. 1590-1550 Ma			Calc-alkaline magmatism of the Krackatinny Supersuite	U-Pb zircon geochronology	Maidment (2007), Maidment (2014)
c. 1475-1450 Ma	Crystallisation of monzogranite (post-D2 pre D4)		Crystallisation of granodiorite (post D2- pre D4)	U-Pb zircon geochronology	Nelson (1996); Bagas (2004)
c. 1330 Ma	Isochron age from orthogneiss (interpreted as metamorphic)			Rb-Sr	Chin and de Laeter (1981)
c. 1310-1222 Ma		Crystallisation of post D2 garnet microgneiss, reinterpreted as metamorphic age (one analysis)	Crystallisation of interpreted post D2 intrusives, pegmatite	U-Pb zircon	Bagas (2004); Nelson (1995; 1996); Kirkland et al (2013)
***c.* 650 Ma Miles Orogney (D3-4, M3-4)**	D3: local recumbent folding, D4: upright, tight folding, SW directed compression, S4 axial surface cleavage	D4: upright, tight folding, SW directed compression, S4 axial surface cleavage	D4: upright, tight folding, SW directed compression, S4 axial surface cleavage, formation of the Camel-Tabletop Shear Zone	Minimum age constrained by post-D4 intrusive crystallisation age	Czarnota et al (2009) and references therin
	M3-4: greenschist facies metamorphism	M3-4: greenschist facies metamorphism			
***c.* 800-610 Ma Blake Movement (D5)**	Local deformation, NW- directed compression, open folds	Local deformation	Local deformation		Bagas, (2004); Bagas et al. (2000)
***c.* 550 Ma Paterson Orogeny (D6)**	D6: Brittle deformation, NNE- directed compression, WNW-NW striking strike slip and thrust faults	D6: Brittle deformation, NNE- directed compression, WNW-NW striking strike slip and thrust faults	D6: Brittle deformation, NNE-directed compression, WNW-NW striking strike slip and thrust faults	Maximum age constrained by deposition of the *c.* 610 Ma glaciogenic Boondawari Formation, correlated with the Petermann Orogeny	Bagas (2004) and references therein; Bagas et al. (2000)

* May be inherited ^ Disputed in this study ? Unknown

garnet-bearing microgneiss as metamorphic based on Cathodoluminescence zircon imagery.

Quantitative $P-T$ estimates for metamorphic mineral assemblages in the Connaughton Terrane are based on conventional thermobarometry for garnet–clinopyroxene, orthopyroxene–clinopyoxene, garnet–biotite and orthopyroxene–garnet bearing assemblages (Smithies and Bagas, 1997). The $P–T$ conditions have been attributed to M_2 (i.e. *c*. 1800–1765 Ma). Estimated peak $P-T$ conditions of up to ~12 kbar and ~770 °C were obtained from mafic amphibolite from the 'kyanite zone', and ~800 °C at 7 kbar were obtained from orthopyroxene-clinopyroxene bearing amphibolite from the 'sillimanite zone' (Smithies and Bagas, 1997). The $P-T$ evolution of the Connaughton as well as Talbot Terrane was inferred by Smithies and Bagas (1997) to have followed a steeply decompressive clockwise path, based on the presence of symplectic plagioclase-hornblende coronas on garnet in some mafic amphibolites. $P-T$ estimates corresponding to very high thermal gradient conditions (~2.4−3.7 kbar, ~770−860 °C; thermal gradient of approximately 210–360 °C $kbar^{-1}$) were obtained from an orthopyroxene–garnet gneiss that is interpreted to record post M_2–D_2 conditions driven by magmatism (Smithies and Bagas, 1997).

2.3 Tabletop Terrane

The Tabletop Terrane is separated from the Talbot and Connaughton Terranes by the southeast trending Camel–Tabletop Fault that postdates the Kalkan Supersuite. Outcropping areas of the Tabletop Terrane are comprised of volumetrically extensive felsic and mafic intrusives that have been metamorphosed to greenschist facies, dolerite dykes, ultramafic schists and low-volume supracrustal rocks (Bagas and Smithies, 1998). The Krackatinny Supersuite exhibits calc-alkaline geochemical signatures and were largely emplaced at *c.* 1590−1550 Ma (Maidment, 2007; Neumann and Fraser, 2007). Other felsic intrusives record U−Pb zircon magmatic crystallisation ages of *c.* 1476 Ma and 1310 Ma (Nelson, 1996; Bagas, 2004). No metamorphic work has been undertaken on rocks from the Tabletop Terrane.

2.4 Constraints on tectonic boundaries in the Rudall Province

Earlier work on the Rudall Complex assigned rocks in the Talbot Terrane to belong to an eastern and western supracrustal suite based on distinct lithologies and magmatic ages (Bagas, 2004). Bagas (2004) suggested that the eastern and western supracrustal suites of the Rudall Province preserved early magmatic and metamorphic histories that were similar to the Paleoproterozoic Arunta Region (eastern supracrustal) and Gascoyne Complex (western supracrustal), and suggested that the boundary between these supracrustal suites may represent a terrane boundary between the NAC and WAC. Whereas there is an apparent absence of the Kalkan Supersuite in the Tabletop Terrane, the Camel-Tabletop Fault is not interpreted as a major crustal boundary given the common crustal source region of the Kalkan Supersuite and Tabletop granitic rocks (Kirkland et al., 2013). Kirkland et al. (2013) presented Hf isotopic data for interpreted magmatic and inherited zircon from previously dated (U–Pb zircon), variably deformed granitoids of the Kalkan Supersuite and intrusive rocks with younger crystallisation ages or age components between 1450 and 1200 Ma from the Connaughton, Talbot and Tabletop Terrane (Kirkland et al., 2013). The isotopic dataset of Kirkland et al. (2013) indicates the rocks of the Rudall Province were sourced from crust similar to that of the WAC. As such, the location of the suture between the WAC and NAC is likely to be to the east of the Rudall Province.

3. Sample descriptions

The aim of this study is to directly determine the timing of the peak regional metamorphism by dating minerals that grew during the metamorphic development, as opposed to previous studies that sought to constrain the timing of deformational/ metamorphic events via dating of magmatic rocks with inferred emplacement relationships to deformation.

Samples for this study come from the Connaughton and Talbot Terranes and were obtained from the Geological Survey of Western Australia legacy collections. U–Pb zircon geochronology was conducted on an unmigmatised garnet-diopside bearing amphibolite. Additionally, zircon and garnet trace element chemistry was collected to assist in linking metamorphic silicate phases to zircon growth. U−Pb monazite geochronology was conducted on three metapelitic samples from the Talbot Terrane (within the Tjingkulatjatjarra Formation of Clarke, 1991) and three metasedimentary samples from the Connaughton Terrane. *P–T* pseudosections were calculated for one of the dated metapelitic samples from the Talbot Terrane and a garnet–diopside bearing amphibolite from the Connaughton Terrane.

3.1 Sample 103603D: Kyanite-bearing metapelite (Talbot Terrane)

Bladed kyanite (up to 5 mm) forms aggregates of up to ~15 mm that have aspect ratios of 1:1 to 1:3 (the latter with long axis aligned parallel to schistosity, Figure 3a). Albite is blocky and sub to euhedral (up to 10 mm along long axis). Chlorite (up to 2 mm) and muscovite (up to 6 mm) occur as grains oriented parallel with the foliation and as unoriented grains, and commonly surround and stop at the boundaries of kyanite. Muscovite and chlorite additionally separate kyanite and plagioclase. Fine-grained rutile–ilmenite grains and apatite occur in contact with chlorite, plagioclase, muscovite and retrograde sericite (<0.5 mm). Monazite grains occur as inclusions in chlorite, muscovite and sericite. Kyanite, plagioclase, quartz and rutile–ilmenite are interpreted to comprise the peak metamorphic assemblage, which has been overprinted by retrograde chlorite–muscovite and later sericite.

3.2 Samples 103617 and 103618: staurolite-biotite bearing metapelites (Talbot Terrane)

Sample 103617 exhibits a single foliation defined by subhedral biotite (up to about 10 mm) and in places by staurolite (up to 15 mm long, aspect ratio about 1:1–1:15). Staurolite occurs as poikiloblasts with inclusions of quartz, plagioclase and ilmenite (<0.5 mm), and inclusion poor grains, with some poikiloblastic staurolite occurring as rims on inclusion-poor staurolite grains (Figure 3b). Quartz (up to 6 mm), plagioclase (up to 5 mm), subhedral apatite (< 1 mm), intergrowths of rutile−magnetite (potentially previously ilmenite <1 mm) and fine grained magnetite (<< 1 mm) comprise the matrix. Fine-grained ilmenite additionally occurs within staurolite fractures. Subhedral to anhedral chlorite (up to 10 mm, aspect ratio 1:1−1:3) typically occurs as oriented and unoriented grains, in contact with biotite and staurolite, and commonly infills embayed staurolite grain boundaries. Chlorite is interpreted to have grown at the expense of staurolite, and there is late sericite development. Monazite occurs as inclusions in staurolite and within the matrix. The peak assemblage for sample 103617 is interpreted to be staurolite–plagioclase–quartz–ilmenite–magnetite. Chlorite is interpreted to post-date peak metamorphism. All minerals except chlorite and sericite have previously been interpreted as being stable during S_2 (Clarke, pers. comm).

Sample 103618 contains an S–C style fabric in which biotite, staurolite and chlorite define the S and C planes. Staurolite grains are curvilinear in 2D sections, up to 8 mm long and typically have aspect ratios from 1:1 to 1:10 (Figure 3c). Staurolite commonly occurs in aggregates intergrown with quartz and plagioclase that are interpreted to be poikiloblasts. In places these poikiloblasts are wrapped by biotite and chlorite foliae. Subhedral biotite and chlorite (up to 6 mm long) are intergrown with each other, define the fabric and are in direct contact with matrix quartz (< 2mm), plagioclase (< 5 mm) and magnetite (<1 mm). Both chlorite and biotite are in direct contact with staurolite. Ilmenite grains (and ilmenite-rutile intergrowths) are fine grained (<0.5 mm) occur as inclusions in staurolite, in contact with biotite and in the matrix and are commonly aligned parallel to the foliation. Magnetite grains are typically anhedral, unoriented, up to 1 mm in size and occur in the matrix. Monazite grains occur as staurolite inclusions and in the matrix. The peak assemblage for sample 103618 is interpreted to be staurolite–plagioclase–

quartz–chlorite–biotite–magnetite–ilmenite.

3.3 Sample 115638: Quartz-garnet-sillimanite gneiss (Connaughton Terrane)

Sample 115638 was described by Smithies and Bagas (1997) but not used for thermobarometry. The sample contains equant subhedral garnet grains (< 2 mm) that are typically poikiloblastic, containing fine-grained lobate quartz and K-feldspar, and subhedral rutile inclusions (typically <0.5 mm, Figure 3d). Prismatic sillimanite is <1 mm in length and occurs as oriented and unoriented grains, in areas deflecting around garnet. Sillimanite, quartz and K-feldspar (<0.5–2 mm, aspect ratios of 1:1 to 1:3 aligned with the foliation), rutile and ilmenite grains (< 0.5 mm) comprise the matrix and are in contact with garnet. The foliation is defined in places defined by K-feldspar, quartz and sillimanite. Monazite grains occur the matrix and as inclusions in garnet. The interpreted peak mineral assemblage is garnet–sillimanite–plagioclase–K-feldspar–quartz–rutile–ilmenite. Garnet and sillimanite were interpreted by Smithies and Bagas (1997) as late- to post-D_2 based on the observation that sillimanite grains define as well as cross cut the foliation, and some garnet grains that show minimal or no deflection of the S_2 foliation.

3.4 Sample 115669: Kyanite-sillimanite quartzite (Connaughton Terrane)

Sample 115669 was described by Smithies and Bagas (1997). The sample is quartz -rich and contains kyanite and sillimanite. At the scale of the thin section, localised strain varies from medium to high on the basis of the aspect ratios of quartz in different layers of the fabric (~1:1−1:5, Figure 3e). Prismatic to bladed kyanite (<1 mm long) is interpreted to have been variably recrystallised parallel to foliation, and is partly replaced by acicular to fibrolitic sillimanite (<<1 mm). Sillimanite defines the fabric and also cross cuts the fabric, overprinting quartz and kyanite. Ilmenite–magnetite porphyroblasts (up to about 5 mm long) also occur in the sample and are partially surrounded by chloritoid, which is interpreted to be replacing the porphyroblasts. Quartz (<2 mm) comprises the bulk of the matrix, with minor fine-grained muscovite also present. Monazite grains occur in the matrix. Smithies and Bagas (1997) inferred sample 115669 to be located close to the sillimanite–kyanite isograd. In addition, they inferred and that sillimanite growth was late with respect to D_2, and the change from kyanite to sillimanite stability occurred on the prograde path of a single tectonic cycle.

3.5 Sample 115866: Garnet-orthopyroxene gneiss (Connaughton Terrane)

This sample is located close to the Camel–Tabletop Fault zone in the Connaughton Terrane, and was termed a charnockite by Bagas and Smithies (1998). Bagas et al. (2000) reinterpreted the rock to potentially represent quartzofeldspathic/psammitic metasediment. Smithies and Bagas (1997) used this sample for conventional thermobarometry and retrieved very high thermal gradient conditions (~2–4 kbar, 800 °C). The lithology was interpreted to have a foliation unrelated to S_2 and therefore could relate to a thermal/metamorphic event post-dating D_2 (Smithies and Bagas, 1997). The gneissic fabric is defined by discontinuous layers of orthopyroxene, garnet, ilmenite and magnetite alternating with layers of abundant plagioclase, quartz, K-feldspar and perthite/mesoperthite. Garnet is fine grained (< 1mm) and occurs in a number of morphologies: 1) as equant grains in the matrix; 2) as coronae on fine-grained (<1 mm) magnetite or ilmenite; 3) as quartz–garnet symplectites surrounding, or in contact with, magnetite or ilmenite (e.g. Figure 3f); and 4) in contact and partly surrounded by fine-grained quartz−biotite symplectites. Orthopyroxene occurs as aggregates up to 2 mm in size. Magnetite and ilmenite grains that are mantled by garnet or garnet–quartz symplectites commonly occur next to orthopyroxene. Other grains of magnetite(-spinel) and ilmenite (both <1 mm) are not mantled by garnet, but may be mantled by fine-grained biotite. Anhedral quartz, plagioclase and perthite/mesoperthite (approximately 0.5–2 mm) occur in the matrix, with subhedral to anhedral biotite (<3 mm). Monazite grains occur in the matrix, in contact with quartz/feldspar or magnetite(-spinel), or biotite. The peak assemblage is interpreted to have been orthopyroxene–garnet–magnetite–ilmenite–plagioclase–K-feldspar–quartz and melt.

3.6 Sample 113019: Garnet−diopside amphibolite (Connaughton Terrane)

Sample 113019 is from the western Connaughton Terrane within the kyanite zone from the same lithology for which medium to high−*P* estimates for the Yapungku Orogeny were obtained by Smithies and Bagas (1997). It is a foliated unmigmatised garnet−diopside-bearing amphibolite. Garnet grains

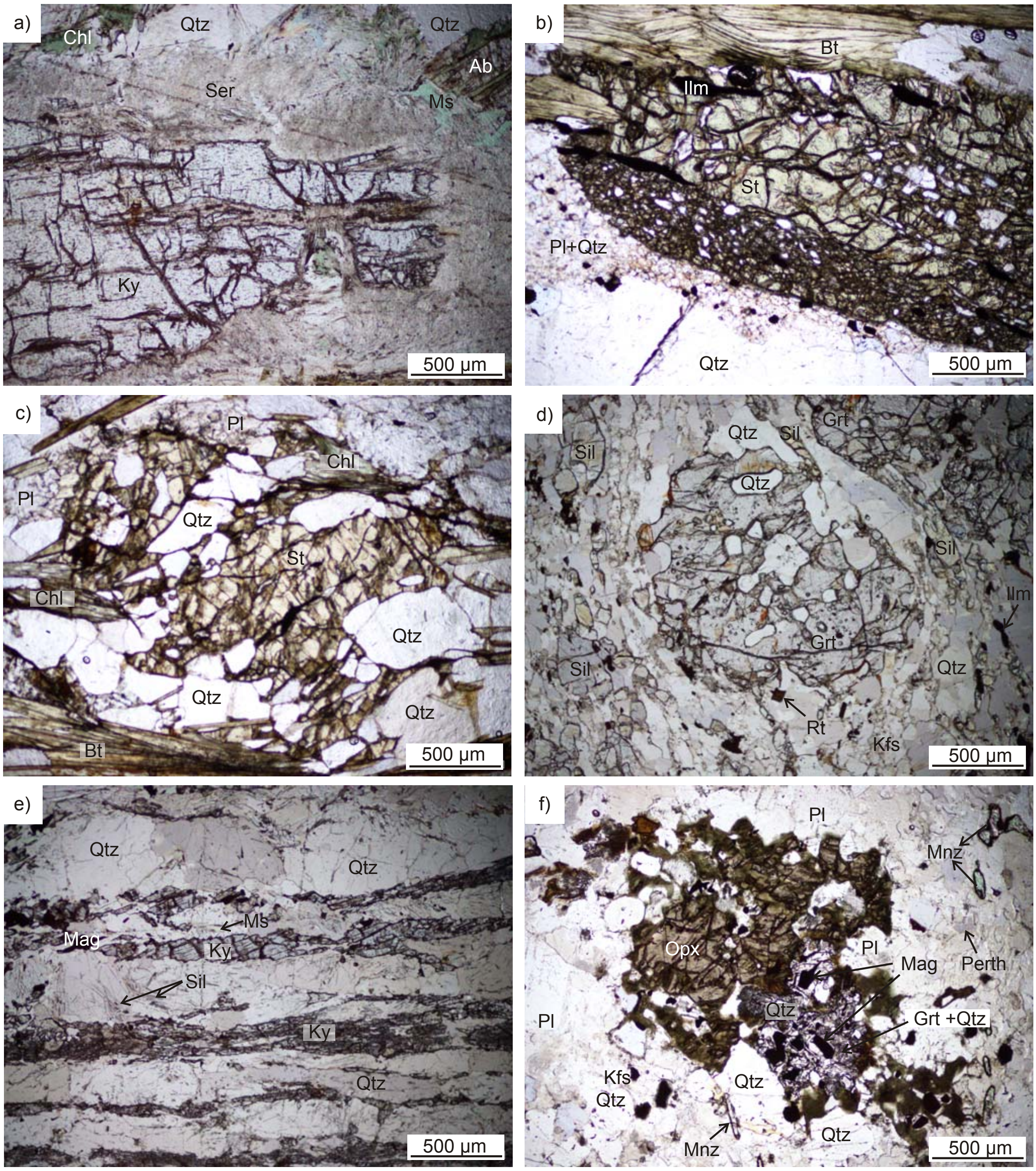

Fig. 3. Thin section photos of samples used in this study: a) Sample 103603D, kyanite surrounded by fine grained sericite, and chlorite, quartz, albite and muscovite, b) sample 103617, staurolite with inclusion rich domains, in contact with plagioclase, quartz, ilmenite and biotite, c) sample 103618, staurolite, plagioclase and quartz wrapped by biotite, d) sample 115638, poikiloblastic garnet in a quartz, K-feldspar, sillimanite, rutile and ilmenite matrix. Sillimanite is both in contact with and in areas wraps around garnet, defining the fabric of the rock, e) sample 115669, kyanite−sillimanite−quartz−magnetite sample, kyanite is in areas recrystallised parallel to the fabric, and fine-grained acicular sillimanite occurs as oriented grains parallel to the fabric and unoriented grains, and f) sample 115866, orthopyroxene adjacent to magnetite mantled by garnet−quartz symplectites in a K-feldspar, (meso)perthite, plagioclase, quartz matrix. Monazite is locally abundant.

(~0.5−1.5 mm in diameter) are typically equant and contain very-fine-grained (<< 0.5 mm) titanite, quartz, plagioclase, hornblende and rare zircon inclusions that are unoriented or occur either as inclusion trails that transect the garnet grain or in the core of the garnet (Fig. 4). Diopside is fine-grained (< 1 mm) and occurs with matrix minerals plagioclase (< 2 mm, anhedral), quartz (< 1mm, anhedral), hornblende (< 2mm, subhedral to anhedral) and minor apatite and pyrite (< 0.5 mm). Hornblende is foliated and also partially surrounds garnet and diopside as fine−medium sized grains (< 2mm). Hornblende also occurs as part of a fine-grained and locally developed symplectic intergrowth with plagioclase ± quartz ± titanite, partially separating garnet from matrix hornblende or diopside grains. The peak mineral assemblage is interpreted to be garnet−diopside−hornblende−plagioclase−quartz−titanite−apatite.

4. Analytical Techniques

4.1 Electron Microprobe Analysis (EPMA) spot and elemental maps

Mineral chemical composition analyses were obtained using a Cameca SXFive electron microprobe at the University of Adelaide using a beam current of 20 nA and accelerating voltage of 15 kV. Monazite elemental maps were obtained using a beam current of 200 nA and accelerating voltage of 15–20 kV. Y, Th, Ce, U and Pb were mapped using WDS and P was mapped using EDS.

4.2 Zircon and Monazite U–Pb Geochronology

Zircon from sample 113019 and monazite from the remaining six samples from the Rudall Province were analysed for U–Pb geochronology using the Laser Ablation–Inductively Coupled Plasma–Mass Spectrometer (LA−ICP−MS) at Adelaide Microscopy, University of Adelaide. Zircon from sample 113019 (garnet−diopside amphibolite) was prepared using panning, Franz and heavy liquid techniques at Geotrack International, and mounted in epoxy resin. Prior to laser ablation, zircon grains were imaged using a Gatan Cathodoluminescence (CL) detector attached to a Phillips XL40 SEM. Monazite grains were imaged using a Phillips XL30 SEM.

U–Pb analyses of zircon and monazite were obtained using an Agilent 7500cs ICP–MS with a New Wave 213 nm Nd–YAG laser in a helium ablation atmosphere. For zircon, a laser spot size of 20–30 µm, repetition rate of 5 Hz and laser intensity of 80–100 % was used. A 30 second gas blank was initially measured followed by 80 seconds of zircon sample ablation. The laser was fired for 10 seconds with the shutter closed prior to ablation in order to allow for beam and crystal stabilization. Analyses measured isotopes ^{204}Pb, ^{206}Pb, ^{207}Pb, ^{208}Pb, ^{232}Th and ^{238}U for 10, 15, 30, 10, 10, 15 ms respectively for zircon. Common lead was not corrected due to an unresolvable interference of ^{204}Hg and ^{204}Pb peaks. However, ^{204}Pb was monitored to assess the common lead of each analysis.

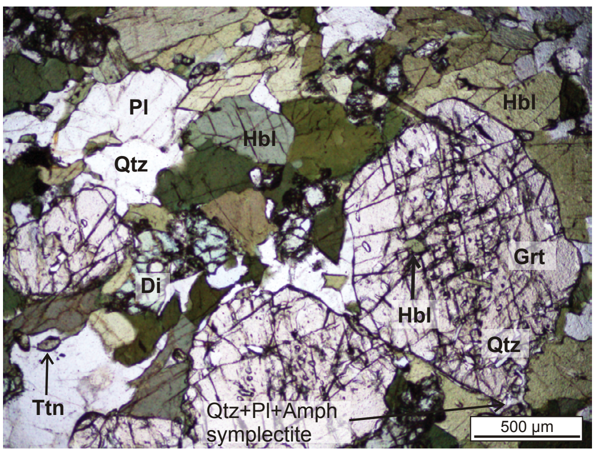

Figure 4. Photomicrograph of sample 113019 showing peak assemblage garnet, diopside, hornblende, quartz, plagioclase and titanite. Quartz, plagioclase, amphibole symplectite separating garnet and matrix hornblende is also shown.

For monazite, a 15–16 μm spot size, repetition rate of 5 Hz and laser intensity of 80–100 % was used. A 30 second gas blank was initially measured followed by 40 to 50 seconds of monazite sample ablation. The laser was fired for 10 seconds with the shutter closed prior to ablation in order to allow for beam and crystal stabilisation. Analyses measured isotopes ^{204}Pb, ^{206}Pb, ^{207} Pb and ^{238}U for 10, 15, 30 and 15 ms respectively for monazite. Common lead was not corrected for zircon or monazite analyses due to an unresolvable interference of ^{204}Hg and ^{204}Pb peaks. However, ^{204}Pb was monitored to assess the common lead of each analysis.

Zircon and monazite data was corrected for mass-bias and fractionation using the real-time correction program Glitter v. 4.23 (Griffin et al., 2008). Gemoc zircon standard GJ-1 was used to correct for mass bias and fractionation (TIMS normalisation data: ^{207}Pb/^{206}Pb = 608.3 Ma, ^{206}Pb/^{238}U = 600.7 Ma and ^{207}Pb/^{235}U = 602.2 Ma; Jackson *et al.* 2004). An uncertainty of 1% was assigned to the age of the GJ-1 zircon standard. Accuracy of zircon analyses were monitored by analysing internal standards Plesovice (ID TIMS ^{206}Pb/^{238}U age = 337.13 ± 0.37 Ma; Sláma *et al.* 2008) and OG-1 (ID TIMS ^{207}Pb/^{206}Pb age = 3465.4 ± 0.6 Ma; Stern et al., 2009) prior to and throughout unknown analysis runs. Average Plesovice ages obtained during this study were ^{207}Pb/^{235}U = 339 ± 4 Ma (95 % confidence, n = 16, MSWD = 1.9), ^{207}Pb/^{206}Pb = 339 ± 17 Ma (MSWD = 0.38) and ^{206}Pb/^{238}U = 340 ± 2.9 Ma (MSWD = 2.9). Average OG-1 ages obtained during this study were ^{207}Pb/^{206}Pb = 3464 ± 15 Ma (95 % confidence, n = 6, MSWD = 0.6), ^{207}Pb/^{235}U = 3461 ± 37 Ma (MSWD = 6.3), and ^{206}Pb/^{238}U = 3458 ± 110 Ma (MSWD = 9.4).

Monazite standard Madel was used to correct for mass bias and fractionation for monazite analyses (TIMS Madel age: ^{207}Pb/^{206}Pb = 490.0 Ma, ^{206}Pb/^{238}U = 518.37 Ma and ^{207}Pb/^{235}U = 513.13 Ma; Payne et al., 2008, updated with additional TIMS data). 1% uncertainty was given to the age of the Madel standard for sample age error calculations. Accuracy was monitored by analysing the 222 (*c.* 450 Ma; Maidment, 2005) monazite standard prior to and throughout unknown analysis runs. Average 222 ages obtained throughout this study were ^{207}Pb/^{235}U = 454 ± 2 Ma (95 % confidence, n = 59, MSWD = 1.2), ^{207}Pb/^{206}Pb = 461 ± 7 Ma (MSWD = 0.46) and ^{206}Pb/^{238}U = 452 ± 2 Ma (MSWD = 1.5). Conventional concordia, weighted averages, and linear probability plots were generated using Isoplot version 4.11 (Ludwig, 2008).

4.3 Zircon and garnet REE: Sample 113019

REE and trace elements of zircon and garnet grains were analysed using the LA−ICP−MS at Adelaide Microscopy). Zircon grains were analysed in grain mounts, whereas garnet grains were analysed in situ. Moderately luminescent zircon with homogenous, fir-tree zoned and irregular/patchy zones with pre-collected U–Th–Pb data were analysed. LA–ICP–MS REE chemistry of garnet grains were obtained via transects across garnet grains over pre-collected EPMA spot analysis transects. Analyses for zircon and garnet were conducted using 30 μm laser spot size at 100 % intensity and 5 Hz repetition rate. Total acquisition time was 100 seconds for zircon and 150 seconds for garnet, and incorporated 30 seconds of background acquisition and 10 seconds of laser firing with the shutter closed at the start of each zircon and garnet analysis. External standard Nist 610 was used to correct for fractionation and mass bias (Pearce *et al.* 1997), and standards Nist 612 and BHVO were used as internal standards to monitor the accuracy of analyses. Data was corrected using GLITTER software (Van Achterbergh *et al.* 2001). Analyses were calibrated internally using Hf oxide weight percent measurements on zircon domains and Ca oxide weight percent measurements on garnet corresponding to spot locations of LA–ICP–MS REE and trace element analyses using Cameca SX51 microprobe at Adelaide Microscopy. An accelerating voltage of 15 kV and beam current of 20 nA was used.

4.4 Mineral equilibria modelling

Bulk chemical compositions of samples 103618 and 113019 were determined using whole-rock geochemical analyses. Major element concentrations were determined by X-ray fluorescence (XRF), using a Panalytical

2404 XRF unit at Franklin and Marshall College, United States. Samples were prepared for analysis by fusion of the milled sample with lithium tetraborate. Estimates on the proportion of Fe_2O_3 to FeO in the rocks were made by estimating the modal abundance of minerals in a sample and combining that information with oxide wt% compositions of Fe^{3+} bearing minerals recast for Fe_2O_3 using the stoichiometric method of Droop (1987). For staurolite–magnetite–ilmenite bearing sample 103618, 85% of the analysed Fe_2O_3 was converted to FeO.

P−T pseudosections were calculated using THERMOCALC v3.33 (October 2009 update of Powell and Holland, 1988), with the internally consistent dataset of Holland and Powell (1998; tc-ds55, Nov. 2003 update). The model chemical system NCKFMASHTO ($Na_2O-CaO-K_2O-FeO-MgO-Al_2O_3-SiO_2-H_2O-TiO_2-Fe_2O_3$) was used for *P−T* pseudosection calculations for sample 103618 using *a−x* relationships of White et al. (2007) for biotite, garnet and silicate melt, White et al. (2000) for ilmenite and hematite, Holland and Powell (2003) for K-feldspar and plagioclase, Holland and Powell (1998) for cordierite, staurolite and epidote, Coggon and Holland (2002) for muscovite and paragonite, Holland et al. (1998) for chlorite and White et al. (2000) for magnetite.

For sample 113019, the model chemical system NCFMASHTO ($Na_2O-CaO-FeO-MgO-Al_2O_3-SiO_2-H_2O-TiO_2-Fe_2O_3$) was used for sample 113019 using *a−x* relationships of Green et al. (2007) for clinopyroxene, Diener et al. (2007) for hornblende, White et al. (2007) for garnet, Holland and Powell (1998) for epidote, Holland et al. (1998) for chlorite, Holland and Powell (2003) for plagioclase and White et al. (2000) for ilmenite. Estimates on the proportion of Fe_2O_3 to FeO were made by estimating the modal abundance of minerals in the sample and combining that information with oxide wt.% compositions of Fe^{3+} bearing minerals recast for Fe_2O_3 using the stoichiometric method of Droop (1987). 90% of the analysed Fe_2O_3 was converted to FeO for sample 113019. Water was set to excess (water saturated) for samples 103618 and 113019 as peak *P–T* conditions of both samples are interpreted to be subsolidus.

5. Results

Representative EPMA spot analyses are provided in Table 2 and mineral chemistry is detailed in Appendix 1.

5.1 In situ monazite U–Pb Geochronology

Representative EPMA maps and BSE images of monazite for sample 115638 and 115866 are shown in Figure 5. BSE images of monazite grains from samples 103603D, 103617, 103618 and 115669 are shown in Figure 6a−d. Cathodoluminescence images of zircon from sample 113019 are show in Figure 6e. U−Pb geochronology data are provided in Appendix 2.

5.1.1. Sample 103603D (kyanite−bearing pelite, Talbot Terrane)

Monazite grains occur as inclusions in chlorite, muscovite and sericite, do not show zoning in BSE imagery and range in size from ~50 to 200 μm. Twenty analyses were obtained (Fig. 7a, b). Seventeen analyses are within 5 % concordance, lie on a linear array in the plotted linear probability diagram, and are interpreted to comprise one age population. The above concordant analyses yield a Pb^{207}/Pb^{206} age weighted average of 1275 ± 11 Ma (*n* = 17, MSWD = 0.3, 95 % confidence).

5.1.2. Sample 103617 (staurolite−bearing pelite, Talbot Terrane)

Monazite grains range from ~20 to 100 μm and show variable internal morphologies in BSE imagery varying from no zoning, irregular/patchy zoning to monazite grains with lighter cores. Thirty-five analyses were obtained from monazite grains located within the matrix and as inclusions in staurolite grains (Fig. 7c). 100 ± 5 % concordant analyses were included in the linearised probability plot (Fig. 7d). 25 analyses form a linear array on Figure 7d and are interpreted as one age population. These analyses yield a Pb^{207}/Pb^{206} age weighted average of 1666 ± 8 Ma (*n* = 25, MSWD = 0.73, 95 % confidence).

Table 2. Representative mineral compositions for samples 103617 and 103618

Sample	103617	103617	103617	103617	103617	103617	103618	103618	103618	103618	103618	103618	103618
Mineral	Chl	Bt	St	Qtz	Pl	Mag	Chl	Bt	St	Qtz	Pl	Mag	Ilm
ID number	1	51	18	30	34	40	72	42	4		44	67	36
SiO_2	26.29	34.93	26.36	98.66	65.80	0.35	24.65	33.96	25.90	99.11	67.42	0.31	0.04
TiO_2	0.42	1.13	0.55	0.00	0.01	0.06	0.08	1.42	0.55	0.01	0.00	0.03	52.12
$Al2O_3$	22.56	17.96	52.88	0.01	19.79	0.14	22.46	19.30	52.02	0.02	18.57	0.46	0.01
$Cr2O_3$	0.02	0.00	0.00	0.01	0.00	0.00	0.01	0.03	0.00	0.01	0.00	0.00	0.01
FeO	19.63	17.41	13.23	0.02	0.00	90.49	21.38	18.19	14.67	0.00	0.00	87.10	44.52
MnO	0.07	0.08	0.26	0.01	0.00	0.04	0.10	0.05	0.22	0.00	0.01	0.01	1.28
MgO	18.83	14.51	2.07	0.00	0.00	0.05	18.48	13.33	1.83	0.00	0.00	0.01	0.31
ZnO	0.00	0.00	0.14	0.00	0.03	0.05	0.02	0.03	0.00	0.00	0.03	0.03	0.06
CaO	0.00	0.00	0.01	0.01	0.49	0.04	0.02	0.07	0.01	0.00	0.78	0.03	0.00
Na_2O	0.01	0.16	0.00	0.02	11.75	0.02	0.00	0.20	0.00	0.00	11.72	0.04	0.01
K_2O	0.56	8.13	0.00	0.00	0.05	0.04	0.06	7.37	0.01	0.01	0.04	0.00	0.01
Total	88.39	94.31	95.51	98.73	97.92	91.29	87.25	93.95	95.22	99.17	98.56	88.02	98.37
No. Oxygens	14	11	46	2	8	4	14	11	46	2	8	4	3
Si	2.67	2.65	7.51	1.00	2.95	0.01	2.56	2.59	7.46	1.00	3.00	0.01	0.00
Ti	0.03	0.06	0.12	0.00	0.00	0.00	0.01	0.08	0.12	0.00	0.00	0.00	1.00
Al	2.70	1.61	17.75	0.00	1.04	0.01	2.75	1.73	17.65	0.00	0.97	0.02	0.00
Cr	0.00	0.00	0.00	0.00	0.00	0.00	0.00	0.00	0.00	0.00	0.00	0.00	0.00
Fe^{3+}						1.97						1.95	0.00
Fe^{2+}	1.66	1.10	3.15	0.00	0.00	1.00	1.86	1.16	3.53	0.00	0.00	1.00	0.95
Mn^{2+}	0.01	0.01	0.06	0.00	0.00	0.00	0.01	0.00	0.05	0.00	0.00	0.00	0.03
Mg	2.85	1.64	0.88	0.00	0.00	0.00	2.86	1.51	0.78	0.00	0.00	0.00	0.01
Zn	0.00	0.00	0.03	0.00	0.00	0.00	0.00	0.00	0.00	0.00		0.00	0.00
Ca	0.00	0.00	0.00	0.00	0.02	0.00	0.00	0.01	0.00	0.00	0.04	0.00	0.00
Na	0.00	0.02	0.00	0.00	1.02	0.00	0.00	0.03	0.00	0.00	1.01	0.00	0.00
K	0.07	0.79	0.00	0.00	0.00	0.00	0.01	0.72	0.00	0.00	0.00	0.00	0.00
Total Cations (S)	10	8	29.5	1	5	3	10	8	30	1	5	3	2
X(Mg) = (Mg/(Fe+Mg))	0.63	0.60	0.22				0.61	0.57	0.18				0.01
X(Na) = (Na/(Na+Ca)					0.98						0.96		
X(Mg) = (Mg/(Mg+Zn+Fe^{2+}+Mn)													0.01

5.1.3. Sample 103618 (staurolite−bearing pelite, Talbot Terrane)

Monazite grains are ~40–200 μm in size, occur both in the matrix and as inclusions within staurolite, and display internal morphologies in BSE imagery that vary from no zoning to patchy zoning. 25 analyses were obtained, with 23 analyses are within 100 ± 5 % concordance and are shown in linearised probability plot (Fig. 7e, f). A Pb^{207}/Pb^{206} age weighted average of 1283 ± 9 Ma (*n* = 22, MSWD = 0.58, 95 % confidence) was calculated from analyses which lie along a linear array. One older analysis from a monazite grain located in the matrix was excluded from the weighted average.

5.1.4. Sample 115638 (garnet−sillimanite gneiss, Connaughton Terrane)

Monazite grains are ~20–150 μm in size and show internal morphologies in BSE imagery that range from no visible zoning, zoning with either darker or lighter cores, and concentric zoning. Th and Y elemental maps of representative monazite grains show monazite grains commonly contain a Th enriched core and do not show appreciable Y zoning. Th-poor rims were too narrow to be analysed using LA–ICP–MS. Eighteen analyses were obtained from monazite grains located within the matrix and as inclusions in garnet grains. Sixteen analyses yield results within 100 ± 5 % concordance. These concordant analyses were included in the linearised probability diagram and lie on a linear array (Fig. 8a, b). The above concordant analyses are interpreted to comprise one age population and yield Pb^{207}/Pb^{206} age weighted average of 1307 ± 12 Ma (*n* = 16, MSWD = 0.87, 95 % confidence).

5.1.5. Sample 115669 (kyanite−sillimanite quartzite, Connaughton Terrane)

Monazite grains vary in size from 20 to 200 μm and exhibit internal morphologies that vary from no visible zoning, patchy/irregular zoning to darker or lighter cores under BSE. Nineteen analyses were obtained on monazite

Table 2. Representative mineral compositions for samples 115866 and 113019

Sample	115866	115866	115866	115866	115866	115866	115866	115866	115866	113019	113019	113019	113019	113019	113019	113019
Mineral	Grt- matrix	Grt-Corona	Opx	Pl	Kfs	Qtz	Mag	Ilm	Bt	Grt-rim	Grt-core	Di	Hbl	Pl	Ttn	Qtz
ID number	54	91	86	27	30	22	83	97	13	3	19	99	34	103	37	36
SiO_2	38.31	37.59	45.13	60.00	65.35	97.45	0.04	0.05	39.44	38.47	38.08	51.85	41.38	62.67	30.42	96.53
TiO_2	0.04	0.03	0.24	0.04	0.03	0.07	0.04	49.07	2.03	0.03	0.14	0.19	1.16	0.00	37.02	0.00
$Al2O_3$	21.37	20.98	9.89	24.50	19.77	0.16	0.27	0.02	15.15	20.85	20.62	4.11	11.95	23.43	1.17	0.02
$Cr2O_3$	0.03	0.01	0.02	0.00	0.01	0.02	0.10	0.01	0.00	0.04	0.01	0.05	0.03	0.06	0.01	0.00
FeO	25.85	26.96	23.07	0.06	0.04	0.05	87.96	45.92	9.69	25.05	24.61	10.42	17.55	0.08	0.57	0.52
MnO	2.31	2.49	0.64	0.01	0.00	0.00	0.08	0.76	0.08	1.04	0.82	0.10	0.11	0.01	0.01	0.00
MgO	10.02	9.30	19.04	0.00	0.00	0.01	0.00	0.70	19.76	3.18	3.45	11.14	10.35	0.00	0.00	0.00
ZnO	0.00	0.05	0.00	0.04	0.00	0.00	0.04	0.09	0.00	0.00	0.00	0.01	0.05	0.00	0.00	0.00
CaO	0.85	0.81	0.05	6.36	0.89	0.00	0.02	0.02	0.01	11.68	12.35	19.85	10.63	4.77	29.05	0.05
Na_2O	0.01	0.00	0.02	8.06	2.62	0.00	0.02	0.01	0.04	0.00	0.00	2.02	2.19	8.86	0.01	0.00
K_2O	0.00	0.01	0.00	0.14	11.66	0.04	0.00	0.01	9.37	0.00	0.01	0.00	0.22	0.05	0.00	0.00
Total	98.78	98.24	98.11	99.21	100.37	97.80	88.57	96.65	95.57	100.34	100.10	99.74	95.62	99.91	98.26	97.12
No. Oxygens	12	12	6	8	8	2	4	3	11	12	12	6	23	8	5	2
Si	2.99	2.97	1.70	2.69	2.96	1.00	0.00	0.00	2.85	3.02	3.00	1.94	6.36	2.78	1.01	1.00
Ti	0.00	0.00	0.01	0.00	0.00	0.00	0.00	0.96	0.11	0.00	0.01	0.01	0.13	0.00	0.93	0.00
Al	1.96	1.95	0.45	1.30	1.05	0.00	0.01	0.00	1.29	1.93	1.91	0.18	2.17	1.22	0.05	0.00
Cr	0.00	0.00	0.00	0.00	0.00	0.00	0.00	0.00	0.00	0.00	0.00	0.00	0.00	0.00	0.00	0.00
Fe^{3+}			0.13				1.98	0.08				0.09				
Fe^{2+}	1.69	1.78	0.60	0.00	0.00	0.00	1.00	0.91	0.58	1.64	1.62	0.33	2.26	0.00	0.02	0.00
Mn^{2+}	0.15	0.17	0.02	0.00	0.00	0.00	0.00	0.02	0.00	0.07	0.05	0.00	0.01	0.00	0.00	0.00
Mg	1.16	1.10	1.08	0.00	0.00	0.00	0.00	0.03	2.13	0.37	0.40	0.62	2.37	0.00	0.00	0.00
Zn	0.00	0.00	0.00	0.00	0.00	0.00	0.00	0.00	0.00	0.00	0.00	0.00	0.01	0.00	0.00	0.00
Ca	0.07	0.07	0.00	0.31	0.04	0.00	0.00	0.00	0.00	0.98	1.04	0.80	1.75	0.23	1.04	0.00
Na	0.00	0.00	0.00	0.70	0.23	0.00	0.00	0.00	0.01	0.00	0.00	0.15	0.65	0.76	0.00	0.00
K	0.00	0.00	0.00	0.01	0.67	0.00	0.00	0.00	0.86	0.00	0.00	0.00	0.04	0.00	0.00	0.00
Total Cations (S)	8	8	4	5	5	1	3	2	8	8	8	4	16	5	3	1
XMg = (Mg/(Fe+Mg))	0.41	0.38	0.64					0.03	0.78	0.18	0.20	0.66	0.51			
XMg = (Mg/(Mg+Zn+Fe^{2+}+Mn)								0.03								
X(Alm)	0.55	0.57								0.54	0.52					
X(Py)	0.38	0.35								0.12	0.13					
X(Grs)	0.02	0.02								0.32	0.33					
X(Spss)	0.05	0.05								0.02	0.02					
X(An) = (Ca/(Ca+Na+K)				0.30	0.05									0.23		
X(Or) = (K/(Na+Ca+K)				0.01	0.71									0.00		

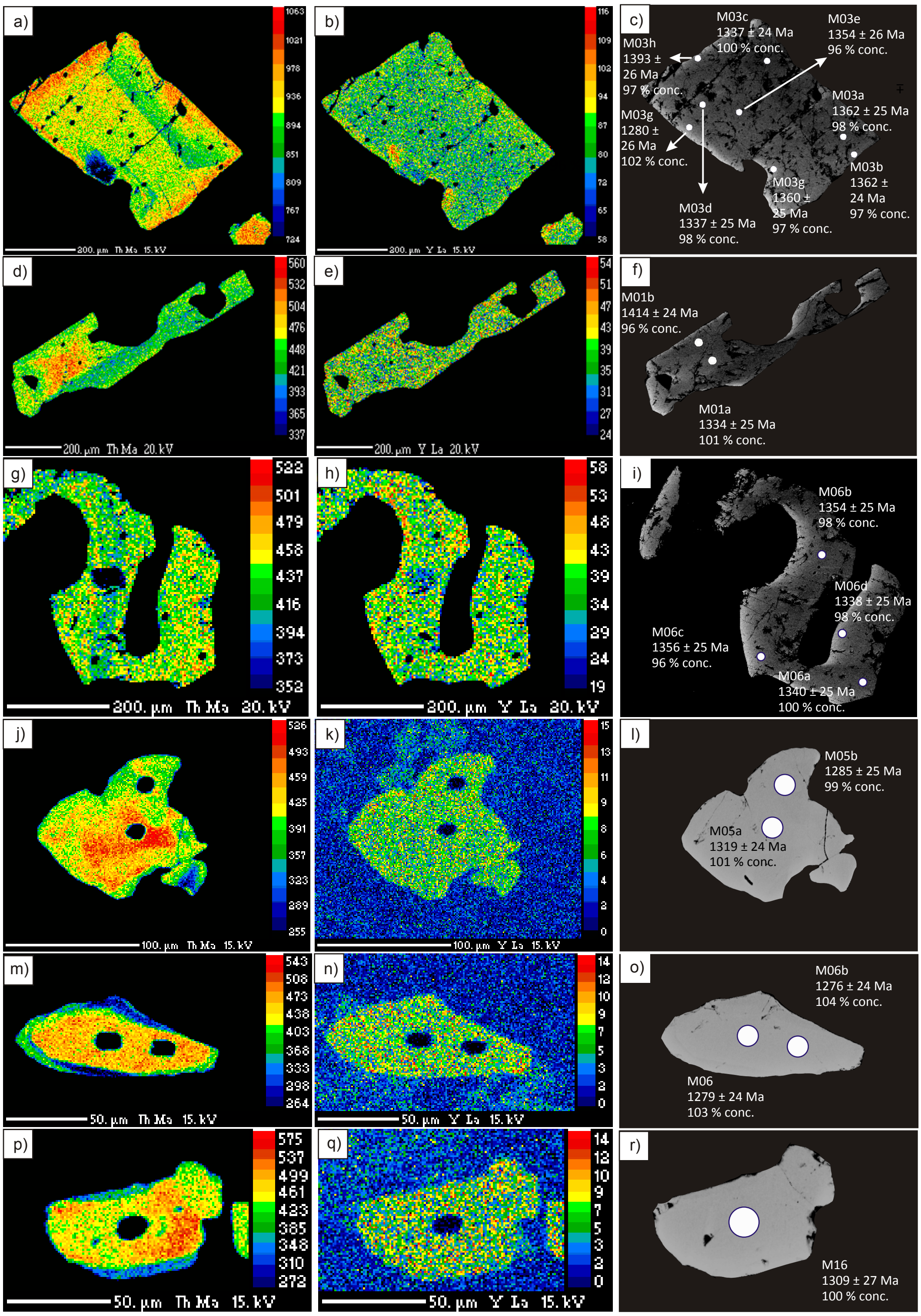

Fig. 5. Th and Y EPMA maps, and BSE images of monazite grains from samples 115866 (a–i) and 115638 (j–r) with location of LA-ICP-MS spot and $^{207}Pb/^{206}Pb$ ages shown.

grains from the matrix. Seventeen analyses yield results within 100 ± 5 % concordancy and plot on a linear array (Fig. 8c, d). These analyses are considered to be one population and yield a Pb^{207}/Pb^{206} age weighted average of 1295 ± 11 Ma (n = 17, MSWD = 0.63, 95 % confidence).

5.1.6. Sample 115866 (garnet−orthopyroxene gneiss, Connaughton Terrane)

Monazite grains are ~50 to 1000 µm in size and show internal morphologies in BSE imagery that vary from no visible zoning, lighter cores to irregular zoning. Th and Y

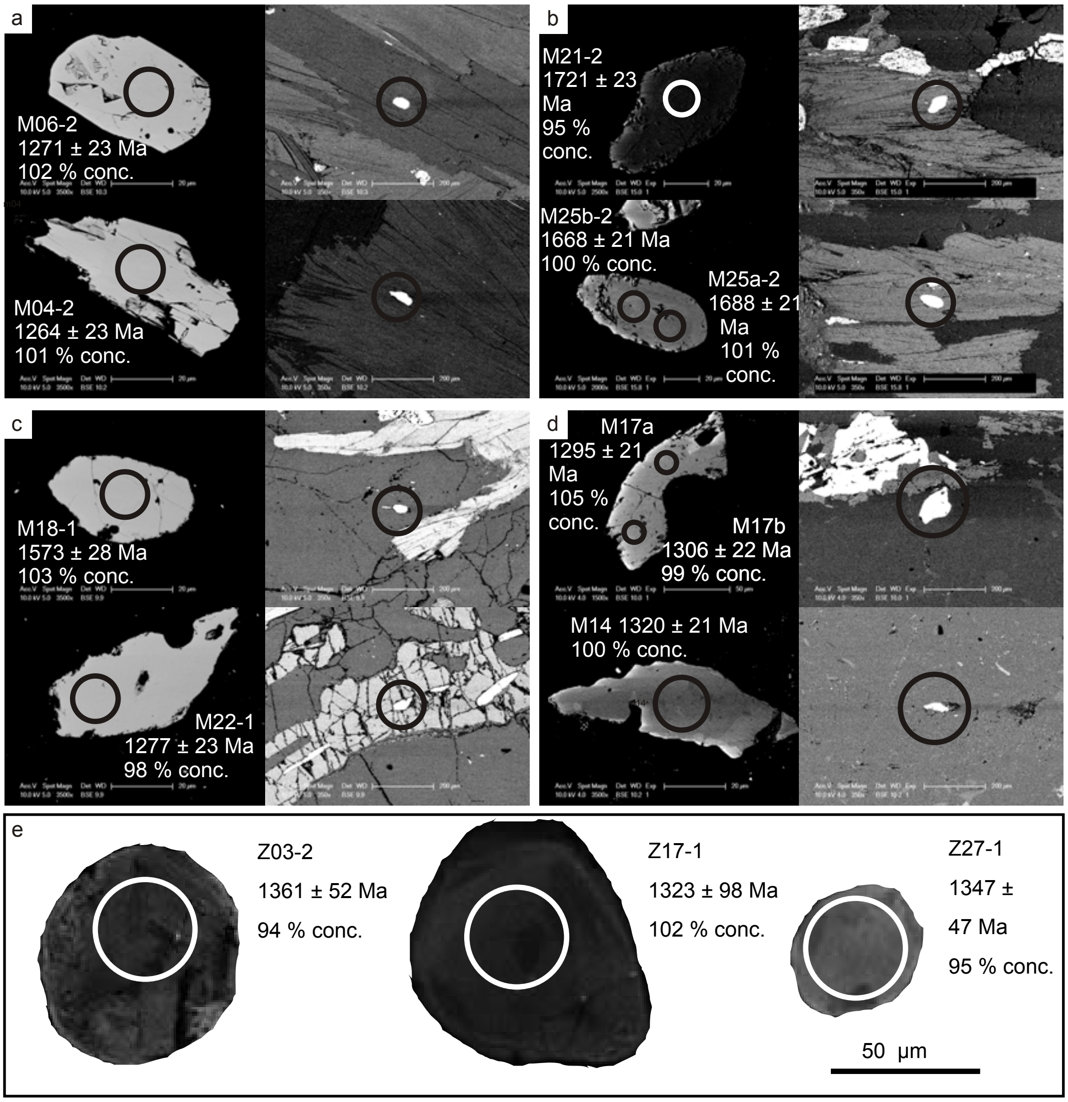

Fig. 6. BSE images of monazite grains from a) sample 103603D, b) sample 103617, c) sample 103618, and d) 115669. Cathodoluminescence images of zircon from sample 113019 (e).

elemental maps for representative monazite grains show zoning in Th, with higher Th in cores for some grains, and at grain boundaries for other grains (Fig. 5a–i). Y zoning in monazite grains are limited to patchy domains of higher or lower Y or some increase in Y at the edges of grains. There is no consistent correspondence between Th or Y and age. Thirty-three analyses were obtained from grains located in the matrix; in contact with quartz and feldspar with some grains also in contact with magnetite and/or spinel or fine grained biotite. Thirty-one analyses are within 100 ± 5 % concordance and of these analyses all but one are considered to be one population using a linearised probability plot (Fig. 8e, f). The age population yields a calculated Pb^{207}/Pb^{206} age weighted average of 1341 ± 10 Ma (n = 30, MSWD = 1.13, 95 % confidence). No correspondence between age and internal morphology or textural location was observed.

5.2 Zircon U−Pb Geochronology

In cathodoluminescence imagery, zircon grains typically show moderately luminescent irregular/patchy zoning that in some grains overprint faint linear or concentric zoning or surround a small (<20 μm), strongly luminescent core. Fir-tree zoning in some grains is similar to those of zircons that have grown or recrystallized during high-grade metamorphism (Fig. 5e; Corfu et al., 2003). Sixty-six analyses were obtained from homogeneous, patchy/irregular and fir-tree zoned domains. Rims and highly luminescent cores were too narrow or small to be analysed via LA−ICP−MS. Zircon analyses commonly

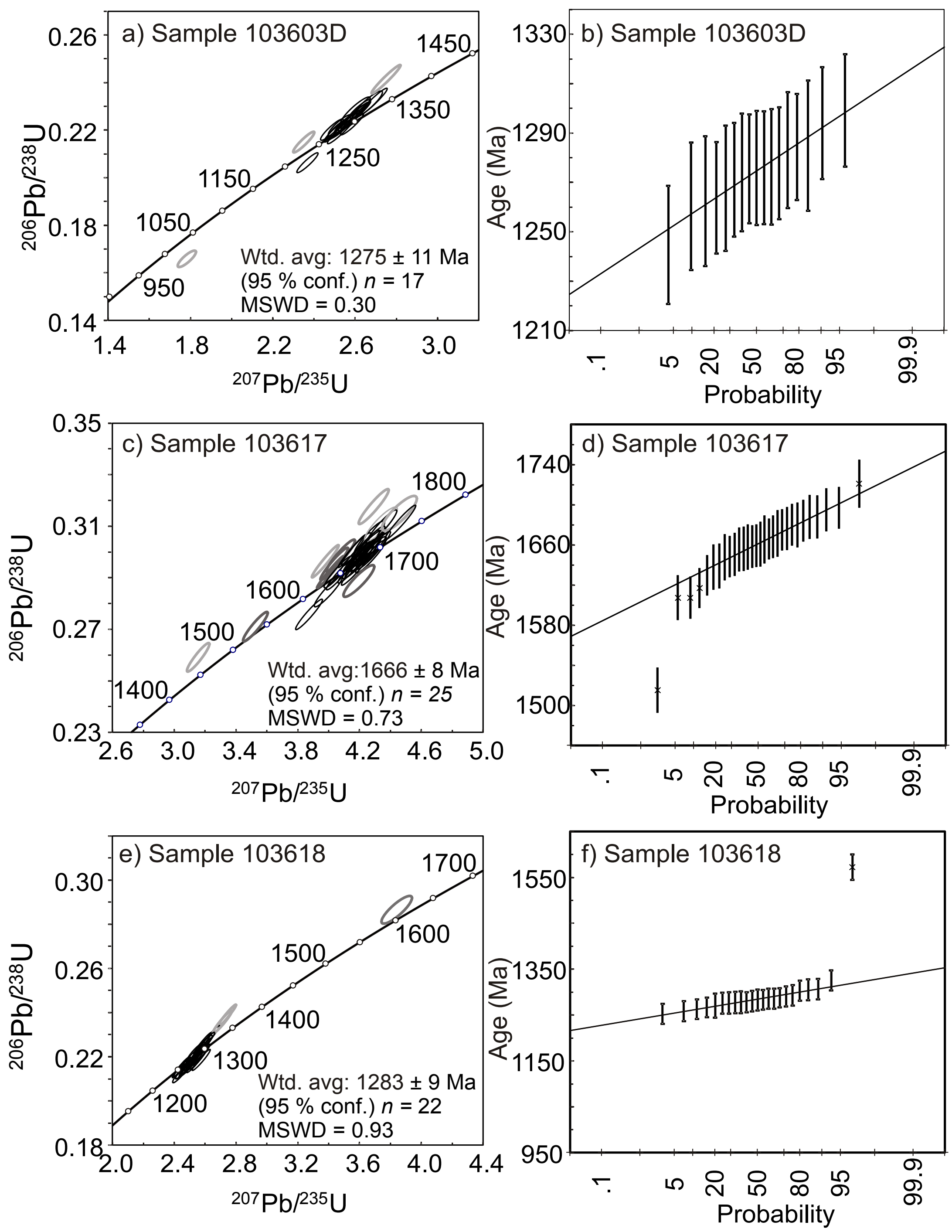

Fig. 7. Monazite age data for the Talbot Terrane showing $^{207}Pb/^{206}Pb$ age weighted averages, concordia and linearised probability diagrams for samples. Black ellipses indicate 100 ± 5 % concordant analyses that form along a straight line in linearised probability density diagrams, and are used to calculate age weighted averages. Light grey ellipses indicate >5 % discordant analyses that are not included in either weighted average calculations or the linearised probability diagrams. Medium grey ellipses indicate analyses indicate analyses that are within 100 ± 5 % concordancy but do not lie on a straight line in the linearised probability plots (shown as analyses with crosses), and are not included in weighted average calculations.

yielded low ^{206}Pb, ^{207}Pb, ^{208}Pb and ^{238}U cps, and analyses with noisy isotopic signals were not included in calculations (full dataset is provided in Appendix 2). Thirty analyses are displayed in Figure 8g–h. Nineteen analyses are within 100 ± 10 % concordance and yield a $^{207}Pb/^{206}Pb$ age range between 1433 and 1323 Ma. A $^{207}Pb/^{206}Pb$ weighted average age for the above < 10 % discordant analyses of 1377 ± 26 Ma was calculated (n = 19, MSWD = 0.35, 95 % confidence).

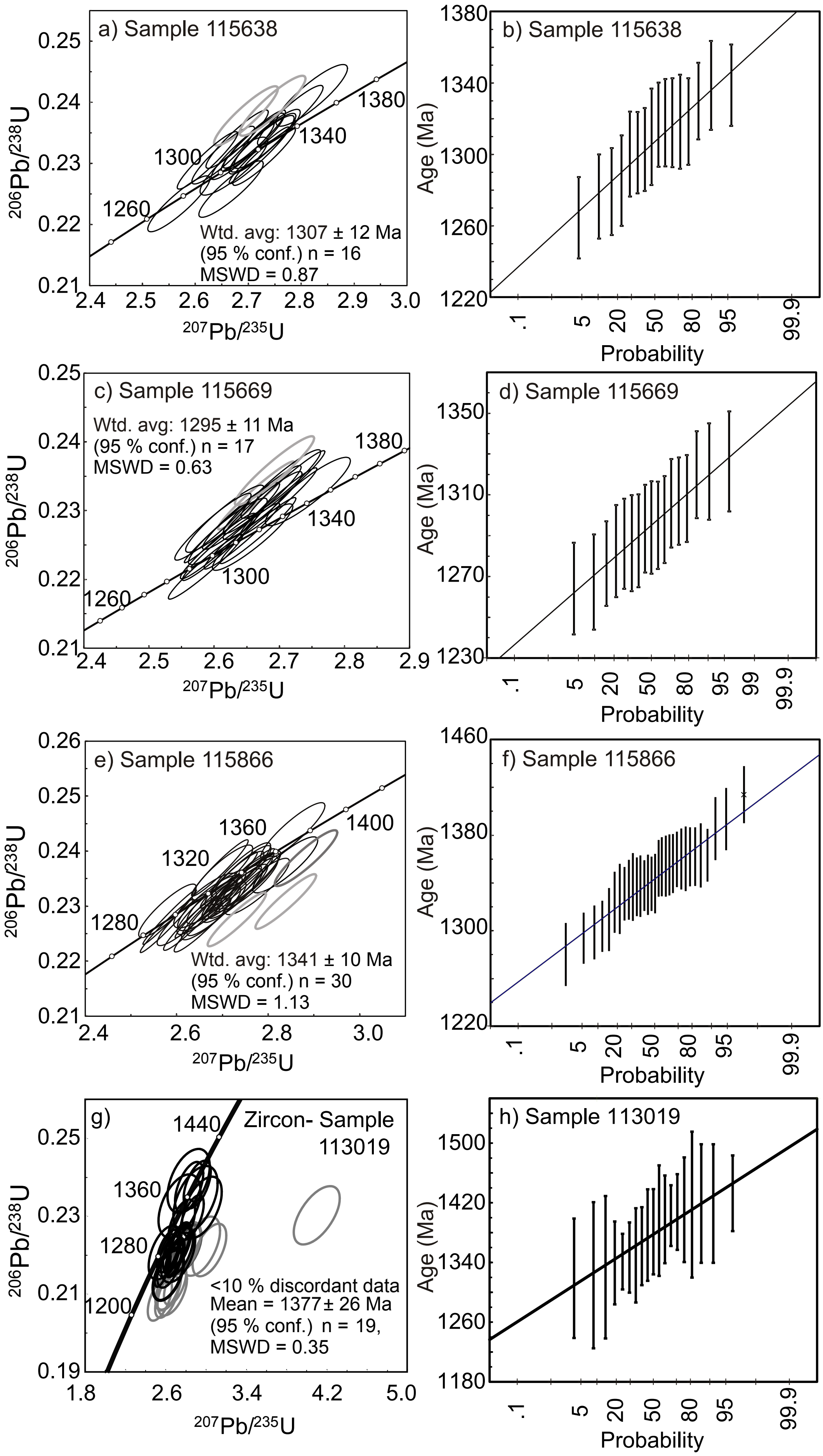
a) Sample 115638
Wtd. avg: 1307 ± 12 Ma
(95 % conf.) n = 16
MSWD = 0.87
b) Sample 115638
c) Sample 115669
Wtd. avg: 1295 ± 11 Ma
(95 % conf.) n = 17
MSWD = 0.63
d) Sample 115669
e) Sample 115866
Wtd. avg: 1341 ± 10 Ma
(95 % conf.) n = 30
MSWD = 1.13
f) Sample 115866
g) Zircon- Sample 113019
<10 % discordant data
Mean = 1377± 26 Ma
(95 % conf.) n = 19,
MSWD = 0.35
h) Sample 113019
206Pb/238U
207Pb/235U
Age (Ma)
Probability

Fig. 8 (previous page), a−f) monazite age data for the Connaughton Terrane showing $^{207}Pb/^{206}Pb$ age weighted averages, concordia and linearised probability diagrams. See Figure 7 caption for monazite concordia ellipse shading explanation, g−h) zircon age data for sample 113019 showing $^{207}Pb/^{206}Pb$ age weighted average, concordia and linearised probability diagrams. Black ellipses are 100 ± 10% concordant analyses used in calculation of $^{207}Pb/^{206}Pb$ age weighted average. Light grey ellipses are analyses are >10% discordant.

5.3 Zircon and garnet trace element characteristics

Representative trace-element chemistry for garnet and zircon grains from sample 113019 is provided in Appendix 2 and chondrite normalised REE patterns are shown in Fig. 9. Trace element abundances in garnet were measured by LA–ICP–MS spot analyses across two garnet grains ~1500 µm in diameter. Both garnet grains contain inclusion-rich cores and inclusion-poor rims. Chondrite-normalized REE patterns for garnet show variable but more enriched and steeper HREE within the cores of garnet (Lu_N/Gd_N = 12.64–72.96; Lu_N = 60–373) relative to garnet rims (Lu_N/Gd_N = 1.71–5.07; Lu_N = 13–34). 100 ± 10% concordant zircon grains have HREE patterns are enriched relative to chondrite and show patterns that vary from shallow to steep (Lu_N = 24–557; Lu_N/Gd_N = 1.66–11.35). Core analysis 06 contains two orders of magnitude higher concentration of Zr, and is considered likely to be contaminated by very fine (~5 µm) inclusion(s) of zircon present in garnet grains (Appendix 2, not plotted in Figure 9). Eu anomalies were not able to be calculated for some garnet analyses due to Sm concentrations below detection limit. However, for analyses where the Eu anomaly was able to be calculated, the garnet 1 core lacks a pronounced Eu anomaly (Eu/Eu* = 1.04), whereas the garnet 1 rim has a negative Eu anomaly (Eu/Eu* = 0.63). For zircon analyses where the Eu anomaly was able to be calculated, zircon has a positive Eu anomaly (Eu/Eu* = 1.18−1.55).

5.4 P–T phase diagram modelling

5.4.1. Sample 103618 (staurolite−biotite-bearing pelite, Talbot Terrane)

The calculated *P−T* pseudosection for sample 103618 based on the geochemical whole rock analysis is presented in Figure 10a. The peak assemblage for sample 103618 is interpreted as staurolite−biotite−chlorite−plagioclase−quartz−ilmenite−magnetite and is interpreted to have formed under subsolidus conditions. H_2O was set to excess and for simplicity is assumed to have been part of the peak assemblage. The stability field corresponding to the peak *P−T* assemblage occurs at ~5.5−8.5 kbar, 600−650 °C (70−120 °C $kbar^{-1}$), which is taken as the best estimate for peak *P−T* conditions.

5.4.2. Sample 113019 (garnet−diopside bearing amphibolite, Connaughton Terrane)

A *P–T* pseudosection calculated for sample 113019 is presented in Fig. 10b. The stability field corresponding to the interpreted peak assemblage garnet–diopside–plagioclase–hornblende–quartz–titanite(sphene)−H_2O (outlined in bold), occurs at ~8–11 kbar, ~620–650 °C, and corresponds to apparent thermal gradients of ~60−80 °C.$kbar^{-1}$. The post-peak evolution is interpreted to involve a relative decrease in garnet and diopside abundance, and relative increase in plagioclase and hornblende abundance. Using relative modal proportion trends for garnet, diopside, hornblende and plagioclase, the post-peak evolution is inferred to have involved a decrease in *P* and *T*. This *P−T* evolution is similar to that inferred by Smithies and Bagas (1997).

6. Discussion

6.1 Garnet and zircon chemistry

Trace element analyses from garnet-bearing amphibolite (sample 113019) in the Rudall Province show enriched, positive sloping normalized HREE trends for garnet cores, and typically show enriched, shallowly positive sloping to negatively sloping normalized HREE trends for garnet rims (Fig. 9), suggesting that during the growth of garnet rims, garnet may have been competing with another phase for HREE (cf. Rubatto, 2002). Zircon REE analyses show positive sloping HREE trends, suggesting that zircon grains may have grown at a time where chemical communication with a HREE reservoir

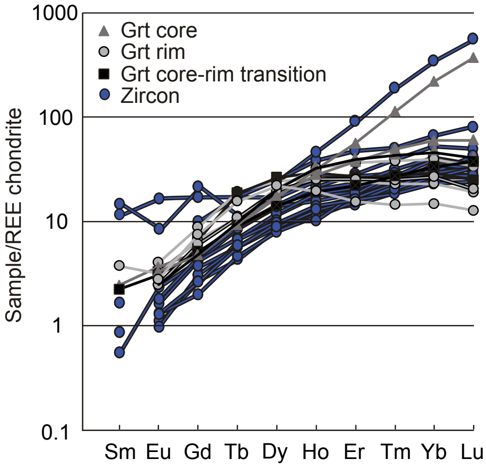

Fig. 9. Chondrite normalised garnet and zircon REE data for sample 113019.

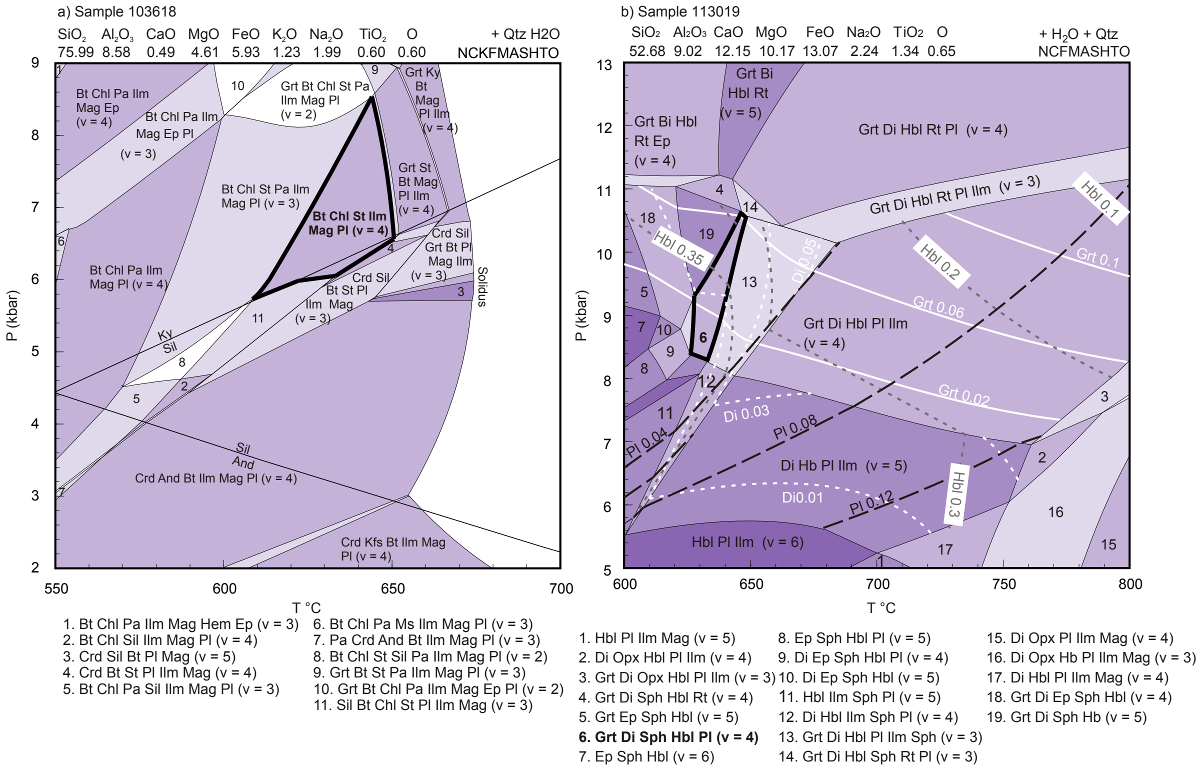

Fig. 10. *P–T* pseudosections for a) sample 103618, peak stability field biotite–chlorite–staurolite–plagioclase–ilmenite–magnetite–quartz–H_2O (v = 4) is shown in bold, and b) P–T pseudosection for sample 113019. Peak stability field garnet–diopside–plagioclase–sphene–hornblende–quartz–H_2O (v = 4) is shown in bold. Modal abundance contours are shown for hornblende (Hbl), plagioclase (Pl) and diopside (Di).

occurred (Fig. 9; cf. Rubatto et al., 2013). Titanite can also incorporate Zr and REEs (e.g. Storkey et al., 2005; Hayden et al., 2008), and it is therefore possible that the positive HREE slope in zircon reflects zircon growth while either titanite or garnet was decreasing in abundance. Mid to heavy REE distribution coefficients of zircon/garnet (${}^{REE}D_{zir}/_{gt}$) are close to 1 (Fig. 9), which is similar to empirical ${}^{REE}D_{zir}/_{gt}$ values obtained where zircon and garnet are interpreted to have co-existed together (e.g. Whitehouse and Platt, 2003; Taylor et al., 2014). The zircon U–Pb age data from diopside–garnet bearing amphibolite sample 113019 is therefore considered to record the timing of moderate-thermal gradient, medium to high-*P* metamorphism (weighted average of 1377 ± 26 Ma).

6.2 Timing of regional metamorphism in the Rudall Province

The Rudall Province is interpreted to have undergone multiple phases of deformation during the Paleoproterozoic to late Neoproterozoic (e.g. Smithies and Bagas, 1997; Bagas et al., 2000; Bagas, 2004). The earliest identified metamorphic event, the M_1–D_1 phase of the Yapungku Orogeny, produced layer parallel schistosity and is interpreted to have developed poorly preserved andalusite bearing assemblages (Hickman and Bagas, 1999). These rare M_1 assemblages have not been dated directly, but have been inferred to be *c.* 1800 Ma, based on a recently reinterpreted intrusive age of the protolith to a banded orthogneiss (*c.* 1801 Ma; Kirkland et al., 2013) that is interpreted to have intruded pre or early D_1, and the *c.* 1800–1760 Ma ages of post-D_1 intrusives of the Kalkan Supersuite (Nelson, 1995; Hickman and Bagas, 1998). Andalusite bearing assemblages could reflect contact metamorphism associated with the intrusion of the Kalkan Supersuite.

The timing of the D_2−M_2 phase of the Yapungku Orogeny was previously interpreted to be *c.* 1800–1765 Ma based on intrusive protolith ages of the variably deformed Kalkan Supersuite, which is considered to have intruded throughout the Yapungku Orogeny (e.g. Nelson, 1995, 1996; Hickman and Bagas, 1998; Bagas et al., 2000; Bagas, 2004). The minimum age for the Yapunkgu Orogeny was constrained at 1778 ± 16 Ma using zircon U−Pb age data from an aplite dyke that is inferred to have intruded a syn-D_2 serpentinised ultramafic rock (Nelson, 1995; Bagas, 2004). However, Maidment (2014) recognised that aplite dykes in the Rudall Province are variably overprinted by S_2 and therefore may only provide a maximum age constraint for the D_2 Yapungku Orogeny. In this study, zircon and in situ monazite U–Pb age data were collected from samples from the Talbot and Connaughton Terranes in order to provide further direct age constraints on metasedimentary-derived rocks. The samples have previously been inferred to contain: 1) S_1 inclusion trails in garnet (sample 113019), 2) an S_2 fabric (samples 103603D, 103617, 103618, 113019, 115638, 115669); and 3) inferred to be late to post S_2 (sample 115866; garnet in sample 115638; sillimanite in sample 115669; results summarised in Table 3; structural characteristics from Smithies and Bagas, 1997; Bagas and Smithies, 1998; Clarke pers. comm). Metamorphic zircon age data combined with zircon and garnet trace element chemistry from sample 113019 is suggestive of moderate thermal gradient, high grade metamorphism occurring at *c.* 1377 Ma. The zircon U–Pb age data from sample 113019, although imprecise does not show more than one age population. This may indicate that if the inclusion trails in garnet do indeed represent an earlier fabric than the main S_2 fabric of the rock (e.g. Bagas and Smithies, 1998), both fabrics developed in a shorter time span than the resolution of the LA–ICP–MS data, or the analysed zircon does not record or preserve the development of both fabrics.

A number of workers have argued that monazite growth or recrystallisation can occur under a variety of conditions during subsolidus metamorphism (e.g. Pyle and Spear, 2003; Kohn and Malloy, 2004; Rubatto et al., 2006; Corrie and Kohn, 2008; Spear and Pyle, 2010; Gasser et al., 2012), high-grade metamorphism and/or along the retrograde path during high-grade metamorphism in rocks that have melted (e.g. Rubatto, 2002; Rubatto et al., 2006; Kelsey et al., 2007; Kelsey et al., 2008; Gasser et al., 2012; Korhonen et al., 2013; Rubatto et al., 2013; Clark et al., 2014; Yakymchuk and Brown, 2014), and diagenesis, hydrothermal mineralisation or fluid alteration/flow (e.g. Williams et al., 2011; Muhling et al., 2012; Halpin et al., 2014). Monazite U–Pb analyses from samples from the Connaughton Terrane together yield age populations between *c.* 1340−1295 Ma. This age range is somewhat younger than an imprecise U−Pb age weighted average of *c.* 1377 ± 26 Ma from metamorphic zircons obtained from a garnet-bearing amphibolite (sample 113019). Whereas as an absence of leucosomes in sample 115669 (quartz-rich, kyanite−sillimanite−quartz metasediment) may suggest that partial melting was limited or did not occur, samples 115638 and 115866 contain leucosomes that are interpreted as a record of partial melting. For rocks that have melted for a typical metapelitic or greywacke composition, it has been suggested based on thermobarometric modelling that monazite is likely to record an age along the retrograde metamorphic *P–T* path (Kelsey et al., 2008; Yakymchuk and Brown, 2014). The monazite grains in these samples are interpreted to have grown on the high-*T* retrograde part of the *P–T* path and may record the crossing of the elevated solidus at *c.* 1341–1307 Ma (e.g. Korhonen et al., 2013). Sample 115669 (kyanite−sillimanite bearing quartzite) is younger outside of uncertainty of sample 115866. As some of the kyanite grains appear to be partially recrystallised parallel to the foliation, it is possible that the high strain foliation development in sample 115669 occurred locally (e.g. close to shear zones) and/or that tectonism during the Mesoproterozoic may be diachronous or involve multiple phases (discussed below).

In the Talbot Terrane, two monazite U–Pb age brackets are obvious in the dataset from this study, at *c.* 1665 Ma and *c.* 1285–1275 Ma. The *c.* 1665 Ma age population was obtained from a single sample (sample 130617; staurolite-bearing schist), whereas the *c.* 1285–1275 Ma age populations were obtained from a staurolite-bearing schist (sample 103618), which is interpreted to contain a S−C fabric defined by chlorite, biotite and staurolite, and a retrogressed kyanite-bearing metapelite (sample 103603D). Some monazite grains in all three samples occur at silicate mineral grain boundaries, in contact with retrograde chlorite or sericite or contain very fine grained inclusions. It is therefore possible that some grains may have grown or recrystallised after peak metamorphism (e.g. during retrogression in sample kyanite bearing sample 103603D). However, the U–Pb ages obtained from the above monazite grains (i.e. silicate grain boundaries) are instinguishable from the remainder of monazite ages from each sample and from the Talbot Terrane are therefore considered to comprise single population in each sample.

The results do not support the contention that the regional peak metamorphism in the Rudall Province was synchronous with the emplacement of the *c.* 1800−1760 Ma Kalkan Supersuite. Instead, the age data suggests that the Rudall Province underwent its main episodes of metamorphism and associated deformation well after the emplacement of the Kalkan Supersuite in the Mesoproterozoic. We consider that the *c.* 1665 Ma monazite age population obtained from a single metapelite in the Talbot Terrane possibly records a poorly preserved tectonothermal event that reached amphibolite facies in the Talbot Terrane. However, it however remains unclear whether the rocks in the Connaughton Terrane also experienced this event.

6.3 Characterising physical and thermal conditions of metamorphism in the Rudall Province

P–T pseudosections were calculated for staurolite-bearing sample 103618 from the Talbot Terrane, and garnet–diopside bearing amphibolite sample 113019 from the Connaughton Terrane to investigate the physical conditions of metamorphism. Existing metamorphic work from the Rudall Province has focused on the elucidation of the Yapungku Orogeny (D_2–M_2) in both the Talbot and Connaughton Terranes assuming the age is *c.* 1800−1760 Ma (Clarke, 1991; Smithies and Bagas, 1997). Rocks in the Talbot and Connaughton Terrane have been interpreted to have experienced moderate-thermal gradient conditions, followed by a steeply decompressive post-peak *P–T* evolution during the Yapungku Orogeny (Smithies and Bagas, 1997).

In this study, amphibolite sample 113019 of the Connaughton Terrane is interpreted to have reached peak *P−T* conditions of ~8–11 kbar, 620–650 °C (apparent thermal gradients of ~60−80 °C kbar^{-1}), followed by a clockwise post-peak evolution. The inferred clockwise post-peak evolution for amphibolite sample is similar to the steeply decompressive post peak *P–T* evolution inferred by Smithies and Bagas (1997), yet the peak temperature obtained in this study is somewhat lower than those obtained by Smithies and Bagas (1997) for the same garnet-bearing amphibolite lithology (up to ~12 kbar, ~770 °C in Smithies and Bagas, 1997). This may be a result of a difference in methodology (conventional thermobarometry compared to *P–T* pseudosection, see Powell and Holland, 2008). It is possible that the discrepancy in temperature estimates may be partly related to the modelled stability of ilmenite and titanite in the pseudosection for sample 113019. In Fig. 10b, the stability field for the peak assemblage is bounded at the high-T side by the introduction of ilmenite stability, which is not present in the sample. In the adjacent higher-T stability field containing ilmenite (field 13), modelled ilmenite is present in small modal proportions (<0.02). It is possible that the modelled stability of titanite and ilmenite in P–T space may be sensitive to small differences in the modelled bulk rock composition compared to the true bulk composition (e.g. small differences in Fe^{3+} or Ti). As a result, we consider Smithies and Bagas (1997) temperature estimates of ~770 °C as the upper limit for the estimated temperature experienced by the garnet-bearing amphibolite during the D_2 Yapungku Orogeny. $P-T$ constraints from staurolite-bearing sample 103618 from the Talbot Terrane in this study implies a moderate to high thermal-gradient regime during Mesoproterozoic metamorphism (~75−110 °C $kbar^{-1}$), and is comparable to qualitative P–T estimates obtained by Clarke (1991). Due to a lack of reaction microstructures in sample 103618 (Talbot Terrane), the post-peak evolution could not be constrained.

Smithies and Bagas (1997) describe a ~400 m^2 garnet−orthopyroxene bearing outcrop ('charnockite' unit in Bagas and Smithies, 1998), from which they obtained very high-thermal gradient P–T conditions (~2–4 kbar, ~800 ºC), and interpreted the unit to have been metamorphosed after D_2–M_2, resulting from possible higher crustal level, post- D_2 granitoids. Garnet–orthopyroxene sample 115866 comes from the same locality and is petrographically identical to the garnet-orthopyroxene sample of Smithies and Bagas (1997). The inferred $P-T$ evolution of the garnet–orthopyroxene bearing rock (Smithies and Bagas, 1997) contrasts with: a) the constrained lower-thermal gradient regime calculated for the mafic-amphibolites from the Connaughton Terrane, and b) the decompressional post-peak $P-T$ evolution inferred for M_2−D_2 (Smithies and Bagas, 1997; this study). Within the Connaughton Terrane, a post-D_2 garnet microgneiss and pegmatite yield U−Pb zircon crystallisation ages of *c.* 1222 and *c.* 1291 Ma respectively (Nelson, 1995, 1996), with a zircon analysis of *c.* 1200 Ma from the garnet microgneiss recently reinterpreted as metamorphic (Kirkland et al., 2013). These constraints suggest that late partial melts probably accompanied Mesoproterozoic metamorphism in the Rudall Province. It is possible that the orthopyroxene-garnet gneiss underwent metamorphism proximal and related to as yet unidentified *c.* 1340 Ma magmatism.

6.4 Implications for the assembly of the NAC and WAC

The Yapungku Orogeny has been interpreted to reflect the collision of the NAC and WAC, which has been used as a basic element of most models that describe the assembly and development of Proterozoic Australia (e.g. Betts and Giles, 2006; Cawood and Korsch, 2008; Payne et al., 2009). The metamorphic record of the Yapungku Orogeny has been interpreted to record thrust stacking and crustal thickening, leading to amphibolite and granulite facies metamorphism (e.g. Smithies and Bagas, 1997; Bagas, 2004).

Mesoproterozoic monazite U–Pb age populations obtained in this study range from *c.* 1340–1275 Ma, and zircon U–Pb age data from amphibolite sample 113019 yielded an age population of *c.*1377 Ma. We consider that both the moderate- to high thermal gradient Yapungku Orogeny (M_2–D_2) and localised high-thermal gradient metamorphism in the Rudall Province are most likely to be Mesoproterozoic-aged, based on the Mesoproterozoic-aged monazite and zircon obtained in this study. Together the zircon and monazite ages span ~100 M.y. (Fig. 11; Table 3). It is possible that this age range reflects: a) monazite and zircon from moderate thermal gradient rocks growing along different stages of the P–T evolution (e.g. possibly zircon growth on the prograde path, monazite recrystallisation in sample 103603D and 103618 post-dating peak metamorphism), b) diachroneity in metamorphism/deformation between terranes and some magmatically-driven metamorphism at least on a local scale,

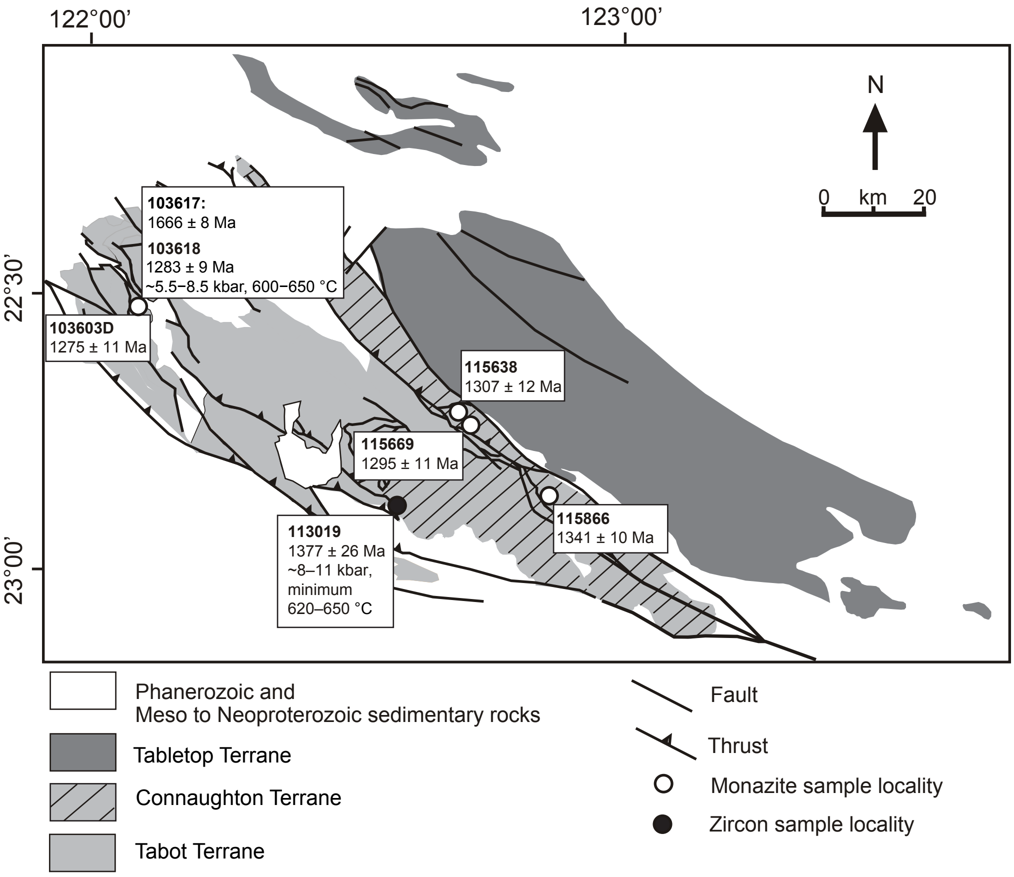

Fig. 11. Simplified map of the Rudall Province showing spatial distribution of zircon and monazite age data and $P-T$ constraints from this study.

Table 3. Summary of U–Pb monazite and zircon age data, and *P–T* estimates obtained in this study

Terrane	Sample	Easting (m E)	Northing (m N)	Mineralogy	Fabric^	Monazite Age (Ma, 95 % conf.)	*P–T* estimates (kbar, °C)
Talbot	103603D	404733	7511111	Ky-Pl-Rt-Ilm (+Chl-Ms-Ser) bearing metapelite	S2	1275 ± 11	
Talbot	103617	405958	7511738	St-Bt-Pl-Ilm-Mag-Qtz, (+Chl) metapelite	S2	1666 ± 8	
Talbot	103618	405958	7511738	St-Bt-Pl-Ilm-Qtz-Chl-Mag metapelite	S2	1283 ± 9	~5.5–8.5, 600–650
Connaughton	115638	466506	7489683	Grt-Sil-Pl-Kfs-Qtz-Rt-Ilm metasediment	S2, late-post S2?	1307 ± 12	
Connaughton	115669	469624	7485385	Ky-Sil-Qtz-Ilm-Mag (+Ms, Ctd) metasediment	S2, sillimanite late-post S2?	1295 ± 11	
Connaughton	115866	485181	7472585	Opx-Grt-Mag-Ilm-Pl-Kfs-Qtz (+ Bt-Chl) gneiss	post-S2	1341 ± 10	
Connaughton	113019	457200	7467600	Di-Grt-Pl-Qtz-Hb-Ttn mafic amphibolite	S1(?)/S2	1377 ± 26	~8–11, 620–650, decreasing *P–T* post-peak evolution

^ From Smithies and Bagas (1997); Bagas and Smithies (1998) or Clarke (pers. comm)

Co-ordinates in UTM, GDA 94, Zone 51K, approximate from aerial photography

c) a long-lived metamorphic/tectonic event, or d) different metamorphic events. Of these alternatives, we tentatively suggest that the range of metamorphic ages is best explained through a stage-wise development of the Rudall Province that involved the accretion of 'ribbons' that were previously derived from the margin of the WAC (cf. Kirkland et al., 2013). In the above proposed tectonic scenario, both moderate thermal gradient and high thermal gradient metamorphic conditions could be attained via accretion (or reattachment) and subsequent outboard migration of subduction, placing accreted the ribbon(s) in a back-arc/arc setting. In this proposed scenario, the final closure of the system probably occurred at *c.* 1300−1280 Ma, or later, marked by the collision of the NAC with ribbons that accreted with the WAC. In this model, the suture between the NAC and accretionary edge to the WAC would lie to the northeast of the Rudall Province, consistent with Kirkland et al. (2013) who showed that the rocks of the Rudall Province have affinities to the WAC.

In the step-wise Mesoproterozoic accretion hypothesis outlined previously, the Yapungku Orogeny is not a single event. Instead, we envisage it to be an accretionary system marked by episodes of thermally contrasting metamorphism that record either the accretion of ribbons or inter-accretionary extension during the Mesoproterozoic. It is not clear to what extent the Rudall Province records the complete amalgamation of the WAC and NAC. The arrangement of rock units and Mesoproterozoic age domains within the Rudall Province have been complicated by later reworking, most notably during the Miles Orogeny and the late Neoproterozoic to Cambrian Paterson Orogeny, the latter involving a substantial amount of strike-slip movement (e.g. Hickman and Bagas, 1999; Bagas, 2004).

The Mesoproterozoic-aged medium-*P* metamorphism in the Rudall Province broadly coincides with the timing of major phases of tectonism in the Musgrave and Albany Fraser Orogens (e.g. Myers et al., 1996; Giles et al., 2004; Betts and Giles, 2006; Cawood and Korsch, 2008; Wade et al., 2008; Aitken and Betts, 2009; Spaggiari et al., 2009; Smithies et al., 2011). Stage I of the Albany Fraser Orogeny (*c.* 1340–1260 Ma) has been interpreted to be a response to the collision of the WAC with the SAC/Mawson Continent (e.g. Clark et al., 2000) and/or alternatively reflect the closure of a marginal ocean basin and accretion of the Loongana Magmatic Arc to the WAC, prior to the final convergence of the WAC and SAC/Mawson Continent (Spaggiari et al., 2014). In the western Musgrave Province, the tectonic setting of the *c.* 1345–1292 Ma Mount West Orogeny remains uncertain. However, the Mount West Orogeny involved the emplacement of metaluminous, calc to calc-alkaline granitoids of the Wankanki Supersuite, which are geochemically similar to those that occur in modern day continental-arc settings (Smithies et al., 2010; Smithies et al., 2011).

The temporal similarities of Mesoproterozoic tectonism in the Albany-Fraser Orogen, Musgrave and Rudall Provinces and the spatial occurrence of these three provinces/orogens either on the margin of, or between, older Archean–Paleoproterozoic cratonic elements suggests that Mesoproterozoic tectonism may reflect the protracted amalgamation of the WAC, NAC and SAC between *c.* 1375 and 1150 Ma (e.g. Myers et al., 1996; Smits et al., 2014).

6.5 Implications for supercontinent Nuna reconstructions

Globally, the *c.* 1400−1300 Ma timeline corresponds to the interpreted initiation of the breakup of supercontinent Nuna (Pisarevsky et al., 2014a; Pisarevsky et al., 2014b). An implication for the proposed Mesoproterozoic assembly of Proterozoic Australia is that the need for the components of Australia to be connected during supercontinent Nuna is no longer required. Recent paleomagnetic constraints from the WAC indicate Australia and Laurentia were widely separated by *c.* 1210 Ma (Pisarevsky et al., 2014b). We suggest that following the accretion of the NAC to Laurentia at *c.* 1550−1500 Ma in either a modified SWEAT (South West U.S.-East Antarctic; Moores, 1991) or AUSWUS (Australia-Western U.S.; Karlstrom et al., 1999) style configuration (Fig. 12a), the NAC migrated as a ribbon away from Laurentia at *c.* 1450 Ma (e.g. Medig et al., 2014) and collided with the WAC at *c.* 1300 Ma (Fig. 12b). In Laurentia, removal of the NAC ribbon coincided with the formation of the rift Belt Superbasin system. The Mawson Continent (SAC and east Antarctica) collided with the NAC−WAC between *c.* 1250−1150 Ma (e.g. Smits et al., 2014). If correct, Laurentia and Australia have been disconnected since the late Mesoproterozoic and a Neoproterozoic SWEAT connection is not likely. In our preferred model, a Mesoproterozoic AUSWUS-style connection by *c.* 1250 Ma (Fig. 12c) allows the transcontinental Musgrave-Albany Fraser orogen (Smits et al., 2014) to directly connect with the Grenvillian super-orogen (cf. Van Kranendonk and Kirkland, 2013).

7. Conclusions

The age of the Yapungku Orogeny in the Rudall Province has long been interpreted to be Paleoproterozoic. However, monazite age data from metasedimentary rocks of the Connaughton and Talbot Terrane indicate the Yapungku Orogeny (D_2−M_2) is Mesoproterozoic-aged. We propose that medium-*P* metamorphism with moderate to high-thermal gradients reflects the amalgamation of the WAC and NAC during the Mesoproterozoic rather than Paleoproterozoic via a stage-wise evolution. If this is correct, a Mesoproterozoic timeline for the amalgamation of the major cratonic elements of Proterozoic Australia is supported, which feasibly occurred during the breakup stages of supercontinent Nuna.

References

Aitken, A.R.A., Betts, P.G., 2009. Constraints on the Proterozoic supercontinent cycle from the structural evolution of the south-central Musgrave Province, central Australia. Precambrian Research 168, 284-300.

Bagas, L., 2004. Proterozoic evolution and tectonic setting of the northwest Paterson Orogen, Western Australia. Precam brian Research 128, 475-496.

Bagas, L., Smithies, R.H., 1998. Geology of the Connaughton 1:100 000 Sheet, 1:100 000 Geological Series Explanatory Notes. Geological Survey of Western Australia, Perth, p. 38.

Bagas, L., Williams, I.R., Hickman, A.H., 2000. Rudall, 1:250 000 Geological Series Explanatory Notes, 2 ed. Western Australia Geological Survey, Perth, p. 50.

Betts, P.G., Giles, D., 2006. The 1800-1100 Ma tectonic evolution of Australia. Precambrian Research 144, 92-125.

Betts, P.G., Giles, D., Lister, G.S., Frick, L.R., 2002. Evolution of the Australian Lithosphere. Australian Journal of Earth Sciences 49, 661-695.

Betts, P.G., Giles, D., Mark, G., Lister, G.S., Goleby, B.R., Ailleres, L., 2006. Synthesis of the proterozoic evolution of the Mt Isa Inlier. Australian Journal of Earth Sciences 53, 187-211.

Brown, M., 2007. Metamorphic conditions in orogenic belts: a re cord of secular change. International Geology Review 49, 193-234.

Camacho, A., McDougall, I., 2000. Intracratonic, strike-slip parti tioned transpression and the formation and exhumation of eclogite facies rocks: An example from the Musgrave Block, central Australia. Tectonics 19, 978-996.

Cawood, P.A., Korsch, R.J., 2008. Assembling Australia: Proterozo

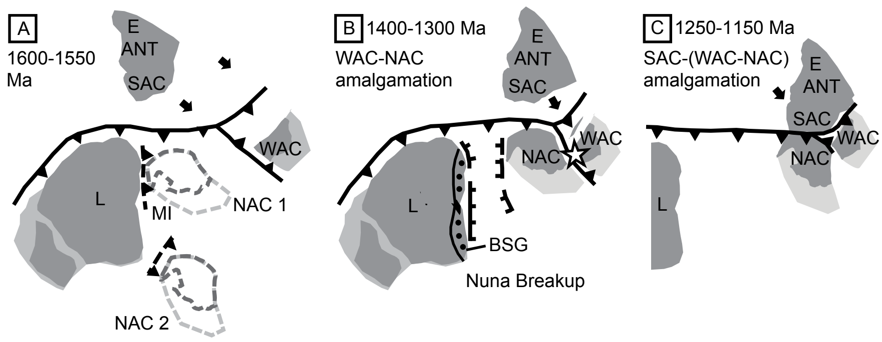

Fig. 12. Simplified schematic tectonic model of Proterozoic Australia and Laurentia at *c.* 1600−1550 Ma− arc extending from Laurentia to the WAC. Also shown are possible modified AUSWUS (NAC1; after Karlstrom et al., 1999) and SWEAT-like configurations (NAC2; after Moores, 1991). B: 1400−1300 Ma− NAC extracted from western Laurentia at around 1450 Ma, associated with development of Belt Supergroup rift system, docking of the WAC to NAC reflected by the Yapungku Orogeny in the Rudall Province (star), and commencement of Stage I of the Albany Fraser Orogeny (AFO) at *c.* 1330 Ma in modified AUSWUS style configuration. C: 1250−1150 Ma− final convergence of major cratonic elements of Proterozoic Australia (reconstruction following Li and Evans, 2011). BSG = Belt Supergroup and equivalents (Medig et al., 2014), L = Laurentia, E ANT = E Antarctica, SAC = South Australian Craton, NAC = North Australian Craton, WAC = West Australian Craton.

ic building of a continent. Precambrian Research 166, 1-38.

Chin, R.J., de Laeter, J.R., 1981. The relationship of new Rb-Sr iso topic dates from the Rudall Complex to the geology of the Paterson Province, Geological Survey of Western Australia Annual Report 1980, Perth, pp. 132-139.

Clark, C., Kirkland, C.L., Spaggiari, C.V., Oorschot, C., Wingate, M.T.D., Taylor, R.J., 2014. Proterozoic granulite forma tion driven by mafic magmatism: An example from the Fraser Range Metamorphics, Western Australia. Precambrian Research 240, 1-21.

Clark, D.J., Hensen, B.J., Kinny, P.D., 2000. Geochronological constraints for a two-stage history of the Albany-Fraser Orogen, Western Australia. Precambrian Research 102, 155-183.

Clarke, G.L., 1991. Proterozoic Tectonic Reworking In the Rudall Complex, Western Australia. Australian Journal of Earth Sciences 38, 31-44.

Coggon, R., Holland, T.J.B., 2002. Mixing properties of phengitic micas and revised garnet-phengite thermobarometers. Journal of Metamorphic Geology 20, 683-696.

Corfu, F., Hanchar, J.M., Hoskin, P.W.O., Kinny, P.D., 2003. Atlas of zircon textures, in: Hanchar, J.M., Hoskin, P.W.O. (Eds.), Zircon. Mineralogical Society of America, Reviews in Mineralogy and Geochemistry, Washington, D.C., pp. 468-500.

Corrie, S.L., Kohn, M.J., 2008. Trace-element distributions in silicates during prograde metamorphic reactions: impli cations for monazite formation. Journal of Metamorphic Geology 26, 451-464.

Czarnota, K., Gerner, E., Maidment, D., Meixner, A., Bagas, L., 2009. Paterson Area 1:250 000 Scale Solid Geology Interpretation and Depth to Basement Model. Geoscience Australia, Canberra.

Diener, J.F.A., Powell, R., White, R.W., Holland, T.J.B., 2007. A new thermodynamic model for clino- and orthoamphi boles in the system Na_2O-CaO-FeO-MgO-Al_2O_3-SiO_2-H_2O-O. Journal of Metamorphic Geology 25, 631-656.

Droop, G.T.R., 1987. A General equation for estimating Fe3+ con centrations in ferromagnesian silicates and oxides from Microprobe analyses, using stoichiometric criteria. Min eralogical Magazine 51, 431-435.

Gasser, D., Bruand, E., Rubatto, D., Stüwe, K., 2012. The behaviour of monazite from greenschist facies phyllites to anatectic gneisses: An example from the Chugach Metamorphic Complex, southern Alaska. Lithos 134–135, 108-122.

Giles, D., Betts, P.G., Lister, G.S., 2004. 1.8-1.5 Ga links between the North and South Australian Cratons and the Ear ly-Middle Proterozoic configuration of Australia. Tec tonophysics 380, 27-41.

Green, E., Holland, T., Powell, R., 2007. An order-disorder model for omphacitic pyroxenes in the system jadeite-diop side-hedenbergite-acmite, with applications to eclogitic rocks. American Mineralogist 92, 1181-1189.

Griffin, W.L., Powell, W.J., Pearson, N.J., O'Reilly, S.Y., 2008. GLITTER: data reduction software for laser ablation ICP-MS, in: Sylvester, P. (Ed.), Laser Ablation ICP-MS in the Earth Sciences: Current Practices and Outstanding Issues. Mineralogical Association of Canada. Shourt Course Series 40, pp. 308-311.

GSWA, 1999. Rudall Sheet SF 51-10, 1:250,000 map sheet, 2 ed. Geological Survey of Western Australia, Perth.

Halpin, J.A., Jensen, T., McGoldrick, P., Meffre, S., Berry, R.F., Everard, J.L., Calver, C.R., Thompson, J., Goemann, K., Whittaker, J.M., 2014. Authigenic monazite and detrital zircon dating from the Proterozoic Rocky Cape Group, Tasma nia: Links to the Belt-Purcell Supergroup, North Ameri ca. Precambrian Research 250, 50-67.

Hayden, L., Watson, E.B., Wark, D., 2008. A thermobarometer for sphene (titanite). Contributions to Mineralogy and Petrol ogy 155, 529-540.

Hickman, A.H., Bagas, L., 1998. Geology of the Rudall 1:100 000 sheet, Western Australia, Western Australia Geological Survey 1:100 000 Geological Explanatory Notes. West ern Australia Geological Survey, Perth, p. 30.

Hickman, A.H., Bagas, L., 1999. Geological evolution of the Palaeo proterozoic Talbot Terrane and adjacent Meso- and Neo-proterozoic successions, Paterson Orogen, Western Australia. Report of the Geological Survey of Western Australia, p. 91.

Holland, T., Baker, J., Powell, R., 1998. Mixing properties and activ ity-composition relationships of chlorites in the system MgO-FeO-Al_2O_3-SiO_2-H2O. European Journal of Miner alogy 10, 395-406.

Holland, T., Powell, R., 2003. Activity–composition relations for phases in petrological calculations: an asymmetric multi component formulation. Contributions to Mineralogy and Petrology 145, 492-501.

Holland, T.J.B., Powell, R., 1998. An internally consistent ther modynamic data set for phases of petrological interest. Journal of Metamorphic Geology 16, 309-343.

Huston, D., Blewett, R.S., Champion, C., 2012. Australia through time: a summary of its tectonic and metallogenic evolu tion. Elements 35, 23-43.

Johnson, S.P., 2013. WA Unearthed: The birth of supercontinents and the Proterozoic Assembly of Western Australia. Geological Survey of Western Australia, Perth.

Karlstrom, K.E., Harlan, S.S., Williams, M.L., McLelland, J., Geiss man, J.W., Ahall, K., 1999. Refining Rodinia: Geologic Evidence for the Australia-Western U.S. connection in the Proterozoic. GSA Today 9, 1-7.

Kelsey, D.E., Clark, C., Hand, M., 2008. Thermobarometric modeling of zircon and monazite growth in melt-bearing systems: examples using model metapelitic and metapsammitic granulites. Journal of Metamophic Geol ogy 26, 199-212.

Kelsey, D.E., Hand, M., Clark, C., Wilson, C.J.L., 2007. On the ap plication of in situ monazite chemical geochronology to constraining P-T-t histories in high-temperature (>850 degrees C) polymetamorphic granulites from Prydz Bay, East Antarctica. Journal of the Geological Society, Lon don 164, 667-683.

Kirkland, C.L., Johnson, S.P., Smithies, R.H., Hollis, J.A., Wingate, M.T.D., Tyler, I.M., Hickman, A.H., Cliff, J.B., Tessalina, S., Belousova, E.A., Murphy, R.C., 2013. Not-so-suspect terrane: Constraints on the crustal evolution of the Rudall Province. Precambrian Research 235, 131-149.

Kohn, M.J., Malloy, M.A., 2004. Formation of monazite via pro grade metamorphic reactions among common silicates: Implications for age determinations. Geochimica Et Cosmochimica Acta 68, 101-113.

Korhonen, F.J., Clark, C., Brown, M., Bhattacharya, S., Taylor, R., 2013. How long-lived is ultrahigh temperature (UHT) metamorphism? Constraints from zircon and monazite geochronology in the Eastern Ghats orogenic belt, India. Precambrian Research 20, 764-781.

Li, Z.X., 2000. Palaeomagnetic evidence for unification of the North and West Australian cratons by ca.1.7 Ga: new results from the Kimberley Basin of northwestern Australia. Geophysical Journal International 142, 173-180.

Li, Z.X., Evans, D.A.D., 2011. Late Neoproterozoic 40 degrees intraplate rotation within Australia allows for a tighter-fit ting and longer-lasting Rodinia. Geology 39, 39-42.

Ludwig, K.R., 2008. Isoplot: A Geochronological Toolkit for Micro soft Excel, 3.7 ed. Berkeley Geochronology Centre, Berkeley.

Maidment, D., 2005. Paleozoic high-grade metamorphism within the Centralian Superbasin, Harts Range region, central Aus tralia (PhD thesis). Australian National University, Can berra, p. 422.

Maidment, D., 2007. New timing constraints on the evolution of the Rudall Complex, Western Australia- Implications for Proterozoic Reconstructions, in: Collins, A.S. (Ed.), SGTSG 2007 Deformation in the Desert, Geological Society of Australia, Alice Springs.

Maidment, D., 2014. When did the WAC whack the NAC? Docking of the West and North Australian Cratons, Australian Earth Science Convention. Geological Society of Austra lia Abstracts, Newcastle.

Medig, K.P.R., Thorkelson, D.J., Davis, W.J., Rainbird, R.H., Gib son, H.D., Turner, E.C., Marshall, D.D., 2014. Pinning northeastern Australia to northwestern Laurentia in the Mesoproterozoic. Precambrian Research 249, 88-99.

Moores, E.M., 1991. Southwest U.S.-East Antarctica (SWEAT) connection: A hypothesis. Geology 19, 425-428.

Muhling, J.R., Fletcher, I.R., Rasmussen, B., 2012. Dating fluid flow and Mississippi Valley type base-metal mineraliza tion in the Paleoproterozoic Earaheedy Basin, Western Australia. Precambrian Research 212–213, 75-90.

Myers, J.S., Shaw, R.D., Tyler, I.M., 1996. Tectonic evolution of Proterozoic Australia. Tectonics 15, 1431-1446.

Nelson, D.R., 1995. Compilation of SHRIMP U-Pb zircon geo chronology data, 1994. West Australian Geological Survey Record 1995/3, 244.

Nelson, D.R., 1996. Compilation of SHRIMP U-Pb zircon geo chronology data, 1995, Record 1996/5. West Australian Geological Survey, Record 1996/5, Perth, p. 168.

Neumann, N.L., Fraser, G.L., 2007. Geochronological synthesis and timespace plots for Proterozoic Australia. Geosci ence Australia, Canberra, p. 216.

Payne, J.L., Hand, M., Barovich, K.M., Reid, A., Evans, D.A.D., 2009. Correlations and reconstruction models for the 2500-1500 Ma evolution of the Mawson Continent, in:

Reddy, S.M., Mazumder, R., Evans, D.A.D., and Collins, A.S. (Ed.), Palaeoproterozoic Supercontinents and Global Evolution, pp. 319-355.

Payne, J.L., Hand, M., Barovich, K.M., Wade, B.P., 2008. Temporal constraints on the timing of high-grade metamorphism in the northern Gawler Craton; implications for assembly of the Australian Proterozoic. Australian Journal of Earth Sciences 55, 623-640.

Pisarevsky, S.A., Elming, S.-Å., Pesonen, L.J., Li, Z.-X., 2014a. Mesoproterozoic paleogeography: Supercontinent and beyond. Precambrian Research 244, 207-225.

Pisarevsky, S.A., Wingate, M.T., Li, Z.-X., Wang, X.-C., Tohver, E., Kirkland, C.L., 2014b. Age and paleomagnetism of the 1210Ma Gnowangerup–Fraser dyke swarm, Western Australia, and implications for late Mesoproterozoic paleogeography. Precambrian Research 246, 1-15.

Powell, R., Holland, T.J.B., 1988. An internally consistent thermo dynamic dataset with uncertainties and correlations: 3. Applications to geobarometry, worked examples and a computer program. J. Metamorphic Geol. 6, 173-204.

Powell, R., Holland, T.J.B., 2008. On thermobarometry. Journal of Metamorphic Geology 26, 155-179.

Pyle, J.M., Spear, F.S., 2003. Four generations of accessory-phase growth in low-pressure migmatites from SW New Hamp shire. American Mineralogist 88, 338-351.

Raimondo, T., Collins, A.S., Hand, M., Walker-Hallam, A., Smithies, R.H., Evins, P.M., Howard, H.M., 2009. Ediacaran intra continental channel flow. Geology 37, 291-294.

Raimondo, T., Collins, A.S., Hand, M., Walker-Hallam, A., Smith ies, R.H., Evins, P.M., Howard, H.M., 2010. The anato my of a deep intracontinental orogen. Tectonics 29, 1-31.

Rubatto, D., 2002. Zircon trace element geochemistry: partitioning with garnet and the link between U-Pb ages and meta morphism. Chemical Geology 184, 123-138.

Rubatto, D., Chakraborty, S., Dasgupta, S., 2013. Timescales of crustal melting in the Higher Himalayan Crystallines (Sikkim, Eastern Himalaya) inferred from trace ele ment-constrained monazite and zircon chronology. Con tributions to Mineralogy and Petrology 165, 349-372.

Rubatto, D., Hermann, J., Buick, I.S., 2006. Temperature and bulk composition control on the growth of monazite and zircon during low-pressure anatexis (Mount Stafford, central Australia). Journal of Petrology 47, 1973-1996.

Smithies, R.H., Bagas, L., 1997. High pressure amphibolite-granu lite facies metamorphism in the Paleoproterozoic Rudall Complex, central Western Australia. Precambrian Re search 83, 243-265.

Smithies, R.H., Howard, H.M., Evins, P., Kirkland, C.L., Kelsey, D.E., Hand, M., Wingate, M.T.D., Collins, A.S., 2010. Geochemistry, geochronology, and pretrogenesis of Mesoproterozoic felsic rocks in the West Musgrave Province, central Australia, and implications for the Mesoproterozoic tectonic evolution of the region. Geo logical Survey of Western Australia, Perth.

Smithies, R.H., Howard, H.M., Evins, P.M., Kirkland, C.L., Kelsey, D.E., Hand, M., Wingate, M.T.D., Collins, A.S., Belouso va, E., 2011. High-Temperature Granite Magmatism, Crust-Mantle Interaction and the Mesoproterozoic Intra continental Evolution of the Musgrave Province, Central Australia. Journal of Petrology 52, 931-958.

Smits, R.G., Collins, W.J., Hand, M., Dutch, R., Payne, J., 2014. A Proterozoic Wilson cycle identified by Hf isotopes in central Australia: Implications for the assembly of Proterozoic Australia and Rodinia. Geology 42, 231-234.

Spaggiari, C.V., Bodorkos, S., Barquero-Molina, Tyler, I.M., Wingate, M.T.D., 2009. Interpreted Bedrock Geology of the South Yilgarn and central Albany-Fraser Orogen, Western Australia. Geological Survey of Western Austra lia, Perth.

Spaggiari, C.V., Kirkland, C.L., Smithies, R.H., Wingate, M.T.D., 2014. Tectonic links between Proterozoic sedimenta ry cycles, basin formation and magmatism in the Alba ny-Fraser Orogen, Western Austraia. Geological Survey of Western Australia, Perth.

Spear, F.S., Pyle, J.M., 2010. Theoretical modeling of monazite growth in a low-Ca metapelite. Chemical Geology 273, 111-119.

Stern, R.A., Bodorkos, S., Kamo, S.L., Hickman, A.H., Corfu, F., 2009. Measurement of SIMS Instrumental Mass Frac tionation of Pb Isotopes During Zircon Dating. Geostan dards and Geoanalytical Research 33, 145-168.

Storkey, A.C., Hermann, J., Hand, M., Buick, I.S., 2005. Using in situ trace-element determinations to monitor partial-melt ing processes in metabasites. Journal of Petrology 46, 1283-1308.

Taylor, R.J.M., Clark, C., Fitzsimons, I.C.W., Santosh, M., Hand, M., Evans, N., McDonald, B., 2014. Post-peak, fluid-me diated modification of granulite facies zircon and monazite in the Trivandrum Block, southern India. Con tributions to Mineralogy and Petrology 168, 1-17.

Van Kranendonk, M.J., Kirkland, C.L., 2013. Orogenic climax of Earth: The 1.2-1.1 Ga Grenvillian superevent. Geology 41, 735-738.

Wade, B.P., Hand, M., Barovich, K.M., 2005. Nd isotopic and geochemical constraints on provenance of sedimentary rocks in the eastern Officer Basin, Australia; implications for the duration of the intracratonic Petermann Orogeny. Journal of the Geological Society, London 162, 513-530.

Wade, B.P., Kelsey, D.E., Hand, M., Barovich, K.M., 2008. The Musgrave Province: Stitching north, west and south Australia. Precambrian Research 166, 370-386.

Walsh, A.K., Raimondo, T., Kelsey, D.E., Hand, M., Pfitzner, H.L., Clark, C., 2013. Duration of high-pressure metamor phism and cooling during the intraplate Petermann Orog eny. Gondwana Research 24, 969-983.

White, Powell, Holland, Worley, 2000. The effect of TiO2 and $F_{e2}O_3$ on metapelitic assemblages at greenschist and amphibo lite facies conditions: mineral equilibria calculations in the system K_2O–FeO–MgO–Al_2O_3–SiO_2–H_2O–TiO_2–Fe_2O_3. Journal of Metamorphic Geology 18, 497-511.

White, R.W., Powell, R., Holland, T.J.B., 2007. Progress relating to calculation of partial melting equilibria for metapelites. Journal of Metamorphic Geology 25, 511-527.

Whitehouse, M.J., Platt, J.P., 2003. Dating high-grade metamor phism - constraints from rare-earth elements in zircon and garnet. Contributions to Mineralogy and Petrology 145, 61-74.

Williams, I.R., Bagas, L., 1999. Geology of the Throssell 1:100,000 sheet, 1:100,000 Geological Series Explanatory Notes.

Geological Survey of Western Australia, Perth, p. 24.
Williams, M.L., Jercinovic, M.J., Harlov, D.E., Budzyn, B., Heth erington, C.J., 2011. Resetting monazite ages during fluid-related alteration. Chemical Geology 283, 218-225.
Yakymchuk, C., Brown, M., 2014. Behaviour of zircon and monazite during crustal melting. Journal of the Geologi cal Society, London 171, 465-479.

Supporting Information

Appendix 1: Mineral chemistry

Garnet

In sample 115866, fine-grained garnet grains located in the matrix typically have X_{Alm} values that increase from core to rim (~0.54–0.62), X_{Py} values that decrease from core to rim (~0.38–0.32), X_{Grs} values of ~0.02 and X_{Spss} values of ~0.05. Garnet occurring as coronas on magnetite or ilmenite, or within quartz-garnet intergrowths have X_{Alm} values of 0.57–0.64, X_{Py} values of ~0.27–0.35, X_{Grs} values of ~0.02 and X_{Spss} values of 0.05–0.06.

Pyroxene

Orthopyroxene is present in sample 115866 and has X_{Mg} values of ~0.59−0.60, with Al_2O_3 content of ~9.70−10.1 wt. %. Orthopyroxene has 4.05–4.35 wt. % Fe_2O_3 using the stoichiometric calculation method of Droop (1987). Calculated y(opx)1 values are 0.18−0.18 without Fe_2O_3 recalculation and 0.15−0.16 recalculated with Fe_2O_3, (y(opx)1 = $C_{\mathrm{Si,\ total}}$ (opx) + $C_{\mathrm{Al,total}}$ (opx − 2), where C_{i} is cations of i). Orthopyroxene has 4.05–4.35 wt.% Fe_2O_3.

Feldspar

Alkali feldspar in sample 115866 has X_{Or} values of ~0.66–0.84 and X_{An} values of ~0.01–0.07. In sample 103617 and 103618, plagioclase is albite, with X_{Na} (= Na/(Na+Ca)) values of 0.98−0.99 and 0.96−0.97 respectively. Plagioclase in sample 115866 has X_{An} (=Ca/(Na+Ca+K)) values of ~0.43–0.44 and X_{Or} values of ~0.01 (=K/(Na+Ca+K)).

Staurolite

In sample 103617, staurolite has X_{Mg} values of 0.19−0.22 and ZnO wt. % values of 0.02−0.13. In sample 103618, staurolite has X_{Mg} values of 0.18−0.20 and ZnO wt. % values of 0.03−0.12.

Biotite

In sample 115866, biotite has X_{Mg} values of 0.66−0.78 and 2.0−4.5 wt. % TiO_2. Biotite in sample 103617 has X_{Mg} values of 0.59−0.60 and wt. % TiO_2 content of 1.12−1.33. Biotite in sample 103618 has X_{Mg} values of ~0.56 and wt. % TiO_2 content of 1.16−1.42.

Chlorite

Chlorite has X_{Mg} values of 0.63−0.64 in sample 103617 and X_{Mg} values of 0.59−0.61 in 103618.

Ilmenite

Ilmenite in sample 115866 has 1.87–4.47 wt. % Fe_2O_3 calculated using the method of Droop (1987)x, 0.12−0.70 wt. % MgO and 1.74−2.91 wt. % MnO.

Magnetite-Spinel

In sample 115866, magnetite usually occurs with spinel and/or corundum and has Al_2O_3 wt. % content of 0.19−0.26. Spinel occurs with magnetite and/or corundum and has ZnO content of ~9.2 wt. %, MgO content of ~3.7 wt. % and Cr_2O_3 values of 0.10 wt. %. In sample 103617, magnetite has Al_2O_3 wt. % content of 0.08−0.15, and in sample 103618, magnetite has Al_2O_3 wt. % content of 0.46−0.47.

Appendix 2. U-Pb isotopic age data for monazite analyses
Sample 103603D

Spot	$^{207}Pb/^{206}Pb$	1 σ	$^{206}Pb/^{238}U$	1 σ	$^{207}Pb/^{235}U$	1 σ	rho	Conc. (%)	$^{207}Pb/^{206}Pb$ age	1 σ	$^{206}Pb/^{238}U$ age	1 σ	$^{207}Pb/^{235}U$ age	1 σ	^{204}Pb	^{206}Pb	^{207}Pb	^{238}Pb
M01-2	0.08429	0.00099	0.22249	0.00297	2.58431	0.0369	0.93489792	99.68	1299.1	22.73	1295	15.64	1296.2	10.45	0	103253	8869	609471
M02-2	0.08329	0.00098	0.22249	0.00297	2.55388	0.03644	0.9355523	101.50	1275.9	22.82	1295	15.65	1287.5	10.41	11	123748	10500	731353
M03	0.08366	0.00093	0.2263	0.00368	2.60882	0.04331	0.97953328	102.39	1284.4	21.51	1315.1	19.36	1303.1	12.19	1	117367	9997	838540
M04	0.08328	0.00094	0.22296	0.00361	2.55837	0.04246	0.97558162	101.72	1275.5	22.02	1297.5	19	1288.8	12.12	0	132627	11274	954624
M04-2	0.08277	0.00097	0.2194	0.00293	2.50268	0.03572	0.93567466	101.18	1263.8	22.57	1278.7	15.49	1272.8	10.36	0	108611	9156	652075
M05†	0.08337	0.00097	0.22606	0.00373	2.59748	0.04432	0.9670247	102.82	1277.8	22.61	1313.8	19.59	1299.9	12.51	3	90540	7701	654079
M05A-2	0.07933	0.00095	0.21498	0.00288	2.35029	0.03395	0.92741924	106.35	1180.4	23.42	1255.3	15.28	1227.6	10.29	0	77066	6228	472453
M05B-2	0.08329	0.00099	0.2063	0.00276	2.36809	0.0341	0.92908121	94.77	1275.8	23.1	1209.1	14.74	1233	10.28	0	120449	10212	768824
M06	0.0836	0.00101	0.21975	0.00362	2.53141	0.04376	0.95293848	99.80	1283.1	23.41	1280.5	19.14	1281.1	12.58	2	110357	9429	818324
M06-2	0.08308	0.00099	0.22303	0.00298	2.55355	0.03683	0.92639377	102.11	1271.1	23.01	1297.9	15.73	1287.5	10.52	12	92784	7861	547838
M07	0.08265	0.00094	0.24141	0.00396	2.74994	0.04659	0.96821195	110.54	1261.1	22.02	1394	20.58	1342.1	12.61	4	120101	10095	810566
M08	0.08331	0.001	0.22529	0.00371	2.5864	0.04463	0.95433488	102.62	1276.3	23.34	1309.8	19.51	1296.8	12.63	12	108670	9237	785487
M08-2	0.08196	0.00101	0.2202	0.00295	2.48707	0.03653	0.91210122	103.07	1244.7	23.94	1282.9	15.58	1268.3	10.64	6	90781	7582	541604
M08B-2	0.08262	0.00111	0.22203	0.00299	2.52815	0.03914	0.86984435	102.56	1260.3	25.86	1292.6	15.75	1280.2	11.26	2	106122	8926	624915
M09	0.08406	0.00098	0.23186	0.00381	2.68617	0.04603	0.95894051	103.88	1294	22.62	1344.2	19.96	1324.7	12.68	0	101091	8632	710797
M10-2	0.08321	0.00102	0.22824	0.00306	2.61752	0.03844	0.91292752	104.03	1274	23.85	1325.3	16.07	1305.6	10.79	0	97200	8234	560905
M11	0.08374	0.00119	0.21548	0.00353	2.486	0.04582	0.88881992	97.78	1286.4	27.36	1257.9	18.73	1268	13.35	0	88984	7579	660745
M11B	0.08368	0.00114	0.23073	0.00378	2.6598	0.04817	0.90460726	104.16	1284.9	26.44	1338.3	19.79	1317.4	13.36	2	152493	13034	1060496
M11-2	0.078	0.00112	0.16591	0.00229	1.78231	0.02937	0.8376107	86.28	1146.8	28.38	989.5	12.64	1039	10.72	0	55559	4396	445105
M12	0.08271	0.00113	0.22818	0.0038	2.60059	0.04768	0.90832583	104.96	1262.4	26.32	1325	19.96	1300.8	13.45	0	97233	8245	695816
M13-2	0.08294	0.00109	0.22068	0.00296	2.52268	0.03853	0.87819688	101.40	1267.7	25.35	1285.5	15.64	1278.6	11.11	9	107849	9095	639376

†Discarded due to noisy isotopic signal or blasted through grain

All individual isotopic abundancesare in cps

Appendix 2. U-Pb isotopic age data for monazite analyses

Sample 103617

Spot	$^{207}Pb/^{206}Pb$	1 σ	$^{206}Pb/^{238}U$	1 σ	$^{207}Pb/^{235}U$	1 σ	rho	Conc. (%)	$^{207}Pb/^{206}Pb$ age	1 σ	$^{206}Pb/^{238}U$ age	1 σ	$^{207}Pb/^{235}U$ age	1 σ	^{204}Pb	^{206}Pb	^{207}Pb	^{238}Pb
M02	0.08833	0.00107	0.25912	0.00367	3.15515	0.0481	0.92905209	106.89	1389.6	23.03	1485.3	18.79	1446.3	11.75	30	176291	15868	947486
M03	0.0991	0.00119	0.29852	0.00415	4.0787	0.06078	0.93290137	104.77	1607.3	22.26	1684	20.61	1650.1	12.15	15	95639	9668	436979
M05	0.10184	0.00124	0.28485	0.00407	3.99963	0.06131	0.93210897	97.45	1658	22.46	1615.7	20.41	1634.1	12.45	0	44006	4561	215751
M09A	0.10081	0.00121	0.29228	0.0041	4.06223	0.06067	0.93923717	100.85	1639	22.03	1652.9	20.45	1646.8	12.17	0	55744	5739	262309
M09B	0.10144	0.00117	0.29146	0.00408	4.07596	0.05995	0.9517479	99.89	1650.6	21.26	1648.8	20.36	1649.5	11.99	1	79107	8174	374404
M09C	0.09736	0.00107	0.2964	0.00415	3.97815	0.0574	0.97037402	106.31	1574.1	20.47	1673.4	20.65	1629.7	11.71	13	167945	16675	787037
M10	0.09962	0.00107	0.29222	0.0041	4.01159	0.05735	0.98142482	102.20	1617	19.85	1652.6	20.47	1636.5	11.62	9	131794	13349	629009
M10	0.1017	0.00121	0.302	0.0043	4.23392	0.06389	0.9435638	102.77	1655.4	21.88	1701.2	21.28	1680.6	12.39	14	36005	3735	166461
M13	0.10278	0.00115	0.29627	0.00417	4.19771	0.06124	0.96477408	99.87	1675	20.52	1672.8	20.72	1673.6	11.96	29	166658	17457	783417
M14	0.10031	0.00109	0.30032	0.00422	4.15136	0.05969	0.9772755	103.87	1629.8	20.02	1692.9	20.92	1664.5	11.76	0	96384	9805	447326
M14	0.10187	0.00117	0.27578	0.00391	3.87293	0.0575	0.95496135	94.67	1658.5	21.05	1570.1	19.78	1608.1	11.98	3	78190	8123	397418
M15	0.10132	0.00112	0.2976	0.00419	4.15507	0.06034	0.96951411	101.89	1648.3	20.39	1679.4	20.83	1665.2	11.89	14	65136	6696	305053
M16	0.09803	0.00115	0.31761	0.00449	4.29185	0.06444	0.94154521	112.04	1587	21.79	1778.1	21.98	1691.8	12.36	13	130007	12973	570973
M20A	0.1035	0.00124	0.2996	0.00421	4.27554	0.06412	0.93699602	100.08	1687.9	21.99	1689.3	20.87	1688.7	12.34	3	74146	7838	341114
M20B	0.10287	0.00119	0.2992	0.00424	4.24359	0.06339	0.94867386	100.64	1676.5	21.31	1687.3	21.01	1682.5	12.27	12	63454	6608	295997
M21	0.10539	0.00137	0.28874	0.00407	4.19573	0.06598	0.89636044	95.01	1721.1	23.75	1635.2	20.35	1673.2	12.89	16	102977	11039	489332
M22	0.09911	0.00113	0.29538	0.00414	4.03632	0.05931	0.95384305	103.79	1607.4	21.02	1668.4	20.61	1641.5	11.96	9	221001	22209	1038721
M24	0.09435	0.00113	0.27101	0.00378	3.52559	0.05282	0.93097902	102.03	1515.2	22.43	1545.9	19.17	1533	11.85	8	265715	25547	1347540
M25	0.10306	0.00117	0.29846	0.00418	4.23873	0.06192	0.95872699	100.22	1680	20.75	1683.7	20.77	1681.6	12	11	89373	9346	414588
M25A	0.1035	0.0012	0.30156	0.00426	4.30347	0.06416	0.94752415	100.66	1687.9	21.18	1699.1	21.12	1694	12.28	0	85681	8982	396832
M25B	0.1024	0.00117	0.29424	0.00417	4.15431	0.06184	0.95205878	99.68	1668.1	21.04	1662.7	20.76	1665.1	12.18	12	156692	16266	746395
M26	0.10227	0.00112	0.29848	0.0042	4.20664	0.06109	0.96894534	101.08	1665.8	20.21	1683.8	20.85	1675.3	11.91	16	119666	12375	559438
M26	0.1039	0.00122	0.29821	0.00423	4.27215	0.0642	0.94390792	99.26	1695	21.44	1682.4	20.99	1688	12.36	0	92910	9793	435863
M27	0.10402	0.00117	0.31149	0.0044	4.46503	0.06547	0.96336443	103.01	1697	20.52	1748	21.61	1724.5	12.16	6	75067	7899	336333
M28†	0.08665	0.00117	0.28249	0.0041	3.37246	0.05186	0.94383282	118.56	1352.8	25.83	1603.9	20.6	1498	12.04	0	186639	19175	921340
M29	0.10265	0.00147	0.315	0.00446	4.45814	0.07473	0.84466213	105.54	1672.6	26.23	1765.3	21.85	1723.2	13.9	21	513981	53284	2237393
M29	0.10329	0.00116	0.29336	0.00414	4.17584	0.06147	0.95869416	98.47	1684.1	20.54	1658.3	20.65	1669.3	12.06	1	188703	19672	900403
M30†	0.09957	0.00141	0.29234	0.0042	4.00931	0.06735	0.85525	102.30	1616.1	26.16	1653.2	20.94	1636.1	13.65	0	225107	22623	1070407
M31	0.10306	0.00125	0.30082	0.00427	4.27462	0.06557	0.92536591	100.92	1680	22.31	1695.4	21.15	1688.5	12.62	0	78296	8158	363143
M31†	0.11059	0.0015	0.29124	0.00415	4.43727	0.072	0.87817371	91.08	1809.1	24.41	1647.7	20.71	1719.3	13.45	152	136741	15311	649041
M33	0.10075	0.00122	0.30103	0.00424	4.17949	0.06308	0.93322783	103.57	1637.9	22.32	1696.4	21.01	1670	12.37	0	68391	7022	313601
M34	0.102	0.00124	0.30359	0.00427	4.2671	0.06446	0.93107128	102.91	1660.8	22.28	1709.1	21.13	1687	12.43	0	61841	6411	280877
M35	0.10191	0.00116	0.29767	0.0042	4.18074	0.06161	0.95745015	101.24	1659.3	20.97	1679.8	20.85	1670.3	12.07	8	59158	6113	276523
M37	0.10259	0.0013	0.29599	0.00417	4.18449	0.06461	0.91243473	99.99	1671.5	23.19	1671.4	20.77	1671	12.65	7	103497	10850	481617
M38A	0.10174	0.00122	0.30973	0.00436	4.34289	0.06527	0.9366308	105.02	1656.2	22.04	1739.4	21.44	1701.5	12.4	17	103846	10776	463486
M39A	0.10225	0.00132	0.302	0.00428	4.25559	0.06669	0.90434864	102.15	1665.4	23.78	1701.2	21.17	1684.8	12.88	9	71246	7439	324946
M39B	0.10127	0.00126	0.30552	0.00431	4.26398	0.06539	0.91990175	104.31	1647.6	22.97	1718.6	21.27	1686.4	12.61	32	56677	5848	255532
M39C	0.10133	0.00139	0.3107	0.00445	4.33852	0.0705	0.88139634	105.80	1648.6	25.23	1744.2	21.89	1700.7	13.41	0	39286	4068	174482

Appendix 2. U-Pb isotopic age data for monazite analyses

Sample 103618

Spot	$^{207}Pb/^{206}Pb$	1 σ	$^{206}Pb/^{238}U$	1 σ	$^{207}Pb/^{235}U$	1 σ	rho	Conc. (%)	$^{207}Pb/^{206}Pb$ age	1 σ	$^{206}Pb/^{238}U$ age	1 σ	$^{207}Pb/^{235}U$ age	1 σ	^{204}Pb	^{206}Pb	^{207}Pb	^{238}Pb	Session
M05†	0.08161	0.00112	0.2204	0.00322	2.47859	0.04087	0.886022	103.87	1236.2	26.79	1284	17	1265.8	11.93	0	98269	8371	631242	1
M01	0.08345	0.00097	0.23575	0.00335	2.71139	0.04033	0.955338	106.64	1279.5	22.5	1364.5	17.48	1331.6	11.03	9	141522	12169	842220	1
M06	0.08333	0.00093	0.23852	0.00336	2.74007	0.03983	0.969094	108.02	1276.6	21.66	1379	17.5	1339.4	10.81	0	189990	16266	1112818	1
M04†	0.08348	0.00118	0.22136	0.00324	2.54637	0.04271	0.872645	100.70	1280.2	27.27	1289.1	17.1	1285.4	12.23	14	96047	8281	614151	1
M03A	0.08274	0.00092	0.21816	0.00308	2.48843	0.03613	0.972373	100.73	1263	21.46	1272.2	16.29	1268.7	10.52	0	88150	7504	564351	1
M03B	0.0836	0.00092	0.21846	0.00308	2.51781	0.03643	0.974412	99.28	1283	21.41	1273.7	16.3	1277.2	10.51	0	86570	7432	553906	1
M07	0.08455	0.001	0.219	0.0031	2.55253	0.03837	0.941665	97.82	1305.1	22.92	1276.6	16.4	1287.2	10.97	13	167333	14549	1066284	1
M09A	0.08254	0.00094	0.21531	0.00305	2.45019	0.03615	0.960124	99.90	1258.4	21.96	1257.1	16.19	1257.5	10.64	9	86028	7301	559808	1
M09B	0.08231	0.00093	0.21513	0.00305	2.44147	0.03594	0.963102	100.25	1253	21.82	1256.1	16.17	1254.9	10.6	0	101262	8564	659647	1
M10	0.08459	0.0011	0.2316	0.00332	2.70075	0.04277	0.9052	102.82	1306.1	24.99	1342.9	17.35	1328.7	11.74	6	135627	11819	819309	1
M12	0.0837	0.00095	0.21607	0.00302	2.49333	0.03633	0.959239	98.12	1285.3	21.94	1261.1	16.03	1270.1	10.56	6	112014	9587	718104	1
M15	0.08337	0.00102	0.22501	0.00316	2.58645	0.03919	0.92686	102.39	1277.7	23.66	1308.3	16.63	1296.8	11.1	0	138163	11769	847777	1
M16A	0.08371	0.00096	0.21542	0.00301	2.48638	0.03649	0.952081	97.81	1285.7	22.32	1257.6	15.97	1268.1	10.63	8	110848	9487	710712	1
M16B	0.08393	0.00096	0.21617	0.00302	2.50146	0.03659	0.955086	97.75	1290.7	22.05	1261.6	16	1272.5	10.61	2	102221	8735	653264	1
M18	0.09729	0.00145	0.28653	0.00415	3.84091	0.06537	0.851008	103.27	1572.8	27.66	1624.2	20.78	1601.4	13.71	10	64012	6510	309019	1
M19	0.08305	0.00112	0.22177	0.00313	2.53986	0.04075	0.879678	101.63	1270.5	26.03	1291.2	16.51	1283.5	11.69	9	126780	10765	785603	1
M21	0.08336	0.001	0.21271	0.00296	2.44482	0.03656	0.93056	97.32	1277.5	23.41	1243.2	15.76	1255.9	10.78	0	131465	11217	848123	1
M22	0.08333	0.00101	0.21447	0.00299	2.46407	0.03674	0.935015	98.10	1276.8	23.45	1252.6	15.85	1261.6	10.77	2	127972	10987	817952	1
M01	0.08379	0.00091	0.22363	0.00321	2.58316	0.03794	0.977302	101.06	1287.3	20.97	1301	16.93	1295.9	10.75	0	212360	18085	1355867	2
M02A	0.08339	0.00093	0.22918	0.00328	2.63465	0.03914	0.963384	104.09	1277.9	21.75	1330.2	17.22	1310.4	10.94	25	201684	17090	1249872	2
M02B	0.0829	0.00092	0.22607	0.00326	2.58334	0.03846	0.968606	103.74	1266.5	21.42	1313.9	17.11	1295.9	10.9	1	180899	15230	1142888	2
M03	0.08461	0.00097	0.21755	0.00313	2.5373	0.03829	0.953392	97.14	1306.3	22.18	1268.9	16.58	1282.8	10.99	12	181287	15570	1186791	2
M08	0.08546	0.00097	0.21857	0.00315	2.57474	0.0387	0.958832	96.13	1325.6	21.8	1274.3	16.67	1293.5	10.99	16	239103	20735	1562628	2
M09	0.08448	0.00097	0.22089	0.00319	2.57225	0.03911	0.949817	98.72	1303.3	22.23	1286.6	16.86	1292.8	11.12	15	210256	18009	1361882	2
M09B	0.08348	0.00096	0.2261	0.00329	2.60166	0.03974	0.952616	102.66	1280	22.36	1314	17.28	1301.1	11.2	7	197316	16697	1255307	2
M10†	0.08403	0.00097	0.21896	0.00318	2.53629	0.03886	0.947891	98.72	1292.9	22.36	1276.4	16.82	1282.5	11.16	14	215173	18306	1412650	2
M14	0.0836	0.00098	0.22077	0.00321	2.54404	0.03928	0.941711	100.26	1282.7	22.72	1286	16.97	1284.7	11.25	5	196916	16651	1283563	2
M15	0.08332	0.00098	0.21475	0.00314	2.46636	0.03824	0.943051	98.27	1276.2	22.82	1254.1	16.64	1262.2	11.2	4	234961	19791	1579914	2

Appendix 2. U-Pb isotopic age data for monazite analyses

Sample 115638

Spot	$^{207}Pb/^{206}Pb$	1 σ	$^{206}Pb/^{238}U$	1 σ	$^{207}Pb/^{235}U$	1 σ	rho	Conc. (%)	$^{207}Pb/^{206}Pb$ age	1 σ	$^{206}Pb/^{238}U$ age	1 σ	$^{207}Pb/^{235}U$ age	1 σ	^{204}Pb	^{206}Pb	^{207}Pb	^{238}Pb
M01†	0.10027	0.00241	0.22379	0.00367	3.09319	0.07487	0.67752317	79.90	1629.2	44.09	1301.8	19.32	1431	18.57	56	14594	1511	86888
M05A	0.08433	0.00104	0.2271	0.00313	2.63933	0.03931	0.92537519	101.47	1300.2	23.8	1319.3	16.42	1311.7	10.97	0	35709	3089	211296
M05B	0.08369	0.00109	0.21839	0.00302	2.51875	0.03876	0.89861878	99.07	1285.3	25.24	1273.4	16	1277.5	11.18	31	31708	2727	194747
M06	0.08343	0.00104	0.22635	0.00312	2.60257	0.03912	0.91701759	102.83	1279.2	24.28	1315.4	16.43	1301.4	11.03	11	27862	2388	165567
M06B	0.08332	0.00101	0.22896	0.00315	2.62886	0.03888	0.93023385	104.13	1276.4	23.66	1329.1	16.51	1308.7	10.88	20	27549	2354	161755
M08	0.08248	0.00104	0.23277	0.0032	2.64559	0.03986	0.9124482	107.34	1256.8	24.28	1349	16.75	1313.4	11.1	9	37319	3162	214924
M10†	0.08513	0.00116	0.22338	0.0031	2.62046	0.04149	0.87649917	98.58	1318.4	26.35	1299.7	16.32	1306.4	11.64	0	25733	2241	153714
M16	0.08476	0.00119	0.22455	0.00313	2.62276	0.04223	0.86570265	99.69	1309.9	27	1305.9	16.47	1307	11.84	0	18620	1613	110724
M16B†	0.08459	0.00127	0.22449	0.00315	2.61683	0.04421	0.83055529	99.96	1306.1	29.01	1305.6	16.6	1305.4	12.41	0	37325	3233	221656
M17	0.08602	0.00112	0.2208	0.00305	2.61739	0.04017	0.90005154	96.08	1338.6	24.95	1286.1	16.11	1305.5	11.27	7	19241	1698	116763
M18	0.08602	0.00102	0.22608	0.00309	2.67984	0.03903	0.9384403	98.15	1338.7	22.71	1313.9	16.27	1322.9	10.77	16	44510	3901	264636
M19A	0.08436	0.001	0.22896	0.00313	2.66156	0.03876	0.93872247	102.16	1300.9	22.77	1329	16.44	1317.9	10.75	7	34636	2975	203431
M19B	0.0828	0.00098	0.22549	0.0031	2.5727	0.03764	0.93966692	103.66	1264.5	22.83	1310.8	16.28	1292.9	10.7	47	39804	3355	238075
M20	0.08563	0.00095	0.22632	0.00306	2.67057	0.0374	0.96545238	98.90	1329.8	21.4	1315.2	16.09	1320.3	10.35	0	163488	14317	967683
M21	0.08445	0.00102	0.22845	0.00314	2.65847	0.03927	0.93048494	101.81	1302.8	23.26	1326.4	16.48	1317	10.9	0	30909	2655	182235
M22	0.0851	0.00108	0.22838	0.00317	2.67809	0.04081	0.91087706	100.63	1317.7	24.38	1326	16.63	1322.4	11.27	2	20585	1782	121831
M22B	0.0851	0.0011	0.229	0.00319	2.68536	0.04144	0.90268862	100.87	1317.7	24.83	1329.2	16.75	1324.4	11.42	0	18487	1602	109343
M24	0.08513	0.00107	0.22805	0.00316	2.67502	0.04062	0.91252363	100.45	1318.4	24.23	1324.3	16.59	1321.6	11.22	0	28125	2437	166697
M25†	0.08473	0.00136	0.22898	0.00328	2.6731	0.04781	0.80088979	101.52	1309.2	30.94	1329.1	17.2	1321	13.22	0	43989	3786	258830
M26	0.08505	0.00104	0.23286	0.00323	2.72927	0.04094	0.92471157	102.50	1316.6	23.63	1349.5	16.9	1336.5	11.15	0	35654	3100	208015
M28	0.08512	0.00116	0.23612	0.00333	2.76984	0.04458	0.87624606	103.66	1318.3	26.36	1366.5	17.39	1347.4	12.01	0	17576	1524	101322
M29	0.08343	0.00106	0.23442	0.00324	2.69571	0.04113	0.90586777	106.14	1279.1	24.57	1357.6	16.9	1327.3	11.3	0	128372	10951	739181

Appendix 2. U-Pb isotopic age data for monazite analyses

Sample 115669

Spot	$^{207}Pb/^{206}Pb$	1 σ	$^{206}Pb/^{238}U$	1 σ	$^{207}Pb/^{235}U$	1 σ	rho	Conc. (%)	$^{207}Pb/^{206}Pb$ age	1 σ	$^{206}Pb/^{238}U$ age	1 σ	$^{207}Pb/^{235}U$ age	1 σ	^{204}Pb	^{206}Pb	^{207}Pb	^{238}Pb
M03	0.08331	0.00089	0.22727	0.0032	2.61064	0.03737	0.98362998	103.44	1276.3	20.74	1320.2	16.82	1303.6	10.51	20	454562	38546	2803357
M06	0.08322	0.00092	0.2322	0.00326	2.66442	0.03865	0.96785115	105.63	1274.2	21.48	1346	17.04	1318.6	10.71	24	499619	42183	2996150
M07A	0.08404	0.00094	0.22485	0.00315	2.60544	0.03789	0.96332789	101.09	1293.4	21.52	1307.5	16.58	1302.2	10.67	19	410232	35053	2535399
M07B	0.08468	0.00093	0.2263	0.00317	2.64239	0.03828	0.96694038	100.53	1308.2	21.29	1315.1	16.69	1312.5	10.67	16	422306	36384	2598236
M08	0.08379	0.00098	0.23387	0.00329	2.70224	0.04046	0.93954897	105.23	1287.5	22.68	1354.8	17.16	1329.1	11.1	14	483845	41004	2872836
M09	0.08373	0.00095	0.23159	0.00327	2.67364	0.03954	0.95476	104.41	1286.1	22.02	1342.8	17.1	1321.2	10.93	25	329310	27961	1987176
M11	0.08374	0.00102	0.22698	0.00319	2.62092	0.03995	0.92201943	102.52	1286.3	23.49	1318.7	16.76	1306.5	11.2	10	320244	27112	1954825
M11B†	0.08477	0.00112	0.22787	0.00323	2.66345	0.04268	0.88457672	101.01	1310.1	25.42	1323.3	16.94	1318.4	11.83	17	326375	27923	1984172
M12	0.08548	0.00109	0.23278	0.00328	2.74386	0.04311	0.89683408	101.70	1326.4	24.59	1349	17.15	1340.4	11.69	25	464613	39980	2760494
M13	0.08526	0.00105	0.22615	0.00319	2.65901	0.04082	0.91884247	99.46	1321.5	23.63	1314.3	16.75	1317.1	11.33	25	253459	21845	1554854
M14	0.08519	0.00094	0.2271	0.00317	2.66722	0.03845	0.96828816	99.95	1319.9	21.29	1319.3	16.65	1319.4	10.64	16	247928	21495	1512111
M15	0.08463	0.00093	0.23132	0.00324	2.69874	0.0389	0.97172477	102.64	1306.9	21.36	1341.4	16.94	1328.1	10.68	25	192968	16626	1157942
M15B	0.08423	0.00093	0.2246	0.00314	2.60815	0.03769	0.96744509	100.63	1297.9	21.33	1306.1	16.53	1302.9	10.61	15	323889	27762	2001143
M16A	0.08411	0.00093	0.23376	0.00327	2.71074	0.03912	0.96931866	104.56	1295.1	21.33	1354.2	17.1	1331.4	10.71	5	369428	31746	2195021
M17B	0.08458	0.00095	0.22184	0.00311	2.58663	0.03768	0.96237415	98.91	1305.8	21.68	1291.6	16.4	1296.9	10.67	9	363556	31382	2275791
M18A	0.08357	0.00097	0.22922	0.00321	2.64122	0.0391	0.94597649	103.73	1282.5	22.55	1330.4	16.83	1312.2	10.9	16	379872	32377	2293922
M18B†	0.09204	0.00127	0.23533	0.00335	2.98719	0.04912	0.86570914	92.79	1468.2	26.14	1362.4	17.46	1404.4	12.51	139	239273	22363	1404321
M23	0.08292	0.001	0.22882	0.00322	2.61611	0.03965	0.92848459	104.81	1267.3	23.36	1328.3	16.87	1305.2	11.13	8	405937	34374	2456670
M24	0.08283	0.00098	0.2358	0.00331	2.69259	0.04019	0.94045153	107.87	1265.2	22.69	1364.8	17.29	1326.4	11.05	0	361822	30652	2130196
M26A	0.08407	0.00099	0.23074	0.00326	2.67427	0.04002	0.94411061	103.42	1294.1	22.66	1338.4	17.07	1321.4	11.06	7	173144	14892	1046789
M26B	0.08278	0.00097	0.22766	0.00321	2.59806	0.03871	0.9463337	104.60	1264.1	22.49	1322.2	16.87	1300.1	10.92	9	280183	23779	1716076

Appendix 2. U-Pb isotopic age data for monazite analyses

Sample 115866

Spot	$^{207}Pb/^{206}Pb$	1 σ	$^{206}Pb/^{238}U$	1 σ	$^{207}Pb/^{235}U$	1 σ	rho	Conc. (%)	$^{207}Pb/^{206}Pb$ age	1 σ	$^{206}Pb/^{238}U$ age	1 σ	$^{207}Pb/^{235}U$ age	1 σ	^{204}Pb	^{206}Pb	^{207}Pb	^{238}Pb	Session
M01	0.08713	0.00099	0.22866	0.00336	2.74652	0.04154	0.97155044	97.37	1363.3	21.82	1327.4	17.61	1341.1	11.26	0	42129	3788	266778	a
M01B	0.08568	0.00099	0.22975	0.00337	2.71395	0.04118	0.96669591	100.17	1331	22.18	1333.2	17.66	1332.3	11.26	6	39336	3476	247380	a
M01C	0.08426	0.00098	0.23195	0.00338	2.69461	0.0409	0.96005239	103.56	1298.5	22.4	1344.7	17.71	1327	11.24	15	39950	3467	247593	a
M01D	0.08605	0.00101	0.22191	0.00326	2.63275	0.04047	0.95569022	96.45	1339.4	22.65	1291.9	17.21	1309.8	11.31	14	38254	3393	249304	a
M01E	0.08697	0.00105	0.22158	0.00324	2.65671	0.04102	0.94702828	94.89	1359.7	23.06	1290.2	17.08	1316.5	11.39	0	36311	3253	234845	a
M01F	0.08663	0.00106	0.23034	0.00337	2.75089	0.04279	0.94057077	98.82	1352.3	23.49	1336.3	17.68	1342.3	11.58	26	35941	3220	223541	a
M01G	0.0912	0.00111	0.22585	0.00328	2.8386	0.04381	0.94098932	90.49	1450.7	22.97	1312.7	17.23	1365.8	11.59	24	41503	3889	261448	a
M01H	0.08904	0.00108	0.2226	0.00322	2.73157	0.04212	0.93811198	92.21	1405	22.96	1295.6	17	1337.1	11.46	2	46064	4199	294408	a
M02A	0.08406	0.00093	0.22301	0.00328	2.58476	0.03863	0.98411312	100.29	1293.9	21.27	1297.7	17.28	1296.3	10.94	10	148108	12880	967942	a
M02B†	0.0945	0.00108	0.21909	0.00322	2.85484	0.04321	0.97102592	84.12	1518.2	21.34	1277.1	17.02	1370.1	11.38	79	99120	9684	656253	a
M05A	0.08699	0.00123	0.22964	0.00341	2.75399	0.04672	0.87531902	97.96	1360.3	27.05	1332.6	17.9	1343.2	12.64	18	40700	3625	253702	a
M05B	0.08537	0.00113	0.22279	0.00327	2.62223	0.04282	0.89882714	97.94	1323.9	25.56	1296.6	17.23	1306.9	12	23	58715	5105	376038	a
M06	0.08814	0.00122	0.22858	0.00338	2.77623	0.04647	0.88340783	95.77	1385.6	26.32	1327	17.74	1349.2	12.49	32	34789	3125	217241	a
M06B†	0.14261	0.00217	0.26859	0.00415	5.27989	0.09366	0.87102171	67.89	2259.1	26.06	1533.6	21.07	1865.6	15.14	79	21730	3174	117153	a
M07†	0.08698	0.00097	0.22834	0.0033	2.73706	0.04076	0.97046994	97.48	1360.1	21.44	1325.8	17.3	1338.6	11.07	90	258227	23007	1617951	a
M07A	0.08598	0.00095	0.22414	0.00323	2.65598	0.03917	0.97713458	97.46	1337.7	21.14	1303.7	17.03	1316.3	10.88	19	148701	13108	949534	a
M08†	0.08416	0.00099	0.22514	0.00324	2.61089	0.03959	0.94906383	101.00	1296.1	22.63	1309	17.04	1303.7	11.13	18	237852	20475	1500752	a
M08B	0.08449	0.00093	0.22139	0.00318	2.57794	0.03791	0.97676062	98.88	1303.8	21.35	1289.2	16.78	1294.4	10.76	21	215216	18694	1384146	a
M01A	0.08583	0.00111	0.23159	0.00326	2.74053	0.04283	0.90070855	100.64	1334.2	24.93	1342.8	17.06	1339.5	11.63	0	24699	2154	146063	b
M01B	0.08946	0.00113	0.23373	0.00335	2.88279	0.04512	0.91574438	95.76	1413.9	23.84	1354	17.5	1377.4	11.8	3	20398	1841	122070	b
M02A	0.08549	0.0013	0.22602	0.00329	2.66408	0.04641	0.83557362	99.01	1326.7	29.16	1313.6	17.3	1318.6	12.86	14	23663	2059	144938	b
M02B	0.08474	0.00116	0.23111	0.0033	2.69997	0.04385	0.87919365	102.36	1309.4	26.38	1340.3	17.27	1328.4	12.03	15	25093	2164	149735	b
M03A	0.08706	0.00112	0.23001	0.0033	2.76171	0.04355	0.90982347	98.00	1361.9	24.58	1334.6	17.28	1345.3	11.76	0	17080	1510	103535	b
M03B	0.08707	0.00111	0.2277	0.00325	2.73423	0.04286	0.91054876	97.10	1362	24.38	1322.5	17.08	1337.8	11.65	9	18441	1630	112684	b
M03C	0.08594	0.00109	0.23001	0.00328	2.72622	0.04259	0.91280999	99.84	1336.8	24.47	1334.6	17.18	1335.6	11.61	0	15693	1370	94679	b
M03D	0.08596	0.00114	0.22669	0.00323	2.68704	0.04286	0.89328929	98.49	1337.3	25.49	1317.1	16.98	1324.9	11.8	0	16056	1402	97795	b
M03E	0.08671	0.00116	0.22372	0.00319	2.67543	0.04279	0.8915325	96.12	1354.1	25.54	1301.5	16.79	1321.7	11.82	22	15210	1339	93720	b
M03F	0.08347	0.00113	0.22417	0.0032	2.57992	0.04156	0.88614173	101.86	1280.1	26.2	1303.9	16.83	1295	11.79	5	20240	1721	124536	b
M03G	0.08699	0.00116	0.22692	0.00322	2.72196	0.0434	0.88996946	96.92	1360.2	25.49	1318.3	16.93	1334.5	11.84	0	15454	1365	93609	b
M03H	0.08851	0.00121	0.23251	0.00336	2.83737	0.04696	0.8731433	96.71	1393.5	26.01	1347.7	17.56	1365.5	12.42	14	20960	1854	126021	b
M03I	0.08712	0.00122	0.22906	0.00333	2.75149	0.04632	0.86356367	97.54	1363.2	26.81	1329.6	17.48	1342.5	12.54	18	16917	1476	103708	b
M05A	0.08593	0.00127	0.22559	0.00332	2.67259	0.04668	0.84259666	98.11	1336.6	28.35	1311.3	17.48	1320.9	12.91	0	26120	2248	163701	b
M05B	0.08676	0.00115	0.23858	0.00345	2.85391	0.0464	0.88942095	101.78	1355.2	25.35	1379.3	17.94	1369.8	12.22	0	22940	1997	135142	b
M06A	0.08606	0.0011	0.23101	0.0033	2.7409	0.04323	0.90571407	100.02	1339.5	24.62	1339.8	17.27	1339.6	11.73	12	22897	1987	137894	b
M06B	0.08669	0.00111	0.22756	0.00326	2.72002	0.04306	0.90493992	97.64	1353.7	24.6	1321.7	17.12	1333.9	11.75	0	19150	1676	117488	b
M06C	0.08681	0.00112	0.22452	0.00322	2.68731	0.04268	0.9030134	96.27	1356.3	24.62	1305.7	16.96	1325	11.75	15	20005	1748	124595	b
M06D	0.08601	0.00112	0.22476	0.00323	2.66534	0.04267	0.89766331	97.65	1338.4	25.06	1307	16.98	1318.9	11.82	6	20380	1764	126683	b
M06E†	0.10754	0.00146	0.24483	0.00357	3.62994	0.05971	0.8864535	80.30	1758.1	24.57	1411.8	18.47	1556.1	13.09	48	17444	1881	100139	b

Appendix 2. U-Pb isotopic age data for zircon analyses

Sample 113019

Spot	$^{207}Pb/^{206}Pb$	1 σ	$^{206}Pb/^{238}U$	1 σ	$^{207}Pb/^{235}U$	1 σ	$^{208}Pb/^{232}Th$	1 σ	rho	Conc. (%)	$^{207}Pb/^{206}Pb$ age	1 σ	$^{206}Pb/^{238}U$ age	1 σ	$^{207}Pb/^{235}U$ age	1 σ	$^{208}Pb/^{232}Th$ age	1 σ	^{204}Pb	^{206}Pb	^{207}Pb	^{238}Pb	^{232}Th	^{238}U	Session
Z01†	0.08529	0.00477	0.22431	0.00553	2.6373	0.1415	0.02919	0.00386	0.459493731	98.67	1322.2	105	1304.6	29	1311.1	40	581.5	76	0	468	40	23	885	2680	1
Z04†	0.08791	0.00365	0.24042	0.00481	2.91421	0.11655	0.06671	0.01213	0.500245338	100.60	1380.6	78	1388.9	25	1385.6	30	1305.3	230	4	579	51	14	224	2933	1
Z05†	0.08303	0.00457	0.24021	0.00566	2.74964	0.14622	0.09003	0.01333	0.443092507	109.28	1270.0	104	1387.8	29	1342.0	40	1742.5	247	33	450	37	17	211	2394	1
Z06†	0.09127	0.00538	0.23974	0.00639	3.01658	0.16943	0.15163	0.03824	0.474553186	95.39	1452.2	108	1385.3	33	1411.8	43	2853.5	671	13	391	36	10	77	2086	1
Z07†	0.09025	0.00395	0.23045	0.00481	2.86747	0.12061	0.01401	0.02386	0.496231043	93.45	1430.6	81	1336.9	25	1373.4	32	281.1	476	2	506	46	1	95	2689	1
Z09†	0.10164	0.00738	0.2398	0.00728	3.3602	0.23305	0.11669	0.01529	0.437721845	83.76	1654.3	129	1385.7	38	1495.2	54	2230.8	277	0	237	24	25	238	1242	1
Z10†	0.09464	0.0091	0.2284	0.00824	2.97999	0.27494	0.41485	0.12466	0.391028121	87.19	1520.9	171	1326.1	43	1402.5	70	7014.2	1781	0	134	12	6	16	734	1
Z11†	0.10796	0.00762	0.2494	0.00818	3.71202	0.24705	0.163	0.05999	0.492813168	81.32	1765.2	124	1435.4	42	1574.0	53	3052.1	1043	28	250	27	5	40	1270	1
Z14	0.08606	0.00252	0.22107	0.0036	2.62311	0.07524	0.06541	0.00506	0.56772812	96.13	1339.4	56	1287.5	19	1307.1	21	1280.6	96	1	2401	211	413	6794	13144	1
Z16†	0.0926	0.00449	0.21825	0.00502	2.78628	0.12969	0.08138	0.00854	0.494160164	86.01	1479.6	89	1272.6	27	1351.9	35	1581.3	160	0	557	52	44	624	3346	1
Z17	0.08532	0.00446	0.23262	0.00538	2.73636	0.13751	0.06902	0.01458	0.460229206	101.92	1322.8	98	1348.2	28	1338.4	37	1348.9	276	0	385	33	11	179	2071	1
Z17B†	0.09321	0.00215	0.23849	0.00364	3.06369	0.07161	0.03241	0.00216	0.652983722	92.41	1492.1	43	1378.9	19	1423.7	18	644.7	42	0	6676	617	377	14318	36080	1
Z18†	0.04574	0.01354	0.24233	0.01762	1.52814	0.44337	1.78147	1.79698	0.250608364	-	0.1	577	1398.8	91	941.8	178	******	*******	0	115	5	2	2	589	1
Z19†	0.09209	0.00474	0.22059	0.00516	2.80065	0.13798	0.15403	0.04363	0.474795483	87.47	1469.0	95	1285.0	27	1355.7	37	2895.6	764	0	353	32	5	44	1978	1
Z20	0.09942	0.00376	0.22134	0.00446	3.03321	0.11056	0.14124	0.0153	0.55281447	79.90	1613.2	69	1289.0	24	1416.0	28	2670.3	271	14	1426	140	63	544	8389	1
Z21†	0.09247	0.00354	0.23946	0.00479	3.05301	0.11308	0.08051	0.00666	0.540063669	93.70	1477.0	71	1383.9	25	1421.0	28	1565.1	125	22	908	83	77	1212	4891	1
Z23†	0.10196	0.00688	0.2315	0.00718	3.25401	0.20736	0.14116	0.23663	0.486706726	80.86	1660.0	120	1342.3	38	1470.1	50	2669.0	4191	0	302	30	0	7	1678	1
Z24†	0.08358	0.00568	0.22508	0.00621	2.59358	0.16899	0.16542	0.08058	0.423441419	102.02	1282.7	127	1308.6	33	1298.8	48	3094.2	1397	0	229	18	2	19	1277	1
Z24B†	0.10098	0.00891	0.23866	0.00908	3.32199	0.27708	-0.44006	2.35907	0.456141256	84.02	1642.2	155	1379.7	47	1486.2	65	******	*******	3	221	21	0	0	1181	1
Z24C†	0.09991	0.00581	0.24197	0.00652	3.33307	0.18437	0.1539	0.03149	0.487124811	86.10	1622.5	104	1396.9	34	1488.8	43	2893.3	552	8	306	30	10	79	1646	1
Z25A	0.0793	0.0063	0.22809	0.00413	2.75802	0.08799	0.07308	0.02116	0.567554929	96.21	1376.7	61	1324.5	22	1344.3	24	1425.7	399	1	1701	149	171	2599	9682	1
Z25A†	0.08774	0.00286	0.2419	0.0073	2.6445	0.20231	0.07295	0.00437	0.394469303	118.40	1179.6	149	1396.6	38	1313.1	56	1423.3	82	4	239	18	7	125	1275	1
Z26A†	0.11202	0.01289	0.22115	0.01124	3.41491	0.3673	0.70505	0.40879	0.472539047	70.29	1832.4	195	1288.0	59	1507.8	84	******	4846	0	138	15	4	7	825	1
Z26B†	0.09341	0.00416	0.22688	0.0049	2.92126	0.12435	0.07899	0.00529	0.507369421	88.10	1496.2	82	1318.1	26	1387.4	32	1536.7	99	0	475	44	59	797	2575	1
Z27	0.08637	0.00214	0.22053	0.00335	2.62489	0.06424	0.07	0.00769	0.620701372	95.40	1346.6	47	1284.7	18	1307.6	18	1367.6	145	20	3131	272	33	496	17193	1
Z28A	0.09035	0.00245	0.22971	0.00378	2.86028	0.07695	0.08583	0.00555	0.611662455	93.04	1432.7	51	1333.0	20	1371.5	20	1664.3	103	8	2235	200	111	1416	12516	1
Z28B†	0.09201	0.00329	0.22688	0.00431	2.87752	0.09914	0.04635	0.0097	0.551379345	89.81	1467.6	67	1318.1	23	1376.0	26	915.7	187	16	690	63	11	268	3776	1
Z29†	0.11242	0.00583	0.23187	0.00603	3.59259	0.17609	0.16361	0.01451	0.530573694	73.10	1838.9	91	1344.3	32	1547.9	39	3062.7	252	25	486	54	59	393	2702	1
Z30A†	0.09099	0.00356	0.21297	0.00419	2.67149	0.10035	0.09681	0.01462	0.523759325	86.05	1446.4	73	1244.6	22	1320.6	28	1867.7	269	0	700	63	16	171	4032	1
Z30B†	0.09392	0.00549	0.23253	0.00607	3.01028	0.1678	0.15974	0.07783	0.468300516	89.46	1506.5	107	1347.7	32	1410.2	42	2995.5	1356	0	301	28	3	25	1628	1
Z31†	0.09207	0.00323	0.22626	0.00416	2.87161	0.09752	0.10836	0.00953	0.541398829	89.52	1468.8	65	1314.9	22	1374.5	26	2079.5	174	14	769	70	34	328	4220	1
Z32A	0.0924	0.00423	0.23228	0.00522	2.95862	0.12973	0.25207	0.03292	0.512516033	94.88	1419.0	79	1346.4	27	1397.1	33	4543.7	531	0	976	89	33	139	5403	1
Z32B	0.08962	0.00473	0.23429	0.0057	2.89473	0.14502	0.0877	0.01048	0.485625255	95.72	1417.5	98	1356.9	30	1380.5	38	1699.1	195	0	922	83	61	691	4520	1
Z33A	0.0897	0.00383	0.22	0.00461	2.72025	0.1112	0.06268	0.00594	0.512604337	90.34	1419.0	79	1281.9	24	1334.0	30	1228.8	113	0	997	90	66	1082	5590	1
Z33B†	0.11361	0.00615	0.22698	0.00605	3.555	0.18164	0.13166	0.01478	0.521670039	70.97	1858.0	95	1318.6	32	1539.6	40	2499.9	264	27	354	40	30	231	2009	1
Z01	0.0883	0.00283	0.20875	0.00368	2.54084	0.07911	0.08116	0.0064	0.566196614	87.99	1389.0	60	1222.2	20	1283.8	23	1577.2	120	0	1949	175	85	998	11688	2
Z02	0.08894	0.00192	0.21939	0.0032	2.68948	0.05851	0.06813	0.00232	0.670457682	91.15	1402.8	41	1278.6	17	1325.6	16	1332.1	44	0	3779	341	734	10197	21267	2
Z03	0.08706	0.00241	0.2195	0.00344	2.63434	0.07178	0.06902	0.01288	0.575164788	93.93	1361.8	52	1279.2	18	1310.3	20	1349.1	243	10	1355	119	17	238	7524	2
Z05	0.08613	0.00168	0.21643	0.003	2.5695	0.05103	0.0675	0.00267	0.697954078	94.18	1341.1	37	1263.0	16	1292.0	15	1320.3	51	7	5501	479	567	7868	30807	2
Z06	0.0905	0.00274	0.20935	0.00358	2.61117	0.07713	0.07406	0.00695	0.578924431	85.32	1436.1	57	1225.3	19	1303.8	22	1444.0	131	29	1964	180	62	805	11649	2
Z07	0.08871	0.00278	0.23816	0.00404	2.91198	0.08889	0.07174	0.00482	0.555709761	98.52	1397.8	59	1377.1	21	1385.0	23	1400.3	91	2	1389	124	84	1113	7088	2
Z09†	0.09504	0.00344	0.22766	0.00431	2.98265	0.1044	0.07652	0.00591	0.540869303	86.48	1528.9	67	1322.2	23	1403.2	27	1490.4	111	0	781	75	66	826	4297	2
Z10	0.09078	0.00278	0.22093	0.00384	2.7647	0.08274	0.056	0.00866	0.58077649	89.24	1441.9	57	1286.8	20	1346.1	22	1101.4	166	0	1600	148	26	466	9224	2
Z11	0.09194	0.00254	0.21246	0.00342	2.69233	0.07294	0.08246	0.01027	0.594171013	84.71	1466.0	52	1241.9	18	1326.4	20	1601.5	192	4	1486	138	31	369	8488	2
Z13	0.08651	0.0029	0.23748	0.00429	2.83188	0.09252	0.16822	0.01769	0.552929135	101.79	1349.5	63	1373.6	22	1364.0	25	3142.6	306	0	1353	119	44	255	7243	2
Z14†	0.08594	0.00347	0.22046	0.00426	2.61151	0.10225	0.05178	0.03729	0.493523881	96.07	1336.8	76	1284.3	23	1303.9	29	1020.5	717	4	683	59	3	58	3875	2

Sample 113019 continued

Spot	$^{207}Pb/^{206}Pb$	1 σ	$^{206}Pb/^{238}U$	1 σ	$^{207}Pb/^{235}U$	1 σ	$^{208}Pb/^{232}Th$	1 σ	rho	Conc. (%)	$^{207}Pb/^{206}Pb$ age	1 σ	$^{206}Pb/^{238}U$ age	1 σ	$^{207}Pb/^{235}U$ age	1 σ	$^{208}Pb/^{232}Th$ age	1 σ	^{204}Pb	^{206}Pb	^{207}Pb	^{238}Pb	^{232}Th	^{238}U	Session
Z15	0.09188	0.00313	0.22186	0.00393	2.80971	0.093	0.1023	0.01049	0.535170407	88.18	1464.9	63	1291.7	21	1358.1	25	1968.7	192	1	768	71	28	268	4257	2
Z16	0.08863	0.00352	0.21485	0.00426	2.62484	0.10046	0.08725	0.0113	0.518064583	89.86	1396.1	74	1254.6	23	1307.6	28	1690.7	210	21	1120	100	33	381	6572	2
Z17†	0.08814	0.00337	0.23582	0.00455	2.86518	0.1065	0.11047	0.01026	0.519078529	98.51	1385.6	72	1364.9	24	1372.8	28	2118.0	187	0	900	80	42	378	4885	2
Z18†	0.09315	0.00279	0.21915	0.00372	2.81356	0.08244	0.05909	0.00735	0.579321522	85.68	1490.9	56	1277.4	20	1359.2	22	1160.4	140	19	1033	97	24	404	5853	2
Z19	0.08931	0.00335	0.22111	0.00422	2.72186	0.09871	0.07943	0.00662	0.526270102	91.28	1410.7	70	1287.7	22	1334.4	27	1544.9	124	24	877	79	56	692	4915	2
Z20	0.0858	0.00437	0.2391	0.00543	2.82667	0.13827	0.07393	0.01351	0.464266556	103.63	1333.6	96	1382.0	28	1362.6	37	1441.6	254	25	786	68	20	265	3943	2
Z22	0.08916	0.00241	0.22258	0.00374	2.73509	0.07398	0.06552	0.00629	0.62121618	92.04	1407.6	51	1295.5	20	1338.0	20	1282.7	119	14	4055	362	73	1124	24386	2
Z23†	0.08893	0.00507	0.23736	0.00589	2.90952	0.15931	0.09317	0.02126	0.453196003	97.89	1402.5	105	1372.9	31	1384.4	41	1800.5	393	0	412	37	12	129	2225	2
Z24†	0.10145	0.0059	0.21759	0.00594	3.04208	0.16706	0.07949	0.02419	0.497102179	76.88	1650.8	104	1269.1	31	1418.2	42	1546.0	453	15	591	61	12	152	3337	2
Z27†	0.08369	0.00407	0.2333	0.00499	2.69132	0.12595	0.00429	0.01653	0.457038698	105.17	1285.3	92	1351.7	26	1326.1	35	86.5	333	0	609	51	0	138	3135	2
Z28	0.09152	0.00324	0.22213	0.00419	2.8029	0.09633	0.06809	0.00356	0.548848965	88.73	1457.4	66	1293.1	22	1356.3	26	1331.5	67	19	1070	98	143	2098	6170	2
Z29	0.09615	0.00431	0.22232	0.00502	2.94712	0.1262	0.08795	0.01388	0.527307135	83.45	1550.7	82	1294.1	26	1394.1	32	1703.8	258	12	879	84	25	291	5148	2
Z31	0.08794	0.00267	0.21726	0.0037	2.63401	0.07824	0.09198	0.00847	0.573337735	91.76	1381.2	57	1267.4	20	1310.2	22	1778.6	157	2	1247	110	41	432	7161	2
Z32†	0.10205	0.00568	0.21772	0.00586	3.06311	0.16128	0.22679	0.04466	0.511188846	76.41	1661.8	100	1269.8	31	1423.5	40	4131.4	736	28	710	72	23	106	4299	2
Z33	0.12913	0.00502	0.23026	0.00495	4.09871	0.15064	0.27961	0.01968	0.58491611	64.04	2086.1	67	1335.9	26	1654.0	30	4983.5	311	16	767	99	105	363	4130	2
Z34	0.08515	0.00361	0.22068	0.00458	2.59039	0.10599	0.13854	0.02493	0.50722747	97.47	1318.8	80	1285.5	24	1297.9	30	2622.4	443	24	1056	90	20	148	6160	2
Z35	0.09175	0.00347	0.21065	0.00405	2.66414	0.09642	0.06895	0.00503	0.53123108	84.28	1462.1	70	1232.3	22	1318.6	27	1347.6	95	0	1248	114	106	1464	7079	2
Z36	0.09006	0.00291	0.21137	0.00361	2.62466	0.08168	0.0592	0.00299	0.548808941	86.64	1426.7	61	1236.1	19	1307.6	23	1162.5	57	0	1854	166	488	7521	10168	2
Z37†	0.08487	0.00345	0.24344	0.0047	2.84797	0.1117	0.0862	0.0127	0.492252755	107.02	1312.4	77	1404.5	24	1368.3	29	1671.3	236	17	704	59	18	206	3471	2
Z38†	0.08217	0.00358	0.22209	0.00448	2.51579	0.10588	0.06198	0.00974	0.479302246	103.47	1249.5	83	1292.9	24	1276.6	31	1215.5	185	3	634	52	17	271	3505	2

† indicates analysis was discarded due to noisy isotopic signal and/or low counts

Appendix 2. Sample 113019- trace element abundance of zircon and garnet

Garnet trace element concentrations with minimum detection limit filtered.

Element	GT01	1 σ	GT02	1 σ	GT03	1 σ	GT05	1 σ	GT06	1 σ	GT07	1 σ	GT08	1 σ	GT09	1 σ	GT10	1 σ	GT11	1 σ
Mg24	23524.49	925.26	25367.03	1005.21	26040.54	1042.53	18964.5	774.85	23324.15	972.65	20267.72	879.07	20415.6	897.48	21885.56	979.12	22137.41	1005	18879.62	870.33
Al27	133745.3	4873.31	130215.48	4751.49	129860.82	4755.42	114943.05	4224.92	126617.7	4653.5	112979.8	4170.3	110254.15	4071.52	116175.74	4314.51	115222.98	4283.51	105665.34	3934.03
Si29	241081.88	13061.28	238734.11	13009.85	230739.73	12688.05	208341.39	11662.33	242935.91	13826.89	215395.22	12667.68	197242.69	11746.18	220908.67	13354.46	205754.48	12604.02	185647.22	11528.54
Ca43	87429.37	2941.32	87059.15	2933.09	89005.28	3016.42	83475.64	2836.05	89005.28	2998.22	78431.28	2626.7	76687.41	2554.62	82690.9	2773.83	80117.97	2674.56	76330.05	2537.42
Ti47	328.58	14.91	373.63	16.8	648.64	28.03	233.47	11.63	678.87	30.55	479.12	22.68	482	23.03	460.03	22.71	515.97	25.57	511.38	25.68
Ti49	323.97	36.78	387.17	43.47	637.03	70.2	251.14	34.12	706.69	88.95	475.49	67.47	496.34	72.94	473.64	72.87	512.96	81.55	540.99	88.94
Cr53	58.89	4.16	47.09	3.69	88.24	5.25	65.84	4.5	78.89	5.08	14.47	2.52	35.35	2.86	54.67	3.91	66.02	4.13	104.3	5.72
Mn55	7483.21	265.07	6756.49	240.54	6305.19	226.24	6228.89	226.53	6190.31	227.72	6743.33	254.3	6502.56	247.19	6052.62	233.17	5992.49	232.98	5858.35	230.01
Fe56	229732.94	13476.69	218084.48	13026.45	215064.59	13123.62	189327.25	12114.89	205845.84	13872.76	189517.58	13897.52	188644.98	14231.89	193415.88	15029.7	190886.91	15259.19	171238.89	14079.65
Fe57	86511.43	4243.22	83392.45	4166.9	82078.67	4192.57	72433.5	3881.68	79432.83	4484	75525.02	4649.08	73768.14	4676.49	76410.97	4998.33	75102.16	5061.37	69387.36	4818.28
Y89	57.19	2.2	61.49	2.39	73.28	2.87	67.04	2.7	67.25	2.77	54.86	2.37	44	1.93	65.27	2.92	72.08	3.28	40.39	1.88
Zr90	0.49	0.15	1.56	0.18	0.93	0.17	0.66	0.16	113.68	5.69	2.65	0.2	2.16	0.17	3.71	0.28	2.51	0.2	0.448	0.093
La139	<0.118	0.042	<0.108	0.04	<0.114	0.041	<0.119	0.042	<0.109	0.04	0.096	0.031	<0.077	0.03	<0.078	0.03	<0.074	0.028	<0.067	0.025
Ce140	<0.090	0.032	0.275	0.04	<0.103	0.038	<0.106	0.038	<0.091	0.034	<0.073	0.029	0.18	0.026	0.121	0.029	0.213	0.032	<0.057	0.022
Pr141	<0.080	0.03	<0.077	0.029	<0.077	0.028	<0.079	0.029	<0.082	0.03	<0.056	0.021	<0.053	0.02	<0.058	0.023	<0.059	0.021	<0.046	0.018
Nd146	<0.48	0.18	<0.46	0.17	<0.51	0.19	<0.49	0.18	<0.52	0.19	<0.35	0.14	<0.31	0.12	<0.37	0.14	0.47	0.12	<0.31	0.11
Sm147	<0.63	0.24	<0.55	0.2	0.56	0.2	0.86	0.25	<0.65	0.23	<0.45	0.17	0.51	0.14	<0.48	0.18	<0.44	0.17	<0.36	0.14
Eu153	0.351	0.064	0.285	0.057	0.319	0.061	0.275	0.057	0.275	0.055	0.217	0.044	0.266	0.045	0.288	0.049	0.217	0.045	0.243	0.037
Gd157	2.7	0.26	2.01	0.26	1.56	0.23	2.05	0.21	1.36	0.24	1.86	0.18	1.57	0.18	1.46	0.21	1.47	0.18	2.28	0.19
Tb159	1.116	0.065	1.087	0.066	0.536	0.046	0.629	0.05	0.545	0.047	0.631	0.044	0.527	0.04	0.537	0.044	0.568	0.044	0.903	0.058
Dy163	9.28	0.39	10.05	0.42	6.49	0.31	8.01	0.37	6.27	0.3	7.49	0.32	5.44	0.25	6.75	0.31	7.78	0.33	8.41	0.35
Ho165	2.18	0.1	2.51	0.12	2.67	0.13	2.76	0.13	2.45	0.12	2.16	0.11	1.631	0.086	2.38	0.12	2.75	0.14	1.667	0.091
Er166	5.99	0.28	6.58	0.3	14	0.59	9.08	0.41	12.28	0.53	6.33	0.3	5.47	0.27	9.36	0.44	9.8	0.46	3.87	0.2
Tm169	0.815	0.052	0.985	0.057	4.03	0.17	1.353	0.072	3.04	0.14	0.892	0.051	0.969	0.054	1.761	0.088	1.542	0.079	0.517	0.037
Yb172	5.72	0.31	7.19	0.36	54.77	2.17	9.82	0.48	37.26	1.56	6.63	0.34	8.31	0.41	14.88	0.71	11.43	0.56	3.67	0.22
Lu175	0.728	0.051	0.951	0.058	14.2	0.55	1.292	0.073	10.29	0.41	0.778	0.048	1.434	0.072	2.3	0.11	1.544	0.079	0.485	0.036
Hf178	<0.37	0.13	<0.37	0.13	<0.37	0.13	<0.35	0.13	2.82	0.27	<0.27	0.11	<0.253	0.091	<0.28	0.11	<0.251	0.092	<0.213	0.079
Pb206	<0.42	0.15	0.44	0.16	<0.45	0.17	<0.39	0.15	<0.48	0.18	0.41	0.12	<0.27	0.11	0.46	0.14	<0.36	0.14	<0.235	0.091
Pb208	<0.233	0.084	0.38	0.09	<0.248	0.091	<0.211	0.078	0.248	0.09	0.44	0.07	<0.171	0.066	0.481	0.076	0.379	0.067	<0.136	0.051
Th232	<0.091	0.033	<0.139	0.046	<0.103	0.038	<0.107	0.038	<0.104	0.039	<0.065	0.026	<0.067	0.024	<0.084	0.031	<0.074	0.027	<0.061	0.024
U238	<0.078	0.029	<0.081	0.029	<0.066	0.026	<0.072	0.026	<0.079	0.031	<0.048	0.019	<0.051	0.019	0.074	0.019	<0.049	0.019	<0.047	0.018

Garnet grain 1
Garnet grain 2

Garnet trace element concentrations normalised to chondrite.

Element	GT01	GT02	GT03	GT05	GT06	GT07	GT08	GT09	GT10	GT11
Location	rim	int	core	rim	core	rim	int	core	int	rim
Mg24	0.1645	0.1774	0.1821	0.1326	0.1631	0.1417	0.1428	0.153	0.1548	0.132
Al27	10.37	10.09	10.07	8.91	9.82	8.76	8.55	9.01	8.93	8.19
Si29	1.507	1.492	1.442	1.302	1.518	1.346	1.233	1.381	1.286	1.16
Ca43	6.48	6.45	6.59	6.18	6.59	5.81	5.68	6.13	5.93	5.65
Ti47	0.502	0.571	0.992	0.357	1.038	0.733	0.737	0.703	0.789	0.782
Ti49	0.495	0.592	0.97	0.384	1.08	0.73	0.76	0.72	0.78	0.83
Cr53	0.0148	0.01185	0.0222	0.0166	0.0198	0.00364	0.00889	0.01375	0.0166	0.0262
Mn55	2.545	2.298	2.145	2.119	2.106	2.294	2.212	2.059	2.038	1.993
Fe56	0.826	0.784	0.774	0.681	0.74	0.682	0.679	0.696	0.687	0.616
Fe57	0.311	0.3	0.295	0.261	0.286	0.272	0.265	0.275	0.27	0.25
Y89	25.42	27.33	32.57	29.8	29.89	24.38	19.56	29.01	32.03	17.95
Zr90	0.088	0.282	0.169	0.12	20.52	0.478	0.389	0.669	0.453	0.081
La139	0	0	0	0	0	0.262	0	0	0	0
Ce140	0	0.288	0	0	0	0	0.188	0.126	0.223	0
Pr141	0	0	0	0	0	0	0	0	0	0
Nd146	0	0	0	0	0	0	0	0	0.66	0
Sm147	0	0	2.44	3.74	0	0	2.23	0	0	0
Eu153	4.04	3.28	3.67	3.17	3.16	2.49	3.06	3.31	2.5	2.79
Gd157	8.83	6.57	5.11	6.69	4.45	6.08	5.13	4.78	4.81	7.45
Tb159	19.24	18.73	9.24	10.84	9.39	10.87	9.09	9.26	9.8	15.57
Dy163	24.37	26.37	17.02	21.01	16.46	19.66	14.28	17.71	20.41	22.07
Ho165	25.58	29.44	31.35	32.44	28.75	25.38	19.17	27.96	32.28	19.59
Er166	24.07	26.44	56.23	36.45	49.32	25.42	21.96	37.58	39.37	15.54
Tm169	22.89	27.68	113.18	37.99	85.41	25.05	27.23	49.48	43.31	14.52
Yb172	23.08	29.01	220.84	39.59	150.23	26.73	33.52	60	46.08	14.8
Lu175	19.1	24.96	372.81	33.91	270.06	20.43	37.64	60.4	40.54	12.74
Hf178	0	0	0	0	15.73	0	0	0	0	0
Pb206	0	0.121	0	0	0	0.112	0	0.125	0	0
Pb208	0	0.104	0	0	0.068	0.121	0	0.132	0.104	0
Th232	0	0	0	0	0	0	0	0	0	0
U238	0	0	0	0	0	0	0	6.09	0	0
LREE (Sm/La)	-	-	-	-	-	-	-	-	-	-
HREE (Lu/Gd)	2.16	3.80	72.96	5.07	60.69	3.36	7.34	12.64	8.43	1.71
MHREE (Lu/Sm)	-	-	152.79	9.07	-	-	16.88	-	-	-
Eu/Eu*	-	-	1.04	0.63	-	-	0.90	-	-	-

Gt06 not plotted due to potential zircon contamination

Garnet grain 1
Garnet grain 2

Appendix 2. Sample 113019- trace element abundance of zircon and garnet

Zircon trace element concentrations with minimum detection limit filtered.

Element	Z06-1	1 σ	Z07-1	1 σ	Z10-1	1 σ	Z17-1	1 σ	Z25A-1	1 σ	Z32A-1	1 σ	Z32B-1	1 σ	Z01-1	1 σ	Z02-2	1 σ	Z03-2	1 σ	Z07-2	1 σ
Al27	1565.48	99.7	27.79	1.87	10.64	0.9	2.39	0.45	35.76	2.67	<1.71	0.71	40.92	3.57	261.5	19.81	6846.63	434.59	1994.12	129.84	3910.71	251.66
Si29	210042.94	23069.73	200352.61	22027.12	201494.11	22183.52	183774.33	20289.28	191206.98	21204.96	184856.34	20644.99	193481.2	21732.33	228765.72	27551.98	210995.72	23983.98	291500.19	34641.85	229666.61	26978.92
Ti49	122.71	11.98	16.99	6.63	<19.22	7.98	21.7	6.68	<26.87	10.95	<27.15	11.33	<53.22	22.48	<236.21	113.58	<107.39	54.48	<250.62	124.65	<212.65	89.52
V51	37.01	2.14	0.28	0.1	<0.31	0.13	<0.26	0.11	<0.38	0.16	<0.42	0.18	<0.84	0.37	<4.04	1.91	19.63	1.82	<4.09	2.11	<3.12	1.32
Fe57	2750.08	125.21	<13.10	5.36	18.19	6.72	<12.73	5.13	<21.66	8.9	<21.87	9.19	<42.77	18.21	<192.98	90.48	<84.44	44.28	<210.82	105.29	281.45	73.3
Y89	34.38	1.44	39.71	1.68	51.95	2.23	48.74	2.17	55.2	2.6	58.65	2.96	32.57	1.79	38.37	2.74	114.69	5.67	105.96	6.02	48.23	2.72
Zr90	536731.88	21174.89	592522	23604.46	551329.75	22202.2	555290.13	22915.08	566582.31	24048.93	543533.81	24190.78	522171.75	23644.51	516854.91	19828.34	556370.56	21314.21	567058.38	21854.93	560932.5	21582.43
Nb93	2.74	0.14	2.87	0.15	2.67	0.15	2.66	0.14	2.59	0.18	2.33	0.18	2.38	0.24	2.36	0.79	2.51	0.5	2.35	0.7	2.95	0.65
La139	<0.024	0.01	<0.0222	0.0092	0.027	0.012	<0.0212	0.0086	<0.036	0.015	<0.036	0.016	<0.075	0.034	<0.33	0.16	5.75	0.31	<0.32	0.17	1.18	0.15
Ce140	0.296	0.019	0.191	0.015	0.047	0.01	0.189	0.016	0.206	0.024	0.215	0.026	0.503	0.056	1.3	0.2	4.78	0.28	0.83	0.17	0.75	0.12
Pr141	0.0467	0.0077	<0.0166	0.0068	<0.0191	0.008	<0.0156	0.0062	<0.027	0.011	<0.026	0.011	<0.051	0.023	<0.23	0.11	1.93	0.14	<0.24	0.12	<0.211	0.087
Nd146	0.11	0.036	<0.094	0.038	0.152	0.045	0.138	0.04	<0.152	0.066	<0.153	0.068	<0.31	0.14	<1.45	0.67	17.7	1.09	<1.57	0.7	<1.30	0.53
Sm147	<0.094	0.038	<0.130	0.052	0.204	0.058	0.13	0.048	<0.196	0.083	<0.187	0.084	<0.37	0.16	<1.60	0.79	2.69	0.49	<1.75	0.84	<1.58	0.66
Eu153	0.097	0.014	0.085	0.014	<0.037	0.016	0.206	0.017	0.143	0.024	0.159	0.027	0.116	0.045	<0.44	0.21	1.45	0.16	<0.50	0.24	<0.41	0.17
Gd157	0.848	0.056	0.955	0.066	0.818	0.072	1.282	0.081	1.3	0.12	1.41	0.13	0.62	0.17	<1.59	0.79	5.26	0.61	3.07	0.96	<1.41	0.6
Tb159	0.255	0.014	0.337	0.017	0.393	0.021	0.403	0.02	0.493	0.03	0.513	0.033	0.272	0.034	0.39	0.14	1	0.1	1	0.18	0.51	0.1
Dy163	3.35	0.14	3.61	0.15	4.48	0.19	4.59	0.2	5.4	0.27	5.52	0.3	3.05	0.23	3.88	0.65	6.47	0.53	9.52	0.96	5.38	0.53
Ho165	1.098	0.049	1.168	0.053	1.511	0.07	1.567	0.076	1.738	0.095	1.83	0.11	0.947	0.071	0.87	0.17	2.42	0.17	3.28	0.28	1.34	0.14
Er166	3.64	0.16	4.24	0.19	4.77	0.22	5.27	0.25	5.81	0.31	7.12	0.42	3.89	0.27	4.56	0.53	6.58	0.46	11.86	0.9	4.7	0.42
Tm169	0.679	0.029	0.814	0.035	0.916	0.04	0.959	0.043	1.124	0.057	1.383	0.074	0.77	0.056	1.01	0.14	0.974	0.096	1.81	0.2	0.93	0.11
Yb172	6.58	0.25	8.67	0.33	8.63	0.34	9.68	0.39	10.19	0.45	13.06	0.61	7.29	0.41	6.61	0.8	6.67	0.54	16.47	1.26	8.17	0.64
Lu175	1.018	0.041	1.244	0.05	1.154	0.048	1.371	0.058	1.349	0.066	1.897	0.096	1.231	0.076	1.23	0.17	1.09	0.11	3.05	0.26	1.29	0.13
Hf178	11012.95	348.41	11540.14	365.07	11638.08	368.2	11262.09	356.27	11180.01	353.94	10579.98	335.02	11485.36	364.08	10903.65	351.3	12246.17	390.86	11749.17	379.02	11743.15	374.4
Ta181	0.051	0.017	<0.039	0.017	0.074	0.019	0.062	0.017	<0.064	0.029	<0.051	0.025	<0.149	0.057	<0.58	0.25	0.22	0.12	<0.53	0.31	<0.47	0.21
Th232	0.566	0.038	0.295	0.029	0.126	0.026	0.929	0.055	0.86	0.075	0.387	0.053	0.613	0.098	0.73	0.3	2.18	0.31	0.82	0.38	0.85	0.23
U238	12.94	0.66	12.12	0.64	3.38	0.19	11.82	0.7	9.06	0.6	12.21	0.89	4.88	0.4	5.84	0.65	11.42	0.85	10.02	0.97	6.58	0.56

Element	Z22-2	1 σ	Z29-2	1 σ	Z31-2	1 σ	Z05-2	1 σ
Al27	6845.83	448.25	79.14	5.37	119.42	8.76	2506.92	176.44
Si29	266527.59	31725.02	144684.39	16446.46	191460.05	21950.31	299409.81	44303.85
Ti49	<206.07	106.05	<30.80	12.51	48.67	26.85	<623.47	309.03
V51	4.99	1.98	<0.53	0.2	0.86	0.46	<9.28	4.75
Fe57	280.57	92.12	<24.78	10.1	35.2	21.62	<501.63	244.21
Y89	72.67	4.52	39.66	1.9	38.78	2.21	125.32	8.97
Zr90	531580.38	20658.82	504081.28	19525.5	534719	20823.31	496765.59	19768.62
Nb93	1.97	0.68	2.01	0.17	2.76	0.38	<2.69	1.55
La139	4.04	0.34	<0.042	0.016	<0.059	0.039	<0.85	0.46
Ce140	15.25	0.83	0.283	0.025	0.402	0.055	0.96	0.4
Pr141	1.69	0.19	<0.029	0.012	0.05	0.025	0.94	0.31
Nd146	9.07	1.09	<0.190	0.077	<0.23	0.13	<3.54	1.8
Sm147	3.4	0.87	<0.233	0.094	0.39	0.2	<4.14	2.16
Eu153	0.74	0.22	0.114	0.025	<0.080	0.055	<1.10	0.54
Gd157	6.59	1.06	0.81	0.11	1.15	0.23	<4.27	2.05
Tb159	0.65	0.14	0.33	0.025	0.343	0.048	<0.65	0.35
Dy163	6.61	0.77	3.69	0.2	3.42	0.31	9.47	1.6
Ho165	2.1	0.22	1.196	0.059	1.11	0.088	3.95	0.49
Er166	6.8	0.64	4.05	0.19	4.06	0.29	22.71	2.02
Tm169	1.05	0.16	0.66	0.032	0.732	0.062	6.76	0.59
Yb172	7.53	0.84	5.74	0.24	6.84	0.44	85.75	4.79
Lu175	1.63	0.19	0.911	0.04	1.05	0.078	21.23	1.1
Hf178	10800.79	348.53	10406.74	329.51	11267.77	358.65	11764.35	389.64
Ta181	<0.51	0.24	0.087	0.031	<0.094	0.059	<1.55	0.72
Th232	0.59	0.32	0.619	0.065	0.78	0.14	28.01	2.58
U238	3.19	0.49	5.95	0.4	5.37	0.47	51.33	4.43

Zircon trace element concentrations normalised to chondrite.

Element	Z06-1	Z07-1	Z10-1	Z17-1	Z25A-1	Z32A-1	Z32B-1	Z01-1	Z02-2	Z03-2	Z07-2	Z22-2	Z29-2	Z31-2	Z05-2
Al27	0.1214	0.00215	0.00082	0.00019	0.00277	0	0.00317	0.0203	0.531	0.155	0.303	0.531	0.00613	0.00926	0.194
Si29	1.31	1.25	1.26	1.15	1.2	1.16	1.21	1.43	1.32	1.82	1.44	1.67	0.9	1.2	1.87
Ti49	0.188	0.026	0	0.033	0	0	0	0	0	0	0	0	0	0.074	0
V51	0.435	0.0033	0	0	0	0	0	0	0.231	0	0	0.059	0	0.0101	0
Fe57	0.00989	0	0.00007	0	0	0	0	0	0	0	0.00101	0.00101	0	0.00013	0
Y89	15.28	17.65	23.09	21.66	24.53	26.07	14.48	17.05	50.97	47.09	21.44	32.3	17.62	17.24	55.7
Zr90	96883.01	106953.43	99518.01	100232.88	102271.18	98110.8	94254.83	93295.11	100427.9	102357.11	101251.35	95953.14	90989.4	96519.67	89668.88
Nb93	7.31	7.65	7.13	7.09	6.92	6.22	6.35	6.29	6.69	6.27	7.87	5.26	5.35	7.37	0
La139	0	0	0.074	0	0	0	0	0	15.66	0	3.21	11.01	0	0	0
Ce140	0.309	0.2	0.049	0.197	0.215	0.225	0.526	1.36	5	0.87	0.78	15.93	0.296	0.42	1
Pr141	0.341	0	0	0	0	0	0	0	14.08	0	0	12.37	0	0.37	6.83
Nd146	0.155	0	0.213	0.194	0	0	0	0	24.9	0	0	12.76	0	0	0
Sm147	0	0	0.88	0.56	0	0	0	0	11.64	0	0	14.7	0	1.68	0
Eu153	1.12	0.98	0	2.37	1.65	1.83	1.33	0	16.63	0	0	8.47	1.31	0	0
Gd157	2.77	3.12	2.67	4.19	4.26	4.6	2.02	0	17.18	10.04	0	21.54	2.65	3.76	0
Tb159	4.4	5.82	6.77	6.95	8.5	8.84	4.69	6.72	17.3	17.22	8.74	11.15	5.69	5.91	0
Dy163	8.8	9.49	11.75	12.05	14.16	14.49	8.01	10.2	16.99	24.99	14.13	17.35	9.69	8.98	24.85
Ho165	12.9	13.72	17.76	18.41	20.42	21.56	11.13	10.18	28.48	38.54	15.79	24.68	14.06	13.04	46.39
Er166	14.63	17.03	19.14	21.15	23.35	28.58	15.61	18.33	26.43	47.62	18.89	27.3	16.25	16.31	91.2
Tm169	19.08	22.85	25.74	26.95	31.56	38.84	21.64	28.23	27.36	50.74	26.13	29.37	18.53	20.57	189.77
Yb172	26.52	34.97	34.81	39.02	41.1	52.66	29.39	26.65	26.9	66.43	32.96	30.37	23.13	27.56	345.78
Lu175	26.73	32.65	30.29	35.98	35.41	49.79	32.3	32.31	28.59	80.15	33.75	42.76	23.92	27.56	557.28
Hf178	61524.88	64470.07	65017.23	62916.7	62458.13	59106.01	64164.04	60914.25	68414.37	65637.83	65604.19	60339.62	58138.18	62948.45	65722.61
Ta181	1.97	0	2.85	2.37	0	0	0	0	8.59	0	0	0	3.36	0	0
Th232	13.31	6.94	2.97	21.86	20.23	9.09	14.42	17.18	51.26	19.39	20.03	13.89	14.57	18.24	658.95
U238	1060.73	993.56	277.02	969.01	742.45	1000.93	400.27	479.07	936.25	821.65	539.16	261.71	487.84	440.57	4207.61
LREE (Sm/La)	-	-	11.89	-	-	-	-	-	0.74	-	0.00	1.34	-	-	-
HREE (Lu/Gd)	9.65	10.46	11.34	8.59	8.31	10.82	15.99	-	1.66	7.98	-	1.99	9.03	7.33	-
MHREE (Lu/Sm)	-	-	34.42	64.25	-	-	-	-	2.46	-	-	2.91	-	16.40	-
Eu/Eu*	-	-	-	1.55	-	-	-	-	1.18	-	-	1.37	-	-	-

Thesis summary

The aims of this project are to: 1) quantify the tectonothermal regimes that define the southern Arunta Region (Aileron Province) in a structural and temporal framework, 2) quantify the tectonothermal events of the Rudall Province in a temporal framework, 3) characterise the crustal Hf isotopic signature of the Aileron Province during the late-Paleoproterozoic, and 4) present a revised tectonic model for the assembly of Proterozoic Australia using new and existing datasets. The following summarises the findings and outcomes of each chapter in consideration of these aims.

Chapter 1 provides new temporal and physical constraints on the metamorphic evolution of the Anmatjira Range, Arunta Region. The study incorporated in situ monazite geochronology and *P−T* pseudosection modelling for metapelites from the southeast Anmatjira Range. In order to address melt loss during metamorphism, a new *P−T* pseudosection modelling method which effectively 'reintegrates' silicate melt into a residual bulk rock composition was employed.

The results indicate that the Anmatjira Range underwent high-thermal gradient, granulite facies metamorphism (800−900 °C, 5.4−6.6 kbar) during the early Mesoproterozoic (*c.* 1580−1555 Ma), with a post-peak evolution characterised by decompression with cooling. Evidence for a possible but poorly-defined earlier metamorphic event at *c.* 1700−1630 Ma may be manifest as rare pseudomorphed andalusite. In the absence of evidence for contemporaneous magmatism during the Chewings Event and/or regional lithospheric thinning due to extension prior to the Chewings Event, the thermal regime required to attain the high-*T*, low-*P* peak conditions at *c.* 1580−1555 Ma was probably generated by burial of high-heat producing *c.* 1820−1780 Ma granitoids in the Anmatjira-Reynolds Range region.

Chapter 2 provides constraints on the timing and physical conditions of granulite facies metamorphism in the Mount Hay Block and Adla Domain in the southern Aileron Province. The Mount Hay Block and Adla Domain outcrop immediately north of the postulated southern paleo-margin of the North Australian Craton (NAC) during the Paleoproterozoic and are thus are located in a key area with respect to understanding the Proterozoic tectonic evolution of the NAC. Distinct structural domains within the area can be distinguished using Total Magnetic Intensity (TMI) imagery, revealing a km-scale 'boudin', which comprises the Mount Hay Massif. The Mount Hay Massif is bound by a linear structural belt that extends ~100 km in an east–west direction, corresponding to the Adla Domain.

Monazite U–Pb geochronology and *P–T* pseudosection modelling on garnet–sillimanite bearing metasediments indicate that the area experienced granulite facies conditions at *c.* 1760−1740 Ma with the attainment of peak conditions of ~8–10 kbar, ~850−900 °C for Mount Hay and the adjacent Capricorn Ridge, and ~7–10 kbar, ~850−900 °C for the Adla Domain. In addition, minor monazite age groupings at *c.* 1570–1540 Ma that are variably present in the samples and a kinematically late garnet-bearing pegmatite, which yields a single monazite population at *c.* 1540 Ma, suggests the area also experienced a younger phase of metamorphism and structural reactivation.

If deformation preserved on the Mount Hay Massif developed in a contractional setting, whereas the development of the Capricorn Ridge subsequently occurred in an oblique-divergent setting, as proposed by previous studies (Waters-Tormey et al., 2009; Bonamici et al., 2011), the age data obtained in this study it suggests that the switch from contractional to extensional tectonics was relatively rapid. In the context of an envisaged retreating margin setting, the Mount Hay area may have been situated in a back-arc environment in which the deformation and metamorphism preserved on the Mount Hay Massif occurred during a short-lived compressional phase, potentially as a result of the arrival of more buoyant oceanic crust/plateaux, followed by renewed extension. Such a scenario is one way in which deformation and orogenesis could be localised into narrow belts (< 100 km wide), such as the Mount Hay area and Adla Domain.

Chapter 3 investigates the zircon Hf isotopic signature of *c.* 1640 Ma granitoids from the Aileron Province in order to gain insights into the crustal and tectonic evolution of the southern Arunta Region during the latest Paleoproterozoic. This timeline in the Arunta Region is interpreted to be significant as it has been postulated to have involved the accretion of the Warumpi Province onto the Aileron Province (NAC) as an exotic terrane (Scrimgeour et al., 2005) or reattachment of the Warumpi Province after rifting from the Aileron Province (Hollis et al., 2013). The samples in this study give zircon εHf values of -6.2 to +1.5, occurring near and below CHUR and crustal model ages between 2200–2700 Ma. The Lu–Hf isotopic results, in combination with existing Lu–Hf data from the Aileron and Warumpi Provinces suggest that the late Paleoproterozoic magmatism in the Aileron Province was mostly derived from melting of NAC crust. Evidence for sedimentation and mafic-ultramafic magmatism approximately contemporaneous with the Liebig Orogeny in the southern Arunta Region is suggestive of at least some component of extension. Combined with the recent identification of extensive Grenvillian-aged reworking in the southern Arunta Region (Morrissey et al., 2011; Wong et al., submitted), which occurs at the interface of a geophysically imaged south-dipping, lithospheric scale structure interpreted to be a fossil subduction zone (Selway et al., 2009), the Paleoproterozoic Liebig Orogeny may feasibly reflect the rifting of the Warumpi Province from the NAC as part of a long lived (>150 M.y.), retreating margin on southern NAC. If true, the Warumpi Province may have been separated from the NAC for *c.*500 Myr until it reamalgamated during the Mesoproterozoic.

Chapter 4 investigates the physical conditions and timing of medium-*P* metamorphism of the Yapungku Orogeny in the Rudall Province, a multiply metamorphosed terrane that has been previously been inferred to record the collision of the NAC and WAC at *c.* 1780 Ma, as reflected by the Yapungku Orogeny. Chapter 4 is the first direct geochronological and modern metamorphic study on rocks with mineral assemblages inferred to have grown during the Yapungku Orogeny. In addition, it provides the first age constraints on a high-thermal gradient metamorphosed garnet- orthopyroxene assemblage that is also present in the area. The results indicate that metamorphism in the Rudall Province is Mesoproterozoic-aged, rather than during the Paleoproterozoic. These results have implications for the amalgamation of Proterozoic Australia. Importantly, if the Yapungku Orogeny in Rudall Province does reflect the amalgamation of the NAC and WAC, it occurred during the Mesoproterozoic and not the Paleoproterozoic as previously assumed. A tectonic scenario for the Mesoproterozoic tectonic evolution of Australia is presented in Chapter 4, which advocates for the protracted Mesoproterozoic amalgamation of cratonic Australia.

Closing comments

This project has endeavoured to provide further constraints on the tectonic evolution of important, yet debated or poorly understood areas of Proterozoic Australia. Key outcomes of this work include: a) new temporal and metamorphic constraints to further understand the southern margin of the NAC during the Paleoproterozoic, b) new temporal and metamorphic constraints on metamorphic rocks in the Rudall Province that provide evidence for the Yapungku Orogeny, and the proposed collision of the WAC and NAC being Mesoproterozoic, rather than Paleoproterozoic in age, and

c) a revised tectonic model of Proterozoic Australia during the Mesoproterozoic, in support of a Mesoproterozoic timeline assembly of cratonic Australia, and coinciding with the breakup of supercontinent Nuna (cf. Pisarevsky et al., 2014). The findings of this project have substantial implications for Nuna reconstructions. If the NAC and WAC did not join until *c.* 1300 Ma, there is no requirement for the NAC and WAC to have been in close proximity during supercontinent Nuna (e.g. Zhang et al., 2012).

As some final remarks, the Rudall Province remains an understudied region, due to its remoteness and limitations on access. The reconnaissance work on Rudall Province in this project has highlighted the importance of the Mesoproterozoic timeline in the Rudall Province, which has not been fully recognised previously. Future work on the Rudall Province involving more age and Hf isotopic studies on targeted sedimentary and igneous derived rocks, and further characterisation of the tectonothermal events recorded in the Rudall Province would be highly beneficial in deciphering the complicated evolution of the area. More broadly, the nature and extent of Mesoproterozoic tectonism in Australia is yet to be fully understood. This study supports hypothesis that the cratonic components of Australia did not assemble until the Mesoproterozoic (Myers et al., 1996; Smits et al., 2014). Future isotopic, structural, metamorphic and geophysical studies targeting data-poor or debated Australian Mesoproterozoic terrains would allow this hypothesis to be further examined and would aid in deciphering the configuration of cratonic Australia in supercontinent assembly and dispersal.

References

Bonamici, C.E., Tikoff, B., Goodwin, L.B., 2011. Anatomy of a 10 km scale sheath fold, Mount Hay ridge, Arunta Region, central Australia: The structural record of deep crustal flow. Tectonics 30, 19.

Hollis, J.A., Kirkland, C.L., Spaggiari, C.V., Tyler, I.M., Haines, P.W., Wingate, M.T.D., Belousova, E., Murphy, R.C., 2013. Zircon U-Pb-Hf isotope evidence for links between the Warumpi and Aileron Provinces, West Arunta Region. Geological Survey of Western Australia, Perth.

Morrissey, L., Payne, J.L., Kelsey, D.E., Hand, M., 2011. Grenvillian-aged reworking in the North Australian Craton, central Australia: constraints from geochronology and modelled phase equilibria. Precambrian Research 191, 141-165.

Myers, J.S., Shaw, R.D., Tyler, I.M., 1996. Tectonic evolution of Proterozoic Australia. Tectonics 15, 1431-1446.

Pisarevsky, S.A., Elming, S.-Å., Pesonen, L.J., Li, Z.-X., 2014. Mesoproterozoic paleogeography: Supercontinent and beyond. Precambrian Research 244, 207-225.

Scrimgeour, I.R., Kinny, P.D., Close, D.F., Edgoose, C.J., 2005. High-T granulites and polymetamorphism in the southern Arunta Region, central Australia: Evidence for a 1.64 Ga accretional event. Precambrian Research 142, 1-27.

Selway, K., Hand, M., Heinson, G.S., Payne, J.L., 2009. Magnetotelluric constraints on subduction polarity: Reversing reconstruction models for Proterozoic Australia. Geology 37, 799-802.

Smits, R.G., Collins, W.J., Hand, M., Dutch, R., Payne, J., 2014. A Proterozoic Wilson cycle identified by Hf isotopes in central Australia: Implications for the assembly of Proterozoic Australia and Rodinia. Geology 42, 231-234.

Waters-Tormey, C., Goodwin, L.B., Tikoff, B., Staffier, K., Kelso, P., 2009. A granulite-facies normal shear zone exposed in the Arunta inlier of central Australia: Implications for deep-crustal deformation during oblique divergence. Geological Society of America Special Papers 456, 267-286.

Wong, B.L., Morrissey, L.J., Hand, M., Fields, C.E., Kelsey, D.E., submitted. Grenvillian-aged reworking of late Paleoproterozoic crust of the southern North Australian Craton, central Australia: implications for the assembly of Mesoproterozoic Australia. Precambrian Research.

Zhang, S., Li, Z.-X., Evans, D.A.D., Wu, H., Li, H., Dong, J., 2012. Pre-Rodinia supercontinent Nuna shaping up: A global synthesis with new paleomagnetic results from North China. Earth and Planetary Science Letters 353, 145-155.